INVESTIGATION OF THE SHEAR-STRENGTH OF BUILT-UP I-SECTION MEMBERS VIA TEST SIMULATION

A Thesis
Presented to
The Academic Faculty

by

Amit Prashant Jha

In Partial Fulfillment
of the Requirements for the Degree
Master of Science in Civil Engineering in the
School of Civil and Environmental Engineering

Georgia Institute of Technology

December 2016

INVESTIGATION OF THE SHEAR-STRENGTH OF BUILT-UP I-SECTION MEMBERS VIA TEST SIMULATION

Approved by:

Dr. Donald W. White, Advisor
School of Civil and Environmental Engineering
Georgia Institute of Technology

Dr. Abdul-Hamid Zureick
School of Civil and Environmental Engineering
Georgia Institute of Technology

Dr. D. Brad Davis
School of Civil Engineering
University of Kentucky

Date Approved: August 22, 2016

To my family, for their unconditional love and support

ACKNOWLEDGEMENTS

I would like to express my sincere gratitude and appreciation for the opportunity and guidance provided my advisor, Dr. Donald W. White., without which this work would not have been possible. His expertise in the field of structural engineering and his love for research is remarkable.

I also wish to thank the rest of my committee members, Dr. Abdul-Hamid Zureick and Dr. Brad Davis for their valuable comments.

I would like to thank my friends for their valuable help and support, especially Lakshmi Subramanian, Ajinkya Lokhande and Oguzhan Togay.

TABLE OF CONTENTS

LIST OF TABLES

LIST OF FIGURES

SUMMARY

The ANSI/AISC 360-10 Specification Chapter G does not account for postbuckling shear strength of unstiffened I-section web panels. Prior research has demonstrated that considerable postbuckling shear strength is available in unstiffened webs. Numerous prediction models have been developed to explain the shear postbuckling resistance of transversely stiffened webs. The number of these theories is an indicator of the complexity of the I-section member shear limit states behavior. A smaller number of prediction models have been recommended to explain the behavior of unstiffened web panels. This research aims to explain the mechanisms of development of shear strength in built-up I-section members having stiffened and unstiffened webs, with emphasis on the behavior for cases with widely-spaced transverse stiffeners. Sensitivities of the shear resistance to imperfection magnitude, flange thickness and potential end anchorage details also are considered.

In this research, Finite Element Analysis (FEA) test simulations are constructed of a suite of experimental tests that were performed by other investigators to evaluate shear strength. The simulation results are compared to the experimental results. Three specimens with panel aspect ratios a/h of 2.0, 4.12 and 8.04 are scrutinized to evaluate the mechanisms behind the development of their shear strength. The stresses are plotted on various section cuts to provide a detailed evaluation of the web behavior. In addition, these specimens are studied with different flange thickness, imperfection magnitude and potential end anchorage conditions, and the influence of these attributes on the shear strength is assessed.

CHAPTER 1

INTRODUCTION

1.1 Problem Statement & Objectives

To minimize cost, built-up I-section members are often constructed using slender webs. In addition, unstiffened webs are common in many situations because of the cost of placing intermediate transverse stiffeners. For such cases, shear strength becomes an important limit state and in certain circumstances may govern the design of the member.

Considerable research has been conducted to understand the mechanism for development of shear strength in transversely stiffened I-girder webs, defined as webs with a panel aspect ratio a/h less than or equal to three, where a is the stiffener spacing and h is the web depth. However, there has been limited research (for example, Höglund (1973 and 1997) and Lee et al. (2008)) addressing the shear strength of unstiffened I-girder webs.

Daley et al. (2016) compared the ratio of the measured ultimate shear resistance from 20 prior and seven new unstiffened I-girder experimental tests to the shear strength obtained from a number of existing prediction equations. They recommended a form of Höglund's (1997) prediction equations, adapted to the traditional format of the shear resistance equations in the AISC Specifications. They showed that this model is much more in agreement with the measured shear strengths, and that it gives predicted strengths as high as 3.66 times the result from Basler's (1961) equations. The recommended method, which is adopted within the AISC (2016) Specification, takes the postbuckling strength of unstiffened webs into account whereas Basler's method is based solely on the idealized web shear buckling resistance. Yoo and Lee (2006) have provided a detailed evaluation of the mechanisms behind the development of postbuckling shear strength in transversely stiffened panels. However, their studies focus predominantly on web panels with an aspect

ratio *a*/*h* of one. There is no literature at present that provides a comparable explanation of the mechanisms behind the development of the shear strength in unstiffened panels.

The primary objective of this research is to improve the understanding of the mechanism of development of shear strength in built-up I-section members having transversely stiffened and unstiffened webs, with emphasis on the behavior for cases with widely-spaced transverse stiffeners. The secondary objective is to evaluate the influence of the slenderness ratio, *a/h* ratio, flange thickness, anchorage at the ends of simply supported girders, and imperfection magnitude on the shear strength.

To achieve the above objectives, finite element analysis simulations are conducted of seven experiments performed at University of Kentucky (Daley and Davis 2015). In addition to these, two unstiffened girder experiments conducted by Höglund (1971) and two transversely stiffened girder experiments conducted by Lee and Yoo (1999) are analyzed. The simulation results were compared with the results from the experiments. Two specimens within the unstiffened range from Daley and Davis (2015); one with comparatively small *a/h* and the other with high *a/h*, and one transversely stiffened specimen from Lee and Yoo (1999) are scrutinized to evaluate the mechanisms behind the development of their shear strength. The stresses are plotted on various sections to provide a detailed assessment of their shear strength behavior.

1.2 Literature Review

Since Wagner (1931), numerous research efforts have been devoted to understanding the shear resistance of steel plate girders; however, these studies have mostly addressed transversely stiffened web panels, that is, web panels bounded by transverse stiffeners with a spacing not exceeding three times the web depth. The following are several of the most prominent theories that aim to quantify the shear strength of built-up I-section members,

with an emphasis on unstiffened webs. White and Barker (2008) and Ziemian (2010) provide an overview of various additional theories. Appendix A summarizes several prominent prediction models for transversely stiffened webs.

1.2.1 Basler's Theory

Basler (1960 and 1961) is the foundation for the shear strength provisions in the American Institute of Steel Construction, *Specifications for Structural Buildings* (AISC 2010) and American Association for State and Highway Transportation Officials, *LRFD Bridge Design Specifications* (AASHTO 2015). Basler established a method to account for the postbuckling strength, referred to as Tension Field Action (TFA), for transversely stiffened plate girders. He theorized that, the web is subjected to a state of pure shear until the shear buckling capacity of the web is reached and that there is no increase in the principal compressive stress thereafter. The Tension Field Action that develops in the web is equilibrated by the transverse stiffeners. The system behaves like a Pratt truss with diagonals in tension and verticals in compression. Basler reasoned that for an unstiffened plate girder there is no Tension Field Action because there are no transverse stiffeners. Therefore, the shear resistance is limited to the shear buckling strength. Basler (1961) references Bleich (1952) for the calculation of the critical elastic shear stress

$$\tau_e = \frac{k_v \pi^2 E}{12(1-\nu^2)(h/t_w)^2} \tag{1-1}$$

where,

k_v = plate shear buckling coefficient

ν = Poisson's ratio of steel

h = web depth

t_w = web thickness

E = modulus of elasticity

The plate shear buckling coefficient, k_v, depends on web aspect ratio (a/h) and varies with the type of boundary condition between the flanges and the web. This coefficient gives the most conservative result when the boundary conditions are assumed to be pinned. The shear buckling coefficient for this simply supported case is given by

$$k_v = 4 + \frac{5.34}{(a/h)^2} \text{ for } a/h \le 1 \tag{1-2}$$

$$k_v = 5.34 + \frac{4}{(a/h)^2} \text{ for } a/h > 1 \tag{1-3}$$

For a long unstiffened panel, this value converges to 5.34. From Mises' yield criterion for plane stress, the shear yield stress, τ_y, is $F_y/\sqrt{3}$. Therefore, the maximum possible shear strength

$$V_p = (F_y/\sqrt{3})A_w = 0.577F_yA_w \tag{1-4}$$

is obtained when yielding occurs throughout the web, where A_w is area of the web, taken by Basler as t_wh, and F_y is the uniaxial yield stress.

Due to the influence of residual stresses and geometric imperfections, the ultimate web shear strength can occur at an average shear stress smaller than the shear yield strength. To account for this, Basler introduced the factor C_v. The corresponding nominal shear strength is given by the equation,

$$V_n = 0.577F_yA_wC_v \tag{1-5}$$

The variable, C_v is defined as the ratio of shear buckling stress and the shear yield stress. The shear strength equation in the AISC (1963) and subsequent AISC Specifications is based on the Basler's method with slight modifications. AISC rounded the shear yield stress from $0.577F_y$ to $0.6F_y$ and increased the area A_w from $t_w h$ to $t_w d$, where d is the overall depth of the beam. Hence, the underlying AISC nominal shear strength is taken as

$$V_n = 0.6F_y A_w C_v \tag{1-6}$$

with $A_w = t_w d$.

For a stocky web with $h/t_w \le 1.10\sqrt{k_v E/F_y}, C_v = 1.0$, there is no reduction in the capacity and the section can reach its plastic shear strength. For a web with an intermediate slenderness ratio, the web buckles inelastically. Basler computed the inelastic buckling stress, τ_{cr}, using a nonlinear transition equation, $\tau_{cr} = c(\tau_e)^n$. The value, $c = (\tau_{pr})^{1-n}$, where τ_{pr} is the proportional limit where the critical shear stress is equal to inelastic shear stress. From trial-fit to the experimental tests he found the value of τ_{pr} to be equal to $0.8\tau_y$ and the value of the exponent n to be 0.5.

$$\tau_{cr} = (\tau_e \tau_y)^{0.5} \tag{1-7}$$

Correspondingly, in this inelastic range, i.e., for $1.1\sqrt{k_v E/F_y} < h/t_w \le 1.37\sqrt{k_v E/F_y}$,

$$C_v = \frac{1.1\sqrt{k_v E/F_y}}{h/t_w} \tag{1-8}$$

For the case of slender webs with $h/t_w > 1.37\sqrt{k_v E/F_y}$, the web is assumed to fail by elastic buckling prior to web yielding. For such cases,

$$C_v = \frac{1.51 k_v \mathrm{E}}{F_y (h/t_w)^2} \tag{1-9}$$

which is determined by substituting $\nu = 0.3$ in Eq. (1-1). AISC (1986) adopted the following modified shear buckling coefficient proposed by Vincent (1969)

$$k_v = 5 + \frac{5}{(a/h)^2} \text{ for } a/h \le 3 \tag{1-10}$$

$$k_v = 5 \text{ for } a/h > 3 \tag{1-11}$$

1.2.2 Höglund's Method

Höglund (1973) stated that transverse stiffeners are not necessary in order to develop post-buckling shear strength. Neglecting the flexural stresses, he assumed the web to be subjected to a state of pure shear up to the elastic buckling strength, τ_e. At this state the principal stresses at the web mid-depth (for a doubly-symmetric I-section) are inclined at 45° and the compressive and tensile principal stresses are equal to $-\tau_e$ and τ_e respectively (Fig. 1-1).

After buckling, Höglund assumed that the tensile stress σ_1 increases, but the compressive stress, σ_2, remains essentially the same. For an unstiffened web the principal stress angle changes such that the vertical force applied to the flanges is zero (see Fig. 1.2). Due to this change in the inclination of the tensile stress, Höglund referred to his theory as "*rotated stress field theory*".

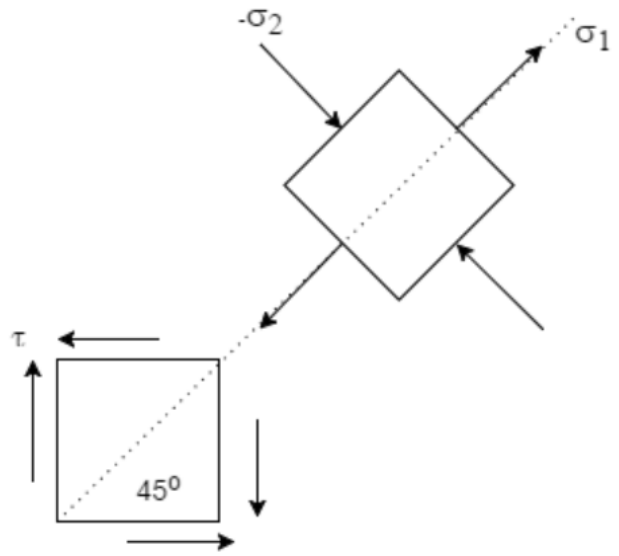

Fig. 1-1. Pure shear state in web at elastic buckling.

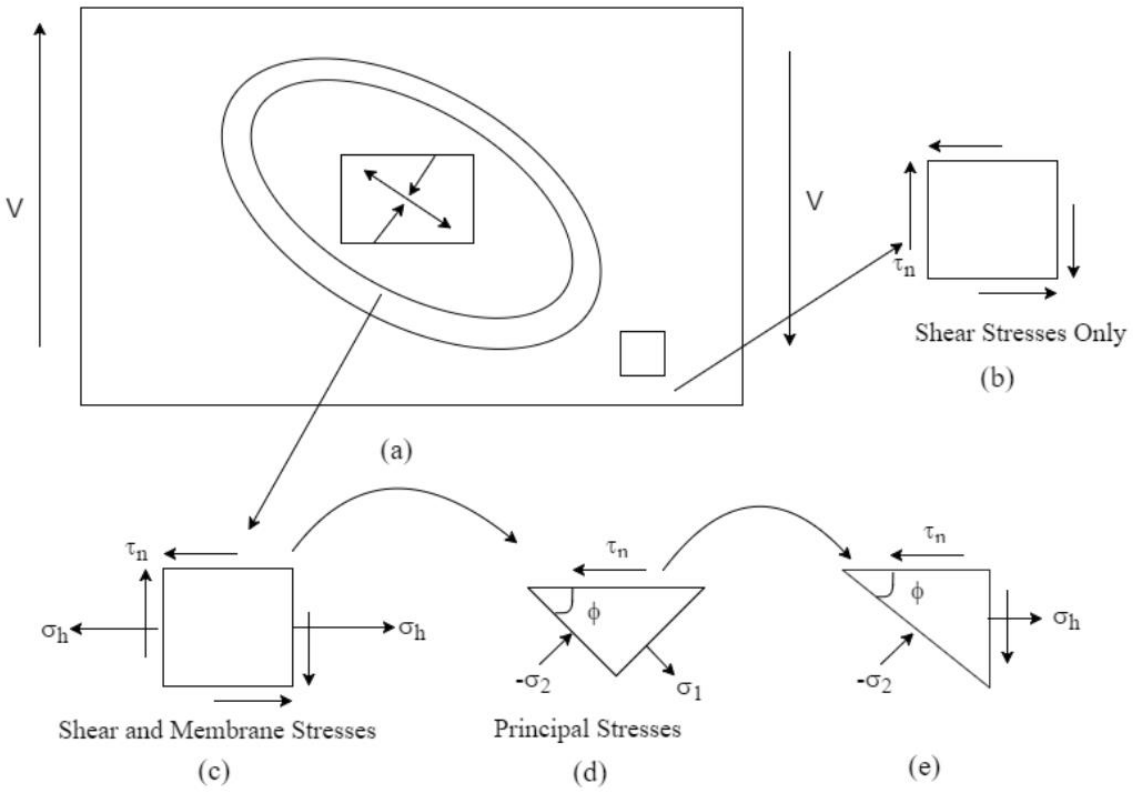

Fig. 1-2. Post-buckling state of stress in a beam web, from (Höglund 1997).

Höglund's rotated stress field theory equations may be derived as follows. In a long member with transverse stiffeners only at its ends, nothing but the web prevents the flanges from moving toward each other. Therefore, Höglund assumed that the membrane stress in the transverse direction is effectively zero. As such, equilibrium of the triangle in Fig. 1-2d gives

$$\sigma_1 = \frac{\tau_n}{\tan\phi} \tag{1-12}$$

$$\sigma_2 = -\tau_n \tan\phi \tag{1-13}$$

where τ_n is the nominal shear resistance of the web in terms of an idealized uniform stress. From Fig. 1-2e, one can determine that this state of stress has a component

$$\sigma_h = \tau_n \left(\frac{1}{\tan\phi} - \tan\phi \right) = \sigma_1 + \sigma_2 \tag{1-14}$$

in the longitudinal direction. Höglund (1997) points out that the total longitudinal force in the web is generally less than

$$N_h = \sigma_h h t_w \tag{1-15}$$

though, because in the physical girder, the stress state is close to pure shear at the top and bottom of the web, adjacent to the flanges. Höglund concludes that the force N_h has to be anchored at the ends of the beam by a "transverse short beam," which he calls a rigid end post. As such, he provides specific requirements detailing configurations with essentially two transverse stiffeners serving as flanges of the effective "transverse short beam" at the beam ends. This end post is supported by the flanges, which results in additional compressive forces in the flanges at the ends of the beam. However, Höglund also shows substantial postbuckling strength, only slightly smaller than that obtained for beams having rigid end posts, for general end details that do not satisfy his rigid end post requirements.

Höglund (1997) derives the ultimate shear strength of the beam using the von Mises yield criterion

$$\sigma_1^2 - \sigma_1\sigma_2 + \sigma_2^2 = F_y^2 \tag{1-16}$$

assuming that the compressive stress remains equal to the shear buckling stress after buckling, i.e.,

$$\sigma_2 = -\tau_n \tan\phi = -\tau_e \tag{1-17}$$

but acting at a smaller angle than 45°, given by

$$\tan\phi = \frac{\tau_e}{\tau_n} \tag{1-18}$$

Furthermore, given Eq. (1-18), the major principal stress may be written as

$$\sigma_1 = \frac{\tau_n}{\tan\phi} = \frac{\tau_n^2}{\tau_e} \tag{1-19}$$

The inclination of the tension stress σ_1, defined by the angle ϕ, decreases when the ratio τ_u/τ_e increases, which is why this method is referred to as the rotated stress field theory.

Upon substituting Eqs. (1-17) and (1-18) and the shear yield strength

$$\tau_y = \frac{F_y}{\sqrt{3}} \tag{1-20}$$

into the yield criterion, Eq. (1-16), then solving for the ratio of τ to τ_y, one can write

$$\frac{\tau_n}{\tau_y} = \sqrt[4]{3}\sqrt{\frac{\tau_e}{\tau_y}}\sqrt{\sqrt{1-\frac{1}{4}\left(\frac{\tau_e}{\tau_y}\right)^2} - \frac{1}{2\sqrt{3}}\left(\frac{\tau_e}{\tau_y}\right)} \tag{1-21}$$

Then, upon introducing the slenderness parameter

$$\lambda_w = \sqrt{\frac{\tau_y}{\tau_e}} \tag{1-22}$$

the following expression is obtained

$$\frac{\tau_n}{\tau_y} = \frac{\sqrt[4]{3}}{\lambda_w}\sqrt{\sqrt{1-\frac{1}{4\lambda_w^4}} - \frac{1}{2\sqrt{3}\,\lambda_w^2}} \tag{1-23}$$

This is Eq. (11) in Höglund (1997), which Höglund uses for $\lambda_w \geq 1.0$. Höglund points out that the term under the outside square root in Eq. (1-23) is close to 1.0 for $\lambda_w \geq 2.5$, and therefore

$$\frac{\tau_n}{\tau_y} \cong \frac{1.32}{\lambda_w} \tag{1-24}$$

for $\lambda_w \geq 2.5$.

Höglund (1997) indicates that the rotated stress field theory based resistance is in Eurocode 3, Part 1.5 (CEN 2006), as

$$V_n = \rho_w F_y h t_w \tag{1-25}$$

for members having non-rigid end posts, where

$$\rho_w = \eta = \frac{1}{\sqrt{3}} \cong 0.6 \tag{1-26}$$

for $\lambda_w \leq 0.48/\eta$, and

$$\rho_w = \frac{0.48}{\lambda_w} \tag{1-27}$$

for $\lambda_w > 0.48/\eta$. In addition to the consideration of non-rigid end post behavior, the term 0.48 in these equations is reduced from $\frac{1.32}{\sqrt{3}}\sqrt{\sqrt{1-\frac{1}{4\lambda_w^4}}-\frac{1}{2\sqrt{3}\,\lambda_w^2}}$ $= 0.76\sqrt{\sqrt{1-\frac{1}{4\lambda_w^4}}-\frac{1}{2\sqrt{3}\,\lambda_w^2}}$ "to allow for scatter in the test results as a result of initial imperfections and plastic buckling." It should be noted that this expression is equal to 0.577 at $\lambda_w = 1.0$, which is the theoretical limit of Eq. (1-23).

Höglund (1997) actually explains that the term η may be taken as 0.7 for steels with $F_y \leq 50$ ksi, in recognition of the strain-hardening characteristics of these steels. The simpler form applicable to all steel yield strengths is shown above.

If one recognizes that

$$\lambda_w = \sqrt{\frac{\tau_y}{\tau_e}} = \sqrt{\frac{F_y/\sqrt{3}}{\dfrac{k_v \pi^2 E}{12(1-\nu^2)(h/t_w)^2}}} = 0.80\sqrt{\frac{F_y}{k_v E}}\frac{h}{t_w} \tag{1-28}$$

such that $\lambda_w = 0.48/\eta = 0.48/0.6 = 0.8$ corresponds to $\frac{h}{t_w} = 1.0\sqrt{\frac{k_v E}{F_y}}$, Eqs. (1-27) can be translated into the common format used within the AISC and AASHTO Specifications of

$$\rho_w = 0.6\left(\frac{1.0\sqrt{\frac{k_v E}{F_y}}}{h/t_w}\right) \tag{1-29}$$

valid for $\frac{h}{t_w} > 1.0\sqrt{\frac{k_v E}{F_y}}$, where the term 0.6 multiplied by F_y is the AISC approximation of the shear yield stress. It should be noted that the term inside the brackets of Eq. (1-29) is simply 1/1.1 of the C_v expression given by Eq. (1-8).

Höglund (1997) uses the above equations to quantify the contribution from the web to the member shear resistance in both unstiffened and transversely stiffened members. For members with unstiffened webs, these equations are taken as the only source of the member shear strength. However, for members with transversely stiffened webs, Höglund recommends that an additional contribution be included based on an approximation of the frame action of the flanges. That is, a flange contribution is added to the above web contribution based on an approximate plastic mechanism resistance of the flanges. It is assumed that the above shear resistance of the web is not influenced by the additional forces developed between the web and the flanges associated with the plastic mechanism response of the flanges. The calculation of this flange contribution is discussed further in Appendix A Section 4, in the context of the model recommended by Daley et al. (2016).

1.2.3 Lee et al. Method

Lee et al. (1996) examined finite element analysis results for over 300 hypothetical plate girders and found that the web top and bottom boundary condition is between pinned and fixed. Bulson (1970) shows the following shear buckling coefficient for a panel that is clamped at its top and bottom edges and simply-supported on the other two edges:

$$k_{sf} = \frac{5.34}{(a/h)^2} + \frac{2.31}{a/h} - 3.44 + 8.39(a/h) \text{ for } a/h < 1 \tag{1-30}$$

$$k_{sf} = 8.98 + \frac{5.61}{(a/h)^2} + \frac{1.99}{(a/h)^3} \text{ for } a/h > 1 \tag{1-31}$$

Lee et al. (1996) concluded that shear buckling coefficient, k_v, for unstiffened web plate depends on flange-to-web thickness ratio and varies between k_{sf} and k_v. They put forward the following equation for k_v:

$$k_v = k_{ss} + 0.8(k_{sf} - k_{ss})\left[1 - \frac{2}{3}\left(2 - \frac{t_f}{t_w}\right)\right] \text{ for } 0.5 < t_f / t_w \le 2 \tag{1-12}$$

$$k_v = k_{ss} + 0.8(k_{sf} - k_{ss}) \text{ if } t_f / t_w > 2 \tag{1-33}$$

where, k_{ss} is same as k_v for pinned conditions as in Equation (1-2) and (1-3).

Lee and Yoo (1998 and 1999) and Lee et al. (2008) observed that the post-buckling strength, V_{PB}, is approximately 40% of the difference between elastic shear buckling strength and the plastic shear strength for a transversely stiffened panel, i.e.,

$$V_{PB} = 0.4(V_P - V_{cr}) \tag{1-34}$$

where,

V_{cr} is the shear buckling strength computed using plate buckling coefficient by Eq. (1-32 and 1-33)

V_p is the plastic shear strength given by $V_p = 0.58F_y t_w h$.

Therefore, they expressed the ultimate shear strength as,

$$V_u = V_{cr} + V_{PB} = V_{cr} + 0.4(V_p - V_{cr}) = V_p(0.6C + 0.4) \quad (1\text{-}35)$$

where C is defined by the ratio of the elastic shear buckling shear strength to the plastic shear strength. The variable C is almost identical to C_v, used by AISC 2010 *Specification* with slight modifications. The variable C_v they used is identical to the equations in the AASHTO (2015) *Specifications.* The difference in C_v values obtained from AISC (2010) and AASHTO (2015) is due to the fact that AASHTO assumes shear yield stress to be $0.58F_y$ as opposed to $0.6F_y$ in AISC.

$$C_v = 1.0 \text{ for } h/t_w \le 1.12\sqrt{k_v E/F_y} \quad (1\text{-}36)$$

$$C_v = \frac{1.12\sqrt{k_v E/F_y}}{h/t_w} \text{ for } 1.12\sqrt{k_v E/F_y} < h/t_w \le 1.40\sqrt{k_v E/F_y} \quad (1\text{-}37)$$

$$C_v = \frac{1.57k_v \mathrm{E}}{F_y (h/t_w)^2} \text{ for } h/t_w > 1.40\sqrt{k_w E/F_y} \quad (1\text{-}38)$$

Lee and Yoo (1998) concluded that the "flange rigidity seems to have very little effect on the postbuckling strength of web panels". They also remarked that the through thickness plate bending stresses in the web have a significant effect near the failure condition.

Lee and Yoo (2008) extended their theory to long panels. They performed nonlinear FEA simulations on hypothetical plate girders with *a/h* between 3.0 to 6.0 and with a wide range of slenderness ratios. They found that their previous equations were accurate for lower values of h/t_w. However, for higher values of h/t_w the equations proved to be unconservative. They developed an adjustment factor, λ, to match better the FEA predictions.

$$\lambda = 1.0 \text{ for } C_v \geq 0.3 \tag{1-39}$$

$$\lambda = 1.35C_v + 0.6 \text{ for } 0.1 < C_v < 0.3 \tag{1-40}$$

$$\lambda = 5.62C_v + 0.145 \text{ for } C_v \leq 0.1 \tag{1-41}$$

They also studied the effect of large initial imperfections the ultimate strength of FEA models. They further formulated an adjustment factor, *R*, to account for the large initial imperfections, *D*/120, which they interpreted to be a maximum value of out-of-flatness allowed in Bridge Welding Code (AWS 2002). They predicted the final shear strength as,

$$V_n = R\lambda V_p(0.6C_v + 0.4) \tag{1-42}$$

where,

$$R = 1.0 - 0.2\frac{h/t_w\sqrt{F_y/(k_vE)}}{1.10} \text{ if } h/t_w < 1.1\sqrt{k_vE/F_y} \tag{1-43}$$

$$R = 0.8 + 0.2\frac{h/t_w\sqrt{F_y/(k_vE)} - 1.10}{1.10} \text{ for } 1.1\sqrt{k_vE/F_y} \leq h/t_w \leq 2.2\sqrt{k_vE/F_y} \tag{1-44}$$

$$R = 1 \text{ if } h/t_w > 2.2\sqrt{k_vE/F_y} \tag{1-45}$$

1.2.5 Daley et al. (2016) Method

Daley et. al (2016) developed a prediction method which is an adaptation of Höglund's (1997) method. For simplicity, they took η equal to 0.6 for all grades of steel. They recognized that the equations recommended by Höglund (1997) to quantify the buckling and postbuckling strength of unstiffened webs with non-rigid end posts (see Eqs. (1-25) and (1-29)) were identical in form to the AISC inelastic shear buckling equation, but gave a strength 10% smaller than the AISC inelastic shear buckling resistance within its range of applicability. Furthermore, they recognized that Höglund's equation, increased by a

factor of 1.1, provided accurate to conservative results relative to experimental data for all ranges of the web slenderness where the web strength is reduced below the AISC fully-plastic shear resistance. Therefore, they simply applied a factor of 1.1 to Höglund's shear strength equation, resulting in the following equations for C_v:

$$C_v = 1.0 \text{ for } h/t_w \le 1.10\sqrt{k_v E/F_y} \tag{1-46}$$

$$C_v = \frac{1.10\sqrt{k_v E/F_y}}{h/t_w} \text{ for } h/t_w > 1.10\sqrt{k_v E/F_y} \tag{1-47}$$

Daley et al. (2016) recommended that these equations be employed with Eq. (1-6) and $A_w = t_w d$ per the AISC Specifications. They used $k_v = 5.34$ for unstiffened panels and beams with no transverse stiffeners.

1.3 Organization

Chapter 2 presents a summary of the experimental setup of all the simulations that have been performed in this study. Chapter 3 details the finite element modelling procedures used in this research. Chapter 4 provides an overview of the results from simulations in comparison to experimental results. Chapter 5, 6 and 7 explain the mechanism of shear strength development of built-up I section members. Chapter 5 addresses a specimen that has a stiffened panel, Chapter 6 focuses on a specimen that has an intermediate length unstiffened panel and Chapter 7 evaluates the behavior of a specimen with a long unstiffened panel. Chapter 8 evaluates the sensitivity of the shear strength to various factors. Chapter 9 provides a summary and conclusions.

CHAPTER 2

OVERVIEW OF EXPERIMENTS EVALUATED BY TEST SIMULATION

2.1 Specimens Tested at University of Kentucky

In this research, the tests of seven specimens of the configuration shown in Fig. 2-1 and with properties listed in Table 2-1 are simulated. One particular Specimen, UK1, is from Studer and Davis (2012) and is referred to as Prismatic 2 in that research. All the other Specimens are from Daley and Davis (2015).

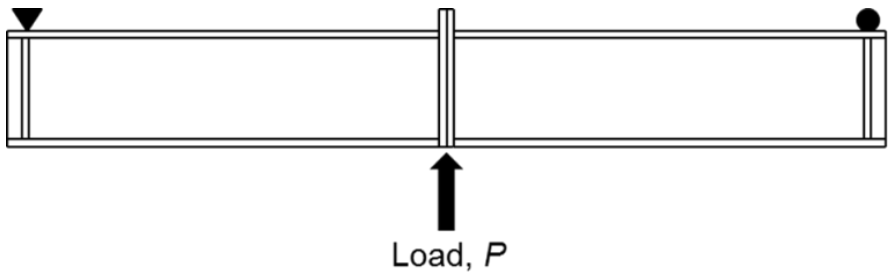

Fig. 2-1. Test configuration employed by Studer and Davis (2012) and Daley and Davis (2015).

In these tests, the load was applied by a hydraulic ram at mid-span. At the ends of the beam, bearing stiffeners were used to prevent web crippling. The specimen was transported in two halves. These halves were joined using a moment end plate which provided a bearing surface for the ram and prevented web crippling at mid-span. The moment end plate had one row of bolts at the bottom flange and two interior rows of bolts and one exterior row of bolts at the top flange. The web-to-flange fillet welds were one sided except for short segments of double sided welds near the supports. In the simulations conducted in this

research, the moment end plates are modeled as transverse stiffeners having a thickness of 0.4 in. and a width of 1 in. less than flange width. This size is sufficient to distribute the applied load to the beam as a bearing stiffener and to restrain the lateral deflections of the web.

Table. 2-1. Summary of Specimen Dimensions: University of Kentucky, from Studer and Davis (2012) and Daley and Davis (2015).

Specimen	V_{meas} (kip)	L (ft)	h (in)	t_w (in)	a/h	h/t_w	b_f (in)	t_f (in)	F_{yw} (ksi)	F_{yf} (ksi)
UK1	33.4	11.4	18.8	0.125	3.65	150	6.00	0.625	61.3	55.8
UK2	49.9	17.8	21.5	0.134	4.97	160	8.00	0.625	65.0	54.8
UK3	49.4	17.8	24.0	0.134	4.45	179	8.00	0.500	65.0	53.2
UK4	50.5	23.8	27.0	0.134	5.29	201	8.00	0.625	66.9	55.0
UK5	41.1	28.8	22.0	0.124	7.85	177	8.00	0.750	60.4	58.6
UK6	75.0	26.8	39.0	0.172	4.12	227	8.00	0.750	63.0	58.9
UK7	43.3	26.8	20.0	0.122	8.04	164	8.00	0.750	64.0	55.0

All of the above specimens failed in shear. The specimens have *a/h* ratios ranging from as low as 3.65 to *a/h* ratio as large as 8.04. Based on the AISC (2010) *Specification*, members having *a/h* ratios greater than 3.0 are classified as unstiffened panels. The web depth and thickness are such that h/t_w ranges from 150 to 227, thus addressing a wide spectrum of slenderness ratios. The web thickness, t_w, given in the table is the thickness of the web on the left-hand side of the specimen. The web thickness on the right-hand side of the specimen was fabricated slightly larger than on the left to ensure that this side did not fail. In the test simulations, the web thickness of the right half is taken as $1/16^{th}$ in. larger than that on the left side of the mid-span.

The length, *L*, listed in the table is the length of the specimen excluding the 6 in. overhang beyond the centerline of the end supports. To ensure that the specimens failed in shear, lateral-torsional buckling of the specimens was prevented by using Watt's linkages to restrain the out-of-plane lateral movement of the bottom (compression) flange at every 3 ft. in the physical tests. These braced points are modeled as rigid lateral constraints in the test simulations conducted in this research. In the test simulations, the out-of-plane deflection of the top flange is restrained at the mid-span and every node at a spacing of 3 ft. from the mid-span.

A 200 kip load cell was placed between the ram and the moment end plate in the physical tests (Daley and Davis 2015). Vertical displacements at each support and at mid-span of the specimen were measured using cable extension sensors. The mid-span deflection was determined as the mid-span displacement minus the average of the end displacements. Load versus Mid-Span Displacement graphs for each of the member were then drawn and the failure mode for each of the specimens was reported. All of the specimens failed by shear buckling and post-buckling action within the half of the beam with the thinner web.

2.2 Höglund Specimens

Two of Höglund's (1971) experimental tests having h/t_w of 209 are analyzed in this research. Bearing stiffeners were installed at both ends and no intermediate stiffeners were employed in these tests. For Specimen B1 (Fig. 2-2), the first load was placed at 1.64 ft. from the left support, followed by eight equal loads placed at equal spacing of 3.28 ft. Both the beams had the same cross-sectional dimensions (Table 2-2).

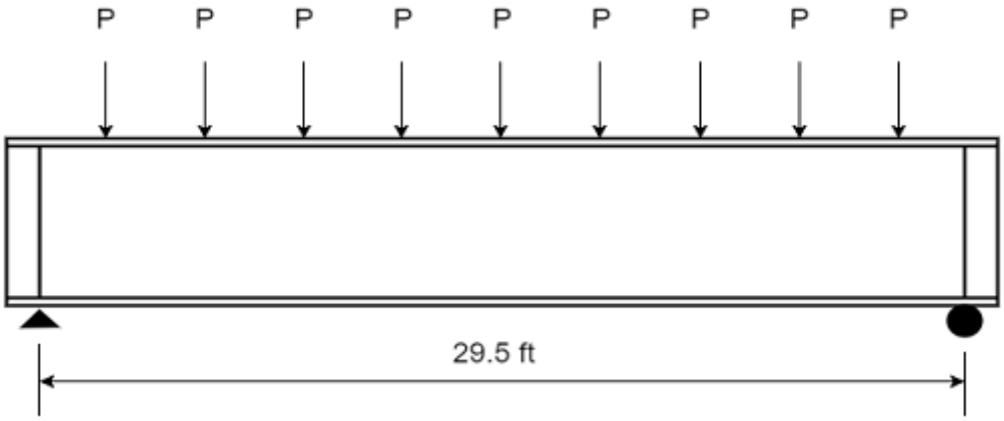

Fig. 2-2. Configuration of Höglund's (1971) test B1.

Specimen K1 (Fig. 2-3) had similar cross-sectional dimensions but was 19.68 ft. long and was subjected to six equally spaced loads of equal magnitude. A support overhang of 6 inches is assumed for both of these tests in the current research.

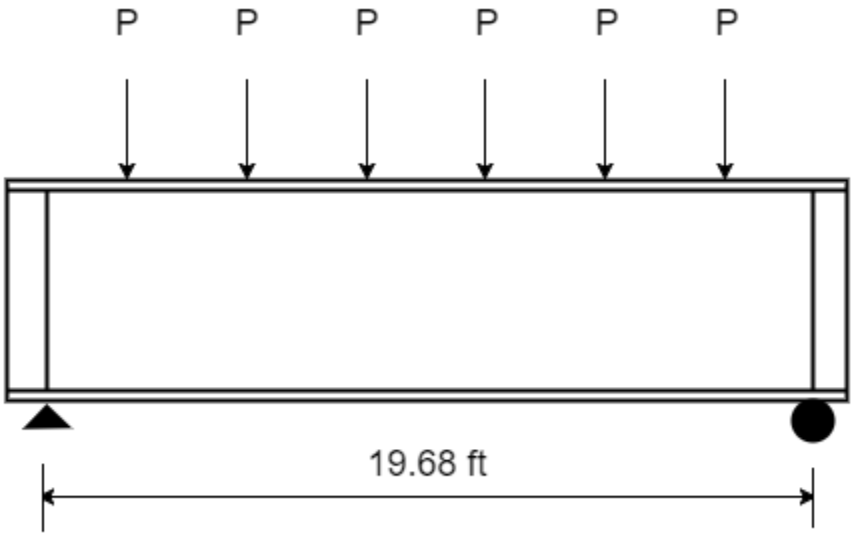

Fig. 2-3. Configuration of Höglund's (1971) test K1.

Table. 2-2. Summary of Specimen Dimensions (Höglund 1971).

Specimen	V_{meas} (kip)	L (ft)	h (in)	t_w (in)	h/t_w	b_f (in)	t_f (in)	F_{yw} (ksi)	F_{yf} (ksi)
B1	25.1	29.5	23.6	0.113	209	8.90	0.39	59.4	41.9
K1	23.3	19.68	23.6	0.113	209	8.90	0.39	59.4	41.9

2.3 Lee and Yoo Specimens

Lee and Yoo (1999) conducted experimental tests on ten specimens to understand the shear strength behavior of stiffened web panels. Two of their tests are considered in this study to validate the correctness of FE model if applied to a stiffened panel and to clarify the similarities and differences between the web behavior for relatively long "stiffened" panels versus short and long "unstiffened" panels. The test G7 and G8 (Fig. 2-4) specimens were selected for the current research studies. The dimensions of these specimens are summarized in Table 2-3. These specimens both failed by shear buckling and post-buckling action.

Table. 2-3. Summary of test G7 and G8 - Specimen Dimensions (Lee and Yoo 1999).

Specimen	V_{meas} (kip)	a (ft)	h (in)	t_w (in)	h/t_w	a/h	b_f (in)	t_f (in)	F_{yw} (ksi)	F_{yf} (ksi)
G7	58.2	3.93	23.6	0.157	150	2	7.87	0.39	41.4	44.1
G8	62.1	3.93	23.6	0.157	150	2	7.87	0.59	41.4	44.1

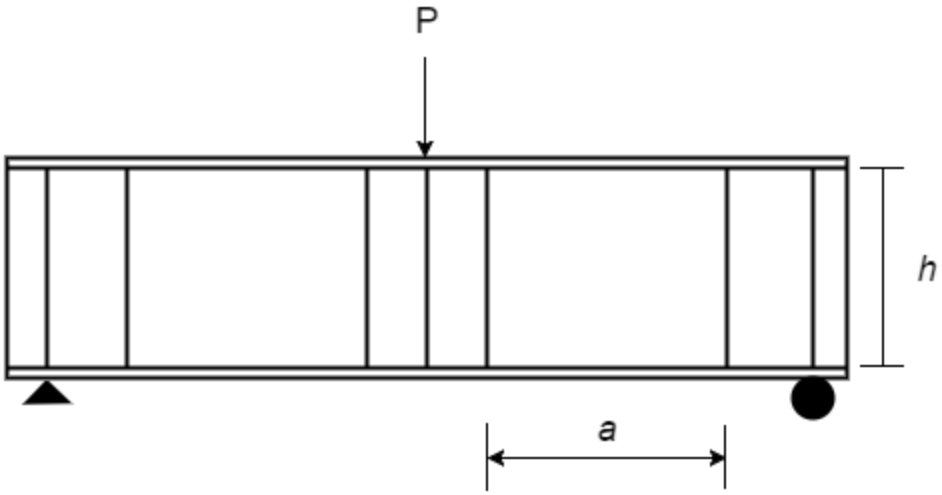

Fig. 2-4. Configuration of Lee and Yoo's (1999) tests G7 and G8.

CHAPTER 3

FINITE ELEMENT MODELLING FOR TEST SIMULATION

All the test simulations in this research are full (geometric and material) nonlinear analyses conducted using the commercial software ABAQUS (Simulia 2013). This chapter describes the Finite Element modelling attributes and parameters used in the simulations.

3.1 Element Type and Mesh Density

The girder flanges and the web are modeled using the general purpose four-node shell element, S4R. The S4R is a large-strain shell element that uses uniformly reduced integration to achieve high computational efficiency and to avoid shear and membrane locking. This element can be employed for either thin or thick shells. The transverse stiffeners are modeled using the compatible B31 beam element in ABAQUS. The B31 is a two node shear deformable one dimensional element.

The ABAQUS default Simpson's rule with five integration points is used for numerical integration through the thickness of the shell elements. The finite element mesh employed in the simulations is relatively dense with 12 elements across the width of the flange. A total of 36 elements is used for UK6, 25 elements for UK4 and 20 elements for all other specimens. The number of elements used along the length of members is selected such that the shell elements have an aspect ratio approximately equal to 1.0 within the web. Fig. 3-1 shows the finite element model for UK6.

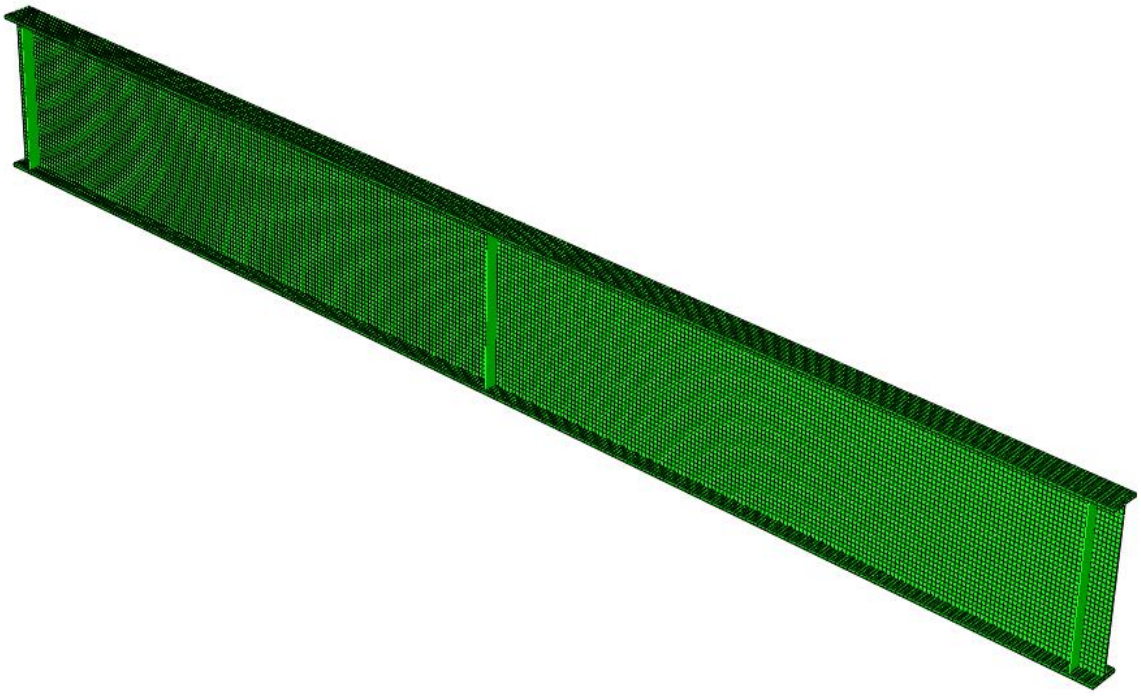

Fig. 3-1. Finite Element Model for test UK6.

3.2 Boundary conditions

The boundary conditions for all the specimens are simply supported as in the experimental tests. To model a hinge support at the left end, all the displacement degrees of freedom are restrained at the bottom web-flange intersection. In addition, the vertical displacement of the bottom flange is restrained at all of the nodes across the bottom flange width. To model the roller support at the right end, the displacement constraints are the same as the above except that the axial displacements are unrestrained. The twist at both beam ends is prevented by restraining the out-of-plane lateral displacements throughout the web-depth.

3.3 Material Properties

The web and flange yield stress for each of the specimens is specified as the measured values. The transverse stiffeners are modeled with a yield stress of 50 ksi. The modulus of elasticity, E, is taken as 29000 ksi. The steel is modeled with a tangent stiffness within the yield plateau region of $E/1000$ up to a strain-hardening strain of $\varepsilon_{sh} = 10\varepsilon_{y,}$ where ε_y is the yield strain of the material. Beyond this point, a constant strain-hardening modulus of $E_{\text{sh}} = E/50$ is used. This simple representation of the strain-hardening response is considered sufficient since the stress-strain response exceeds the strain-hardening strain by only a very minor amount within very localized regions for the studies conducted in this research.

The plastic stress-strain response is captured within the test simulation models using J2 theory (metal plasticity, von Mises yield condition) and isotropic hardening based on the above specified uniaxial stress-strain response.

3.4 RIKS Algorithm

The modified Riks method is used for the nonlinear analysis. The load magnitude is governed by a single scalar parameter in this method. The modified Riks algorithm uses an arc-length procedure in tracing the equilibrium path. The Riks method solves for the load magnitude as an additional unknown such that the equilibrium search within the solution space composed of all the displacement degrees of freedom plus the single load parameter is orthogonal to the tangent in the previous iteration within a given load increment (Simulia 2013).

The reference load applied in the ABAQUS solutions conducted in this research is the strength from the corresponding experimental test. The maximum increment size is

restricted to 0.01 of the reference load. Using this small value of the maximum increment size ensures that the limit load is captured with good accuracy.

3.5 Residual Stress Pattern

Due to uneven cooling of the plates after flame cutting and/or welding, residual stresses are introduced in the members. The selected residual stress pattern for this study is based on the residual stresses measured by Prawel et. al (1974) in three-plate girder construction without longitudinal stiffeners. This self-equilibrating residual stress pattern has been employed previously by Kim (2010) and Subramanian (2015). This pattern is referred to as the "*Best-fit Prawel pattern*".

The maximum compressive stresses at the flange tips is $0.25F_y$ in the above pattern. It decreases linearly within the outside thirds of the flange width. The maximum tensile stress at the web-flange intersection is taken as $0.5F_y$ and is constant over one-sixth width of the flange width. In the web, the maximum tensile residual stress is F_y over a depth of $h/20$. Over a depth of $0.8h$, the compressive stress is $0.176F_y$. This basic residual-stress pattern is illustrated in Fig. 3-2.

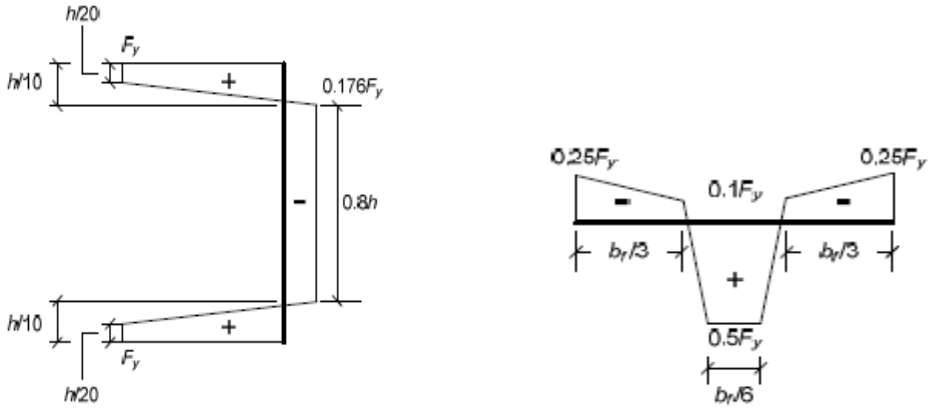

(a) Web Distribution (b) Flange Distribution

Fig. 3-2. Best-fit Prawel residual stress pattern.

Similar to the studies by Kim (2010) and Subramanian (2015), the web residual compression stress is limited to the web local buckling stress under uniform longitudinal compression, calculated using idealized simply-supported boundary conditions at the top and bottom of the web. This restriction is imparted because the physical web cannot be manufactured such that the residual stresses are higher than the web longitudinal buckling stress. To maintain the self-equilibrating nature of the residual stress pattern, the web tensile stresses, F_y, are scaled down by the same ratio.

3.6 Geometric Imperfections

An estimated critical imperfection pattern of the web is determined by conducting an elastic linear buckling analysis of the specimen using the same loading as applied in the experiment. The first mode of the buckling analysis is considered and the corresponding out-of-plane displacements are factored by the fabrication tolerance of $D/150$ as specified in Bridge Welding Code (AWS 2002) for the girder webs and applied to the specimen. The sensitivity to the magnitude of this imperfection is studied in the Chapter 8. Fig. 3-3 shows the imperfection pattern applied to UK6.

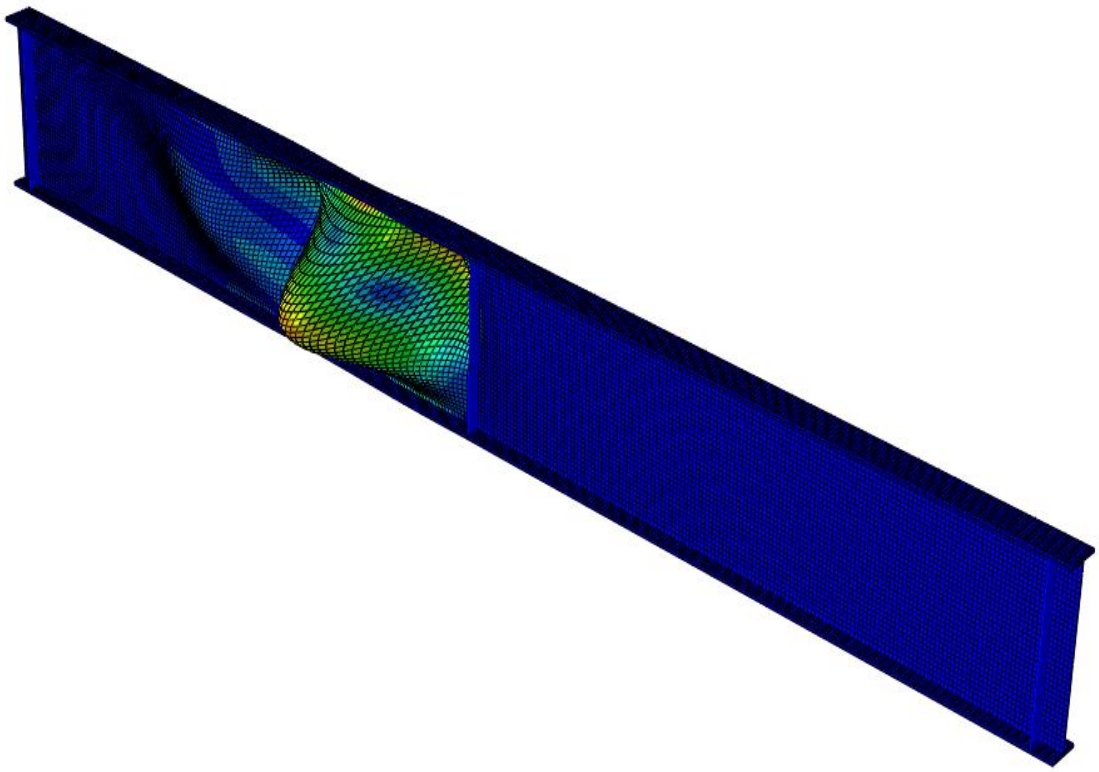

Fig. 3-3. Imperfection pattern for UK6 (the contours indicate the relative magnitude of the out-of-plane displacements).

CHAPTER 4

SIMULATION RESULTS

In this chapter the results from the test simulations listed in Chapter 2 are compared with the experimental results. The main parameters considered here are V_{exp}/V_{sim}, where V_{exp} is the maximum load level achieved in the experiment and V_{sim} is the corresponding maximum load level achieved in the test simulations. Also, the shape and the length of the shear buckles is reported.

4.1 Comparison of Shear Strengths

Table. 4-1 compares the experimental and simulation strengths. From the table, it can be seen that the simulation results match reasonably well with the experimental results, with the exception of Specimen UK1. The average of V_{exp}/V_{sim} is 1.09, excluding UK1. The FE simulation resistances are smaller than the experimentally measured resistances in all of the tests with the exception of G7 and G8 where the FE simulation slightly over predicts the experimental strengths.

The specific magnitudes of the initial geometric imperfections and the details about the actual pattern of the imperfection along the length are not known. In addition, the actual residual pattern is also unknown. The uncertainty in these values is believed to be the primary source of the differences between the experimental and the simulation capacities.

Table 4.2 compares the shear strength obtained from test simulations to that obtained via the prediction equations from Chapter 1. Since the prediction methods for stiffened panels are different and have not been specified in Chapter 1, the shear strengths of G7 and G8 are compared in Table. 4-3.

Table. 4-1. Comparison of experimental and simulation results.

Specimen	*a/h*	h/t_w	V_{exp} (kip)	V_{sim} (kip)	V_{exp}/ V_{sim}
UK1	3.65	150	33.3	46.5	1.40
UK2	4.97	160	48.8	54.9	1.13
UK3	4.45	179	49.3	54.3	1.10
UK4	5.29	201	50.6	56.0	1.11
UK5	7.85	177	41.0	42.3	1.03
UK6	4.12	227	73.6	89.0	1.21
UK7	8.04	164	42.5	43.5	1.03
B1	-	209	25.1	31.1	1.24
K1	-	209	23.3	27.5	1.18
G7	2	150	58.2	56	0.96
G8	2	150	62.1	57.5	0.93

Basler's method (1961) provided extremely conservative results for all specimens. Basler method with the plate buckling coefficient by Lee et al. (1996) also provided very conservative predictions. The Hoglund (1997) method also provided fairly conservative predictions. Lee et al. (2008) predicts strengths extremely well for the Daley et al. (2015) specimens. However, they are unconservative for Höglund (1971) specimens. Daley et al. (2016) proved to be conservative for all the test specimens

Table. 4-2. Ratio of Test Simulation Strengths to Predicted Shear Strengths.

Specimen	Basler	Basler with Lee's k_v	Höglund 1997	Lee et al.	Daley et al.
UK1	3.10	2.00	1.58	1.00	1.37
UK2	3.37	2.18	1.58	1.03	1.38
UK3	3.72	2.40	1.56	1.03	1.39
UK4	4.34	2.80	1.59	1.04	1.40
UK5	3.42	2.20	1.49	0.98	1.27
UK6	4.67	3.01	1.57	1.01	1.41
UK7	3.38	2.18	1.54	1.00	1.31
B1	3.63	2.34	1.34	0.87	1.18
K1	3.21	2.07	1.18	0.77	1.04

Table 4.3 compares the shear strengths obtained from the test simulations of stiffened panels, G7 and G8, to shear strength obtained by using prediction equations from Appendix A. From the table, it is clear that Basler's method with $k_{vincent}$ provides reasonably accurate results. Basler's method with k_v taken from Lee et al. (1996) also predicts strength fairly well but errs on the unconservative side. Lee et al. with $R_d = 1$ also provides unconservative strengths. With R_d taken from Eq. A-3 through A-5, the predicted shear strengths become even more unconservative. Daley et al. provides relatively conservative results for the specimens, even when the contribution from flange frame action is included.

Table. 4-3. Ratio of Test Simulations Strength to Predicted Shear Strength.

Specimen	Basler ($k_{vincent}$)	Basler with Lee's k_v	Lee et al. ($R_d = 1$)	Lee et al. ($R_d < 1$)	Daley et al.	Daley et al. (with frame action)
G7	1.07	0.92	0.91	0.85	1.22	1.18
G8	1.10	0.95	0.94	0.87	1.24	1.17

4.2 Failure Modes (Experimental versus Simulation)

To make the failure modes more easily discerned, only the left side of each specimen is shown for the University of Kentucky tests in the following discussions. Figures 4-1 to 4-14 compare the failure patterns from the experiment and simulation for each of these seven tests. All the failure modes from test simulations are drawn at 95% of the peak load within the post-peak range of the response, and the deflections at this stage are scaled by a factor of 2.0. The discussion of these patterns follows:

1. **UK1:** Specimen UK1 failed with a predominant shear buckle over most of its half span-length. The simulation matches the experimental result. The buckle starts roughly at the juncture of transverse stiffener and bottom flange at the mid-span. This specimen has a relatively small value of a/h (3.65). It behaves similar to a stiffened panel.

Fig. 4-1. Failure mode for Specimen UK1, experiment (Studer and Davis 2012).

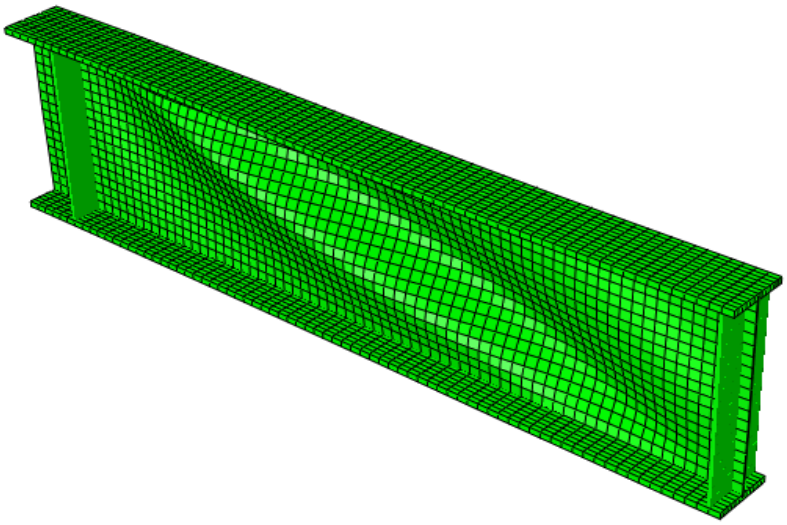

Fig. 4-2. Failure mode for Specimen UK1, simulation.

2. **UK2:** Specimen UK2 failed with a predominant shear buckle over approximately 6 ft. of its half-span length between the end support and mid-span. The buckle forms roughly over this same length in the simulation as in the experiment. This specimen has an *a*/*h* of 4.97 and has one primary buckle that intersects the flanges at distance of about 1.5 ft. from the transverse stiffeners at the end and mid-span.

Fig. 4-3. Failure mode for Specimen UK2, experiment, (Daley and Davis 2015).

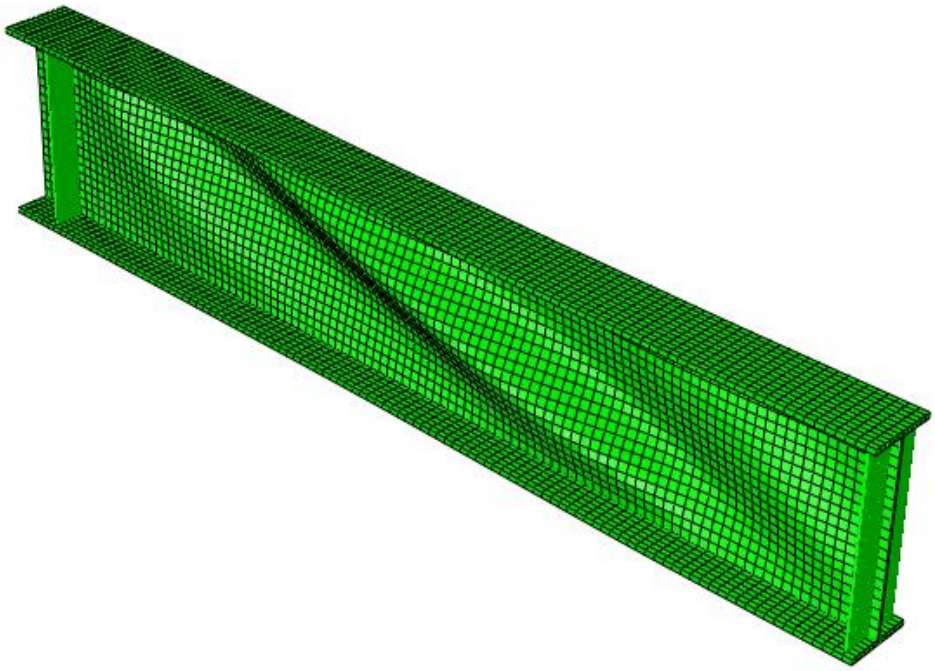

Fig. 4-4. Failure mode for Specimen UK2, simulation.

3. **UK3:** Specimen UK3 failed with a predominant shear buckle over 6 ft. of its half-span length between the end support and the mid-span. The buckle in the simulation follows almost the same pattern as in the experiment.

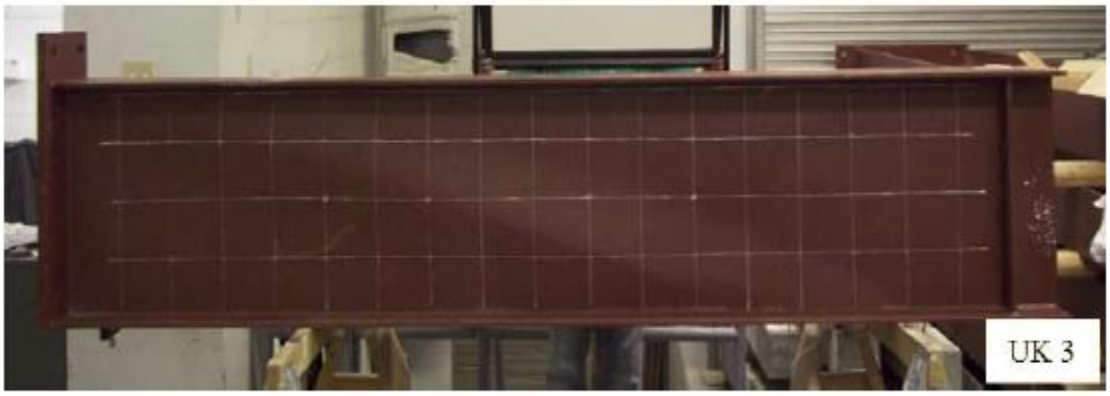

Fig. 4-5. Failure mode for Specimen UK3, experiment, (Daley and Davis 2015).

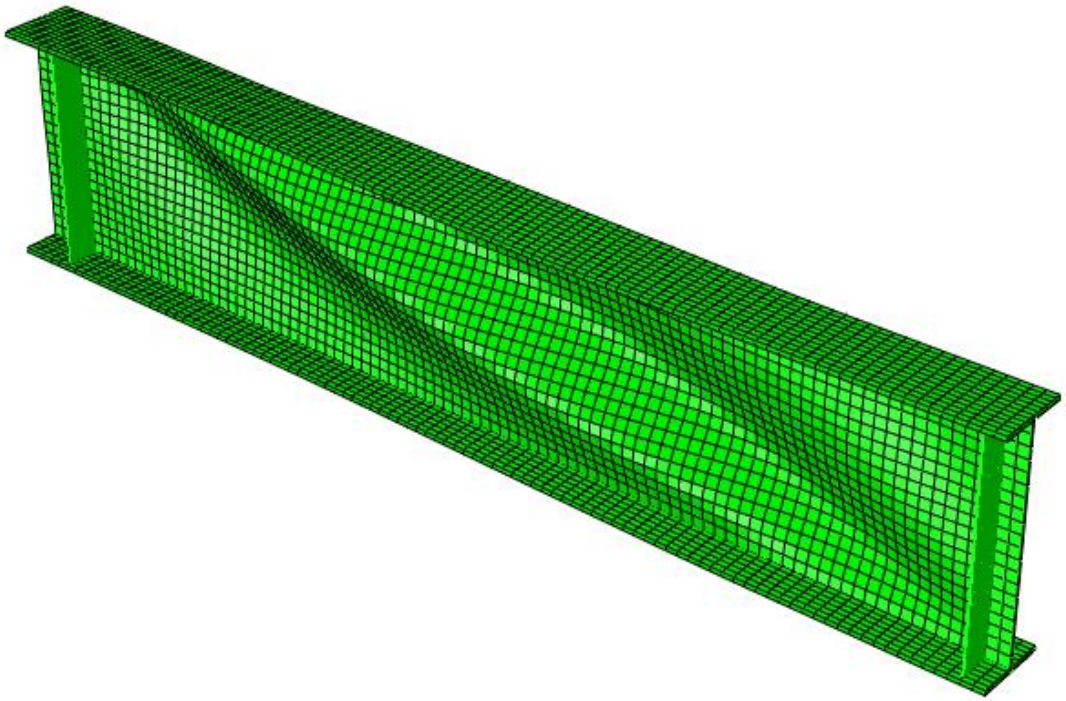

Fig. 4-6. Failure mode for Specimen UK3, simulation.

4. **UK4:** Specimen UK4 failed with a predominant shear buckle over 6 ft. of its half-span length. The buckle in the simulation follows almost the same pattern as in the experiment.

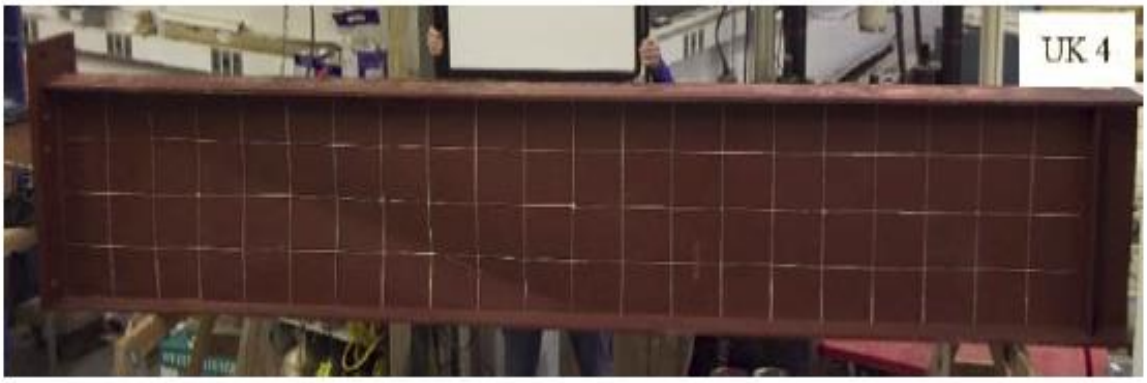

Fig. 4-7. Failure mode for Specimen UK4, experiment, (Daley and Davis 2015).

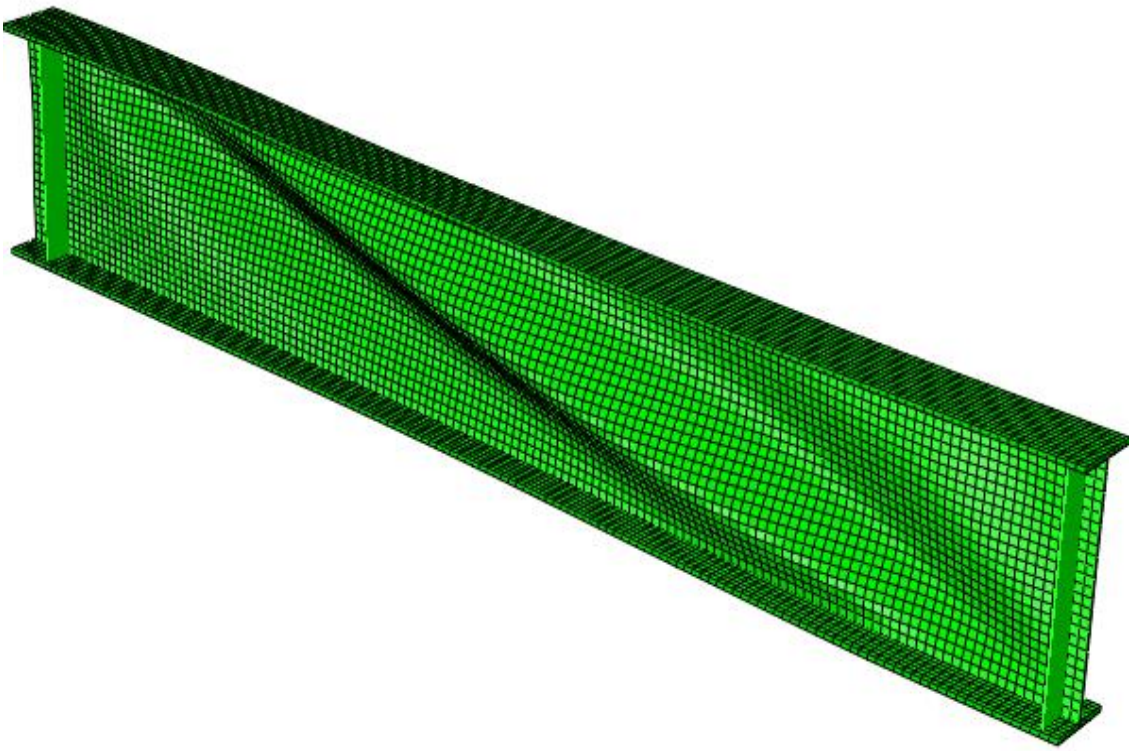

Fig. 4-8. Failure mode for Specimen UK4, simulation.

5. **UK5:** Specimen UK5 failed with a predominant shear buckle over 6 ft. of its half-span length. The buckle in the simulation follows almost the same pattern as in the experiment. This specimen has a relatively large *a/h* of 7.85. It should be noted that the

experimental specimen is being held by a strap at approximately its quarter-span location in the Fig. 4-9 photo.

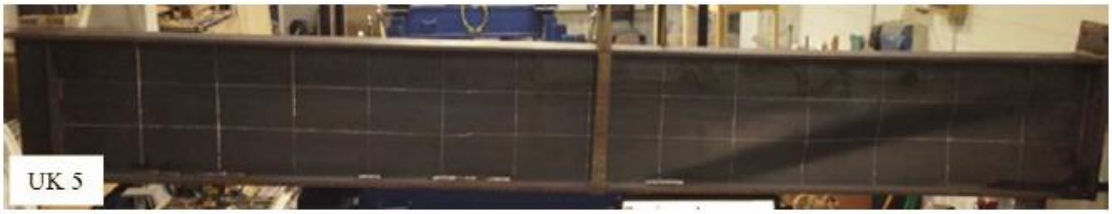

Fig. 4-9. Failure mode for Specimen UK5, experiment (Daley and Davis 2015).

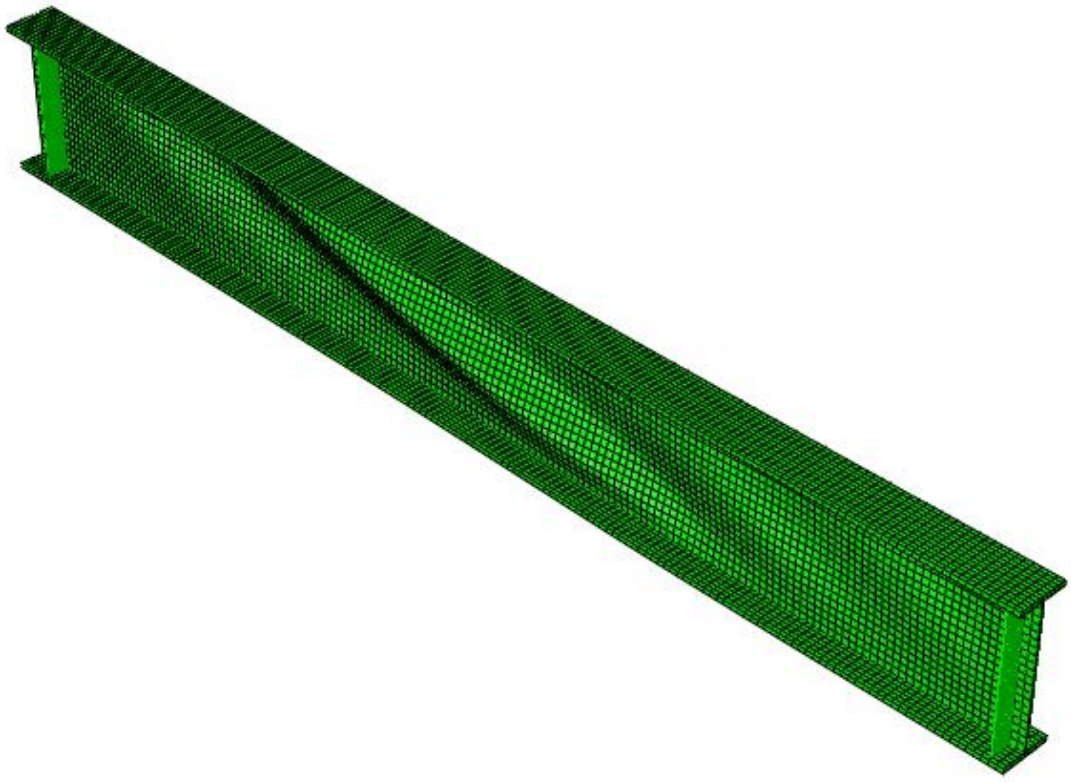

Fig. 4-10. Failure mode for Specimen UK5, simulation.

6. **UK6:** The UK6 Specimen failed with a predominant shear buckle over most of its half span.length The buckle in the simulation follows almost the same pattern as experiment. This specimen has a relatively small *a/h* of 4.12. Again, the experimental

specimen is being held by strap at approximately its quarter-span location in the Fig. 4-11 photo.

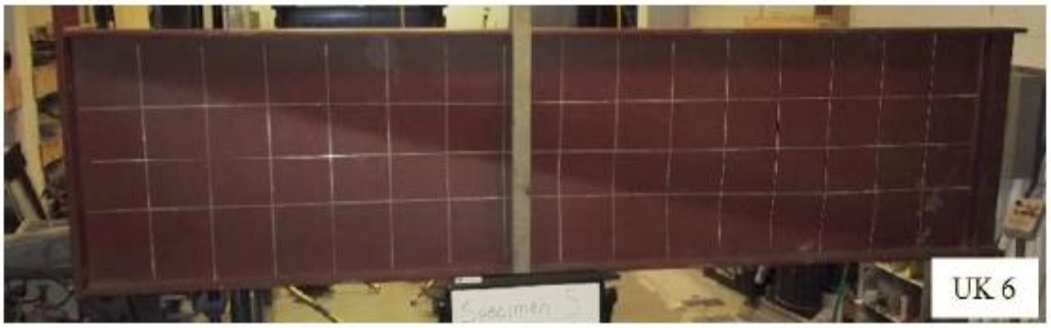

Fig. 4-11. Failure mode for Specimen UK6, expeiment (Daley and Davis 2015).

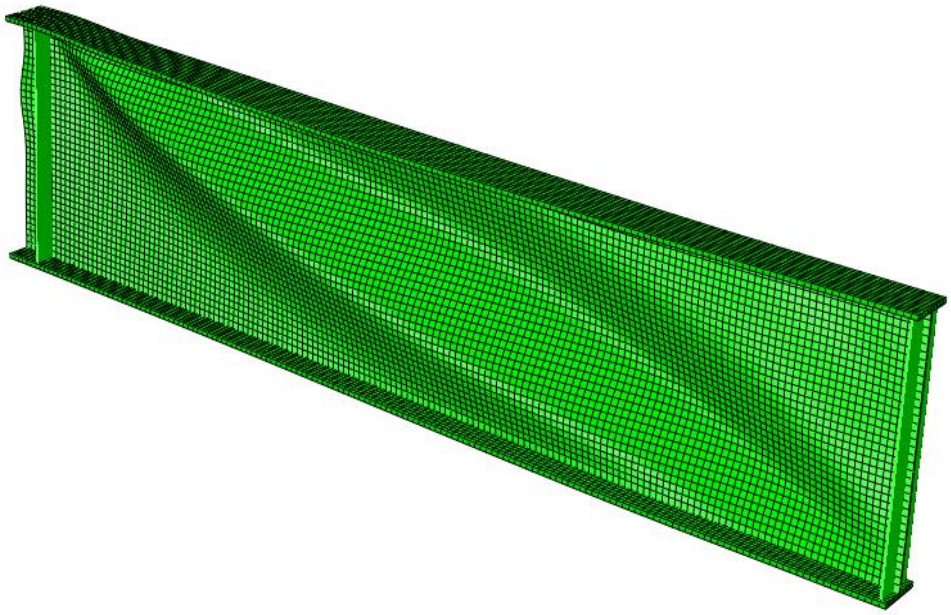

Fig. 4-12. Failure mode for Specimen UK6, simulation.

7. **UK7:** Specimen UK7 failed by forming a predominant shear buckle over 6 ft. of its half-span length. The failure mode in the test simulation and in the experiment are

very similar. This specimen has the largest *a/h* of the specimens considered (*a*/*h* = 8.04).

Fig. 4- 13. Failure mode for Specimen UK7, experiment (Daley and Davis, 2015).

Fig. 4-14. Failure mode for Specimen UK7, simulation.

The results of the simulations of the stiffened specimens from the Lee and Yoo (1999) tests, Specimens G7 and G8, are presented in Figs. 4-15 to 4-18. All the failure modes from test simulations are drawn at 95% of the peak load within the post-peak range of the response, and the deflections at this stage are scaled by a factor of 2.0. The symbol "SYM." marks the symmetry plane at the mid-span of the specimens.

1. **G7:** This specimen reached the ultimate strength point without causing any substantial flange deformations. The buckle starts at the juncture of the transverse stiffener and both the flanges. This specimen has *a/h* of 2.0 and is classified as a stiffened panel.

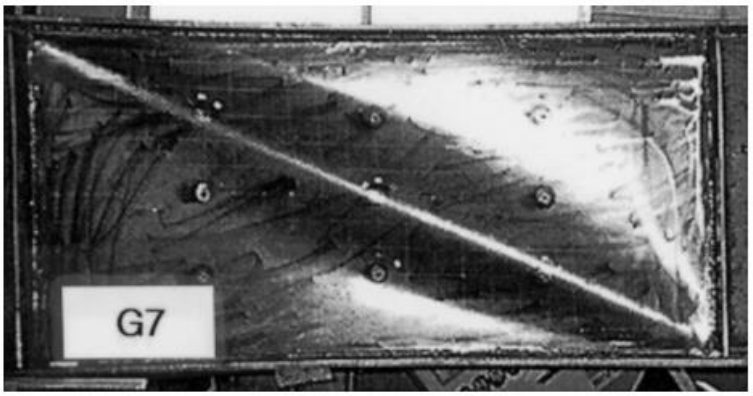

Fig. 4-15. Failure mode for Specimen G7, experiment (Lee and Yoo 1999).

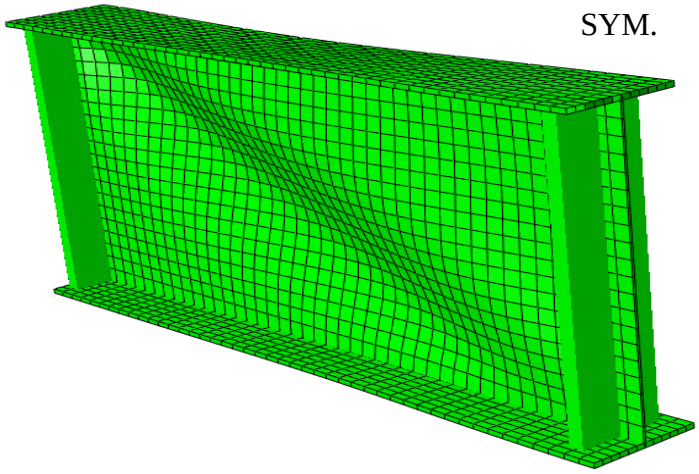

Fig. 4-16. Failure mode for Specimen G7, simulation.

2. **G8:** This specimen is similar to G7 except that it has a thicker flange. The failure pattern is similar to G7, both in the experiment and in the simulation.

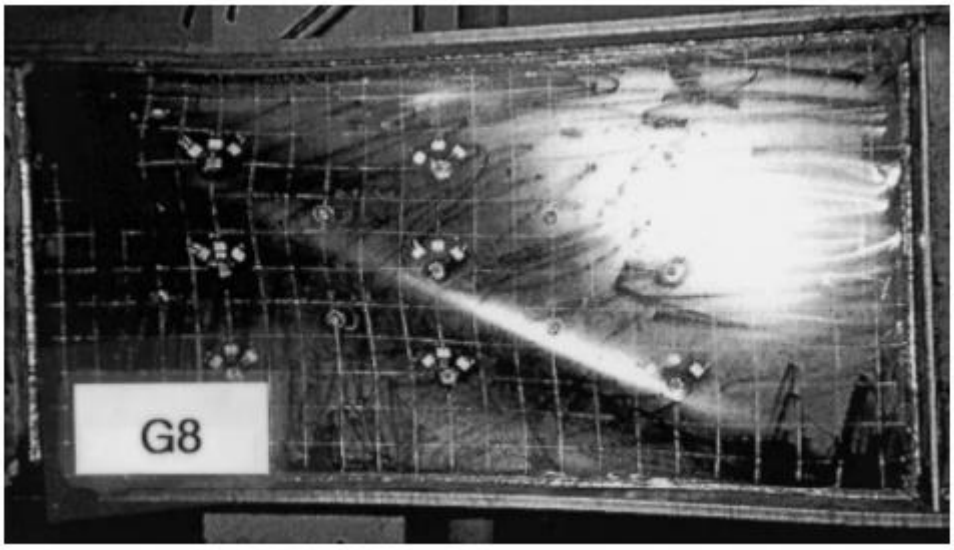

Fig. 4-17. Failure mode for Specimen G8, experiment (Lee and Yoo 1999).

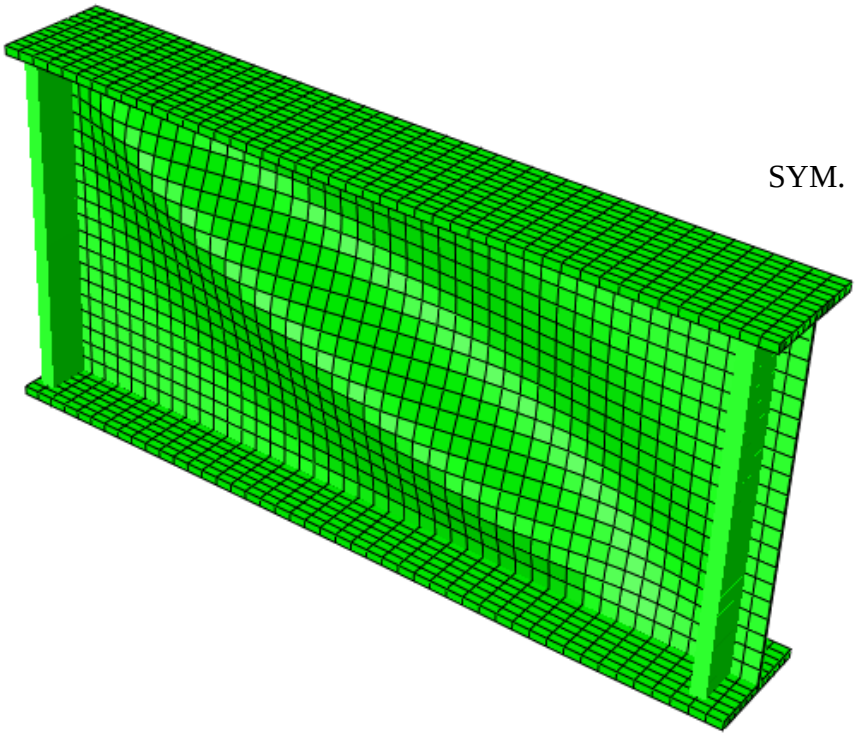

Fig. 4-18. Failure mode for Specimen G8, simulation.

The above results indicate that the simulations correlate reasonably well with the experiments. Test G7 is studied in detail in the following chapter as a case with stiffened web panel. Höglund's (1971) Specimens B1 and K1 are not compared for the experimental failure pattern because pictures from the experimental tests were not available. The failure modes for these tests from the simulations are shown in Figs. 4-19 and 4-20. Due to symmetry of the specimen failure mode, only half of the specimen is shown. The deflections for these specimens are scaled by a factor of 5.0.

1. **Hoglund B1:** Specimen B1 failed with a predominant shear buckle near the end of the specimen where shear force is the highest and almost no buckling near mid-span. The buckle starts roughly at the juncture of the bearing stiffener on the left-end support and the top flange.

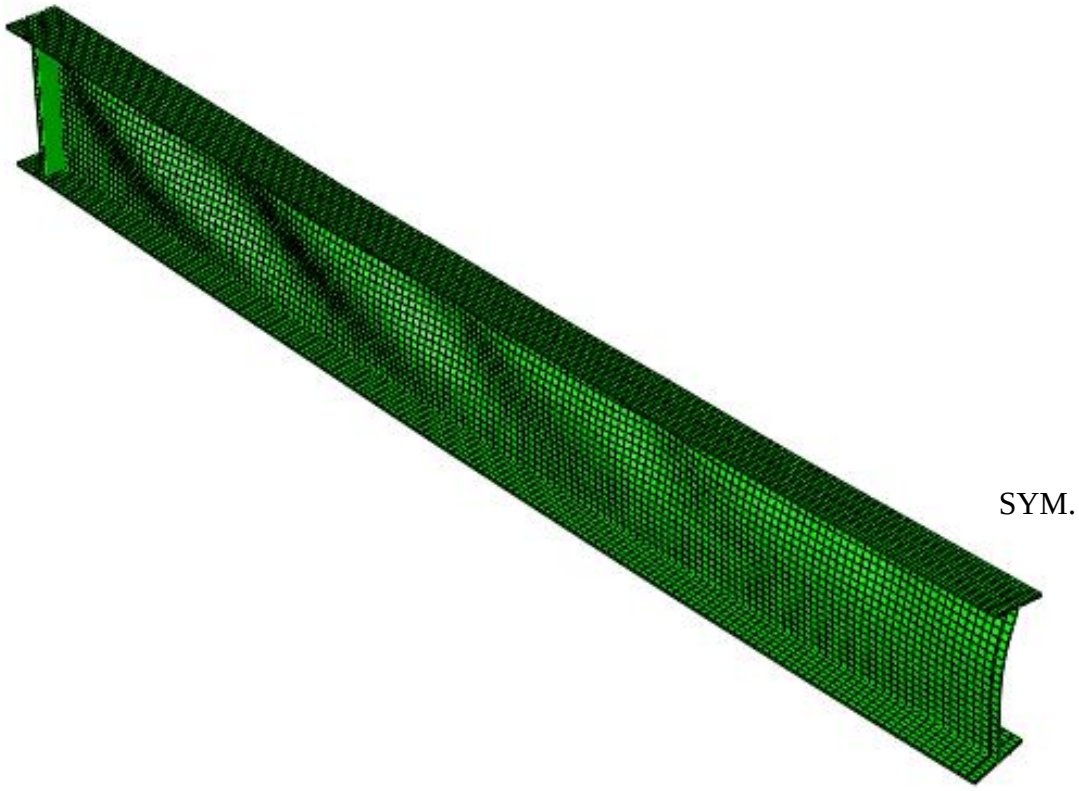

Fig. 4-19. Failure mode for Specimen B1, simulation.

2. **Hoglund K1:** Specimen K1 failed due to shear buckling adjacent to the end supports. However, the failure mode in this specimen appears to involve a web distortional buckling mode centered about the mid-span. The buckle starts roughly at the juncture of the bearing stiffener on the left-end support and the top flange.

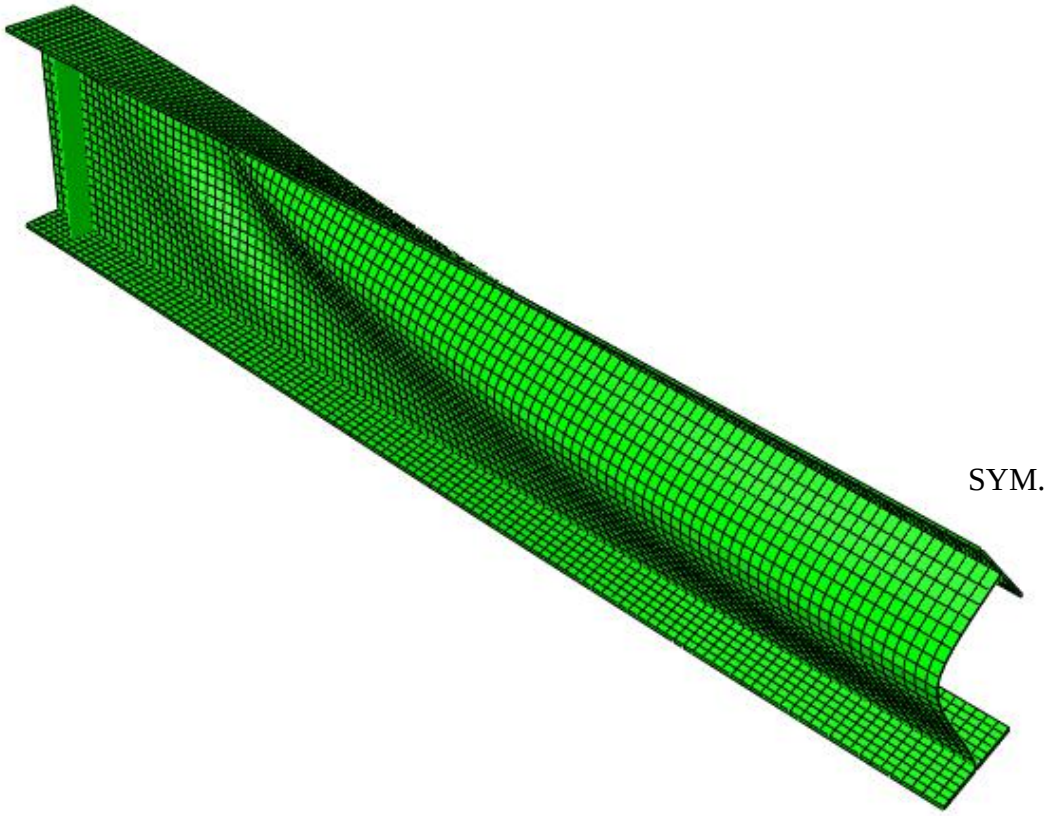

Fig. 4-20. Failure mode for Specimen K1, simulation.

Of the unstiffened shear test Specimens, UK6 and UK7 are scrutinized in detail in this research to explain the mechanism of development of shear strength in unstiffened panels. These results are presented in Chapters 6 and 7 respectively. UK6 is selected because it has a relatively short web panel with an aspect ratio a/h equal to 4.12 and also has the highest h/t_w (227) of the University of Kentucky tests. UK7 is selected because it has the largest panel ratio of a/h equal to 8.04.

CHAPTER 5

MECHANISM OF SHEAR DEVELOPMENT IN A STIFFENED PANEL

The stiffened web specimen selected for this study is G7 from Lee and Yoo (1999). It has an a/h of 2.0 and h/t_w of 150. Experimentally, this specimen failed by the formation of a shear buckle that extended over the entire panel length (see Figs. 4-15 and 4-16). To explain the mechanisms underlying the development of the shear resistance, various cuts are made along the length and depth of the specimen and the displacements and stresses developed are plotted on these cut sections. Figure 5-1 shows the overall geometry for the G7 simulation model.

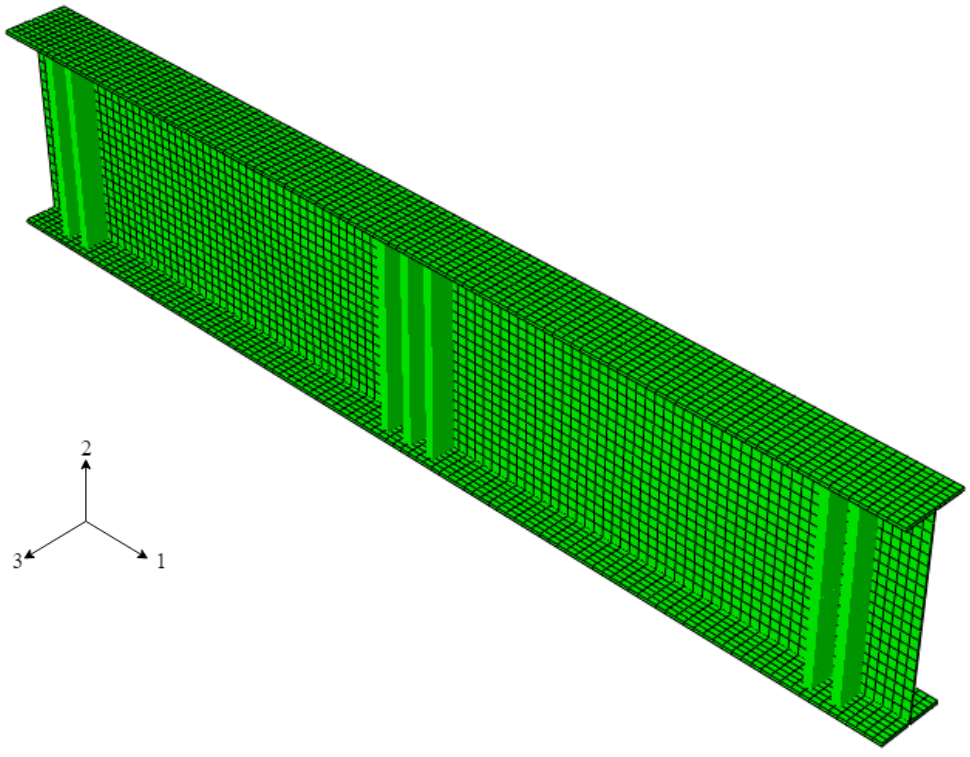

Fig. 5-1. Isometric view of the FE model for Specimen G7.

The displacements in ABAQUS are labeled by the symbol *U*, and *U1*, *U2* and *U3* are the displacements in the 1, 2 and 3 directions respectively. The shell element stresses are displayed in a local coordinate system (Fig. 5-2). The local 1-direction is initially in the longitudinal direction of the beam (i.e., the global 1-direction). The local 2-direction is at right angle to the local 1-direction such that the local 1-direction, local 2-direction and the positive normal to the surface form a right-handed coordinate system.

The stresses *S11* and *S22* are the membrane normal stresses acting in the local-1 and local-2 directions shown in Fig. 5-2, respectively. *S12* is the membrane shear stress acting in the plane of the shell surface. The above stresses are determined in this work by dividing the membrane forces *SF1, SF2, SF3,* respectively, by the thickness of the shell-element. *SF1* is the direct membrane force per unit width in local 1-direction, *SF2* is the direct membrane force per unit width in local 2-direction and *SF3* is the shear membrane force per unit width in the local 1-2 plane. Therefore, *S11*, *S22* and *S12* are the average membrane stresses within the plane of the web.

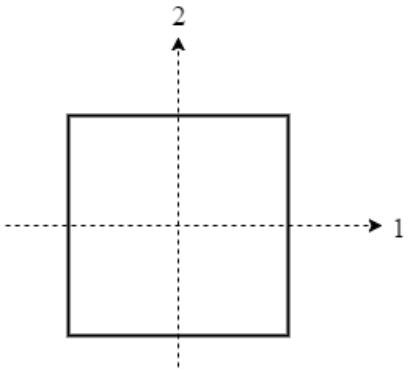

Fig. 5-2. Local directions of a shell-element.

Due to buckling deformations, the above local-1 direction is the orientation of the original longitudinal fibers of the cross-section in the deformed geometry. Similarly, assuming small strain but large displacement and/or rotation, the local-2 direction may be considered approximately as the deformed orientation of the fibers that were originally in

the transverse direction of the web. The local-3 direction is the normal to the plane of the web at a given deformed configuration of the structure.

Fig. 5-3 shows a plot of the applied vertical load versus the vertical displacement (*U2*) at the mid-span of girder G7. The markers in the graph show various stages where the web responses are inspected. The load magnitudes selected for the study are: zero load, 25% peak load (28.2 kips), 50% peak load (59.5 kips), 75% peak load (88 kips), 95% peak load (107 kips), peak load (112 kips) and post peak load (105 kips). The state of stresses and the displacements at each load stage are studied in detail to explain the mechanism by which the web shear forces are developed.

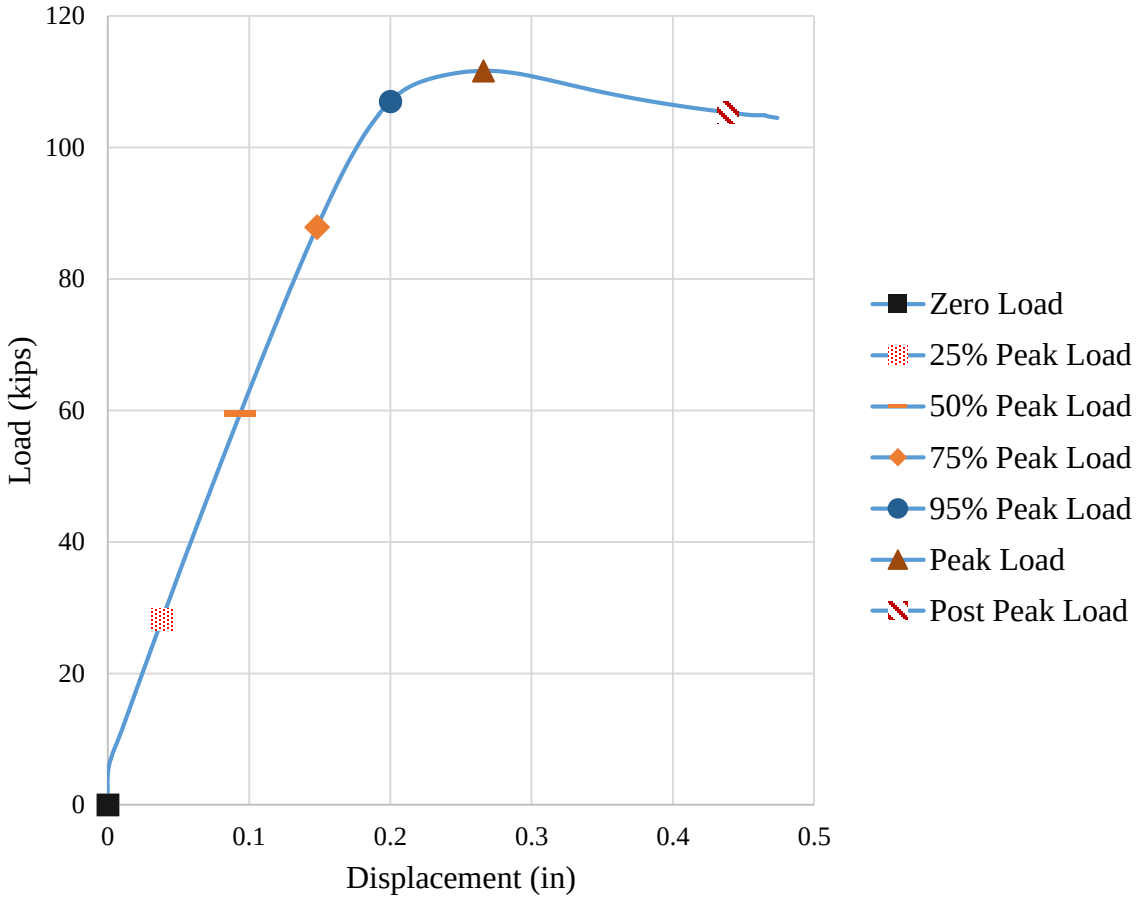

Fig. 5-3. Load versus vertical displacement at the mid-span of Specimen G7.

In the FE simulations, the specified residual stresses are allowed to equilibrate on the imperfect web geometry in the first step (zero load). In the second step the load is incremented using the modified Riks Algorithm as discussed in Section 3.4.

In the following, first a section is considered along the member length at the web mid-depth. Secondly, a section is considered at the intersection of the top flange and the web along the length of the member. Finally, the process is repeated for the bottom flange and web intersection. In all the graphs, unless noted otherwise, the position along the length, measured from the left-hand free end of the specimen, is plotted as the abscissa. The symmetry of the specimen about the mid-span is invoked and the responses for only one-half of the length of the specimen are shown in the plots. The stiffeners are located at a distance of 6.0, 9.3, 56.5 and 60 inches from the left end of the beam. The first stiffener is centered over the left-hand end support, and the fourth stiffener is located at the mid-span of the member.

5.1 Responses at a Section Along the Length at the Web Mid-Depth

In this section, a section is cut at the web mid-depth and the stresses and displacements along the section are plotted. The quantities plotted are the lateral displacement *U3*, the web membrane stresses, *S11*, *S22* and *S12*, the von Mises stress *S*, the maximum principal tensile membrane stress *S1*, the maximum principal compressive membrane stress *S2* and the orientation of the principal stresses θ_p. Figures 5-4 through 5-11 show the variation of these quantities, in that order, at a section along the length at the web mid-depth for the different levels of loading.

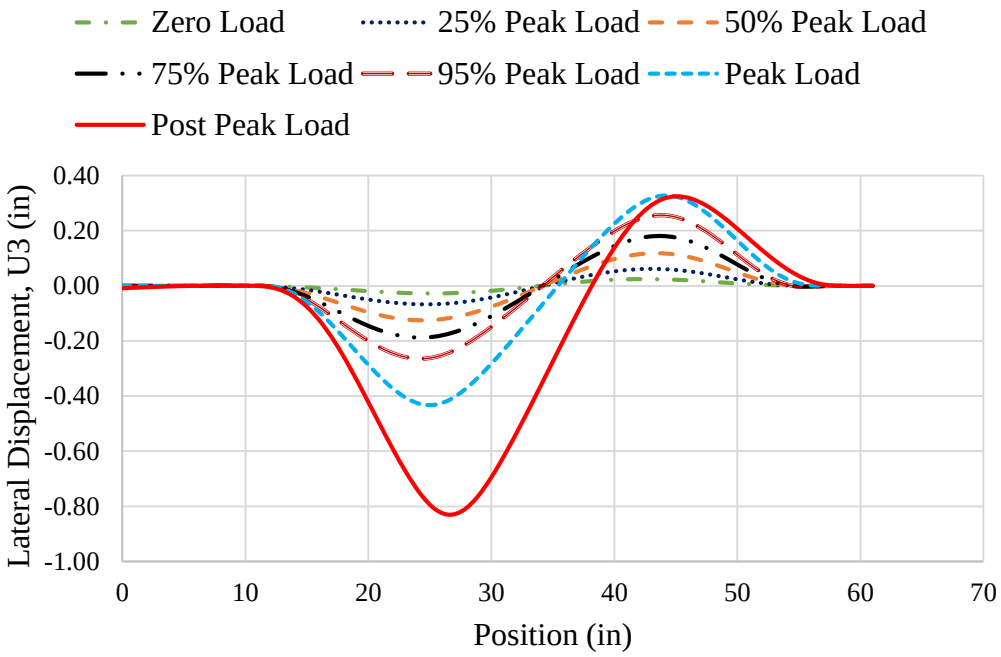

Fig. 5-4. Lateral displacement *U3* versus position along the web mid-depth.

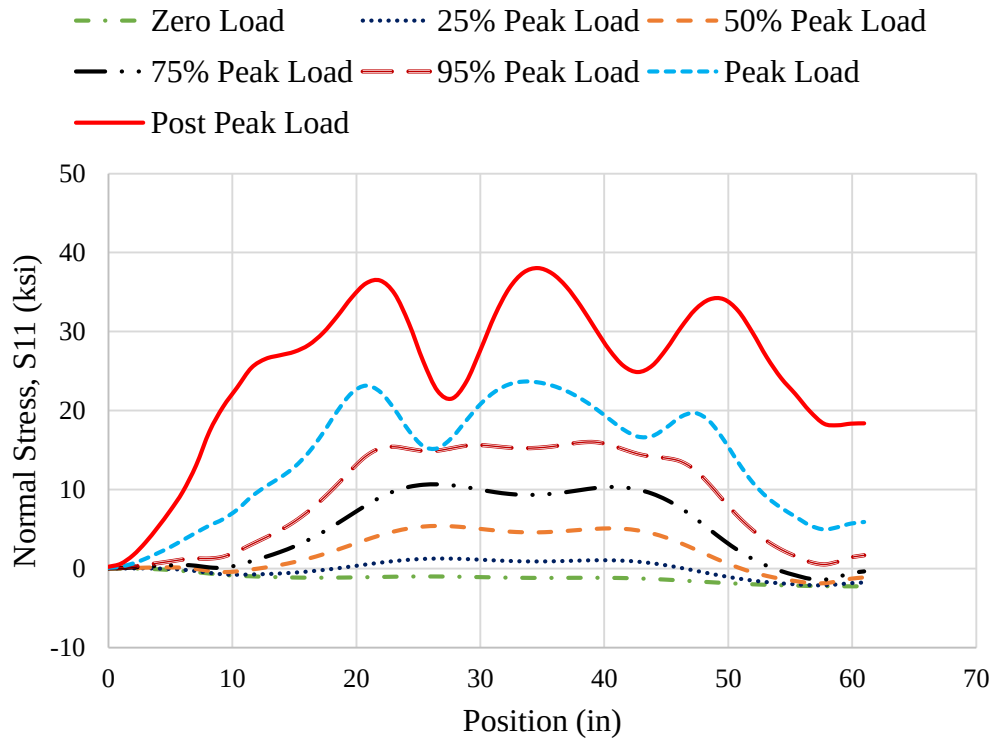

Fig. 5-5. Normal stress *S11* versus position along the web mid-depth.

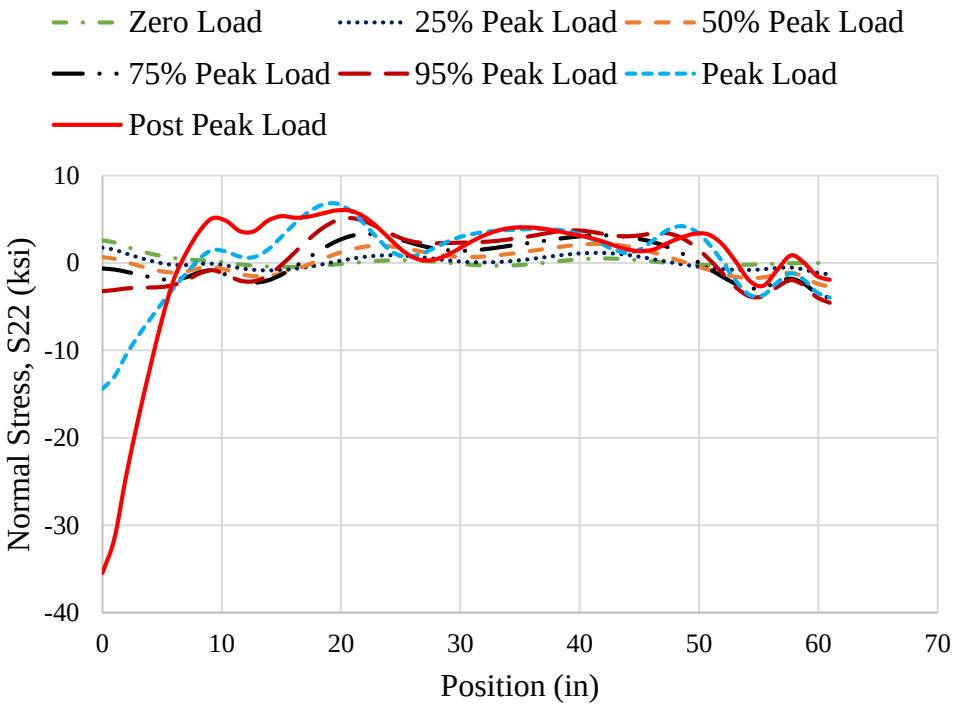

Fig. 5-6. Normal stress *S22* versus position along the web mid-depth.

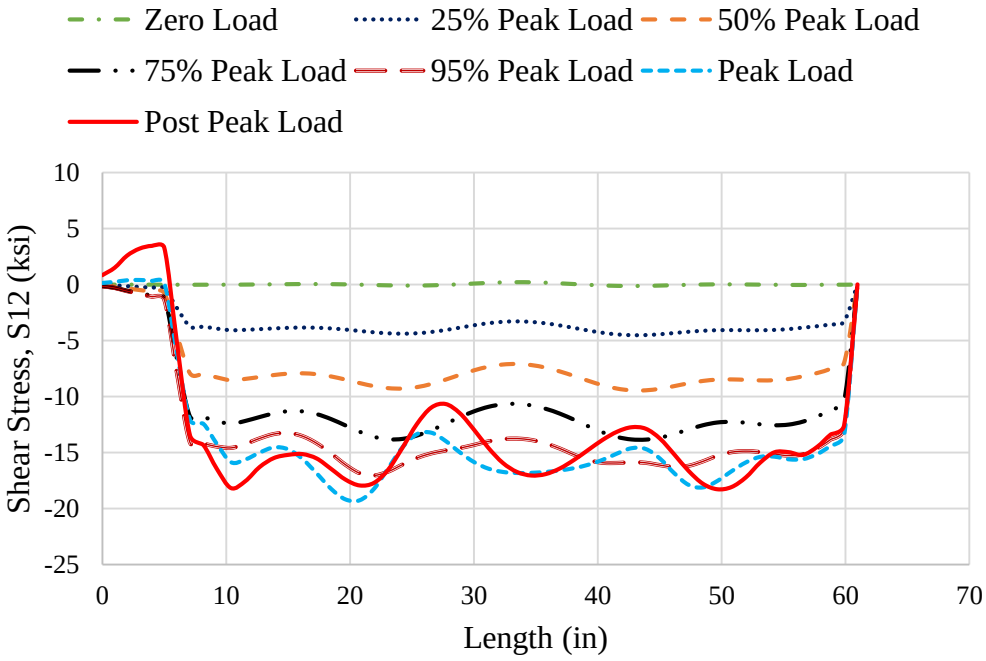

Fig. 5-7. Shear stress *S12* versus position along the web mid-depth.

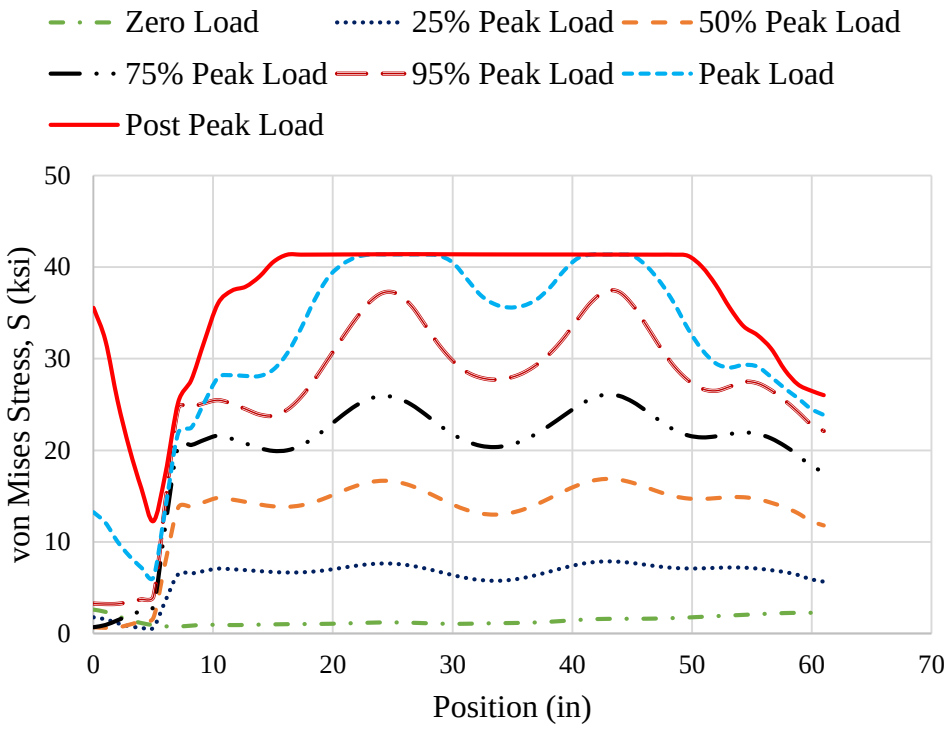

Fig. 5-8. von Mises stress *S* versus position along the web mid-depth.

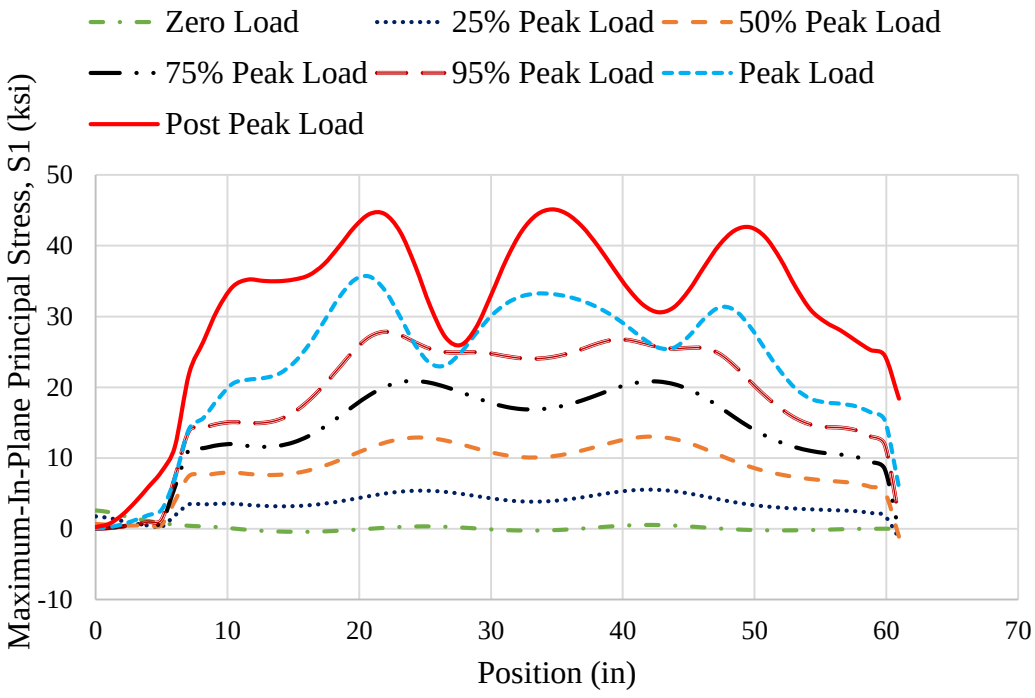

Fig. 5-9. Maximum In-Plane Principal Stress *S1* versus position along the web mid-depth.

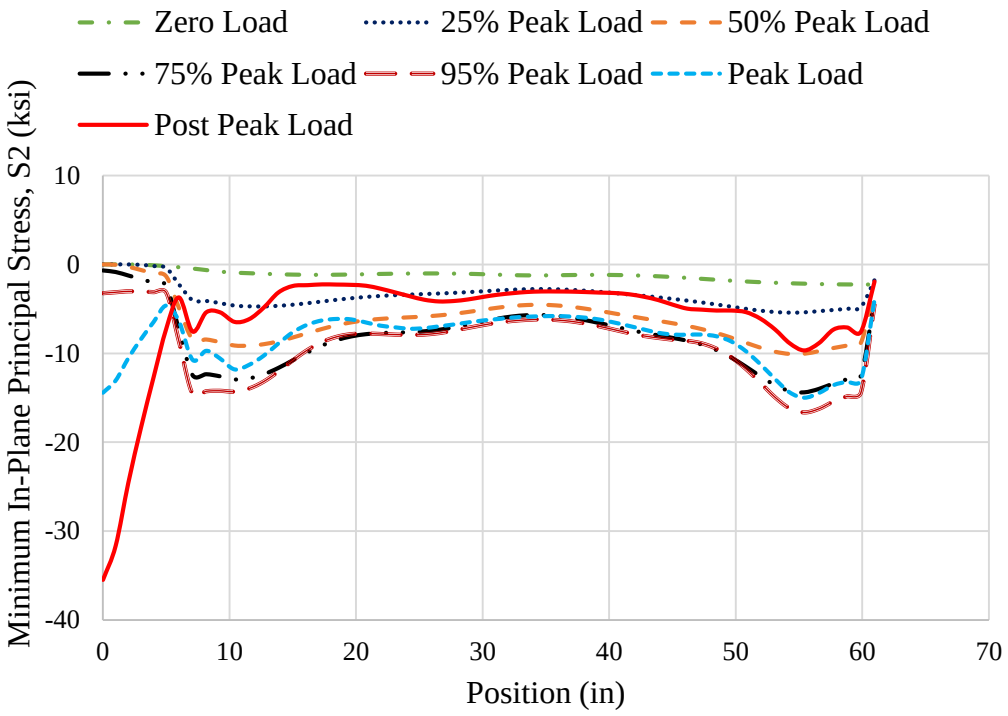

Fig. 5-10. Minimum In-Plane Principal Stress *S2* versus position along web mid-depth.

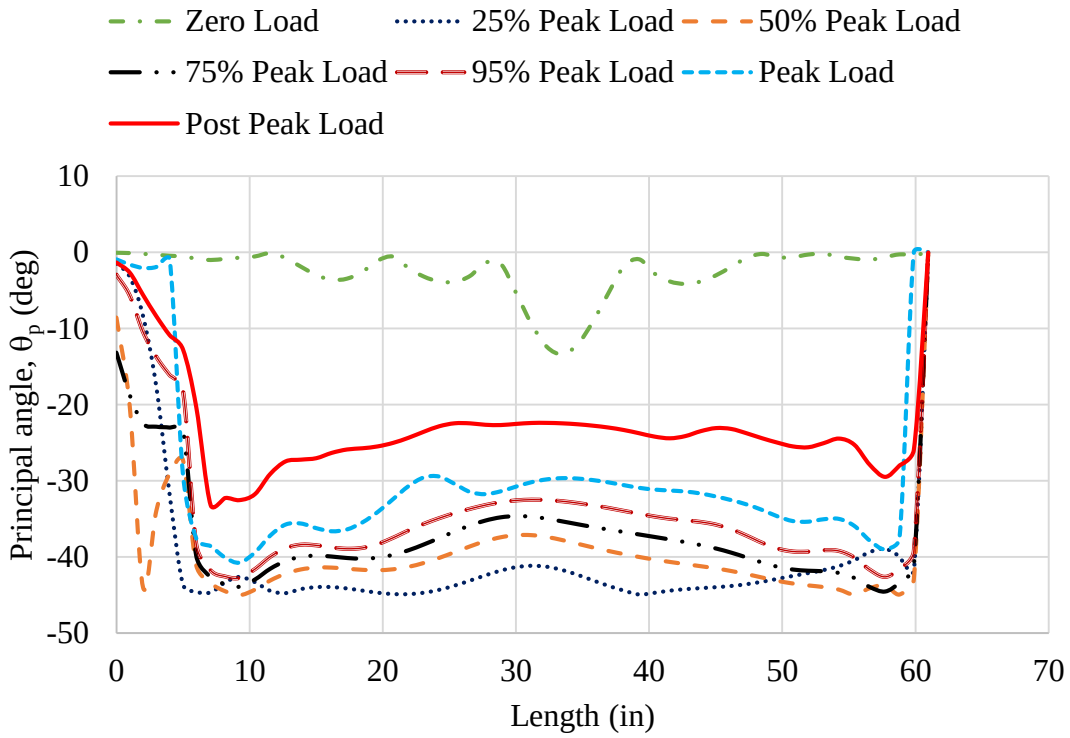

Fig. 5-11. Principal Angle θ_p versus position along the web mid-depth.

At zero load, the small lateral displacement (Fig. 5-4) is due to the lack of equilibrium of the specified nominal residual stresses on the imperfect web. The lateral displacement *U3* is maximum near the quarter-point (at about 40 to 50 inches from free end of the member) for lower levels of the loading. As the limit load is approached, the amplitude of the displacement peak near the left end of the specimen increases compared to the peak on the right. At higher levels of load, *U3* increases at a much higher rate. For a 5% increase in load from 95% of the peak load to the peak load, there is an increase in the maximum lateral displacement of 90%.

As expected, the normal stress *S11* (Fig. 5-5) at zero load is compressive at the web mid-depth due to the specified residual stress pattern. As the load is increased, *S11* increases and is nearly constant for the length of the panel except for the short lengths at the ends of the panel near the transverse stiffeners. This increase in *S11* is associated with the development of diagonal tension within the panel. However, visible peaks form at the peak load. For a 5% increase in load, from 95% of the peak load to the peak load, the maximum *S11* increases from 16 ksi to 23 ksi. At the peak load level, *S11* varies from a minimum of 15 ksi to a maximum of 23 ksi within the middle length of the panel. At the post-peak load level, *S11* varies from a minimum of 22 ksi to a maximum of 38 ksi within this region. Furthermore, as noted above, *S11* is relatively small at the ends of the panel up to 95 % of the peak load. However, these values increase considerably above 95 % of the peak load. This effect is particularly pronounced in the post peak loading range. It appears that the diagonal tension becomes more developed at the ends of the panel in the vicinity of the peak load and within the post-peak range of the response.

Figure 5-6 shows that, at the peak load, the local maximum positive (tensile) *S22* occurs at approximately 10 inches from the stiffener at left end of the panel. Compressive stresses exist in the vicinity of the transverse stiffeners. These are associated with the development of the reaction at the left-hand end and the applied load at the mid-span into the member.

The relatively low values of *S22* for all the load stages are comparable to Höglund's (1997) zero vertical membrane stress assumption.

For lower levels of load, *S12* (Fig. 5-7) is relatively constant within the panel. At higher levels of the load, the variation of *S12* is somewhat similar to the variation of *S11*. Furthermore, peaks in *S12* develop at the peak and post peak load that coincide with the location of the peaks of *S11* and *S22*. At the mid-span of the test member, the shear force in the member is zero. Correspondingly, *S12* approaches zero at the mid-span (i.e., at the 61 in. position).

At lower levels of loading, the von Mises stress *S* (Fig. 5-8) exhibits some oscillation when plotted long the length at the mid-depth of the web. At the peak load there is yielding of the web over several lengths within the panel at the web mid-depth (F_y = 41 ksi). However, at the post peak, almost the entire panel length is yielded at the web mid-depth.

The maximum principal stress *S1* in Fig. 5-9 is calculated using

$$S1 = \left(\frac{S11 + S22}{2} \right) + \sqrt{\left(\frac{S11 + S22}{2} \right)^2 + S12^2} \qquad (5\text{-}1)$$

It is emphasized that this stress and the above stresses are calculated on the deformed geometry of the web. At 25% of the peak load, *S1* is almost equal to *S12* from Fig. 5-7. This shows that up to this level of loading, the web is approximately in a state of pure shear at its mid-depth. *S1* most closely follows the curve of *S11* for higher levels of loading. This is indicative of the fact that for this short panel, a considerable amount of diagonal tension is developed at higher levels of loading, even at 50% of the peak load. At the peak load, there are predominant peaks formed in the plot and the stress *S1* varies significantly over the length of the panel. These peaks become even more predominant at the post peak load.

The minimum in-plane principal stress *S2* in Fig. 5-10 is calculated as

$$S2 = \left(\frac{S11 + S22}{2} \right) - \sqrt{\left(\frac{S11 + S22}{2} \right)^2 + S12^2} \qquad (5\text{-}2)$$

It is emphasized that *S2* is calculated on the deformed geometry of the web. Near the supports and the mid-span, *S2* follows the curve of *S22*. *S2* is essentially unchanged for the loadings above 50% of the peak load for the majority of the panel length, although it increases along with *S22* near the transverse stiffeners. The elastic shear buckling stress, τ_e, calculated using Eq. 1-1 with the plate buckling coefficient taken from Eq. 1-3, is equal to 7.37 ksi. For the majority of the panel length of the specimen, the stress *S2* remains slightly smaller than τ_e.

The principal stress orientation θ_p Fig. 5-11 is calculated using

$$\theta_p = \left(\frac{1}{2}\right)\tan^{-1}\left(\frac{2\,S12}{S11 - S12}\right) \tag{5-3}$$

As indicated above, all the response quantities here are calculated on the deformed geometry of the web. At 25% of peak load, θ_p is almost equal to 45°, and up to this point, the web is approximately in a state of pure shear at its mid-depth. The minor differences are due to the specified residual stress. As the load is further increased, the principal angle in the panel decreases and is almost 30° at the middle of the panel at the peak load. This behavior is similar to the predictions from Höglund's (1997) rotated stress field theory. At the post peak load level, the principal angle at middle of panel decreases to almost 22°. The principal angle according to Höglund (1997) is 21°, calculated using Eq. 1-18. According to Eq. 1-14, *S11* is equal to the sum of *S1* and *S2*, however at the post peak stage near the middle of the panel, S11 is equal to 39 ksi and addition of *S1* and *S2* is equal to 42 ksi. This difference is due to the non-zero value of normal stress, *S22*. The orientation of diagonal principal stress according to the Basler's Tension Field Action Model (1960 and 1961) is 13°.This orientation is given by one-half of the angle of the diagonal between the corners of the panel. The equations employed in the Lee et. al method (Section 1.2.4) are based on other simplified characterizations (i.e., the postbuckling strength is approximately 40% of the difference between elastic shear buckling strength and the plastic shear strength,

Eq. 1-19) without working directly from any assumption of an idealized stress state in the web panels.

Theoretically, *S11* and *S12* at the free ends of the beam should be zero. The small nonzero values are due to the extrapolation of the Gauss point values to the element edges.

5.1.1 Principal Stresses in Selected Elements at the Web Mid-Depth

In this section, three Elements are selected along the mid-depth of the specimen and the principal stresses are drawn as arrows on those Elements to further illustrate the mechanism of the shear strength development. The maximum in-plane principal stress *S1*, the minimum-in-plane principal stress *S2*, and their orientation are illustrated for different levels of loading.

To get a better understanding of the forces near the transverse stiffener of the intermediate panel, Element 1 is located at approximately 2 inches from the left transverse stiffener of the panel. The second Element selected for study is at 21.75 inches from the Element 1. This Element is at the mid-length of the panel. The third Element is at a distance of 2 inches from the left transverse stiffener of the panel. Fig. 5-12 shows the location of these Elements on the specimen.

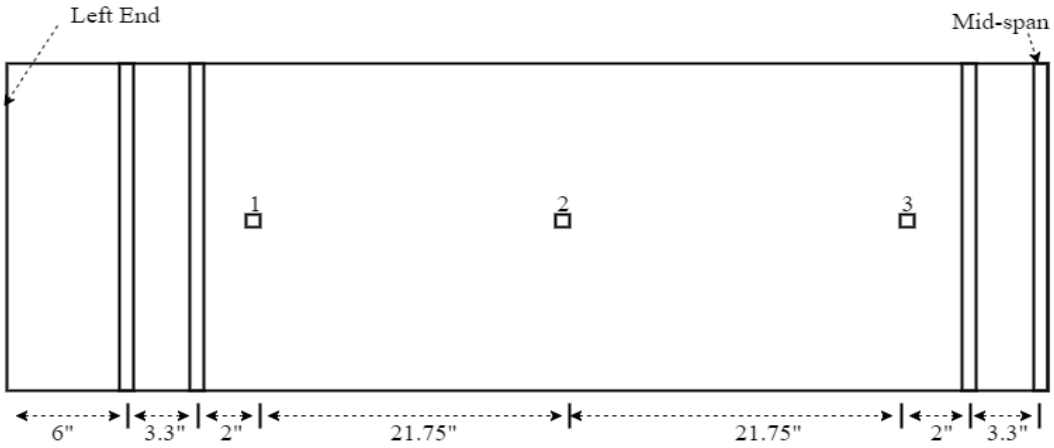

Fig. 5-12. Elements along the web mid-depth.

The arrows on the Elements indicate the orientation of the principal stresses and their numerical values are written in the brackets. Figures 5-13 through 5-26 show the variation in these principal stresses for different levels of loading.

1. Principal Stresses at Zero Load

The values of the principal stresses are small and the principal angle for maximum in-plane principal is almost 90^{o} at zero applied load. However, for some Elements it is slightly different. This because of the effect of the initial web-imperfections and the equilibration of the specified web residual stresses on the deformed web geometry.

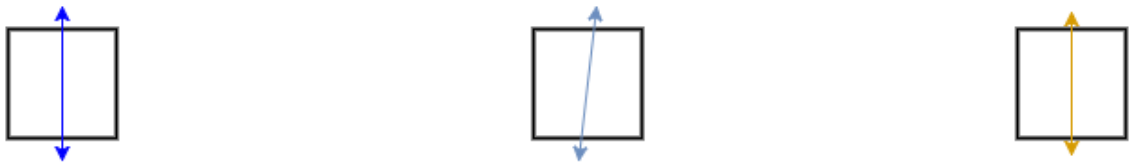

Element 1 (-0.31 ksi) Element 2 (-0.27 ksi) Element 3 (-0.20 ksi)

Fig. 5-13. Maximum In-plane principal stress *S1* and their orientation at zero load.

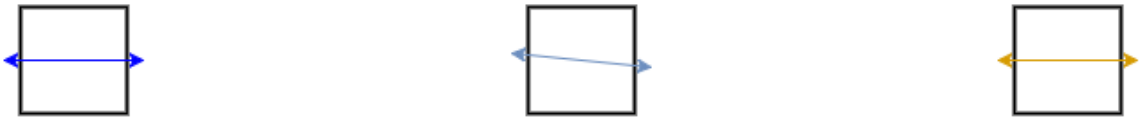

Element 1 (-1.06 ksi) Element 2 (-1.24 ksi) Element 3 (-2.13 ksi)

Fig. 5-14. Minimum In-plane principal stress *S2* and their orientation at zero load.

2. Principal Stresses at 25% Peak Load

All the Elements at 25% peak load are approximately in a state of pure shear. The deviation from this approximation is maximum for Element 3. This is because of the effect of the transverse stiffener.

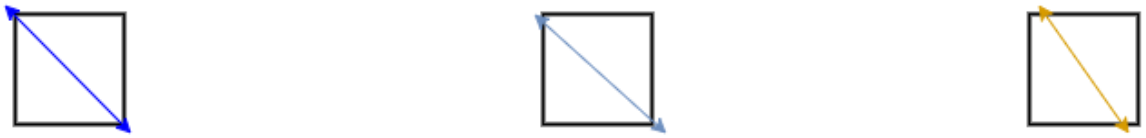

Element 1 (3.24 ksi) Element 2 (3.84 ksi) Element 3 (2.76 ksi)

Fig. 5-15. Maximum In-plane principal stress *S1* and their orientation at 25% peak load.

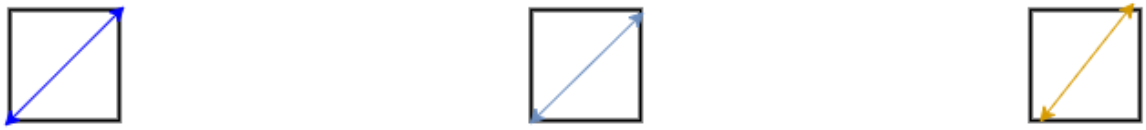

Element 1 (-4.70 ksi) Element 2 (-2.77 ksi) Element 3 (-5.40 ksi)

Fig. 5-16. Minimum In-plane principal stress *S2* and their orientation at 25% peak load.

3. Principal Stresses at 50% peak load

At 50% of the peak load, it is clear that there is a considerable difference between *S1* and *S2* in Element 2. The higher value of *S1* indicates that there is a considerable amount of diagonal tension at the mid-length of the panel. However, for Elements 1 and 3, *S2* is increased considerably at 50% of the peak load compared to 25% of the peak, unlike Element 2. This increase is due the presence of transverse stiffeners, which can be idealized as verticals of a Pratt truss, and the development of the left-hand reaction and the applied load at the mid-span into the web. The web in the vicinity of the transverse stiffeners is the primary component that is developing the vertical forces.

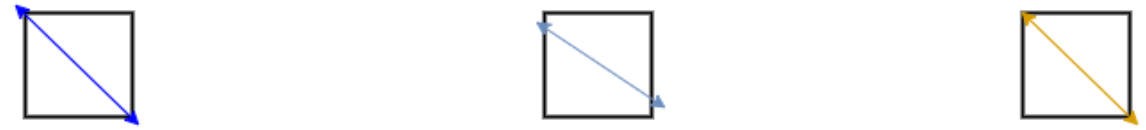

Element 1 (7.61 ksi) Element 2 (10.07 ksi) Element 3 (7.02 ksi)

Fig. 5-17. Maximum In-plane principal stress *S1* and their orientation at 50% peak load.



Element 1 (-8.96 ksi) Element 2 (-4.56 ksi) Element 3 (-10.06 ksi)

Fig. 5-18. Minimum In-plane principal stress *S2* and their orientation at 50% peak load.

4. Principal Stresses at 75% peak load

The trends in the principal stresses at 75% of the peak load are similar to what was observed at 50% of peak load. *S2* increases slightly for Element 2 at this load level. There is a considerable amount of diagonal tension forming in Element 2. Elements 1 and 3 are influenced by the presence of transverse stiffeners, and the development of the vertical forces into the web causing an increase in *S2*.

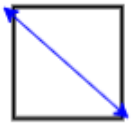
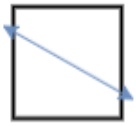


Element 1 (11.59 ksi) Element 2 (16.88 ksi) Element 3 (11.02 ksi)

Fig. 5-19. Maximum In-plane principal stress *S1* and their orientation at 75% peak load.



Element 1 (-12.35 ksi) Element 2 (-5.69 ksi) Element 3 (-14.22 ksi)

Fig. 5-20. Minimum In-plane principal stress *S2* and their orientation at 75% peak load.

5. Principal Stresses at 95% peak load

At 95% peak load, the behavior is similar to what was observed at 50% and 75% of the peak load. The *S1* for Element 2 continues to increase without much increase in *S2*. The minor principal stress *S2* for Elements 1 and 3 also continues to increase.

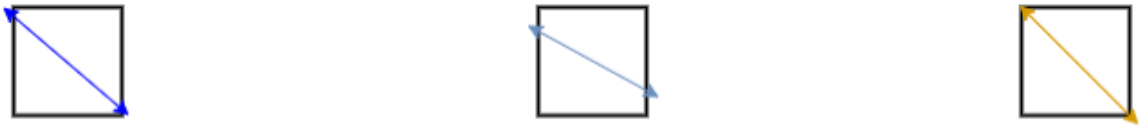

Element 1 (14.97 ksi) Element 2 (24.04 ksi) Element 3 (14.73 ksi)

Fig. 5-21. Maximum In-plane principal stress *S1* and their orientation at 95% peak load.

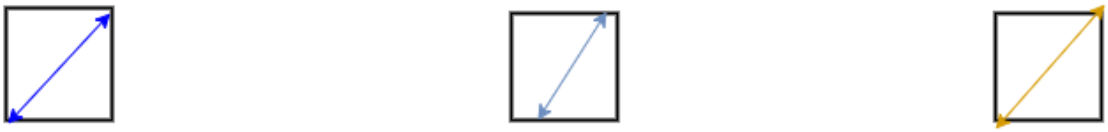

Element 1(-13.16 ksi) Element 2(-6.23 ksi) Element 3(-16.17 ksi)

Fig. 5-22. Minimum In-plane principal stress *S2* and their orientation at 95% peak load.

6. Principal Stresses at Peak Load

At peak load, the stress *S 1* in Element 2 increases significantly when compared to 95% peak load while *S2* remains almost the same. In addition, there is a considerable increase of *S1* for Elements 1 and 3 also. *S2* for Element 1 and 3 decreases when compared to 95% of the peak load. This shows that the effect of diagonal tension is dominant over the entire length of the panel at peak load.

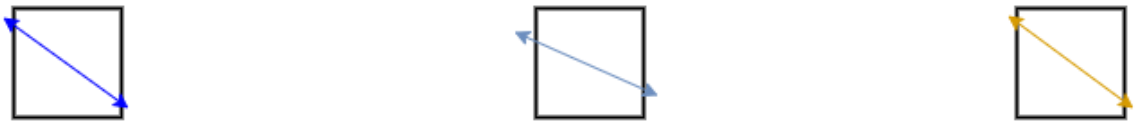

Element 1 (20.86 ksi) Element 2 (33.24 ksi) Element 3 (18.61 ksi)

Fig. 5-23. Maximum In-plane principal stress *S1* and their orientation at peak load.

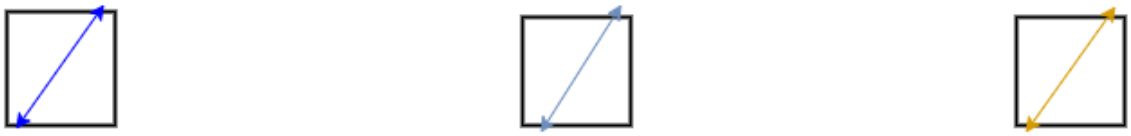

Element 1 (-9.86 ksi) Element 2 (-5.85 ksi) Element 3 (-14.60 ksi)

Fig. 5-24. Minimum In-plane principal stress *S2* and their orientation at peak load.

7. Post peak

The trend at post peak load is the same as the peak load. There is significant diagonal tension throughout the length of the panel causing *S2* in Elements 1 and 3 to decrease. For Element 2, *S2* has not increased after 50% of the peak load.

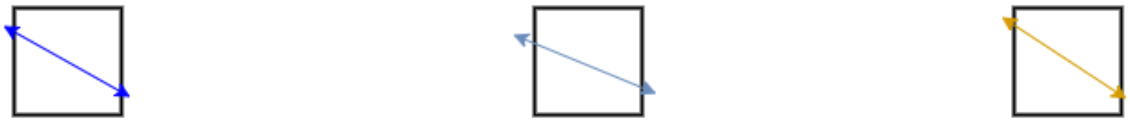

Element 1 (35.02 ksi) Element 2 (44.39 ksi) Element 3 (30.94 ksi)

Fig. 5-25. Maximum In-plane principal stress *S1* and their orientation at post peak load.

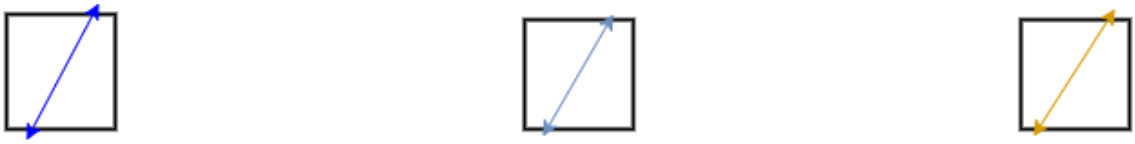

Element 1 (-4.83 ksi) Element 2 (-3.08 ksi) Element 3 (-8.85 ksi)

Fig. 5-26. Minimum In-plane principal stress *S2* and their orientation at post peak load.

5.2 Responses at a Section Along the Length at the Top of the Web

In this section, a section is cut at the web top and the stresses along the section are plotted. The quantities plotted are the web membrane stresses, *S11*, *S22* and *S12*, the von Mises stress, *S*, the maximum principal tensile membrane stress (*S1*), the maximum principal compressive membrane stress (*S2*) and the orientation of the principal stresses (θ_p). Figures 5-27 through 5-33 show variation of these quantities, in that order, at a section along the length at web top for different levels of loading.

At zero load, the normal stress *S11* (Fig. 5-27) is approximately constant for the entire length of the specimen and is equal to the residual stress applied in the test simulation. For 25%, 50% and 75% of the peak load, the results from simulations are identical to results obtained from beam theory if residual stress is accounted in the beam theory. The results

obtained from beam theory are not shown in the graph for clarity. At 95% of the peak load, there is a slight increase in the value of *S11* near the left end of the panel. However, at the peak load there is sudden increase in compressive stress near support at 8 inches from the left transverse stiffener of the panel. At the post peak load level, this behavior is much more pronounced. This is where the web buckle meets the top-flange (see Figs. 4-15 and 4-16).

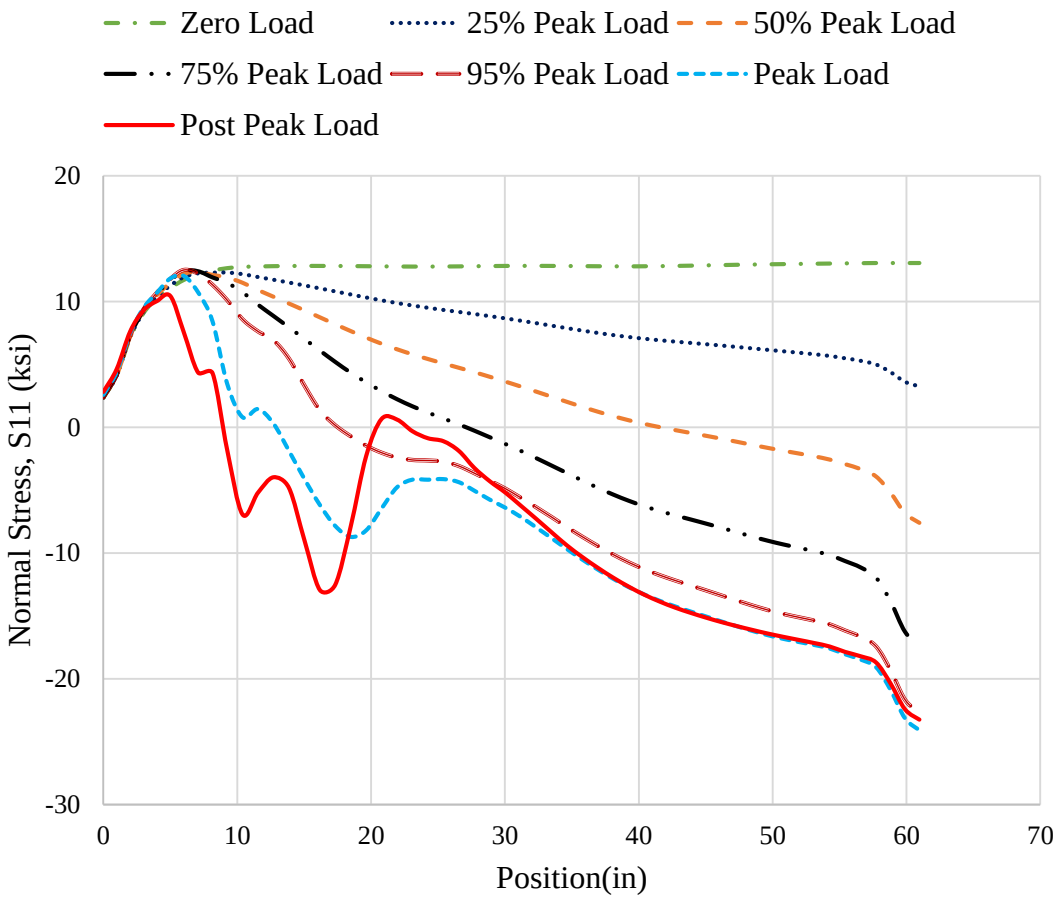

Fig. 5-27. Normal stress *S11* versus position along the web top.

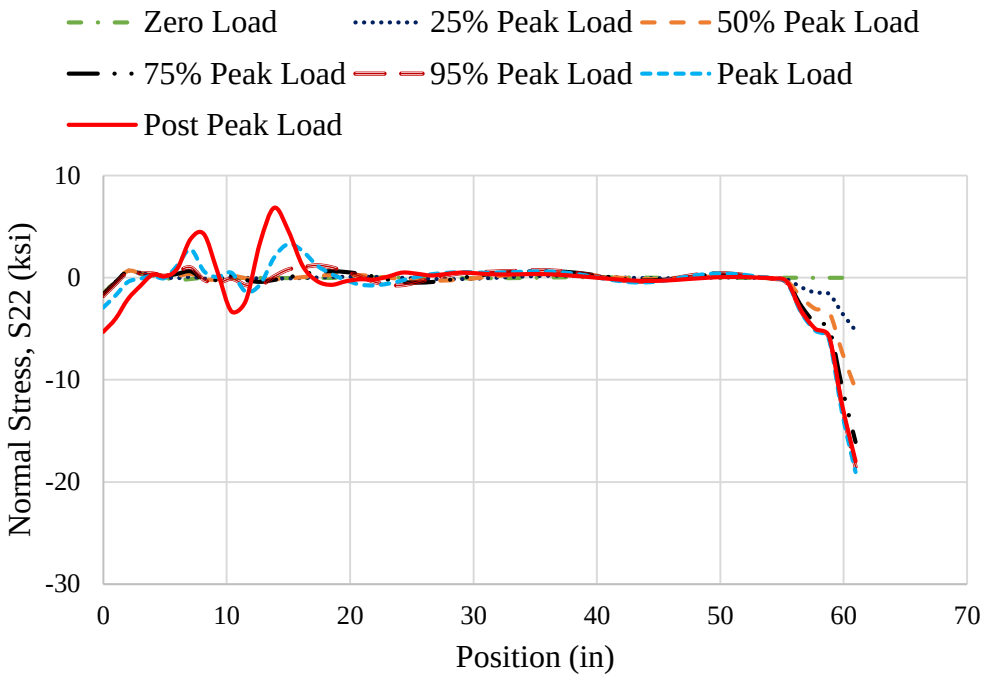

Fig. 5-28. Normal stress *S22* versus position along the web top.

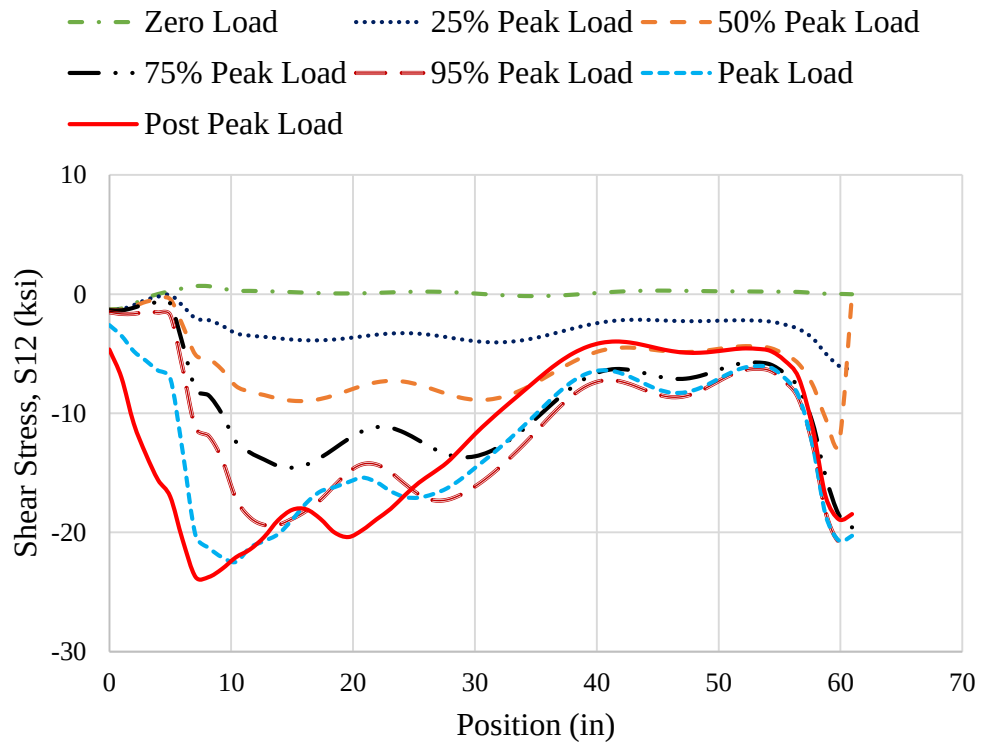

Fig. 5-29. Shear stress *S12* versus position along the web top.

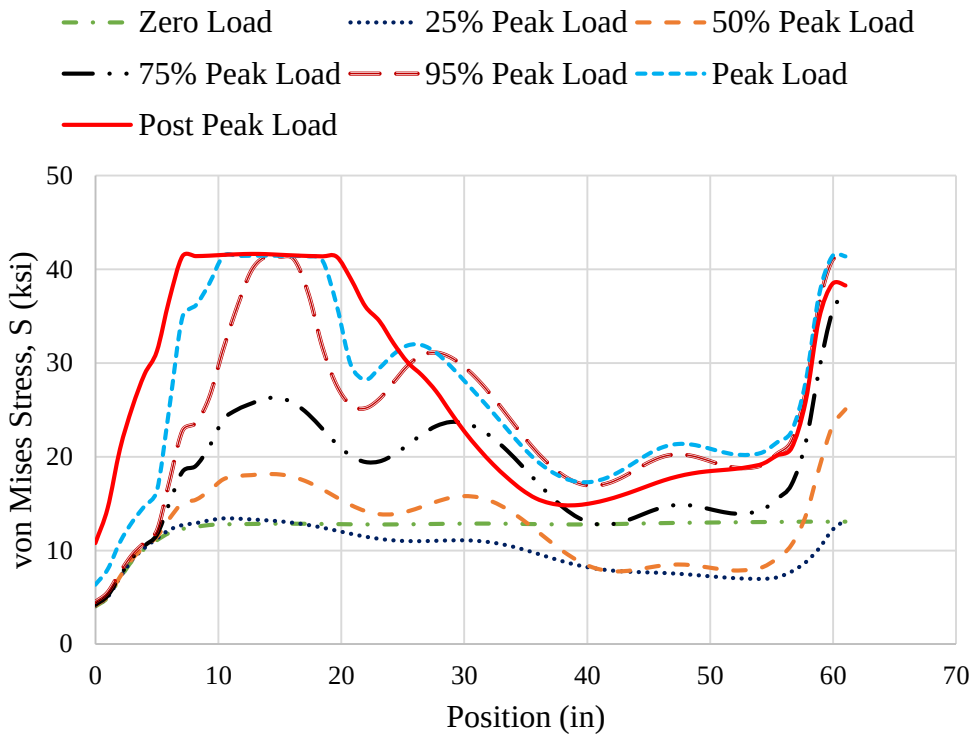

Fig. 5-30. Von Mises stress *S* versus position along the web top.

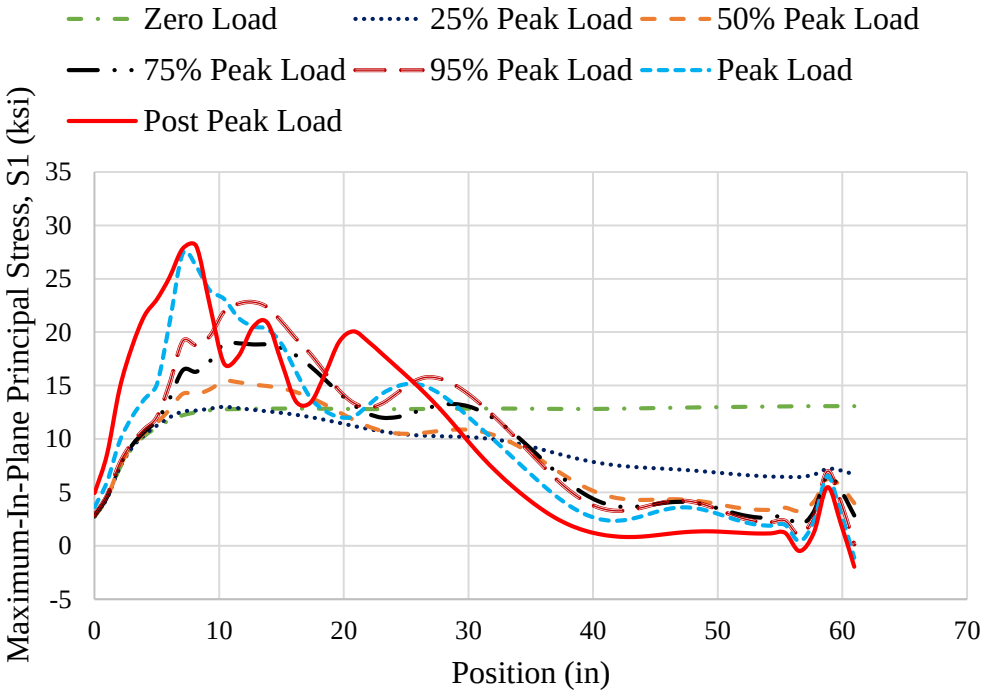

Fig. 5-31. Maximum In-Plane Principal Stress *S1* versus position along the web top.

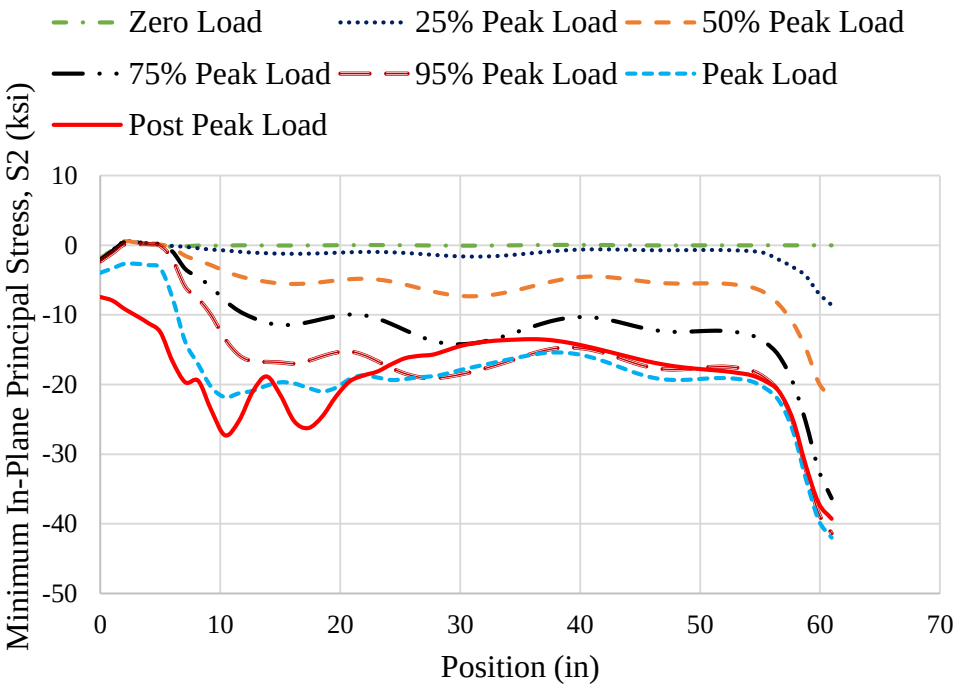

Fig. 5-32. Minimum In-Plane Principal Stress *S2* versus position along the web top.

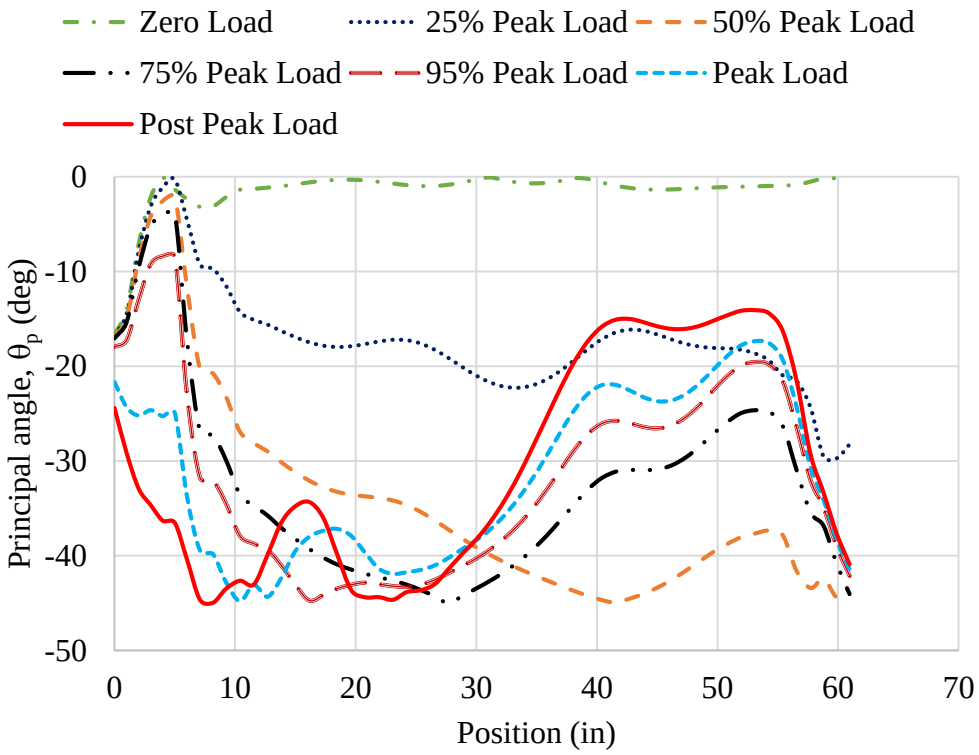

Fig. 5-33. Principal Angle θ_p versus position along the web top.

The normal stress *S22* (Fig. 5-28) is essentially zero for almost the entire half-length of the beam except at its mid-span where the concentrated load is applied. Even at 95% peak load, this stress is small. This indicates that there are no substantial transverse forces applied to the top flange. At 95% of the peak load, the maximum value of stress, other than at near the mid-span, is 1.20 ksi. However, at the peak load, the maximum compressive stress in this region increases to 3.30 ksi. As the load increases from 95 % of the peak load to the peak load, this stress increases by approximately 175%. The top flange is subjected to extremely low transverse forces except near the support and at near the peak load. Even at the post peak load, *S22* remains almost equal to zero except near the left end of the panel. This is where the web buckle meets the top flange as well as where forces transferred by diagonal tension toward the top of the web need to be balanced by a vertical compression force transfer to the left-end support.

At 25% of the peak load, the magnitude of *S12* (Fig. 5-29) at the left-hand end is less than that at the right-hand end of the plot (i.e., at the beam mid-span). However, for higher load levels, the maximum value of *S12* occurs near the transverse stiffener on the left end of the panel (except very locally in the vicinity of the mid-span). The maximum *S12* at the peak load occurs exactly at the position of the transverse stiffener on the left-hand end of the panel. This develops the diagonal tension force in the panel into the stiffener.

At 95% of the peak load, the von Mises stress *S* plot (Fig. 5-30) indicates that there is yielding of small length of the web at its top. However, at the peak load and the post peak load, this yielding is concentrated over a larger length at the location where buckled meets the top flange. The yielding of the web top causes the decrease in the normal stress *S11* in this region, shown in Fig. 5-27.

Yoo and Lee (2006) pointed out that the diagonal compression increases near the edges of the panel after buckling. However, their research focused predominantly on square panels, and they loaded their panels only by shear tractions along all four of the edges.

Although the boundary conditions employed by Yoo and Lee allow a focus on pure shear response and shed important light on the behavior, girder web panels are never actually loaded with these specific boundary conditions. The behavior of the web panels in actual girders is more complex. The current research focuses on the responses in actual girders.

The principal stresses *S1* and *S2* at the web top (Fig. 5-31 and 5-32) increase, particularly at the left-hand end of the panel, up to the peak load level. This is primarily due to the increase in the shear stress, *S12.* The normal stress *S22* remains almost equal to zero except locally and at near the peak load (see Fig. 5-28). However, at the post peak load level, *S22* increases and there is not much increase in the shear stress *S12* resulting in increase in minimum-in plane principal stress *S2* (Fig. 5-32) without much increase in *S1* after the peak load. The increase in *S2* at the right end of the panel is because of increase in compressive normal stress *S11* due to flexure. The fact that the principal angle (Fig. 5-33) is close to 45^{o} for the left end of the specimen and is lesser at the right end of the panel confirms that the increase in *S2* is primarily due to increase in *S12*.

5.2.1 Boundary Condition between the Top Flange and the Web

In this section, three elements at the top of the web are selected and the variation of *S22* on the front, middle and back surfaces of the web at different applied loads is studied to explain the boundary condition between top flange and web. In all the previous sections, *S22* is found by taking the membrane force, *SF2*, and dividing it by the web thickness. To take the plate bending into account, the stresses at the positive, mid-thickness and negative surfaces of the web plate are plotted. Fig. 5-29 illustrates the different shell element surfaces. The top surface, SPOS, is defined as the outer surface in the positive normal direction. The bottom surface, SNEG, is defined as the outer surface in the negative normal direction. By default, ABAQUS reports the stresses at the SPOS, MID and SNEG surfaces.

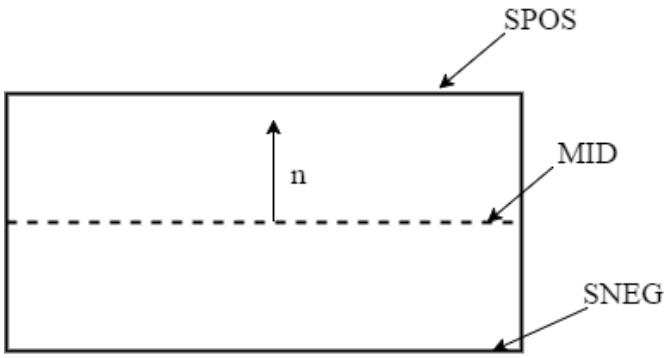

Fig. 5-34. *S*ection through a shell element.

The first Element is selected at 6 inches from the left transverse stiffener of the panel, which is the location where the maximum *S22* occurs at the peak load. The second Element is selected at the mid-length of the panel and the third Element is selected at 2 inches from the right transverse stiffener. Fig. 5-35 shows the location of the selected Elements on the specimen. Figures 5-36 through 5-38 show the variation of *S22* at the different surfaces as a function of the applied load.

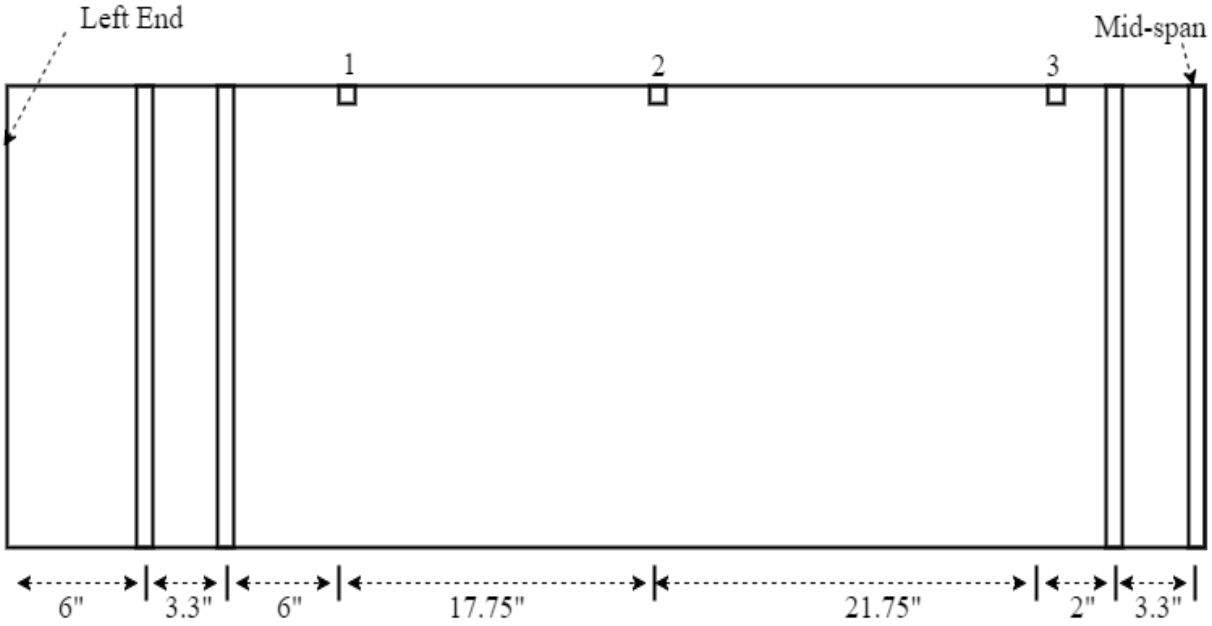

Fig. 5-35. Elements along the web top.

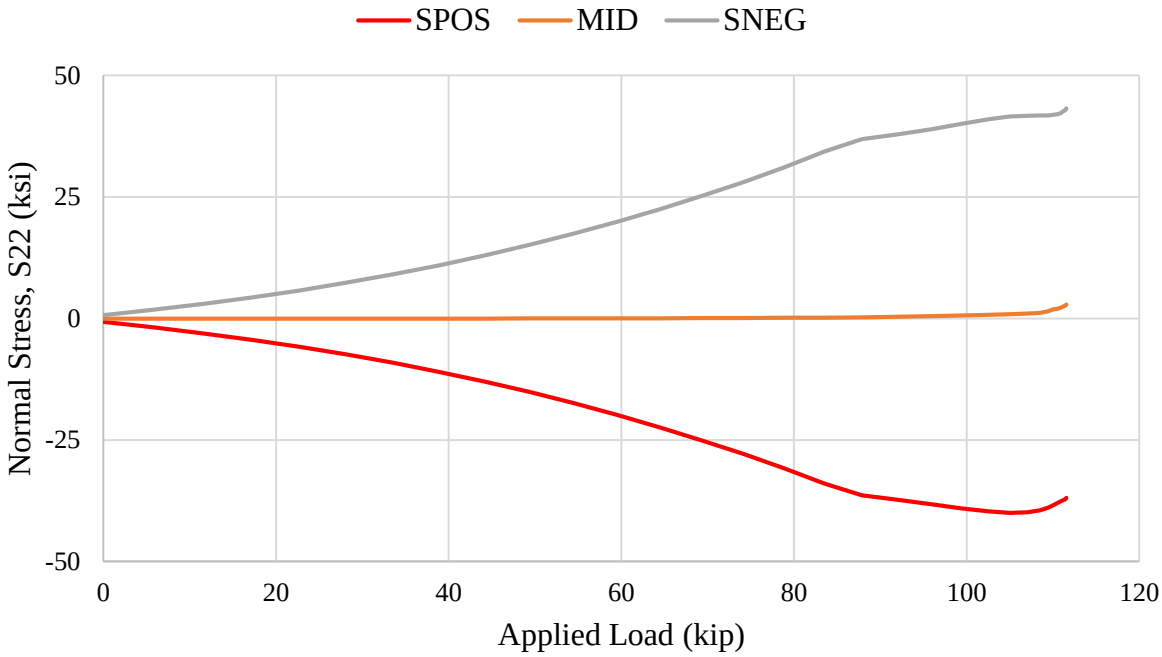

Fig. 5-36. Normal stress *S22* at top, mid and bottom surface of the web versus applied load for Element 1 along the web top.

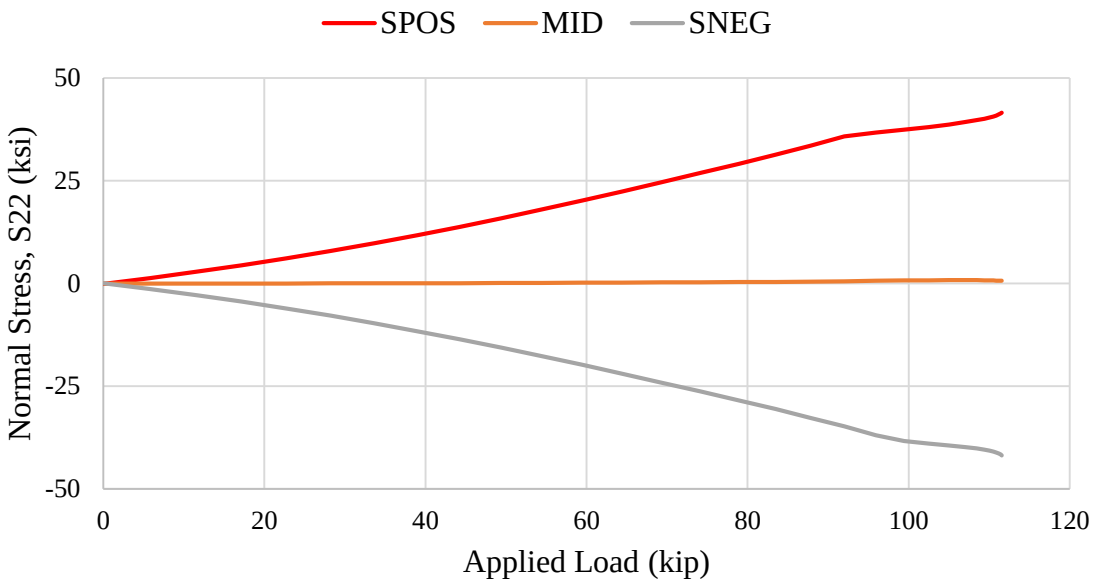

Fig. 5-37. Normal stress *S22* at top, mid and bottom surface of the web versus applied load for Element 2 along the web top.

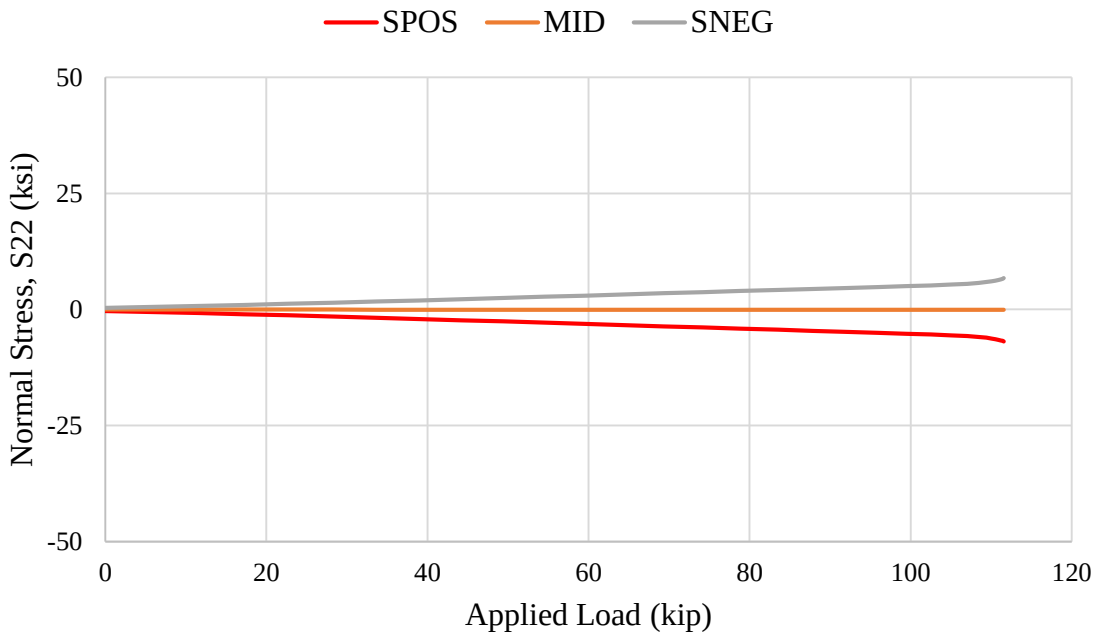

Fig. 5-38. Normal stress *S22* at top, mid and bottom surface of the web versus applied load for Element 3 along the web top.

For Element 1, the stress, *S22* at the mid-surface remains nearly equal to zero up to almost 95% of the peak load. After this, there is a small increase in the stress at mid-surface. The stresses *S22* at the mid-surface in Elements 2 and 3 remain approximately equal to zero for all levels of loading. The *S22* values at the top and bottom surface of the web are smaller for Element 3 compared to Elements 1 and 2, indicating that there is lesser tendency for rotation of the web about the web-flange juncture near the transverse stiffener on the right-hand end of the panel at the top-flange.

From these plots, it can be stated that the top-flange provides substantial torsional restraint to the top of the web throughout the loading and into post-peak. However, from Fig. 5-28, it is clear that the web membrane force remains almost zero until 95% of the peak load but increases significantly at the post peak load level and there is significant pushing and pulling of the top flange in the vicinity of the left-hand end of the panel.

5.3 Responses at a Section Along the Length at the Bottom of the Web

A procedure similar to that discussed in Section 5.2 is repeated in this section for the web and bottom flange juncture. The quantities plotted are the web membrane stresses, *S11*, *S22* and *S12*, the von Mises stress, *S*, the maximum principal tensile membrane stress (*S1*), the maximum principal compressive membrane stress (*S2*) and the orientation of the principal stresses (θ_p). Figures 5-39 through 5-45 show variation of these quantities, in that order, at a section along the length at web bottom for different levels of loading.

At zero load, the normal stress *S11* (Fig. 5-39) is almost constant for the entire length of the specimen and is equal to the residual stress value applied in the simulation. For 25%, 50% and 75% of the peak load, the results from simulations are identical to results from beam theory, if residual stress is accounted for in the beam theory. The results obtained from beam theory are not shown in the graph for clarity. At 95% of the peak load, there is a drop in the value of *S11* at 6 inches from the right end of the panel. At the post peak load level, this behavior is very pronounced and is visible over a longer length.

The normal stress *S22* (Fig. 5-40) is essentially zero for almost the entire half-length of the specimen except at the support and the mid-span. Even at 95% peak load, this stress is very small. This indicates that there are no substantial transverse forces applied to the bottom flange. At 95% of the peak load, the maximum value of this stress, other than near the mid-span and the left-hand support, is 0.5 ksi. However, at the peak load, the maximum compressive stress increases to 1.0 ksi (except at the mid-span and the support). For an increase in 5% load, the stress increases by approximately 100%. The maximum tensile *S22* occurs at 3 inches from the right end of the panel. This indicates that the bottom flange is subjected to extremely low transverse forces. Even at the peak load, these stresses are relatively small. However, at the post peak load level, *S22* increases significantly at 6 inches from the right-hand end of the panel. This where the web buckle meets the bottom

flange as well as where forces transferred by diagonal tension need to be balanced by a vertical compression force transfer to the applied load location. The pushing and pulling of flanges causes the oscillatory variation of the stress *S22*.

The maximum value of *S12* at the bottom of the web (Fig. 5-41) occurs near the right-hand end of the panel whereas for the top of the web, *S12* is maximum at the left-hand end of the panel. At the post peak load level, the maximum *S12* occurs exactly at the same position as the maximum *S22* (Fig. 5-40). This develops the diagonal tension in the panel.

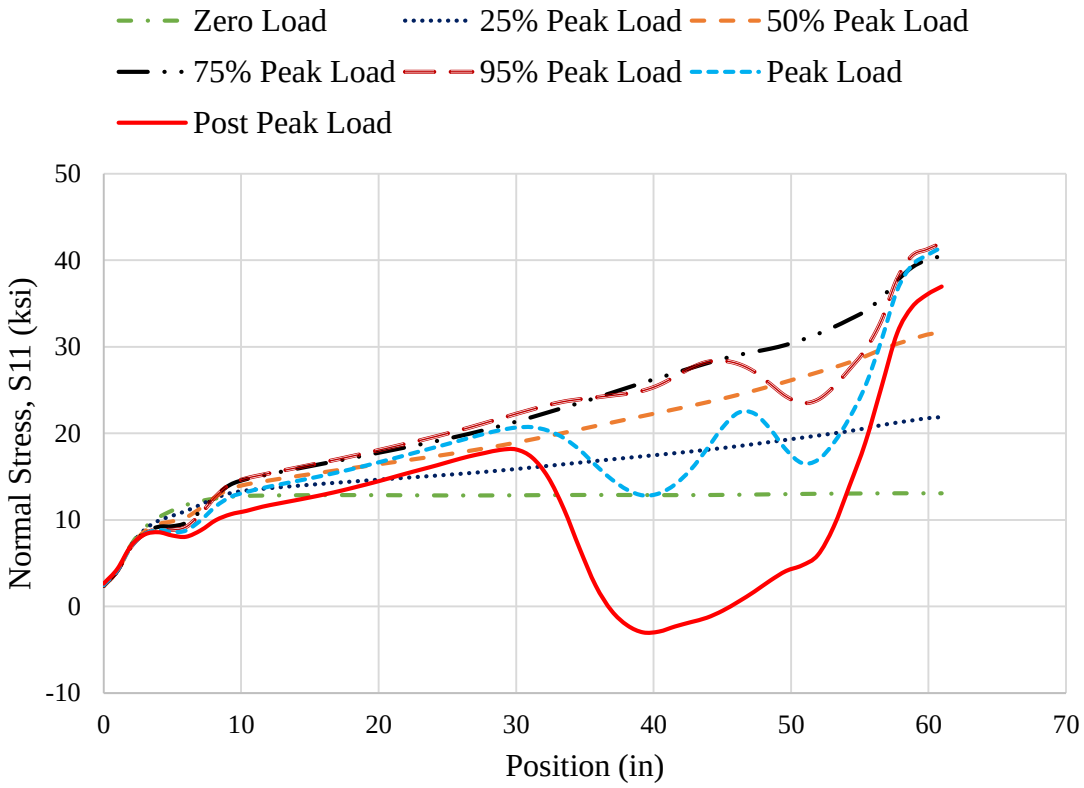

Fig. 5-39. Normal stress *S11* versus position along the web bottom.

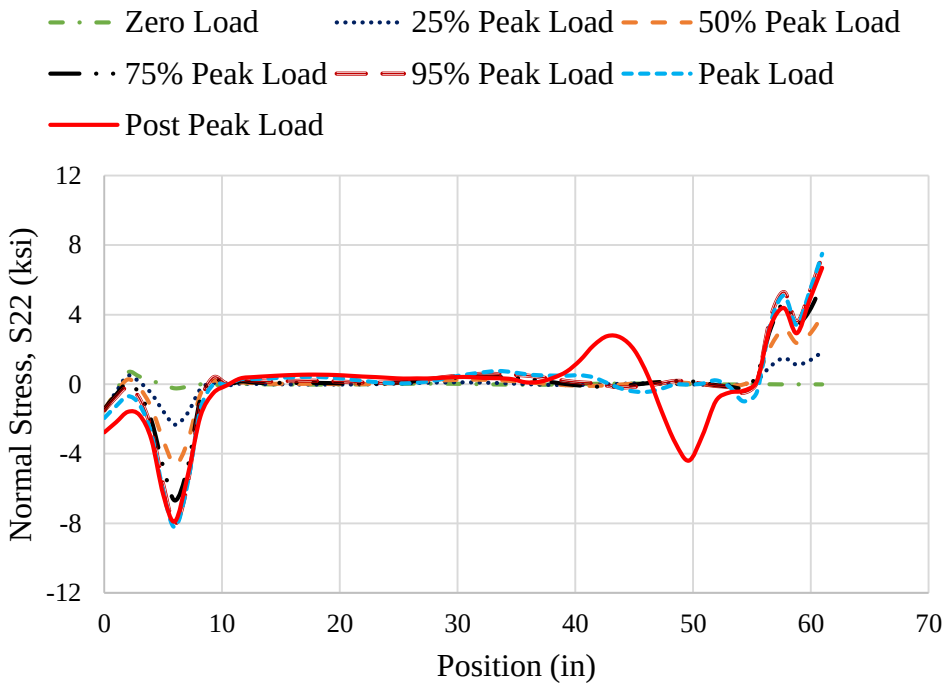

Fig. 5-40. Normal stress *S22* versus position along the web bottom.

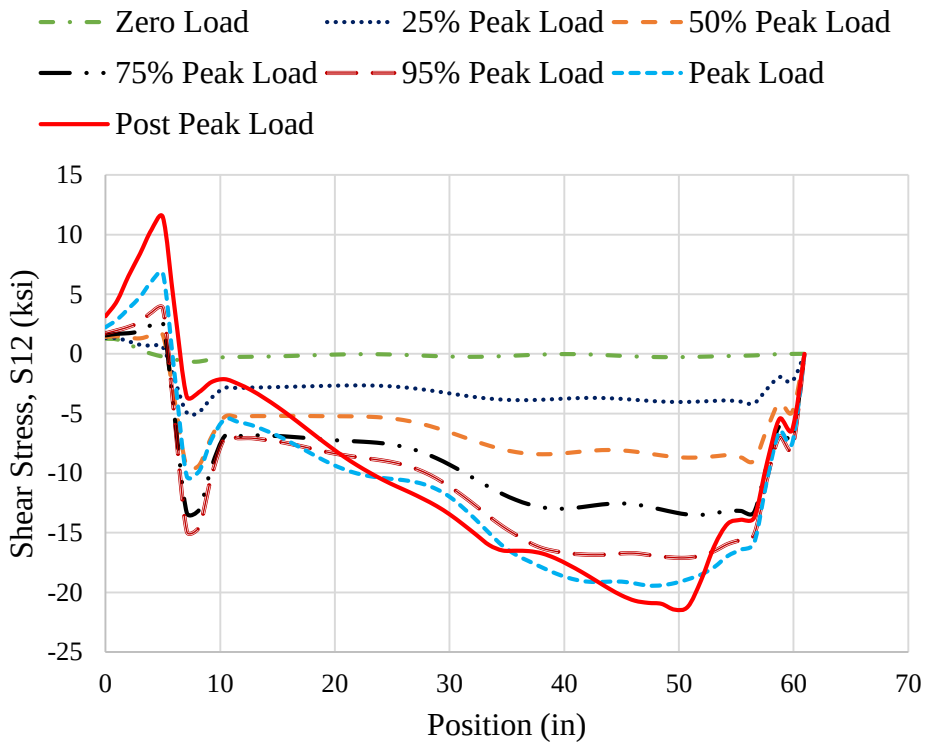

Fig. 5-41. Shear stress *S12* versus position along the web bottom.

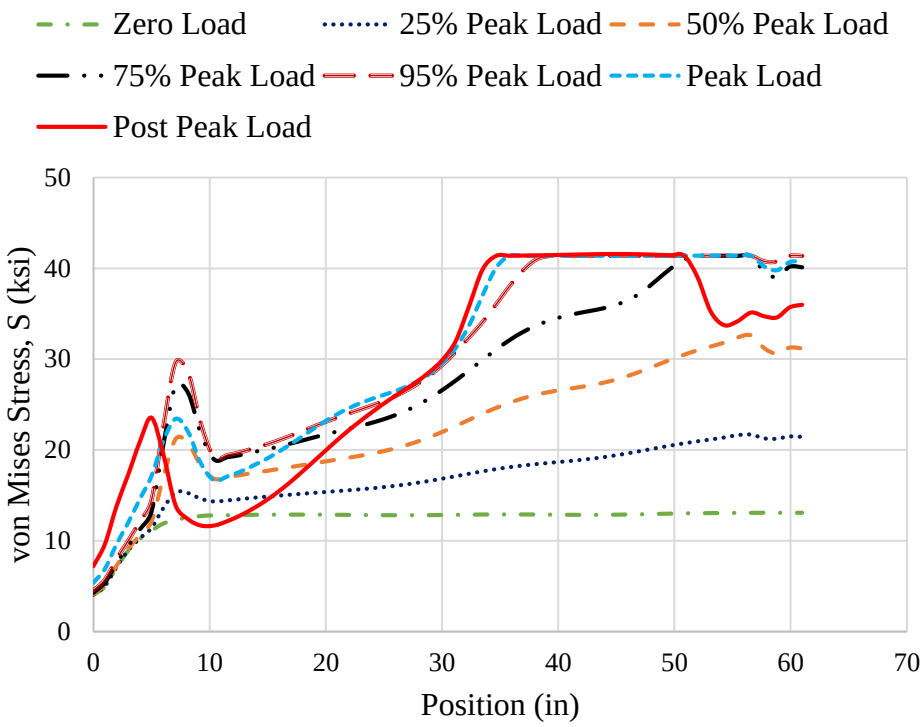

Fig. 5-42. von Mises stress *S* versus position along the web bottom.

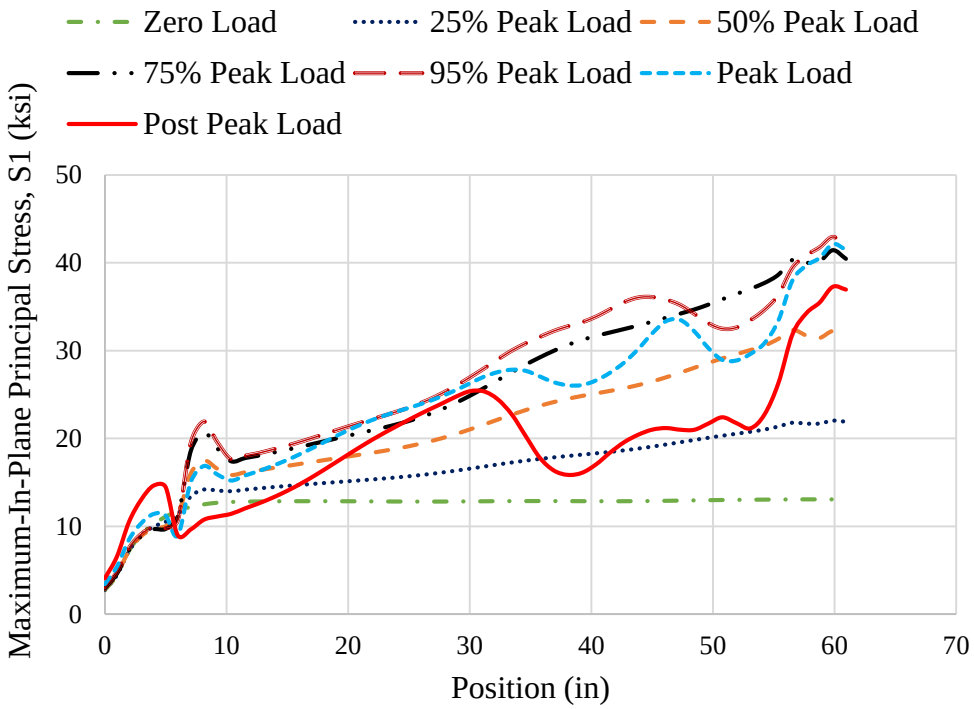

Fig. 5-43. Maximum In-Plane Principal stress *S1* versus position along web bottom.

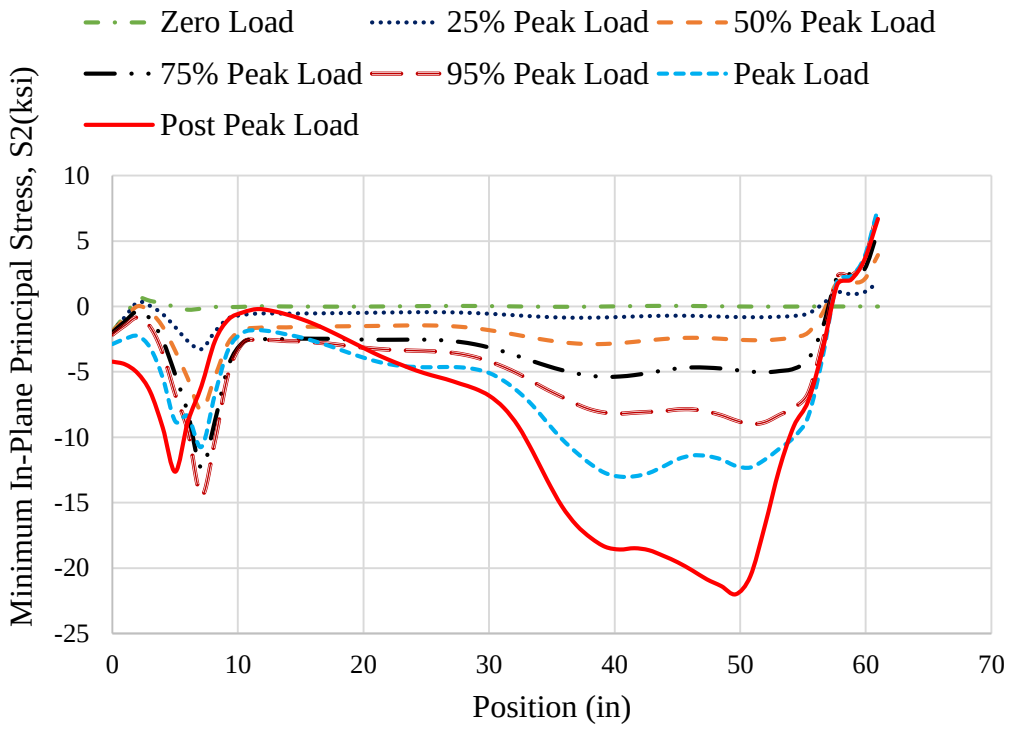

Fig. 5-44. Minimum In-Plane Principal stress *S2* versus position along web bottom.

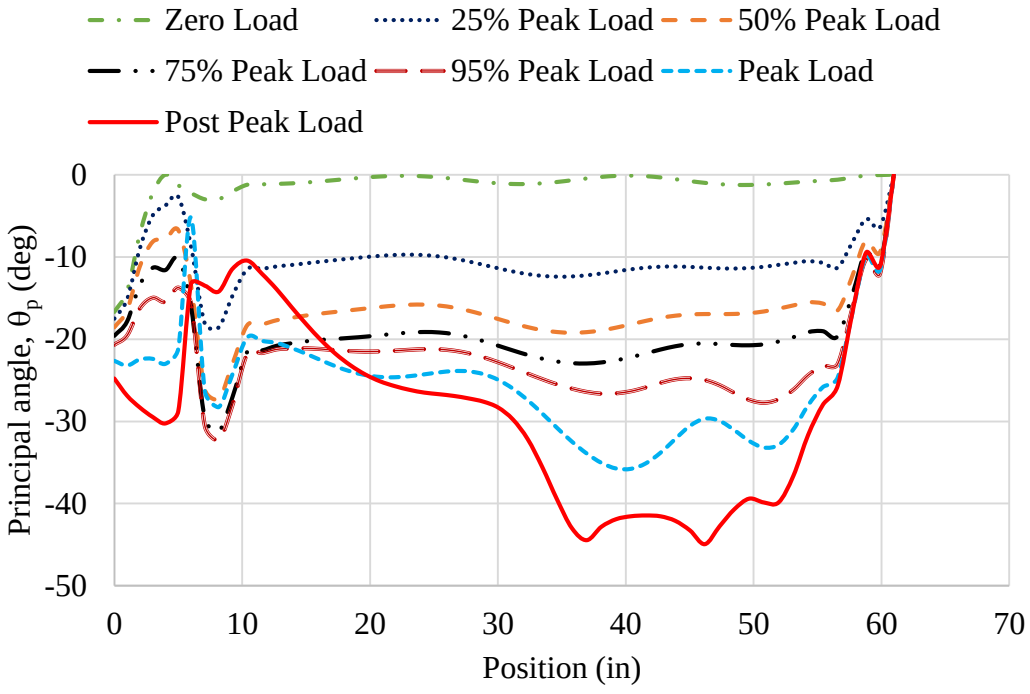

Fig. 5- 45. Principal Angle θ_p versus position along the web bottom.

At 75% of the peak load, the von Mises stress *S* plot (Fig. 5-42) indicates that there is yielding of very small length of the web bottom. However, at 95% of the peak load, at the peak load and at the post peak load level, this yielding is concentrated over a larger length at the location where predominant web buckle meets the bottom flange. The yielding of the web bottom and the plastic stress interaction between the plate bending, pushing and pulling on the flange via *S22* and the high shear stress *S11* causes the decrease in the normal stress *S11*. This yielding occurs at left end of the panel at the web top and at the right end of the panel at the web bottom. It is more extensive at the right end and bottom of the web panel due to the high flexural stress in this region at the smaller load levels.

The principal stress *S1* (Fig. 5-43) can be related to the curve of the normal stress, *S11*. The increase in the diagonal compression, *S2* (Fig. 5-44) can be related to be the interaction between the stresses *S11* and *S12*. The normal stress *S22* remains almost equal to zero except at near the peak load. However, at the post peak load level, *S22* increases and there is not much increase in the shear stress *S12* resulting in increase in minimum-in plane principal stress *S2* (Fig. 5-44).

5.3.1 Boundary Condition between the Bottom Flange and the Web

Similar to the procedure in Section 5.2.1, several Elements are selected in this section to investigate the boundary condition between the bottom flange and the web. The first Element is at a distance of 3 inches from the left transverse stiffener. The second Element is at the mid-span of the panel. The third Element is selected at 3 inches from the right end of the panel, the location where the maximum *S22* occurs at the peak load. The definitions of SPOS, MID and SNEG presented in Section 5.2.1. Figure 5-46 shows the location of these Elements. Figures 5-47 through 5-49 show the variation of *S22* at the different surfaces as a function of the applied load.

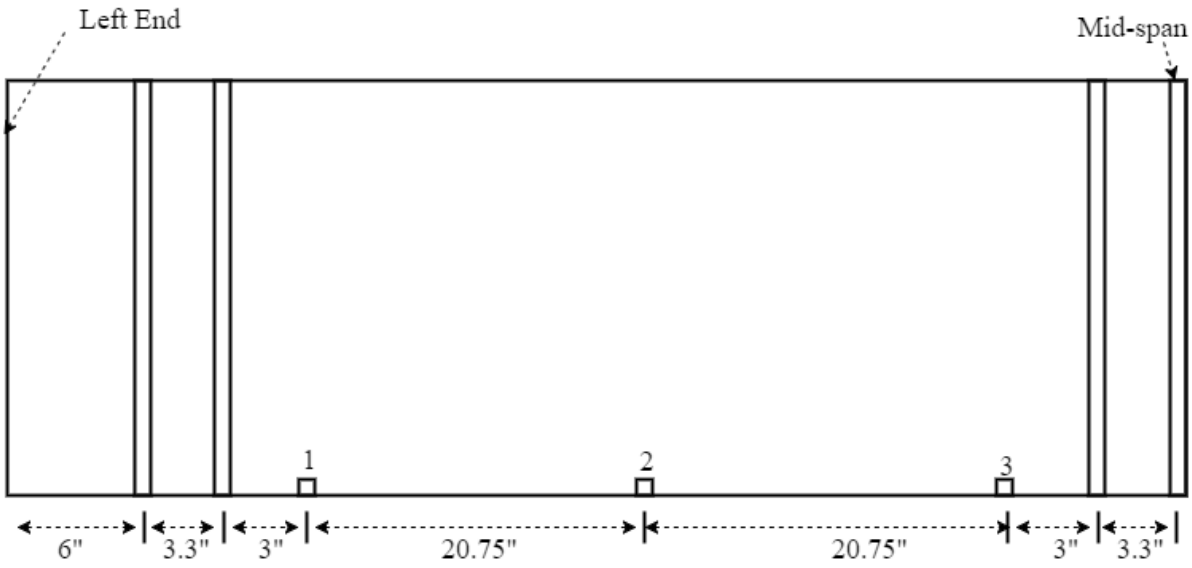

Fig. 5-46. Elements along the web-bottom.

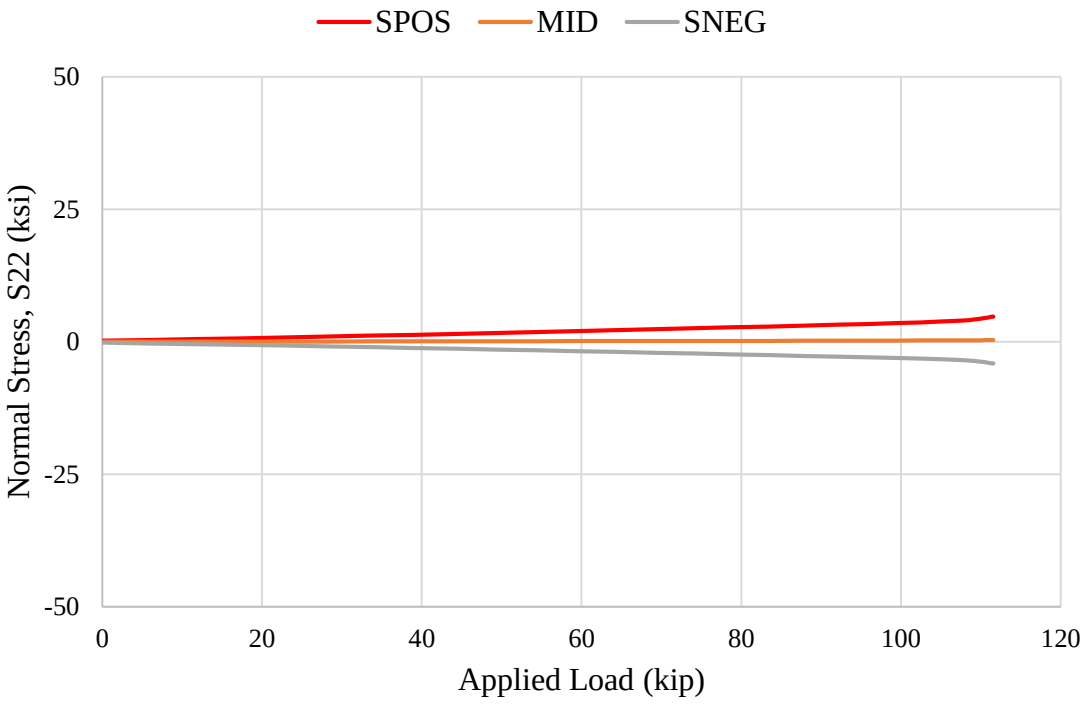

Fig. 5-47. Normal *Stress S22* at top, mid and bottom surface of web versus applied load for Element 1 at web bottom.

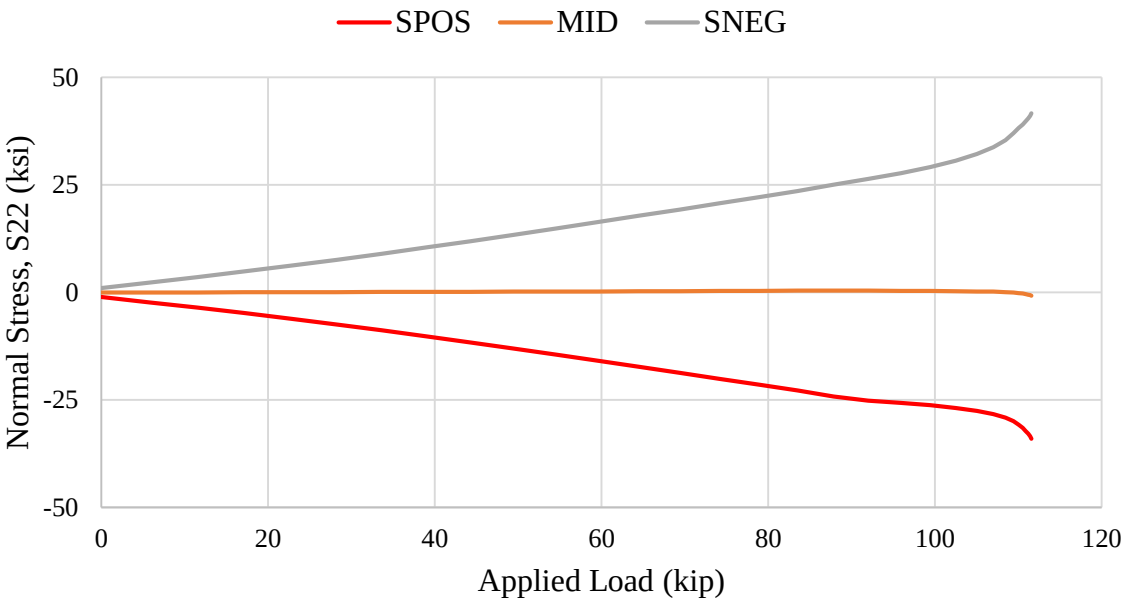

Fig. 5-48. Normal *Stress S22* at top, mid and bottom surface of web versus applied load for Element 2 at web bottom.

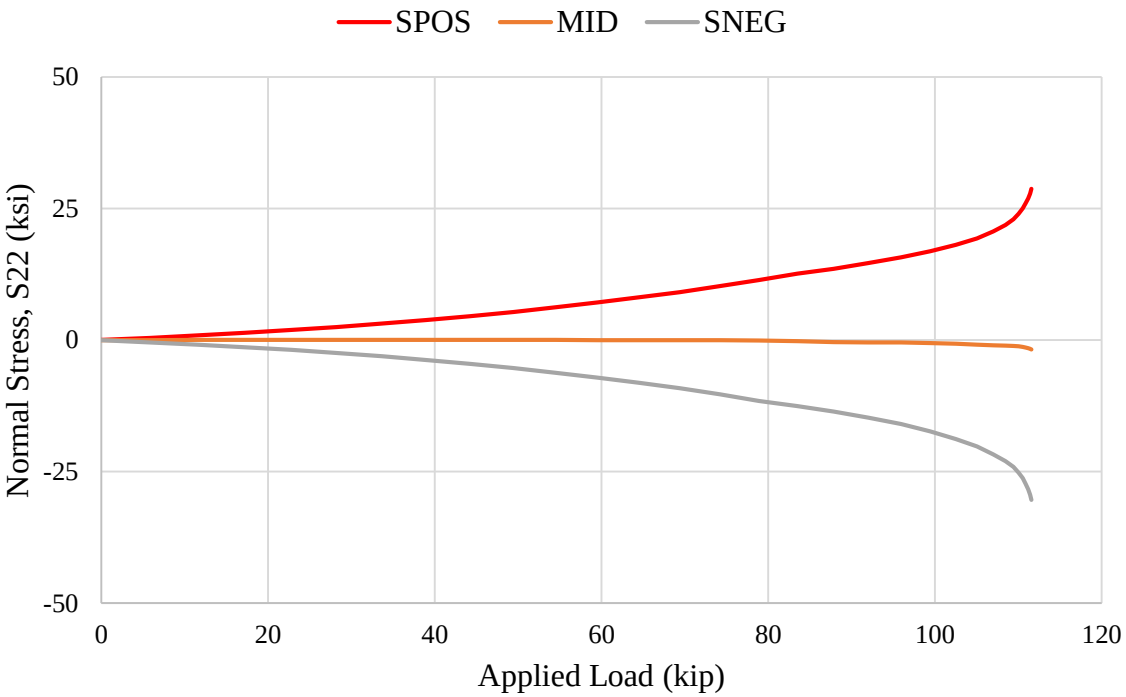

Fig. 5-49. Normal *Stress S22* at top, mid and bottom surface of web versus applied load for Element 3 at web bottom.

The behavior illustrated by these figures is very similar to the behavior at the web top flange juncture, except that the tendency of the web to rotate about the web-to-flange juncture, and the restraint of this rotation, is greatest at the right-hand end in this case. The membrane stress remains close to zero for all the load levels up to the peak load. However, from Fig. 5-40, it is clear that there is significant pushing and pulling of the bottom flange in the vicinity of the right-hand end of the panel at the post peak load level.

5.4 Stresses at Several Sections Through the Web-Depth

In this section, three Sections are cut through the web depth and the corresponding web membrane stresses, *S11*, *S22* and *S12* are plotted. Figures 5-51 through 5-59 show the variation of these quantities, in that order, at these Sections for different levels of loading. The locations of these Sections are shown in Fig. 5-50. The first Section is located at 2 inches from the left end of the panel. The second Section is selected at the mid-length of the panel and the third Section is selected at 2 inches from the right end of the panel.

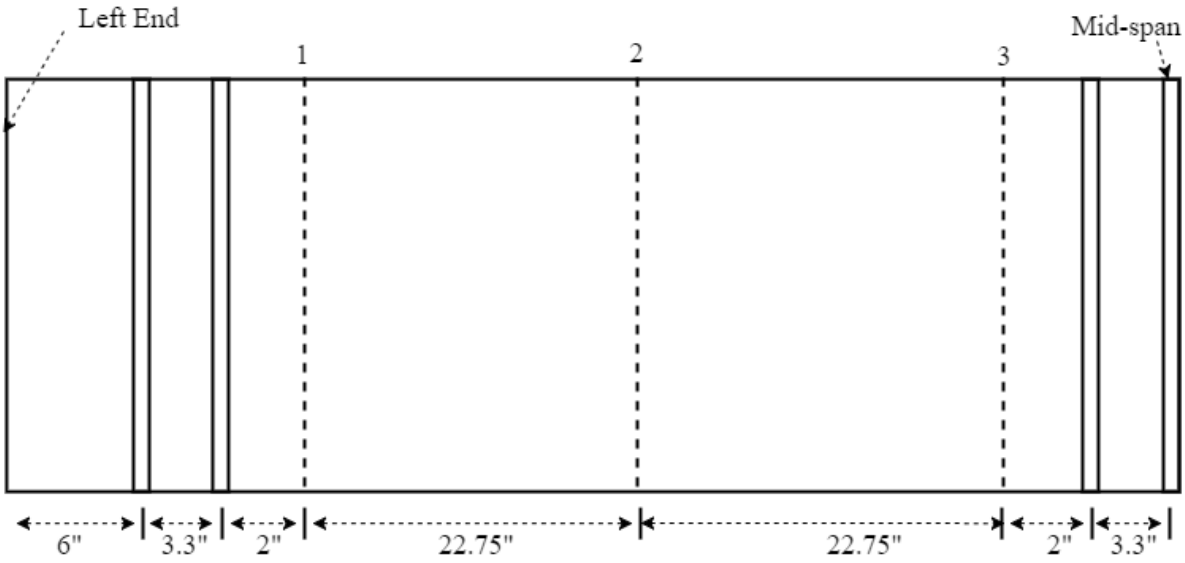

Fig. 5-50. Sections along the web-depth.

To simplify the plots, the normalized position through the web-depth is plotted. The normalized position 0.0 denotes the web bottom and 1.0 denotes the web top. Normalized position 0.5 is the web mid-depth. To facilitate the understanding of the plots, the normalized position is drawn on the ordinate emphasizing the fact that these cuts are vertical rather than horizontal.

1. Stresses at Section 1

This Section is cut at 2 inches from the left end of the panel.

The normal stress *S11* (Fig. 5-51) is almost zero at the web mid-depth until 95% of the peak load. However, at loadings after that load level, significant diagonal tension develops near the transverse stiffener. This increase in normal stress is located more in the top half of the web. The high values at the web bottom are due to the local effects of the reaction at the supports.

The normal stress *S22* (Fig. 5-52) increases with increases in load in the top half of the web at Section 1. The stress *S22* at the bottom of this cut is close to zero. However, it has some compressive stress component at the web top and flange juncture.

The shear stress *S12* (Fig. 5-53) does not increase much at the web bottom after the 50% of the peak load. However, *S12* increases substantially at the top of the web. This is because of the web buckling. *S12* does not change much in the post peak range and is almost equal to *S12* at the peak load.

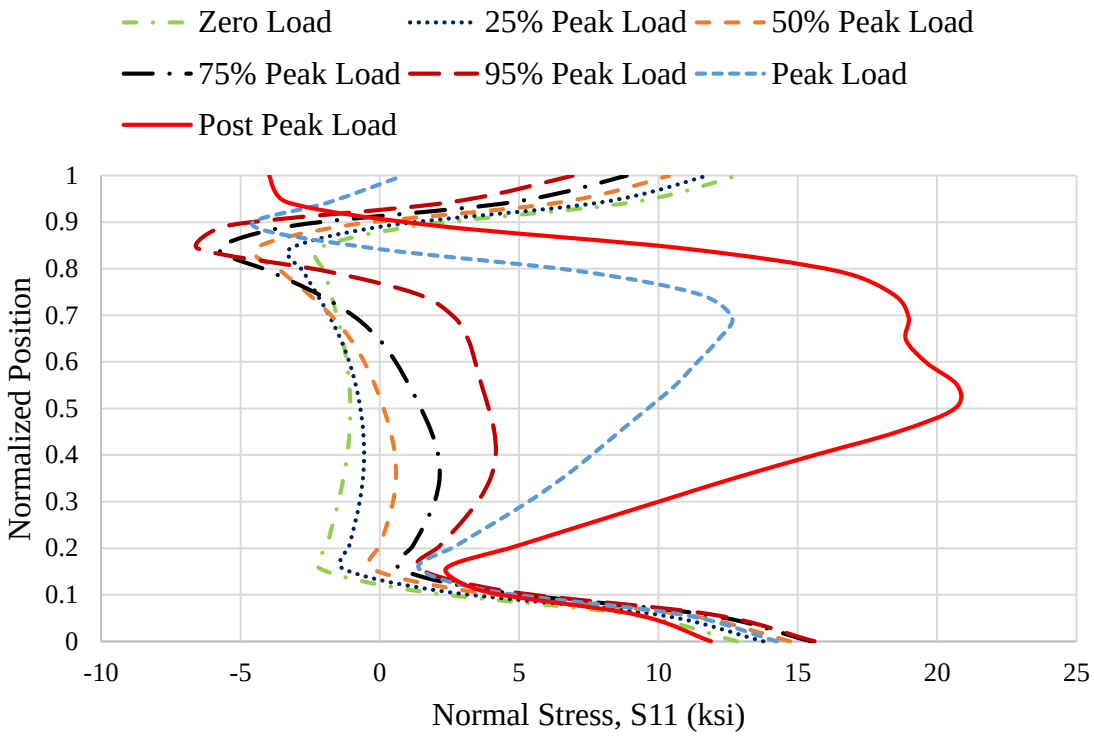

Fig. 5-51. Normalized position versus normal stress *S11* at Section 1.

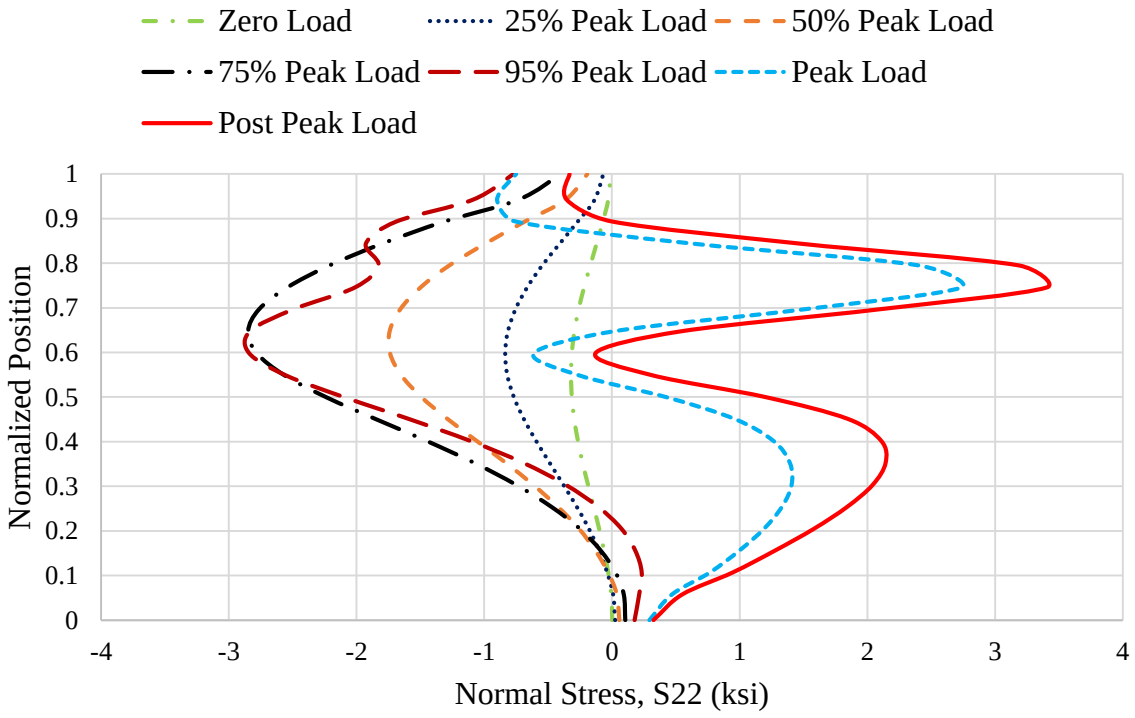

Fig. 5-52. Normalized position versus normal stress *S22* at Section 1.

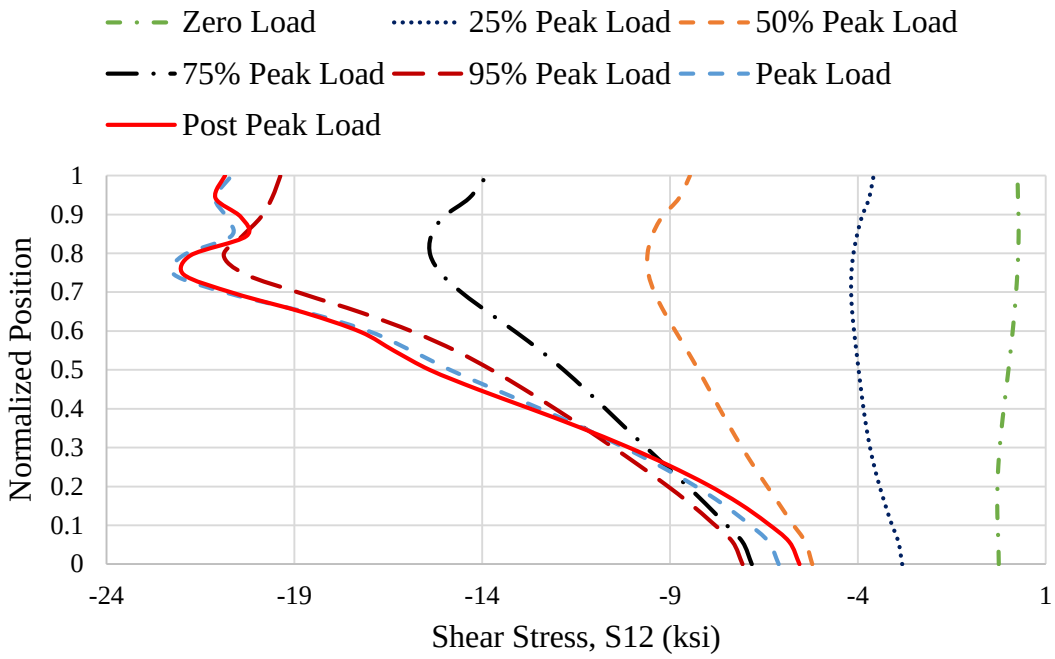

Fig. 5-53. Normalized position versus shear stress *S12* at Section 1.

2. Stresses at Section 2

This Section is cut at the mid-length of the panel.

The normal stress *S11* (Fig. 5-54) is caused by both the diagonal tension and by the flexural stresses. At the mid-depth *S11* due to flexure is zero and we can clearly see considerable diagonal tension forming even at 75% of the peak load. There is similar evidence of this in the *S22* plot (Fig. 5-55).

The shear stresses *S12* (Fig. 5-56) at the web top and bottom are nearly equal until almost 75% of the peak load. Even after that load, the variation between the shear stresses at the top and bottom of the web is not large. However, the difference between *S12* at top and bottom at Sections 1 and 3 is considerably higher. This is because the web buckle meets the top and bottom flange at the ends of the panel, hence affecting *S12* significantly at these locations. There is little action at the top and bottom of the web at the mid-length of the panel.

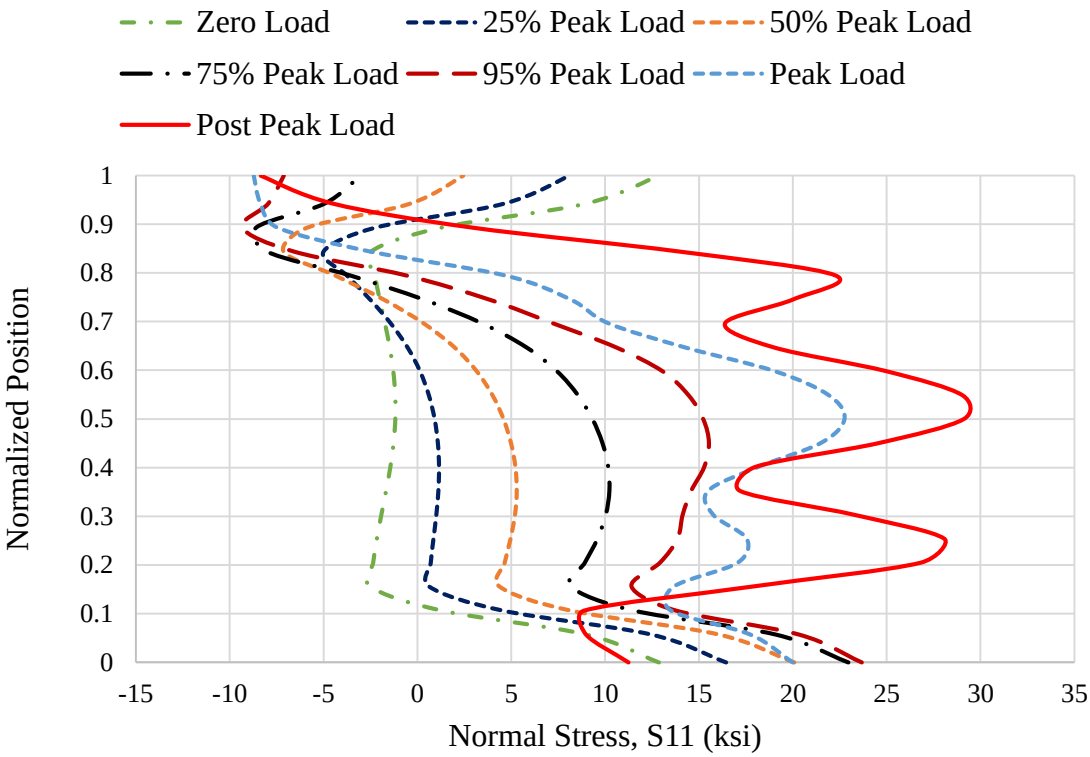

Fig. 5-54. Normalized position versus normal stress *S11* at Section 2.

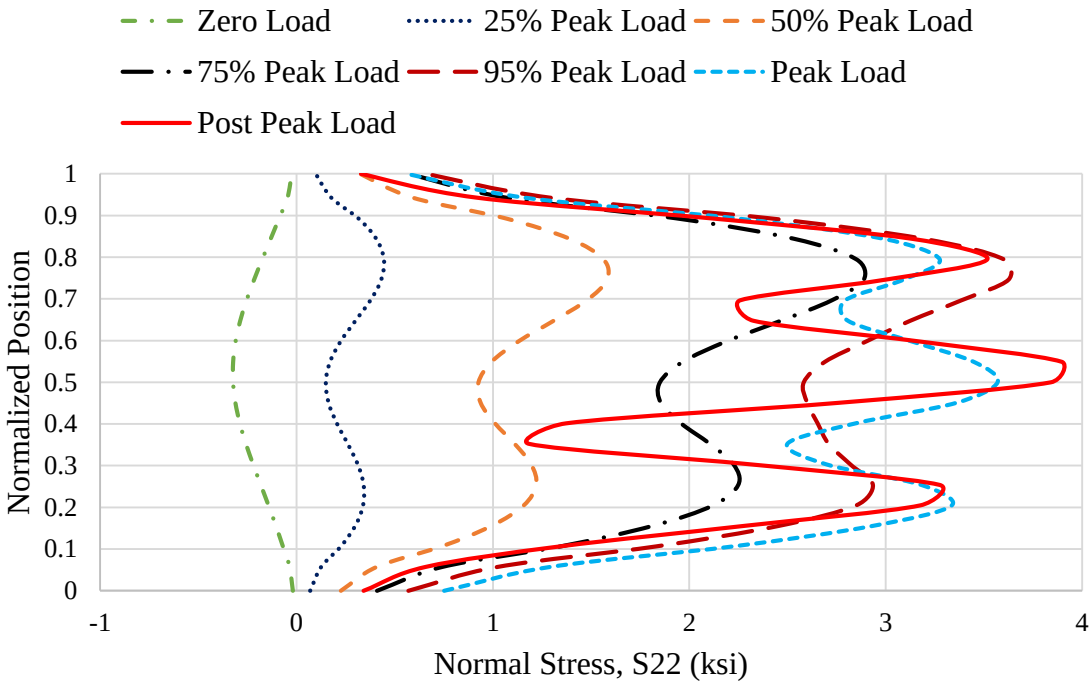

Fig. 5-55. Normalized position versus normal stress *S22* at Section 2.

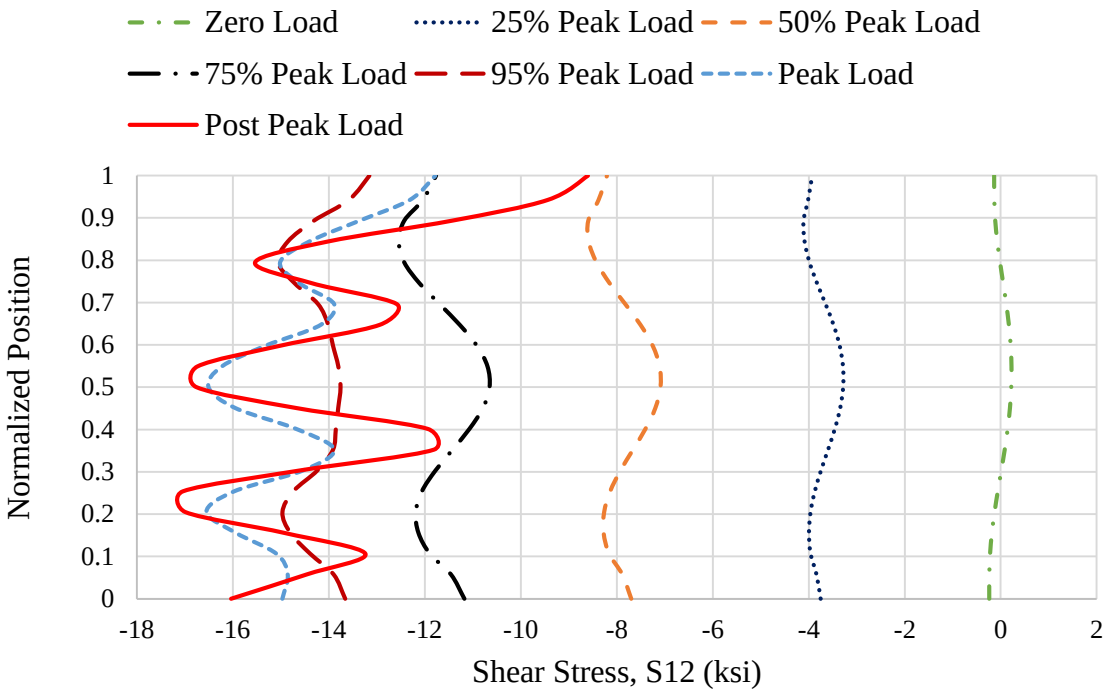

Fig. 5-56. Normalized position versus shear stress *S12* at Section 2.

3. Stresses at Section 3

This Section is cut at 2 inches from the right end of the panel.

A considerable amount of diagonal tension influences *S11* (Fig. 5-57) at web mid-depth of this cut at the peak load. This increase in normal stress with increasing load is located more in the bottom half of the web.

The normal stress *S22* (Fig. 5-58) increases in the bottom half of the web. The stress *S22* at the top is essentially zero. However, it has some compressive stress component at the web bottom due to interaction with the bottom flange.

The shear stress *S12* (Fig. 5-59) does not increase much at the web top after the 50% of the peak load. However, *S12* increases significantly at bottom of the web. This is because of web buckling which causes increase in *S12* at bottom of the web. Similar to Section 1, *S12* does not increase much in the post peak range and is almost equal to *S12* at the peak load.

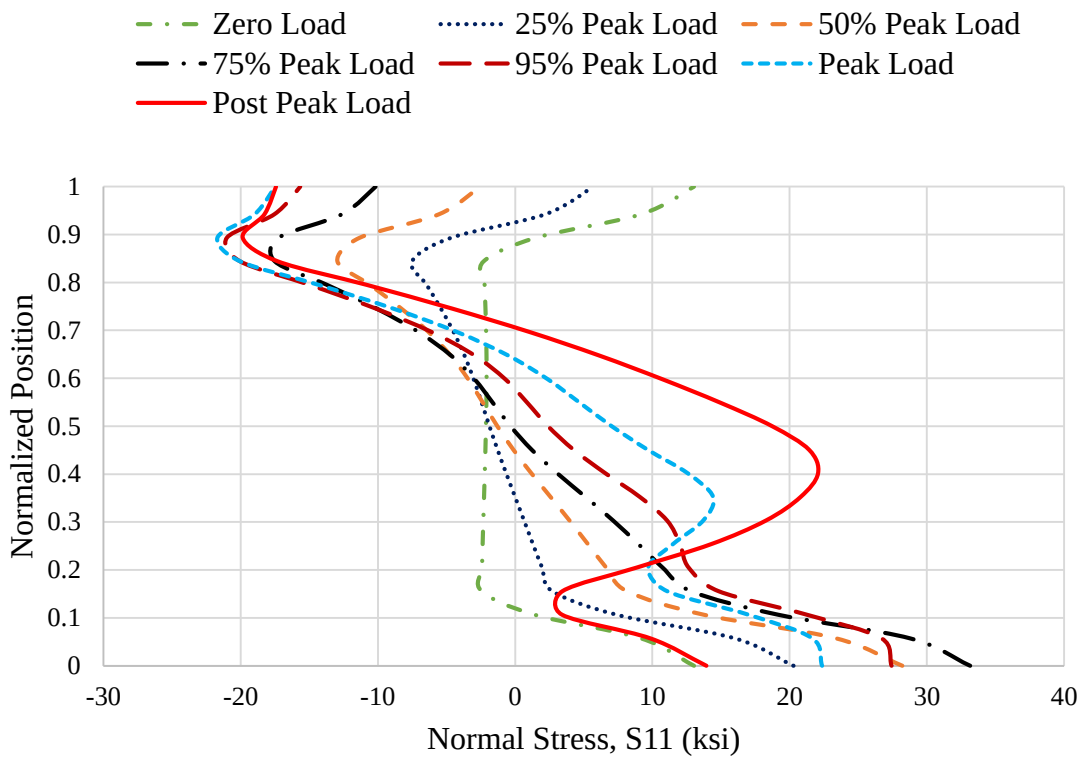

Fig. 5-57. Normalized position versus normal stress *S11* at Section 3.

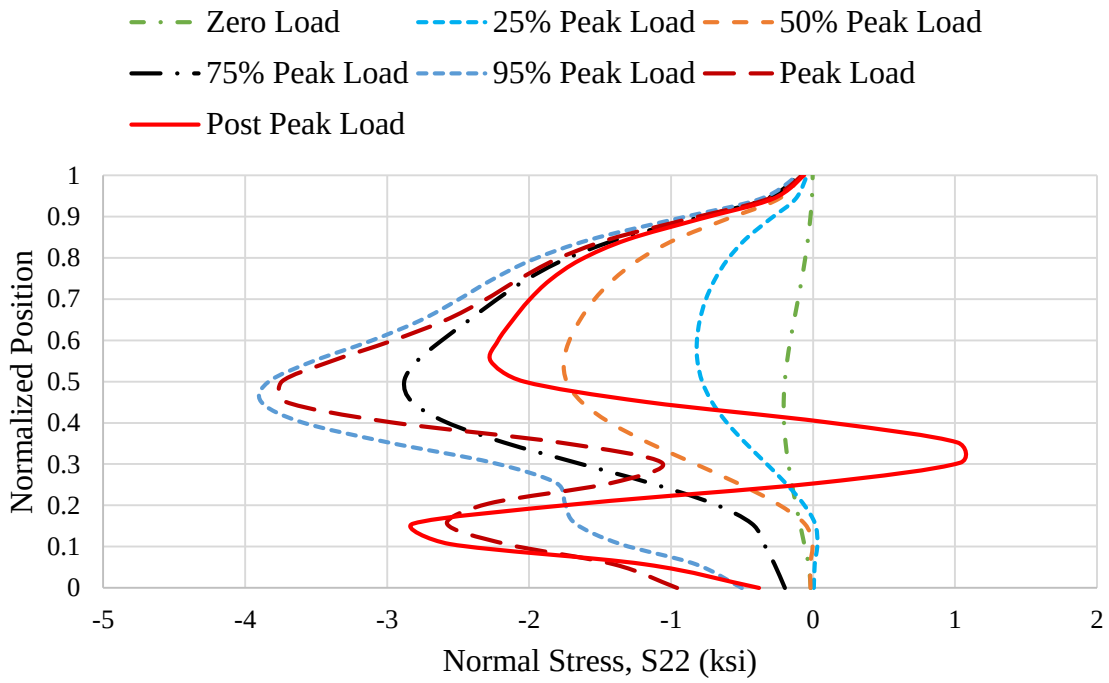

Fig. 5-58. Normalized position versus normal stress *S22* at Section 3.

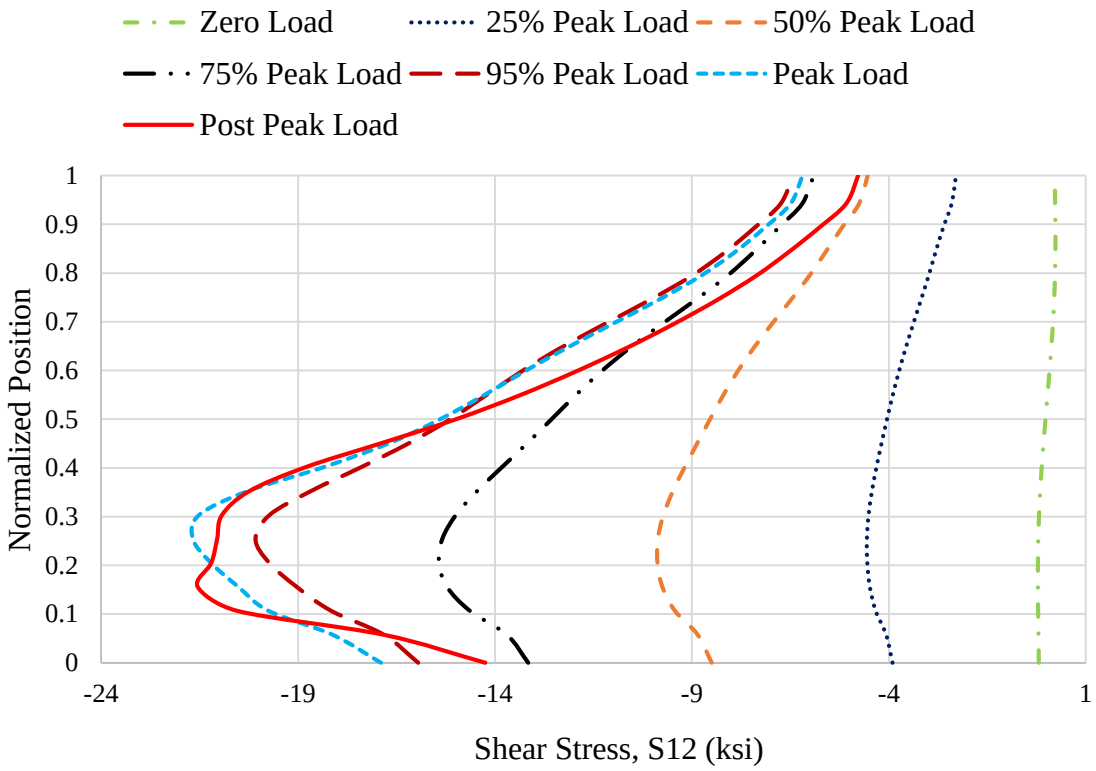

Fig. 5-59. Normalized position versus shear stress *S12* at Section 3.

5.5 Comparison of Results from Simulation and Theory

In this section, the results from simulations are compared with the results from applying Euler-Bernoulli beam theory on the specimen. According to beam theory, the normal stress, *S11* is zero at the mid-span of the specimen and is given by $S11 = My/I_x$, where y is equal to the distance of the Element from the web mid-depth. The shear stress, *S12* is given by $S12 = VQ/I_x t_w$, where Q is the statical moment of area and t_w is the thickness of web. In the results from the beam theory, the specified residual stress pattern is added to get a better understanding of the deviation of the simulation results from idealized beam theory. According to beam theory, the normal stress *S22* is zero at all the sections of the beam. The

plots in this section are plotted predominantly at the peak load. However, the flange stress *S11* is also plotted at 50% of the peak load.

5.5.1 Stress Variations along the Length

The quantities plotted in this section are *S11* at the web top and bottom, flange stress *S11* at top and bottom flange and *S12* at the web top, mid-depth and web bottom along the length. Figures 5-60 through 5-68 show the variation of these quantities, in that order at a section along the length. The abscissa is the position along the length as employed in Section 5.1, 5.2 and 5.3.

S11 (Fig. 5-60) at the top of the web drops near the left end of the panel. This is where the buckled web meets the top flange. The web stress state at the peak load is used up by the shear actions near the left panel (Fig. 5-66).

Similar behavior to Fig. 5-60 occurs at the bottom flange. However, the drop in *S11* (Fig. 5-61) is near the right end of the panel and the drop is much more pronounced at the bottom flange. This is because there is extensive yielding of the web bottom at the peak load due to the interaction of shear, flexural tension and plate bending. Near the left end of the panel, the flexural stresses are small due to the small moment.

Höglund (1997) states that the total longitudinal force, N_h, given by Eq. 1-15, has to be anchored at the ends of the beam by a "transverse short beam," which he calls a rigid end post. This end post is supported by the flanges, which results in additional compressive forces in the flanges at the ends of the beam. However, Höglund also shows substantial postbuckling strength, only slightly smaller than that obtained for beams having rigid end posts, for general end details that do not satisfy his rigid end post requirements. From Figs. 5-62 and 5-63, it is clear that even at 50% of the peak load, there is some additional

compressive stresses being developed in the flanges. This additional compressive stress is the deviation of *S11* from theoretical results.

S11 along the top and bottom flange (Fig. 5-64 and 5-65, respectively) at the peak load also indicate that there is a large compressive stress (deviation from theoretical results) acting on the flanges.

S12 at the web top (Fig. 5-66) follows the expected trend, i.e., *S12* is maximum near the left end of the panel and minimum near the right end of the panel. However, at the web bottom, *S12* (Fig. 5-68) is maximum near the right end of the panel and minimum near the right end of the panel. The shear stress

S12 at the web mid-depth is a reasonable predictor of the results obtained from simulations. There is some oscillatory nature in the shear stresses and the there is one peak at the peak load near the left end of the panel.

Fig. 5-60. Normal stress *S11* at the peak load versus position along the web top.

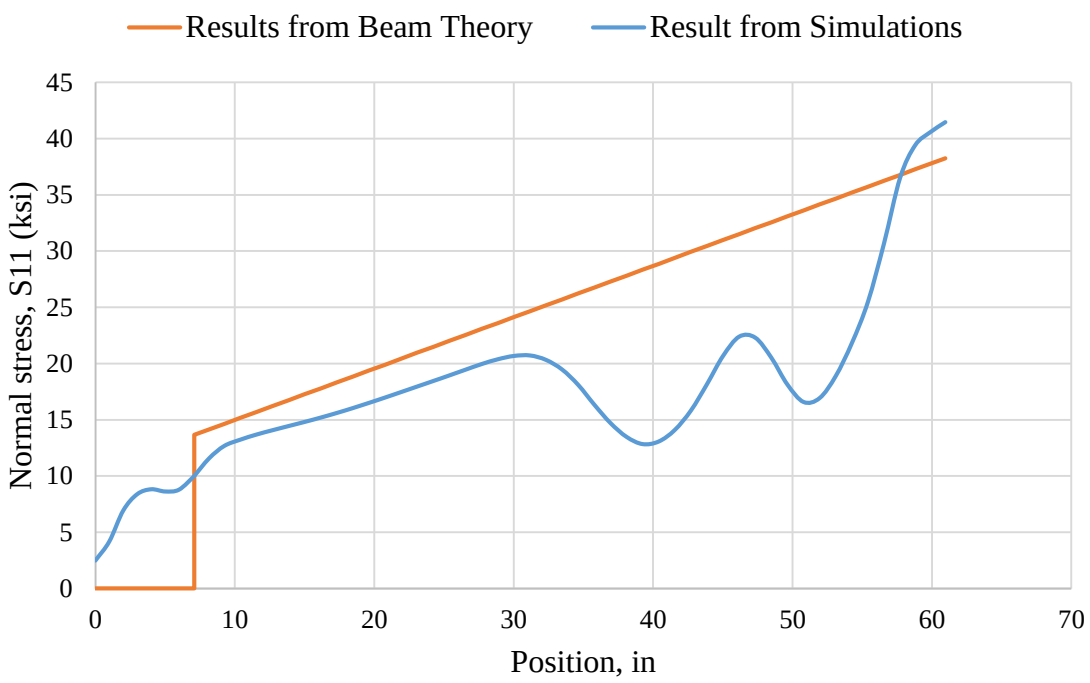

Fig. 5-61. Normal stress *S11* at the peak load versus position along the web bottom.

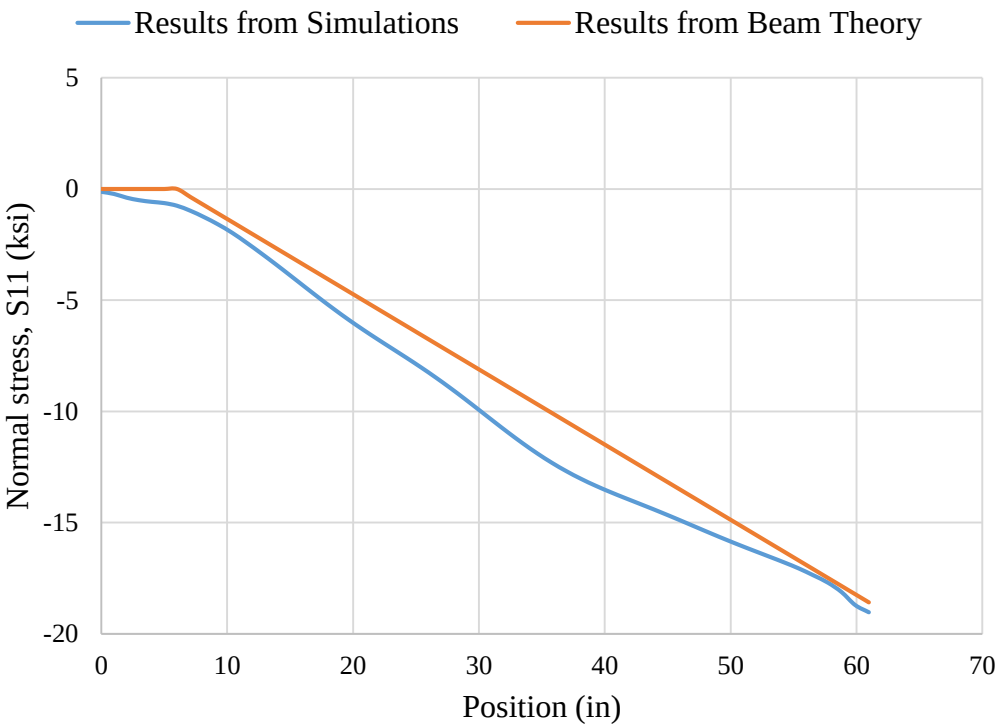

Fig. 5-62. Normal stress *S11* at 50% of the peak load versus position along the top flange.

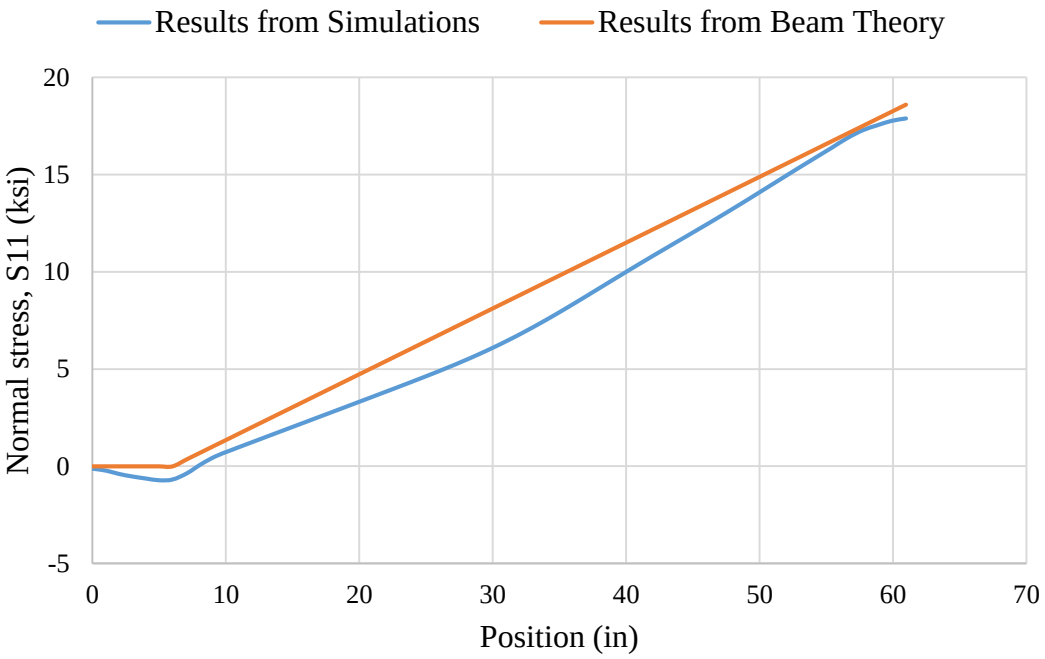

Fig. 5-63. Normal stress *S11* at 50% of the peak load versus position along the bottom flange.

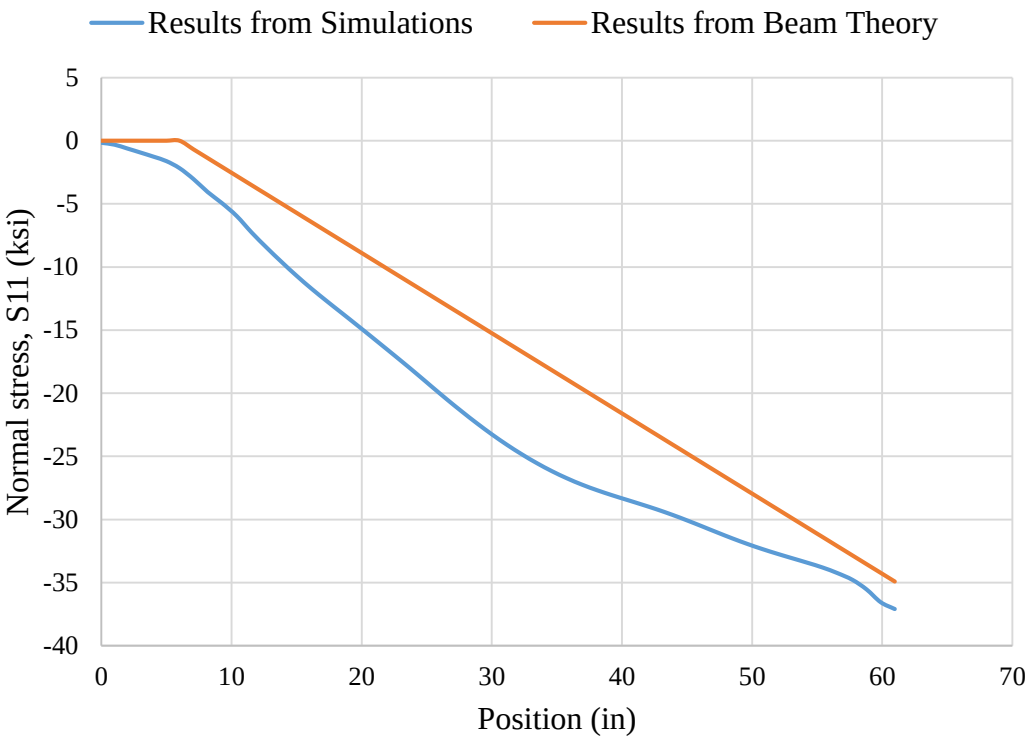

Fig. 5-64. Normal stress *S11* at the peak load versus position along the top flange.

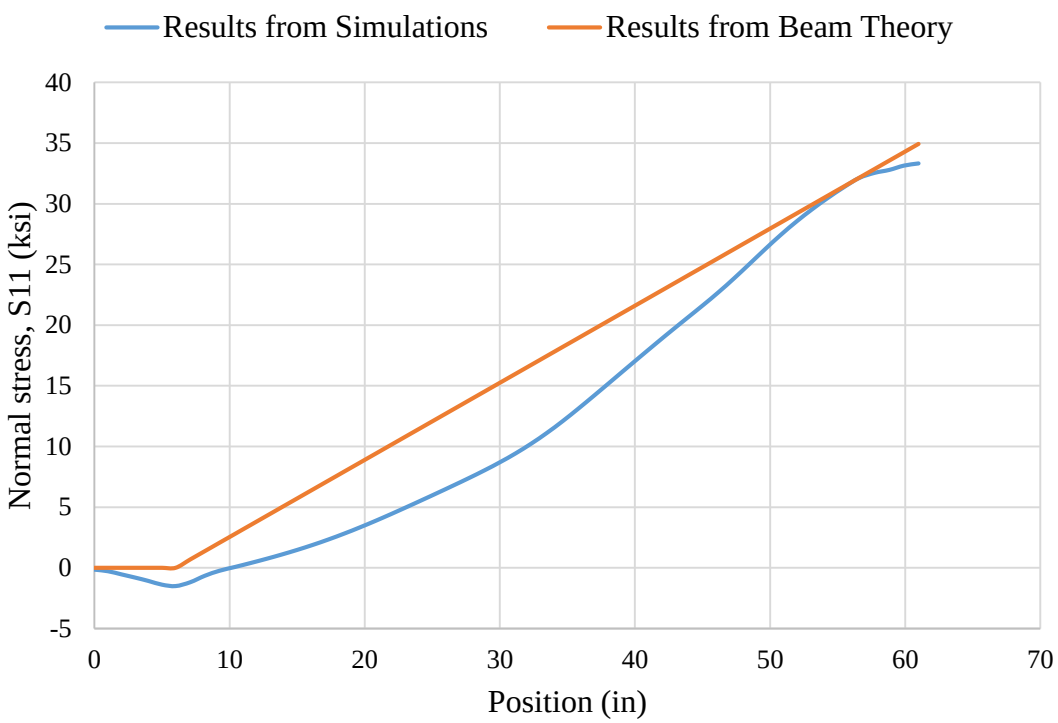

Fig. 5-65. Normal stress *S11* at the peak load versus position along the bottom flange.

Fig. 5-66. Shear stress *S12* at the peak load versus position along the web top.

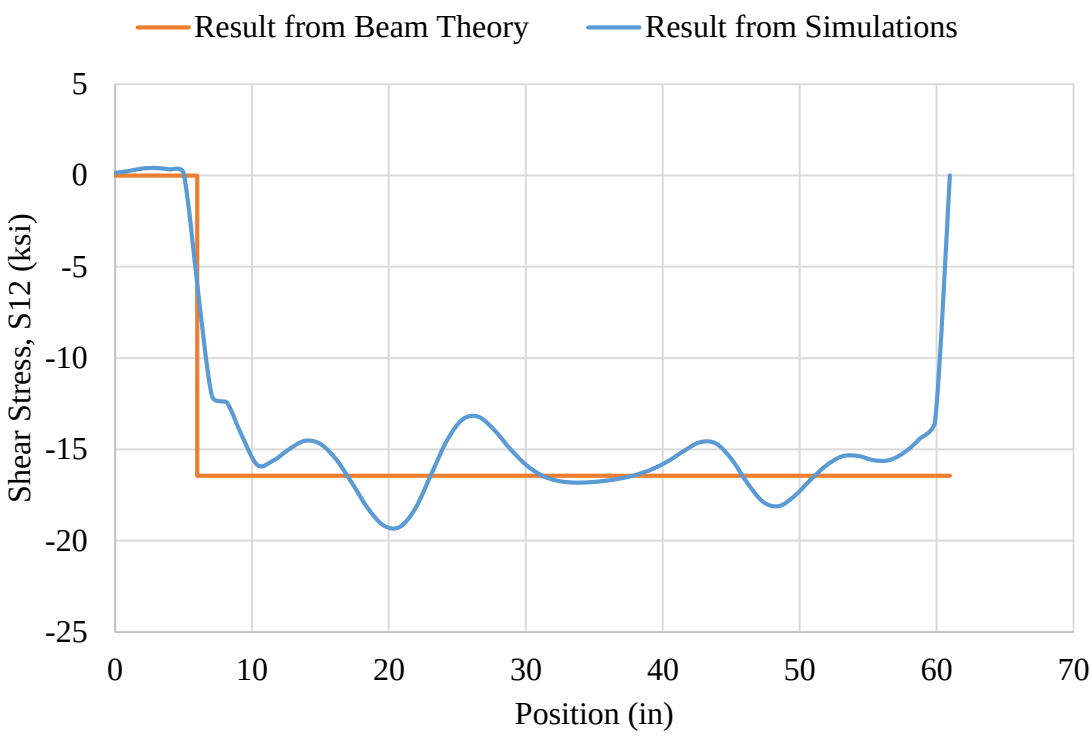

Fig. 5-67. Shear stress *S12* at the peak load versus position along the web mid-depth.

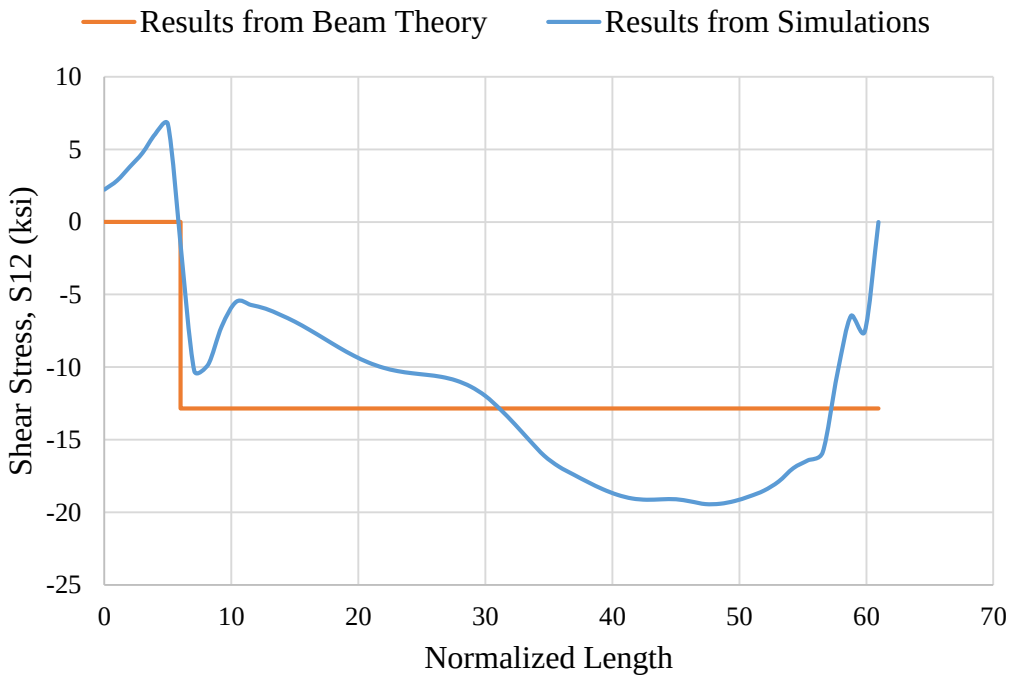

Fig. 5-68. Shear stress *S12* at the peak load versus position along the web bottom.

5.5.2 Stress Variations through the Web-Depth

The locations of Sections employed for this study are already explained in Section 5.4. The quantities plotted in this section are *S11* and *S12* at Sections 1, 2 and 3. Figures 5-69 through 5-74 show the variation of these quantities, in that order, at a section along the web-depth. The ordinate is the same as employed in Section 5.4, i.e., normalized position.

S11 at Section 1 shows evidence of significant diagonal tension at the top half of the web. At Section 2, almost the entire section is under diagonal tension. However, this diagonal tension is maximum at the web mid-depth and minimum at the juncture of the web with the flanges.

S12 is significantly different from the results obtained from theory. At Section 1, the top half of the web has higher stress and at Section 3, the bottom half of the web has higher stress. The deviation in *S12* at Section 2 from the beam theory is small in Section 2 when compared with Sections 1 and 3.

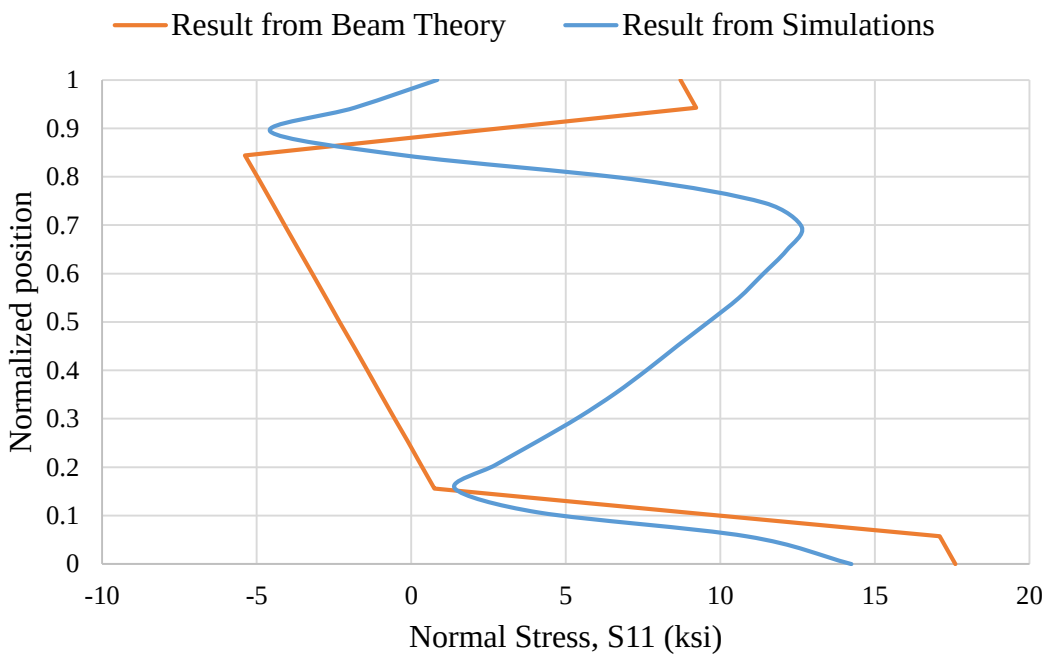

Fig. 5-69. Normalized position versus normal stress *S11* at the peak load at Section 1.

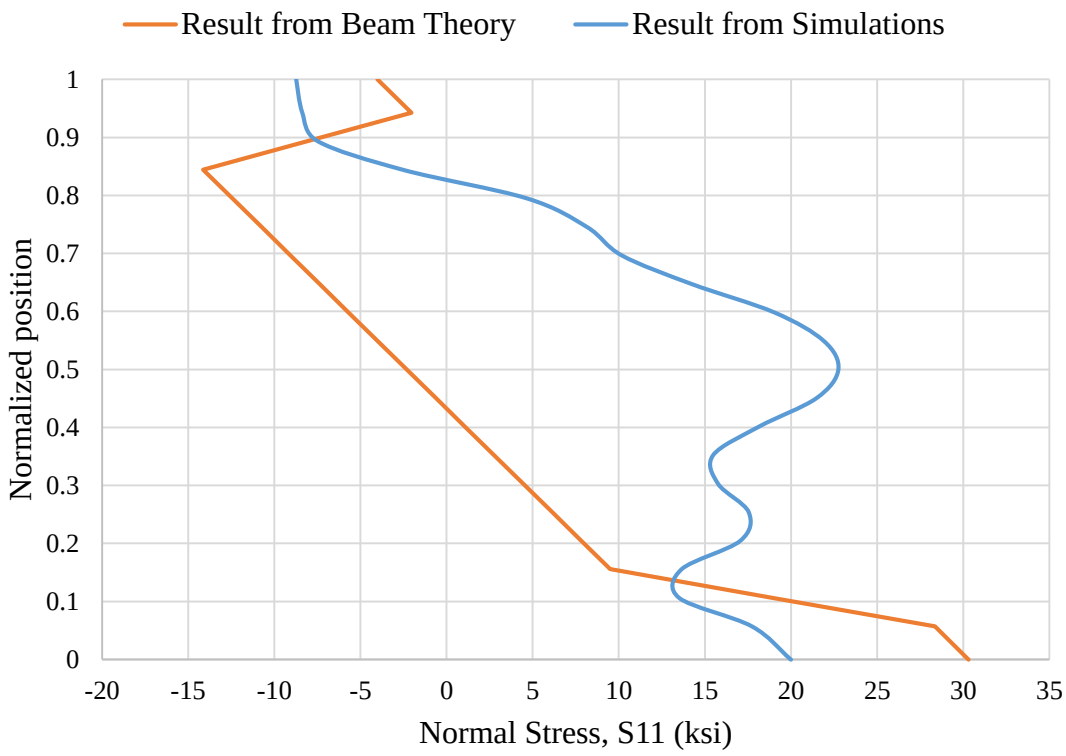

Fig. 5-70. Normalized position versus normal stress *S11* at the peak load at Section 2.

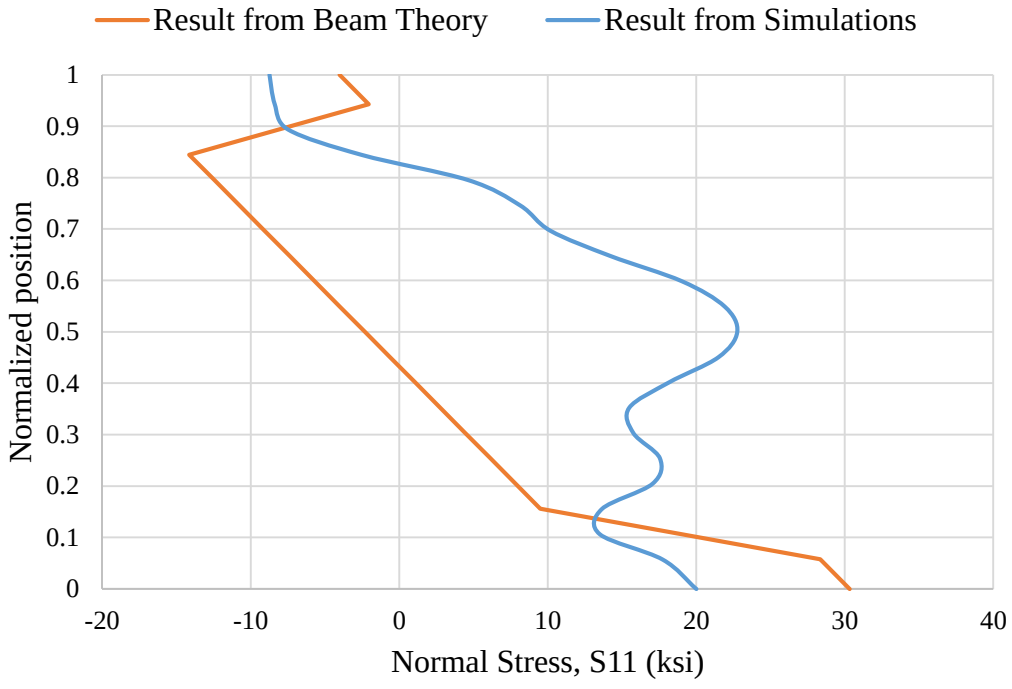

Fig. 5-71. Normalized position versus normal stress *S11* at the peak load at Section 3.

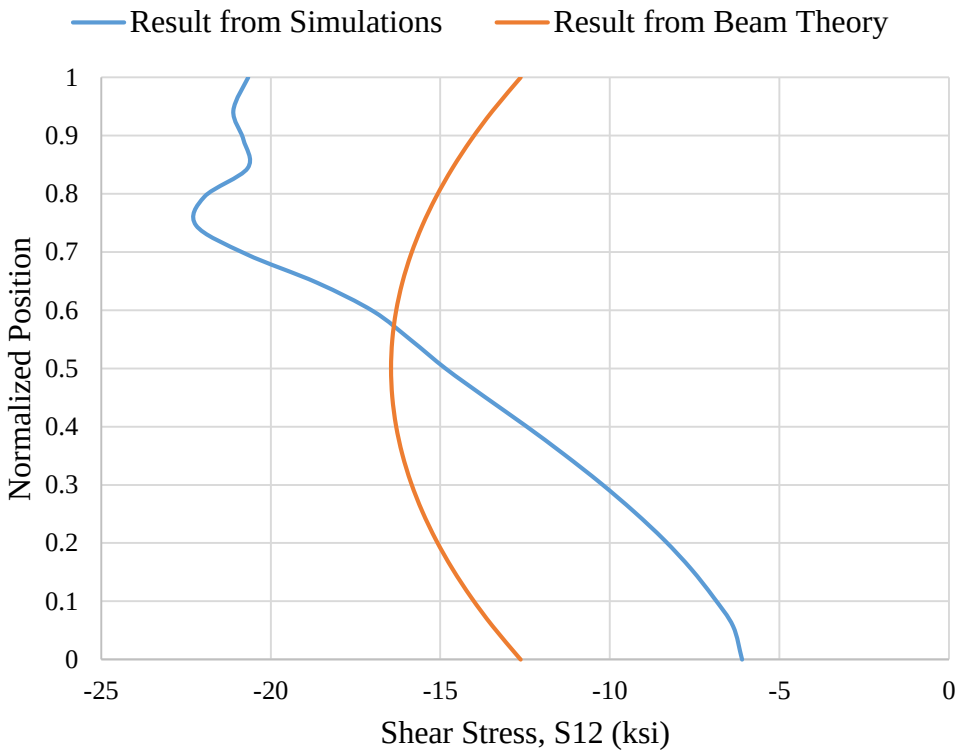

Fig. 5-72. Normalized position versus shear stress *S12* at the peak load at Section 1.

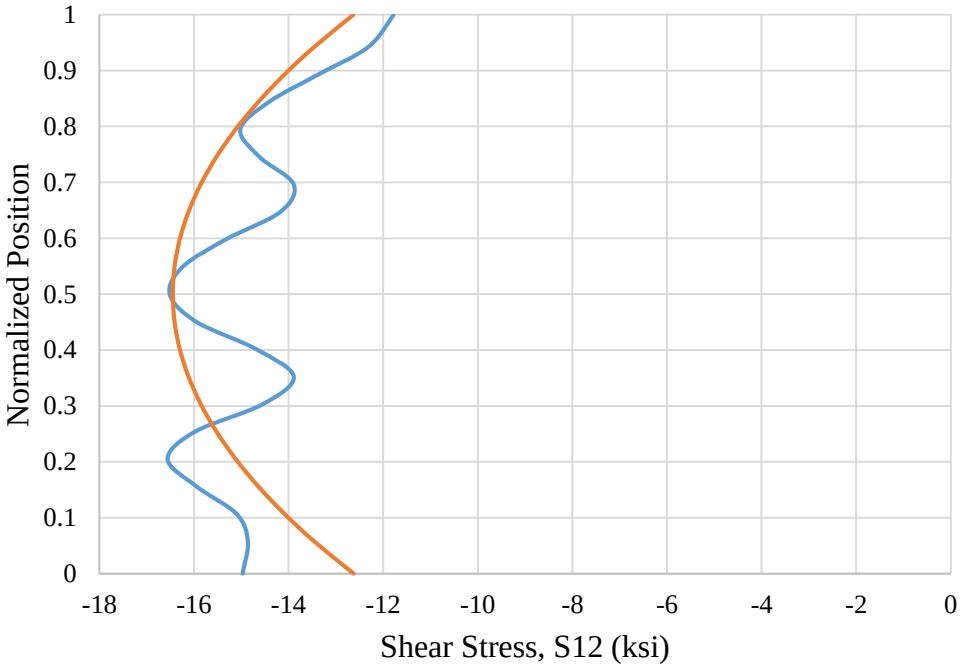

Fig. 5-73. Normalized position versus shear stress *S12* at the peak load at Section 2.

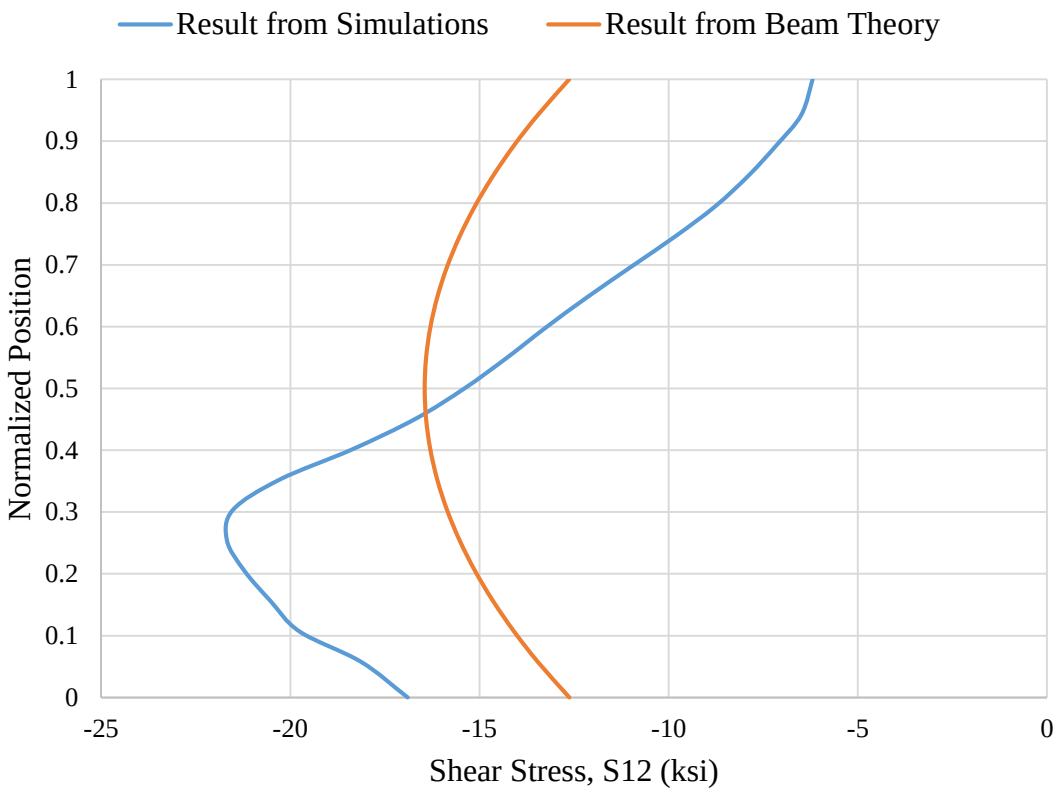

Fig. 5-74. Normalized position versus shear stress *S12* at the peak load at Section 3.

CHAPTER 6

MECHANISM OF SHEAR DEVELOPMENT IN AN INTERMEDIATE LENGTH UNSTIFFENED PANEL

The specimen selected for this study is UK6 from Daley and Davis (2015). It has an a/h of 4.12 and h/t_w of 227. Experimentally, this specimen failed by the formation of a shear buckle over most of its half-span length (see Figs. 4-11 and 4-12). To explain the mechanism of shear development, the procedure followed in Chapter 5 is repeated here. Figure 6-1 shows the overall geometry for the UK6 simulation model.

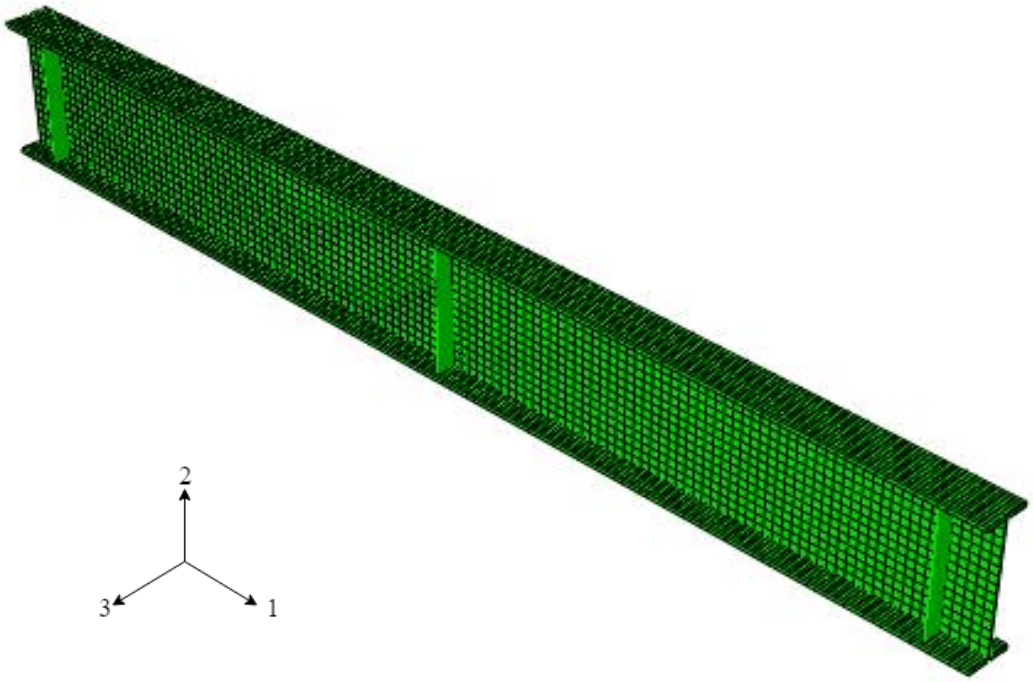

Fig. 6-1. Isometric view of the FE model for Specimen UK6.

The notations for the displacements and stresses are defined in Chapter 5.

Figure 6-2 shows a plot of the applied vertical load versus the vertical displacement (*U2*) at the mid-span of girder UK6. The markers in the graph show the various stages considered in the study. The load magnitudes selected for the study are; zero load, 25% peak load (40.5 kips), 50% peak load (80.2 kips), 75% peak load (127 kips), 95% peak load (170 kips), peak load (178 kips) and post peak load (163.5 kips).

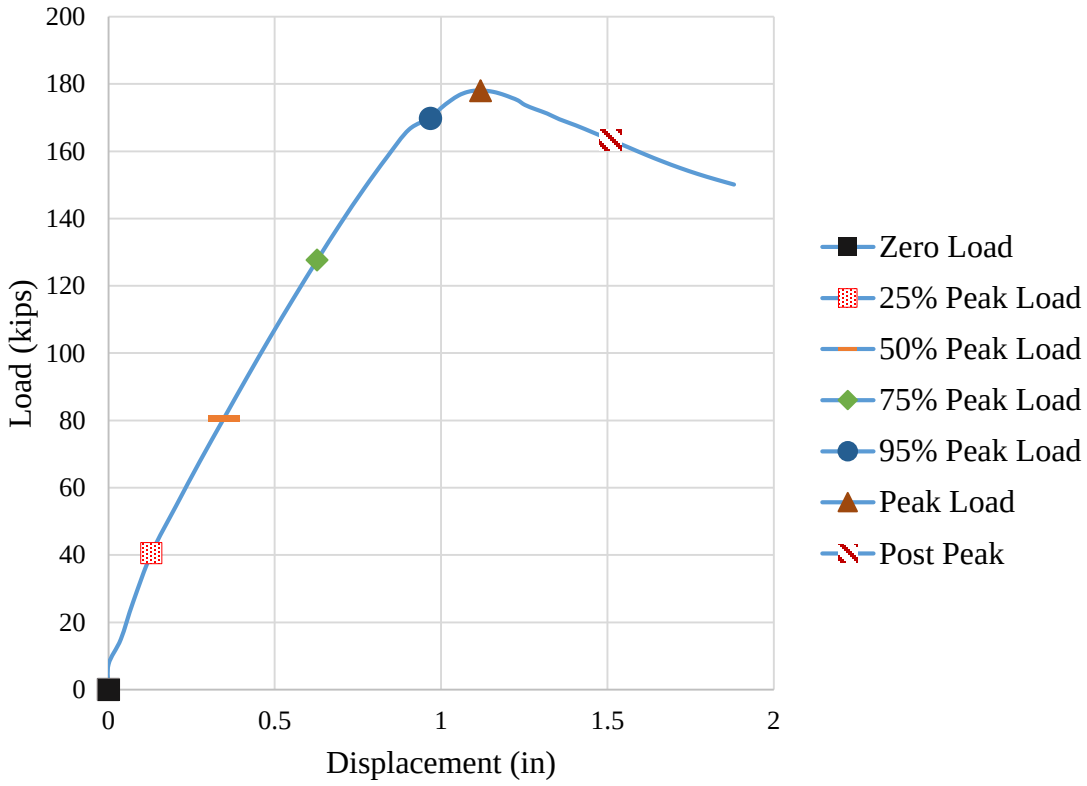

Fig. 6-2. Load versus vertical displacement at the mid-span of Specimen UK6.

The procedure in Section 5.1 through 5.5 is repeated for Specimen UK6. In all the graphs, unless noted otherwise, the position along the length, measured from the left end of the specimen, is plotted as the abscissa. To simplify the plots, the normalized position along the length of the beam is employed. The normalized position 0.0 denotes the left-most free end of the specimen and 1.0 denotes the right-most free end of the specimen. The

left side of the specimen (normalized position less than 0.5) corresponds to the test segment having the thinner web.

6.1 Responses at a Section Along the Length at the Web Mid-Depth

In this section, the procedure of Section 5.1 is repeated for Specimen UK6. The quantities plotted are the lateral displacement *U3*, the web membrane stresses, *S11*, *S22* and *S12*, the von Mises stress *S*, the maximum principal tensile membrane stress *S1*, the maximum principal compressive membrane stress *S2* and the orientation of the principal stresses θ_p. Figures 6-3 through 6-10 show the variation of these quantities, in that order, at a section along the length at the web mid-depth for different levels of loading.

For zero load, *U3* is maximum near the mid-span and almost zero near the supports (Fig. 6-3). At 25% and 50% of the peak load, the maximum displacement is near the quarter length of the member and the displacement is cyclic in nature with peaks of almost the same amplitude. As the load is increased, the peak becomes larger near the quarter length compared to the peaks at other locations. Also, as the limit load is approached the locations of the peaks shift towards the left end of the specimen. This is due to the web buckles becoming much more pronounced at higher load levels. At lower levels of loads, the out-of-plane deflections follow the pattern of the initial imperfections. As the loads are increased, the deflections increase and shift due to the web buckling. At higher levels of load, *U3* is increasing at a much higher rate. For a 5% increase in load, from 95% of the peak load to the peak load, there is an increase in lateral displacement of 40%. At the post peak load level, this increase is even more significant. *U3* is significantly larger at the peak load for Specimen UK6 (Fig. 6-3) compared to G7 (Fig. 5-4).

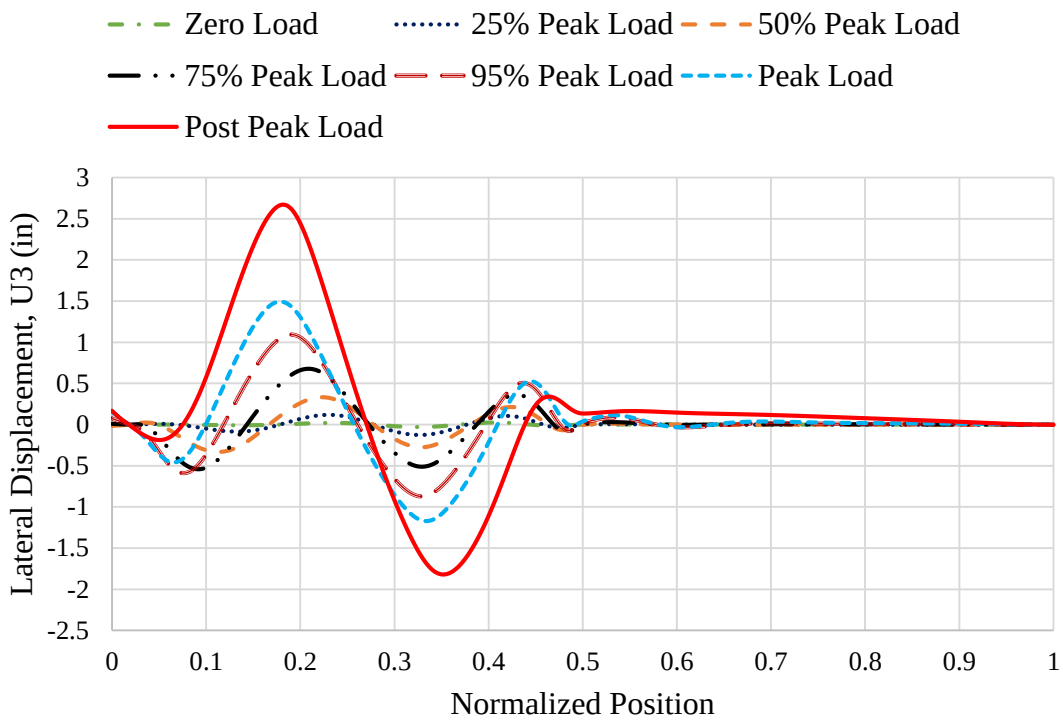

Fig. 6-3. Lateral Displacement *U3* versus normalized position along the web-mid depth.

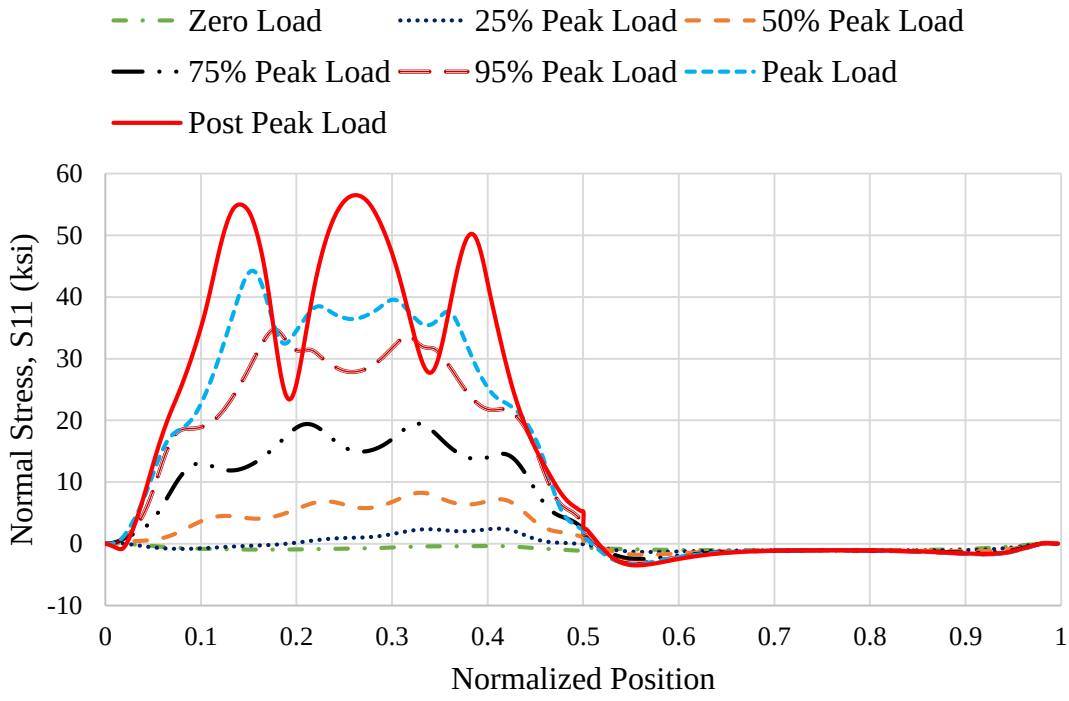

Fig. 6-4. Normal Stress *S11* versus normalized position along the web mid-depth.

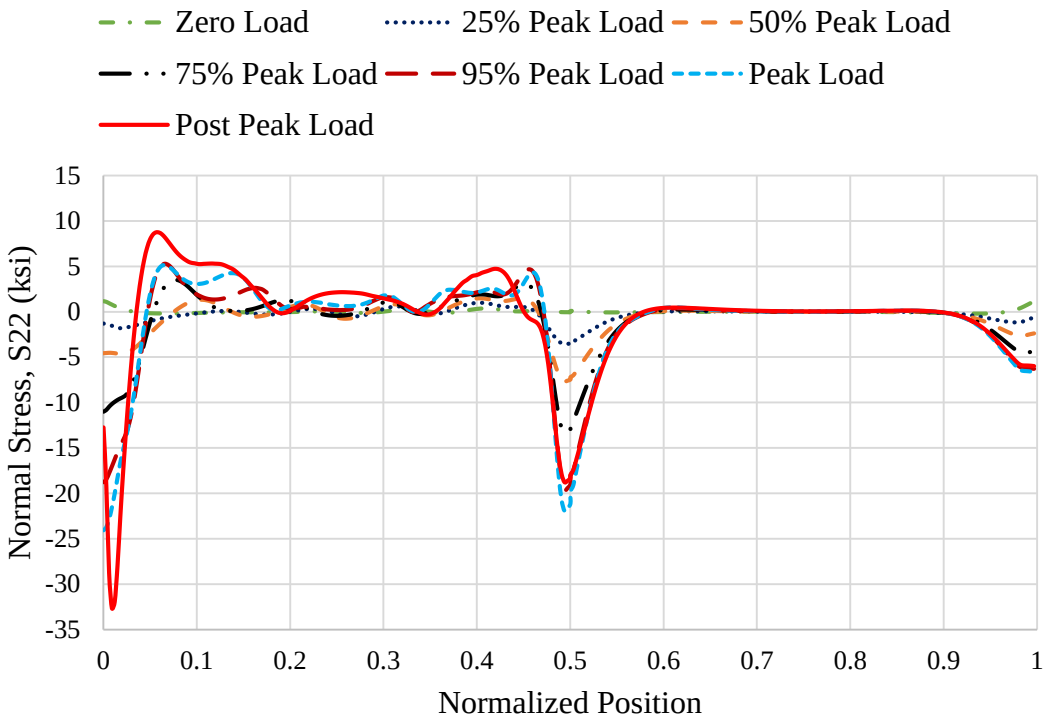

Fig. 6-5. Normal Stress *S22* versus normalized position along the web mid-depth.

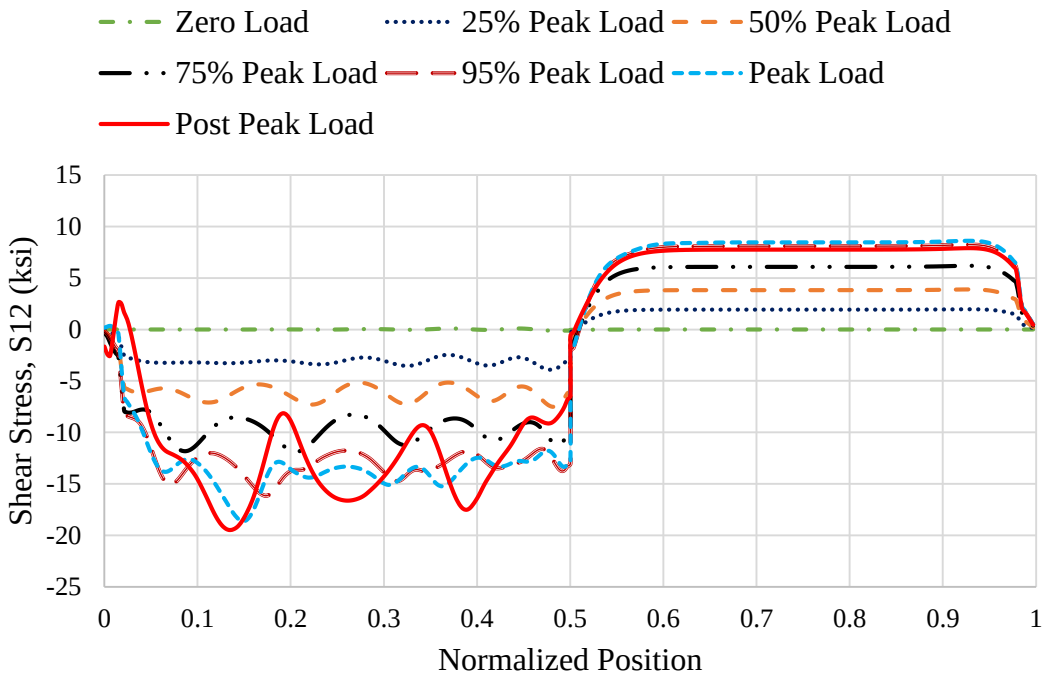

Fig. 6-6. Shear Stress *S12* versus normalized position along the web mid-depth.

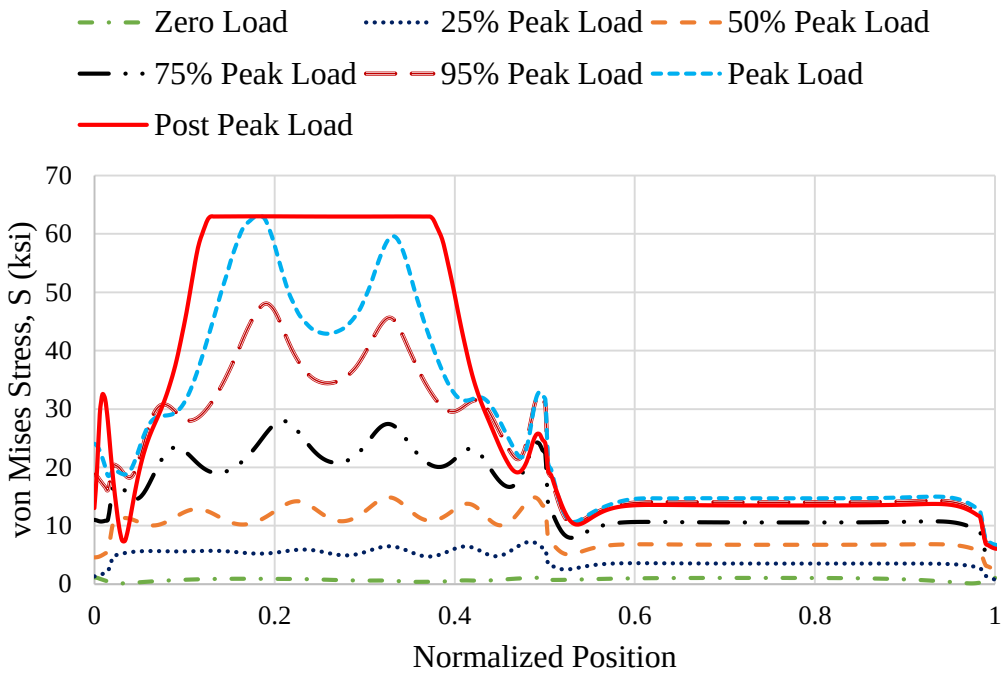

Fig. 6-7. von Mises stress *S* versus normalized position along the web mid-depth.

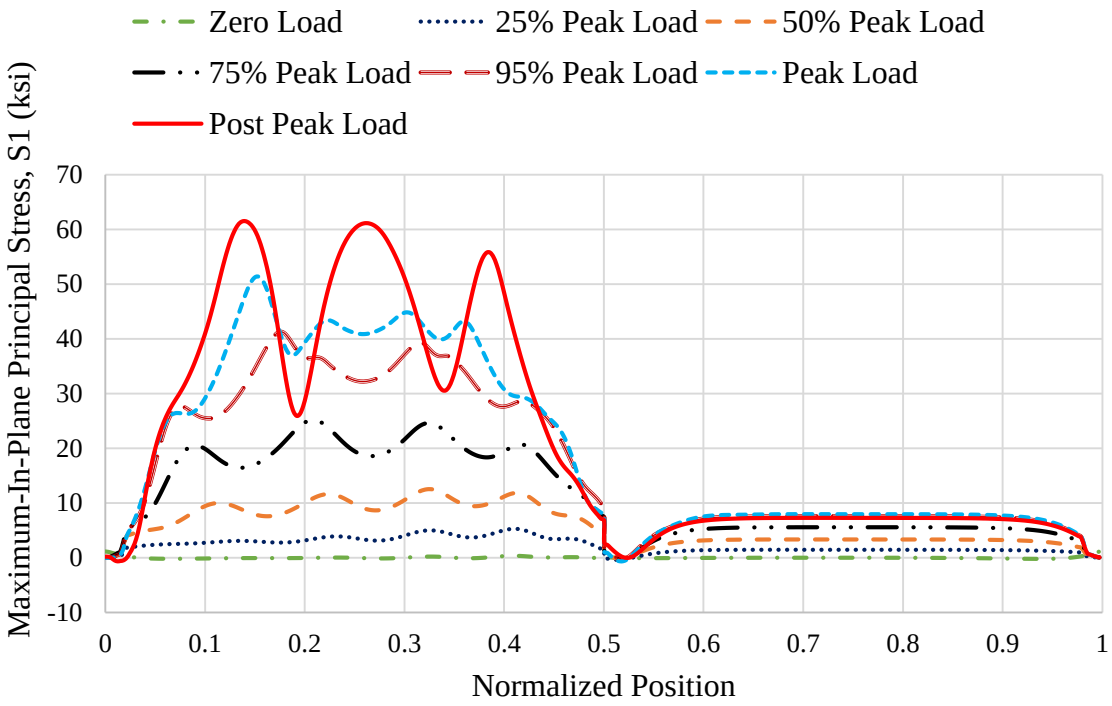

Fig. 6-8. Maximum-In-Plane Principal Stress *S1* versus normalized position along the web mid-depth.

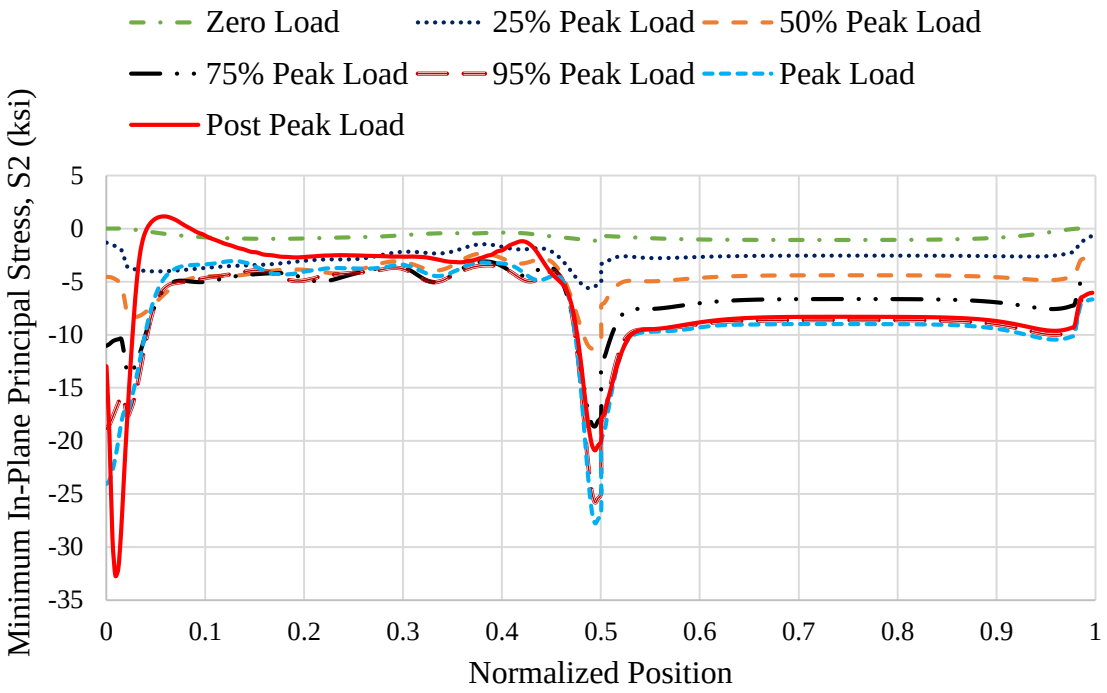

Fig. 6-9. Minimum-In-Plane Principal Stress *S2* versus normalized position along the web mid-depth.

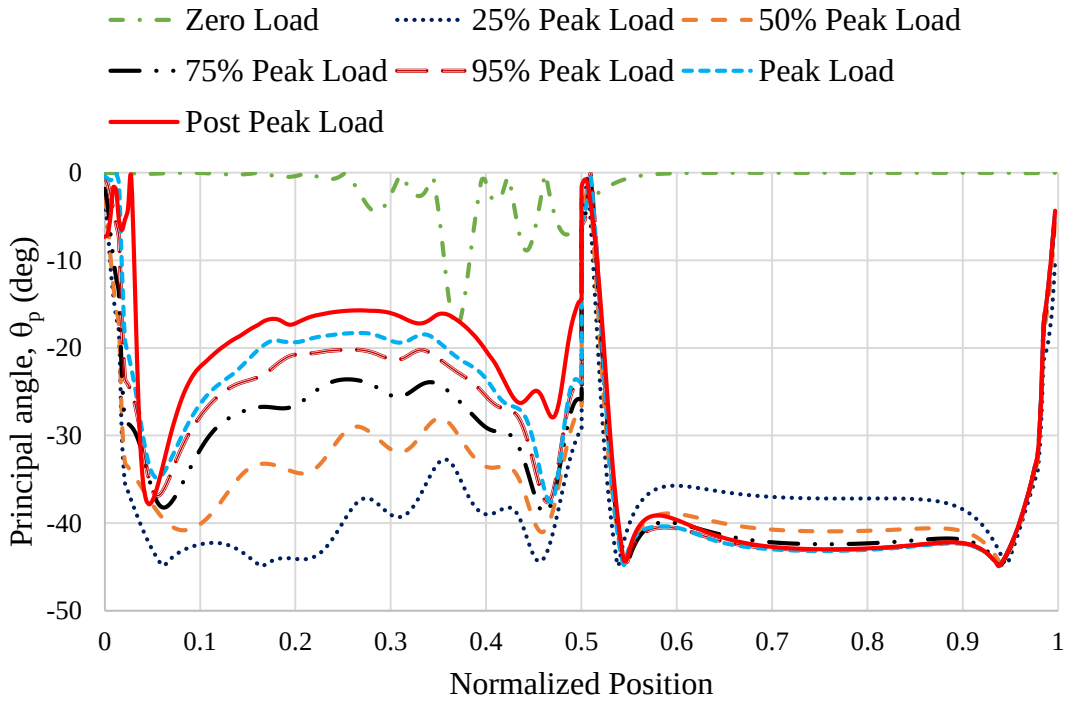

Fig. 6-10. Principal angle θ_p versus normalized position along the web mid-depth.

At 25% of the peak load, *S11* (Fig. 6-4) is tensile between approximately 0.2 and 0.45 of the specimen length. At 50% of the peak load, *S11* is tensile throughout the half-length of the beam corresponding to the test specimen. Some minor cyclic variations in *S11* also appear at this load level. At 75% of the peak load, significant tensile normal stress development is evident and cyclic variations in *S11* are more apparent. These kinds of variations do not appear in G7 until very close to the peak load (Fig. 5-5). There appears to be some correlation between the location of the peak *S11* values and the position of the peak lateral displacements, *U3*. Two distinctive peaks in *S11* can be observed at 95% of the peak load. The overall tensile normal stress increases with increasing load. However, the maximum *S11* occurs at only one position at the peak load and this value is measurably higher than the other peak *S11* values. This prominent band occurs along the primary web buckle shown in Figs. 4-11 and 4-12. The location of the peak *S11* value is approximately 16 % of the total member length from the left end of the specimen. At the post peak load level, several peaks are formed instead of one peak in *S11*. This is an indication of the formation of multiple tensile stress bands. It is important to note here is that the tensile stress *S11* is not constant along the length of the test segment for any of the load levels up to the peak load; however, at the post-peak load level, the cyclic variation in *S11* along the length are more substantial. Throughout all the load levels, the normal stress *S11*, along the right half of the beam remains small and nearly constant. Due to the thicker web on the right side of the test beam, there is no buckling of the web and *S11* remains identical at the initial specified residual stress at the web mid-depth.

The normal stress *S22* (Fig. 6-5) is maximum in compression at the mid-span and at the supports. These are the locations where the load is applied and where the beam end reaction is developed into the web. *S22* is approximately equal to zero in the half of the specimen with the thicker web for all levels of loading, except near the mid-span and the right-hand support where compressive *S22* develops the applied load and the end reaction

into the web. Comparatively lower values of *S22* for all the load stages, mostly verifies the Höglund's (1997) zero vertical membrane stress assumption.

At 25% of the peak load in Fig. 6-6, the maximum *S12* occurs near the mid-span at the location of maximum lateral displacement *U3* and remains constant (approximately equal to the stress value calculated using beam theory, $S12 = VQ / I_x t_w$) for the rest of the specimen. As the load is increased, this maximum shifts towards the left end of the specimen and the profile becomes more and more oscillatory. At the peak load level, the maximum *S12* occurs near the left end of the specimen. The oscillatory nature of *S12* can be related to the profile of the lateral displacement *U3*. *S12* is maximum at the peaks of *U3* and minimum at the points where *U3* is zero. Like *S11*, *S12* has two peaks at 95% of the peak load; however, there is one predominant peak at the peak load. Moreover, the location of largest peak coincides with the location of peak of *S11*, at 50 inches (normalized position equal to 0.16) from the left end of the specimen. For the post peak condition, the plot of *S12* is similar to *S11*. For all levels of loading, the shear stresses predicted by simulations are essentially equal to shear stresses calculated using beam theory, $S12 = VQ / I_x t_w$, on the right side of the specimen (thicker web), which is consistent with the fact that there is no shear buckling of the right side of the specimen.

The variation of von Mises stress *S* for Specimen UK6 (Fig. 6-7) is similar to its variation in G7 (Fig. 5-8). However, at the peak load, one predominant peak can be observed and the extent of yielding is concentrated over a much shorter length in UK6. This is due to high h/t_w of the specimen. Like G7, at the post peak, there is yielding of almost the entire section of the thinner web. For the thicker web, there is no development of diagonal tension and it is evident from a constant value of *S* for a particular load level.

The maximum principal stress *S1* is calculated using Eq. 5-1. For 25% of the peak load, *S1* (Fig. 6-8) is almost identical to *S12* (Fig. 6-6) throughout the left side of the beam. At this stage, the beam can be assumed to be in the state of pure shear. As the loading is

increased, there is a considerable increase in the diagonal tension. *S1* most closely follows the curve of *S11* for higher levels of loading. This behavior is similar to the response of specimen G7 at the mid-length of the panel (Fig. 5-9). This is a clear indication that even for specimens with *a/h* greater than 3.0, significant diagonal tension is developed at higher levels of loading, even at 50% of the peak load. As can be seen, the principal stress *S1* varies significantly throughout the left side of the specimen and at post peak load level three predominant peaks are formed.

The minimum in-plane principal stress *S2* (Fig. 6-9) is calculated using Eq. 5-2. Near the supports and the mid-span, this stress follows the curve of *S22*. This is due to the effect of large compressive load being applied at the mid-span and the reactions at the supports. Basler (1961) stated that for an unstiffened panel there is no increase in principal tensile or compressive stress after the shear buckling of the web. However, Höglund (1973) addressed that, up to the point of theoretical shear buckling of the plate, the web is in a state of pure shear and thus the principal tensile stress, *S1,* is equal to principal compressive stress, *S2.* After the shear buckling of the web, the principal tensile stress, *S1* increases but the principal compressive stress, *S2* remains the same or changes slightly. At 25% of the peak load, *S2* is constant on both the left- and right-hand sides of the specimen, and at this stage the web can be approximated to be in pure shear. After 25% of the peak load, the stress *S2* changes only slightly on the left hand side of the member, except near the mid-span and supports. This is analogous to the behavior of Specimen G7 (Fig. 5-10) within the main portion of the panel length. The elastic shear buckling stress, $\tau_{e,}$ calculated using Eq. 1-1 and the plate buckling coefficient taken from Eq. 1-3, is equal to 2.83 ksi. For the majority of the half-length on the left-hand side of the specimen, the stress *S2* remains close to τ_e. For the right-hand side of the specimen, the difference between *S1* and *S2* is approximately constant, due to the initial residual stress, which once again confirms that the right-hand side of the beam does not undergo web buckling.

The principal stress orientation θ_p (Fig. 6-10) is calculated using the Eq. 5-3. At 25% of the peak load, θ_p is almost equal to 45^o for the entire length of the specimen, and up to this point, the specimen is approximately in a state of pure shear. For the left half of the specimen, as the load is increased the principal angle decreases. This is because of the increase in the value of *S1* without any significant change in *S2* for higher levels of loading. At the peak load, the principal angle decreases to as low as 18^o and it decreases further at the post peak stage. Höglund (1997) describes this behavior using his *"rotated stress field theory"*. This is similar to the behavior of Specimen G7 (Fig. 5-10) near the mid panel length and hence verifies that the Höglund's *rotated stress field theory* is applicable to both the unstiffened and stiffened panels. At the post peak load, the principal angle at middle of the panel decreases to almost 16^o. The principal angle according to Eq. 1-18 (Höglund 1997) is 15^o. For the right hand side of the specimen, the principal angle is close to 45^o for all levels of loading. At the post peak stage near the middle of the panel, *S11* is equal to 56 ksi and addition of *S1* and *S2* is equal to 58 ksi. This difference is due to non-zero value of normal stress, *S22* verifying the complexity of the mechanism. Basler's Tension Field Action Model is not applicable to unstiffened panels. However, if it were applied, the orientation of the diagonal tension comes out to be 7^o.

6.1.1 Principal Stresses in Selected Elements at the Web Mid-Depth

The procedure of Section 5.1.1 is repeated in this section for UK6. Four Elements along the left-half length of the specimen are selected at web mid-depth and the principal stresses are drawn as arrows on these Elements to explain the mechanism of the shear strength development. Figure 6-11 shows the location of Elements along the web mid-depth.

Element 1 is located at approximately 10 inches from the left end of the specimen. The second Element selected for study is at 50 inches from the left end. The maximum *S11* at

peak load occurs at this location. The third Element is at 50 inches from the second Element and fourth Element is selected such that it is near mid-span. The arrows on the Elements indicate the orientation of the principal stresses and their numerical values are written in the brackets. Figures 6-12 through 6-25 shows the principal stresses at different levels of loading. The word "Element" is abbreviated as "Ele." to fit all the Elements in one row to understand the plots better.

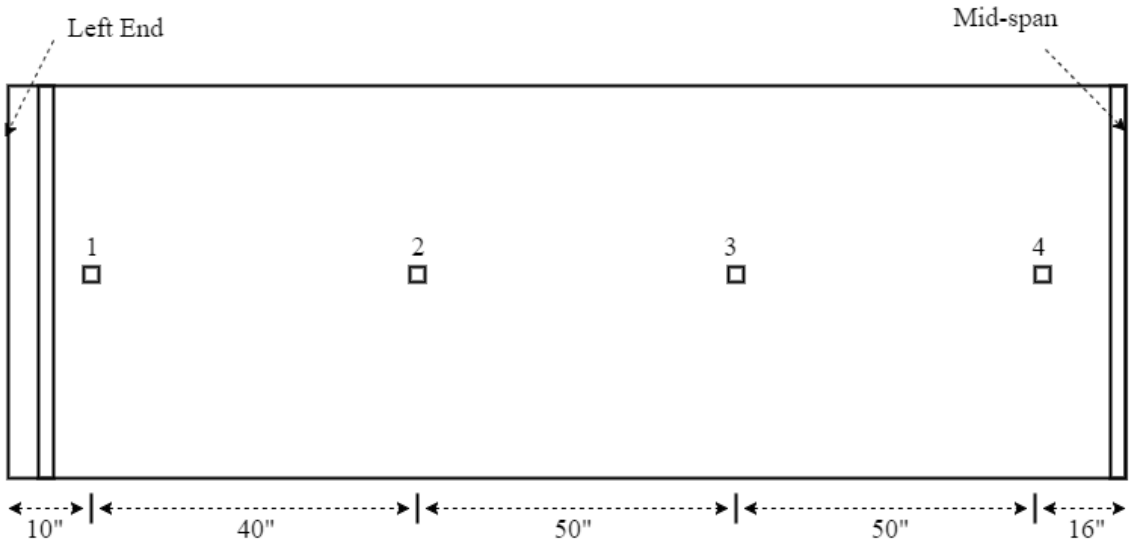

Fig. 6-11. Elements along the web mid-depth.

1. Principal stresses at zero load

The values of principal stresses are almost zero and the principal angle for maximum in-plane principal is almost 90º. However, for some Elements it is slightly different. This is because of the initial web imperfections.

Ele. 1 (-0.02 ksi) Ele. 2 (-0.06 ksi) Ele. 3 (0.04 ksi) Ele. 4 (0.05 ksi)

Fig. 6-12. Maximum In-Plane Principal Stress *S1* and their orientation at zero load.

Ele. 1 (-0.17 ksi) Ele. 2 (-0.95 ksi) Ele. 3 (-0.60 ksi) Ele. 4 (-0.75 ksi)

Fig. 6-13. Minimum In-Plane Principal Stress *S2* and their orientation at zero load.

2. Principal stresses at 25% peak load

All the Elements at 25% of the peak load can be approximated to be in the state of pure shear. The principal plane angles are close to 45°, showing that this state can be approximated as a state of pure shear.

Ele. 1 (2.14 ksi) Ele. 2 (3.00 ksi) Ele. 3 (4.23 ksi) Ele. 4 (3.40 ksi)

Fig. 6-14. Maximum In-Plane Principal Stress *S1* and their orientation at 25% peak load.

Ele. 1 (-3.91 ksi) Ele. 2 (-3.42 ksi) Ele. 3 (-2.16 ksi) Ele. 4 (-2.29 ksi)

Fig. 6-15. Minimum In-Plane Principal Stress *S2* and their orientation at 25% peak load.

3. Principal stresses at 50% peak load

The difference between values of *S2* at 25% and 50% of the peak load is small at the web mid-depth, except at Element 1. The increase in *S2* for Element 1 is due to the development of the left-hand reaction into the web. For Elements 2 and 3, we can clearly see a large diagonal tension forming. There is only a small increase in *S2*, and there is a measurable change in principal stress angle.

It is important to note here is that *S1* is larger in Element 4 compared to Element 2 at 25% of the peak load. This is mainly due to effect of the out of plane displacements due to effect of the initial web-imperfections. However, as the load is increased, this effect of initial imperfections is not pronounced and the effect of web buckling and diagonal tension takes over resulting in higher value of *S1* for Element 2.

Ele. 1 (4.72 ksi) Ele. 2 (7.85 ksi) Ele. 3 (10.92 ksi) Ele. 4 (7.99 ksi)

Fig. 6-16. Maximum In-Plane Principal Stress *S1* and their orientation at 50% peak load.

Ele. 1 (-8.20 ksi) Ele. 2 (-4.19 ksi) Ele. 3 (-3.20 ksi) Ele. 4 (-3.30 ksi)

Fig. 6-17. Minimum In-Plane Principal Stress *S2* and their orientation at 50% peak load.

4. Principal stresses at 75% peak load

The trends at 75% of the peak load are similar to those at 50% of the peak load. The *S2* for Elements 2 and 3 remains constant and is similar to its values at 25% of the peak load.

Ele. 1 (6.57 ksi) Ele. 2 (17.11 ksi) Ele. 3 (22.19 ksi) Ele. 4 (14.95 ksi)

Fig. 6-18. Maximum In-Plane Principal Stress *S1* and their orientation at 75% peak load.

Ele. 1 (-11.68 ksi) Ele. 2 (-4.28 ksi) Ele. 3 (-3.74 ksi) Ele. 4 (-3.81 ksi)

Fig. 6-19. Minimum In-Plane Principal Stress *S2* and their orientation at 75% peak load.

5. Principal stresses at 95% peak load

At 95% of the peak load, *S1* is higher at Element 3 compared to Element 2. There is a small increase in *S1* for Element 4 compared to Element to Elements 2 and 3, because this Element is close to the mid-span and there is not a pronounced effect of the diagonal tension at that location.

Ele. 1 (7.85 ksi) Ele. 2 (34.89 ksi) Ele. 3 (37.74 ksi) Ele. 4 (22.91ksi)

Fig. 6-20. Maximum In-Plane Principal Stress *S1* and their orientation at 95% peak load.

Ele. 1 (-13.50 ksi) Ele. 2 (-3.93 ksi) Ele. 3 (-3.90 ksi) Ele. 4 (-4.02 ksi)

Fig. 6-21. Minimum In-Plane Principal Stress *S2* and their orientation at 95% peak load.

6. Principal stresses at peak load

At the peak load, *S1* at Element 2 becomes greater than *S1* at Element 1. This is because there is one predominant tension band formed at peak load and the maximum *S1* occurs at

50 inches from the left end of the span. The trend for Element 1 remains the same for all the levels of loading.

Ele. 1 (9.25 ksi) Ele. 2 (51.33 ksi) Ele. 3 (44.81 ksi) Ele. 4 (24.14 ksi)

Fig. 6-22 Maximum In-Plane Principal Stress *S1* and their orientation at peak load.

Ele. 1 (-12.32 ksi) Ele. 2 (-3.60 ksi) Ele. 3 (-3.48 ksi) Ele. 4 (-4.42 ksi)

Fig. 6-23 Minimum In-Plane Principal Stress *S2* and their orientation at peak load.

7. Principal stresses at post peak

Even at the post peak load level, the maximum value of *S1* occurs at Element 2. The maximum in-plane principal angle for Elements 2 and 3 is almost 15^{o}. The compressive stress, *S2* remains almost constant (close to τ_e) for all the levels of loading after 25% of the peak load except for Element 1. Elements 2 and 3 behave in a similar manner when compared to the Element 2 of girder G7 (Figures 5-12 through 5-25) and Element 1 behave in a similar manner to Element 1 of G7.

Ele. 1 (5.66 ksi) Ele. 2 (59.44 ksi) Ele. 3 (49.47 ksi) Ele. 4 (18.72 ksi)

Fig. 6-24. Maximum In-Plane Principal Stress *S1* and their orientation at post peak load.

Ele. 1 (-2.34 ksi) Ele. 2 (-2.21 ksi) Ele. 3 (-2.63 ksi) Ele. 4 (-4.45 ksi)

Fig. 6-25. Maximum In-Plane Principal Stress *S2* and their orientation at post peak load.

6.2 Responses at a Section Along the Length at the Top of the Web

In this section, the procedure of Section 5.2 is repeated for Specimen UK6. The quantities plotted are the lateral displacement *U3*, the web membrane stresses, *S11*, *S22* and *S12*, the von Mises stress, *S*, the maximum principal tensile membrane stress (*S1*), the maximum principal compressive membrane stress (*S2*) and the orientation of the principal stresses (θ_p). Figures 6-26 through 6-33 show variation of these quantities, in that order, at a section along the length at web top for different levels of loading.

The lateral displacement *U3* (Fig. 6-26) plots follow the expected pattern for the load levels; zero, 25%, 50% and 75% of the peak load, i.e. the lateral displacement is zero at all the lateral bracing locations and follows the expected deflected shape. However, at 95% of the peak load, near the supports, there is a sudden change in the direction of curvature in the unbraced length. This is due to the folding of the web near the support. This behavior is not visible until about 95% of the peak load. At the peak load, this effect is clearly visible. At the post peak load, the folding of web increases to a greater length of the web and is much more visible. The lateral displacement near the middle of the half-span follows the profile as expected even at the post peak load level.

At zero load, the normal stress *S11* in Fig. 6-27 is almost constant for the entire length of the specimen and is equal to the residual stress pattern in the test simulation. At 25% of the peak load, the results from simulations and results obtained from the beam theory (when

the residual stress is applied to the specimen) is identical. The results obtained from beam theory are not shown in the graph for clarity. The behavior remains same for 50% of the peak load. However, the difference between values from simulation and beam theory reduces to zero at 75% peak load. This is mainly due to the increase in the lateral displacement *U3* of the web top. At 95% of the peak load and thereafter, the variations in *S11* is much more cyclic in UK6 compared to G7 (Fig. 5-27). At 95% of the peak load, there are no peaks and the variation of *S11* on the left part of the specimen follows the sinusoidal nature of lateral displacement *U3*. However, at the peak load there is sudden decrease in the compressive stress at 12 inches from the left end of the beam. This is where the web buckle meets the top-flange (see Figs. 4-11 and 4-12). At the post peak load, this behavior is much more pronounced and is visible over a longer length. For the thicker part of the web on the right-hand half of the beam, the difference between the results obtained from simulations and the results obtained from the beam theory is identical for all the levels of loading. This verifies that for the right side of the specimen, the beam theory can still be applied and there is no shear buckling of the right side of the specimen.

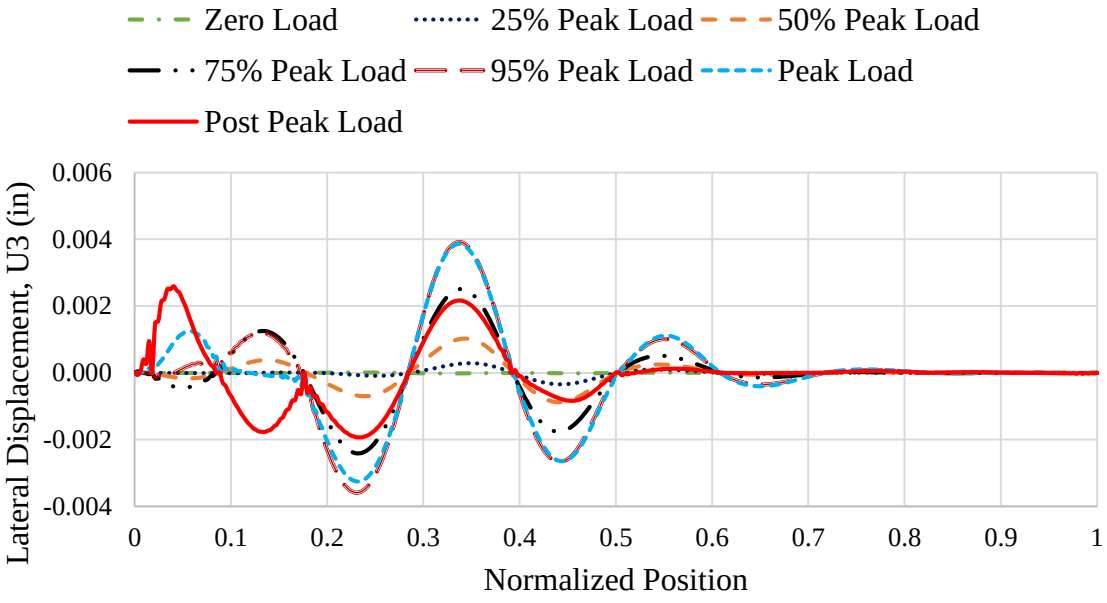

Fig. 6-26. Lateral Displacement *U3* versus normalized position along the web top.

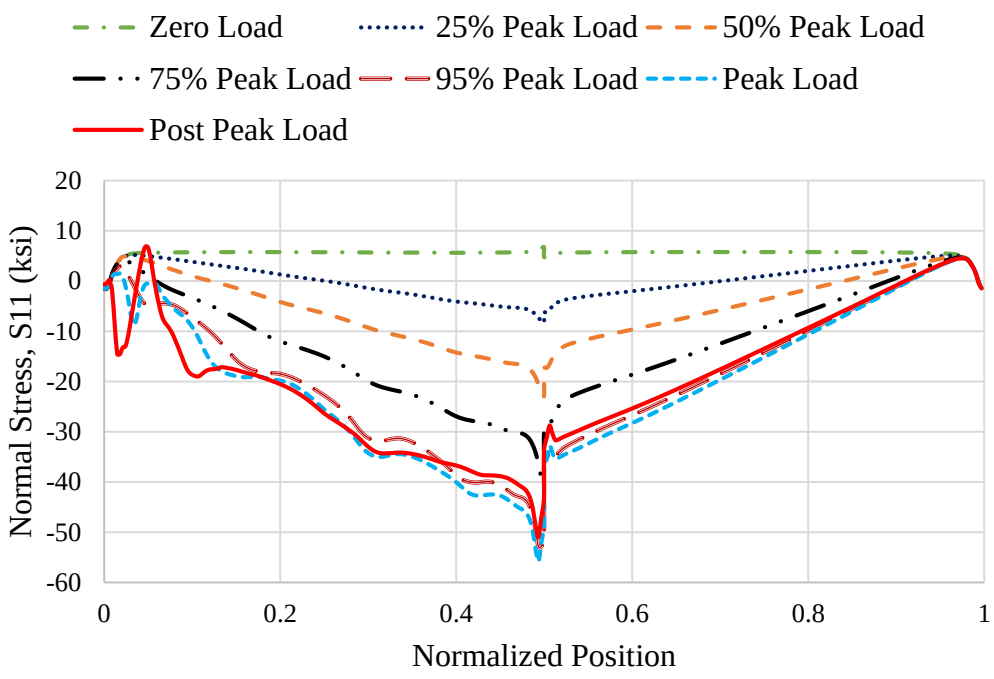

Fig. 6-27. Normal Stress *S11* versus normalized position along the web top.

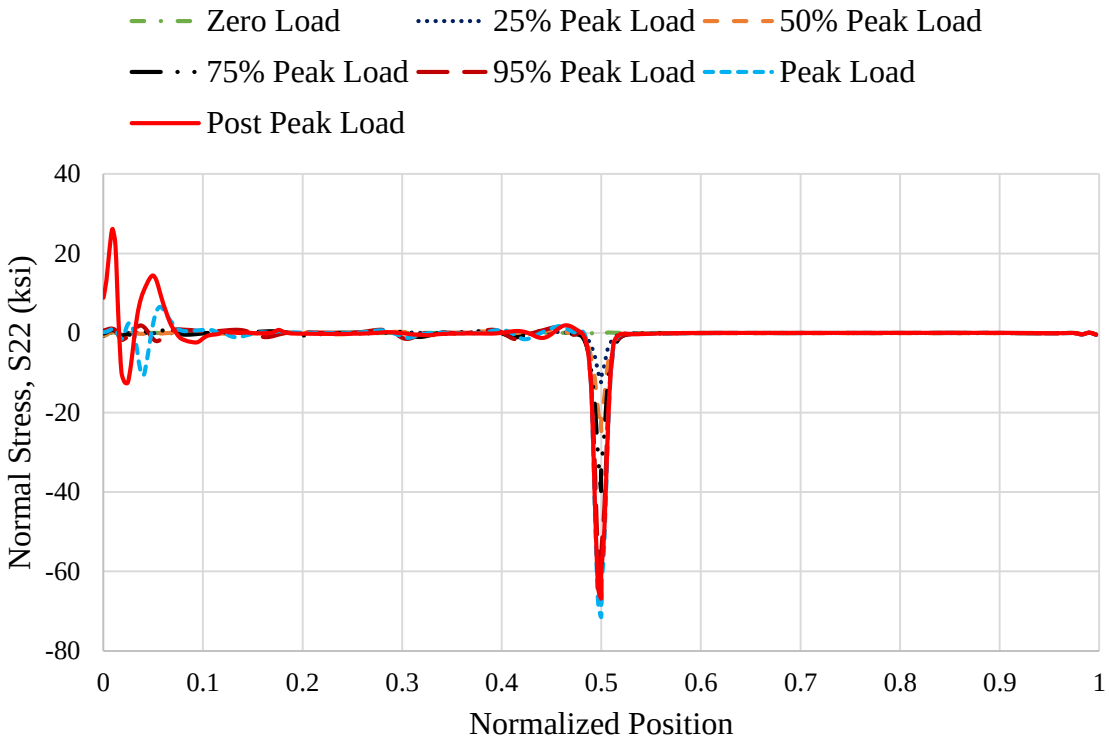

Fig. 6-28. Normal Stress *S22* versus normalized position along the web top.

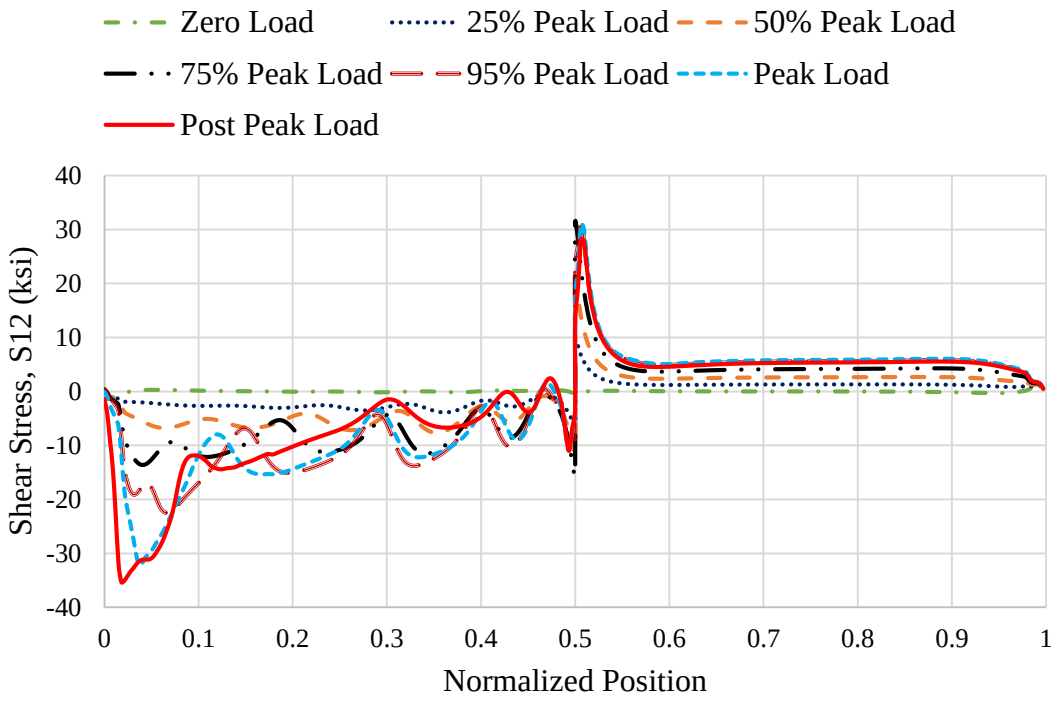

Fig. 6-29. Shear Stress *S12* versus normalized position along the web top.

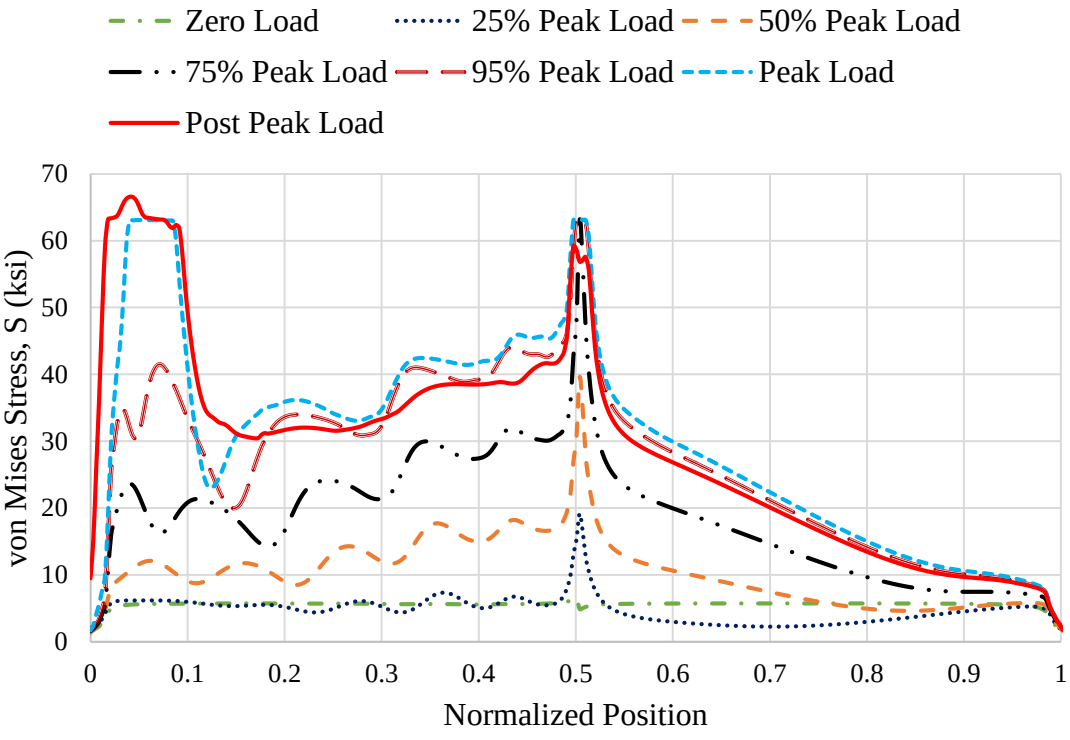

Fig. 6-30. von Mises stress *S* versus normalized position along the web top.

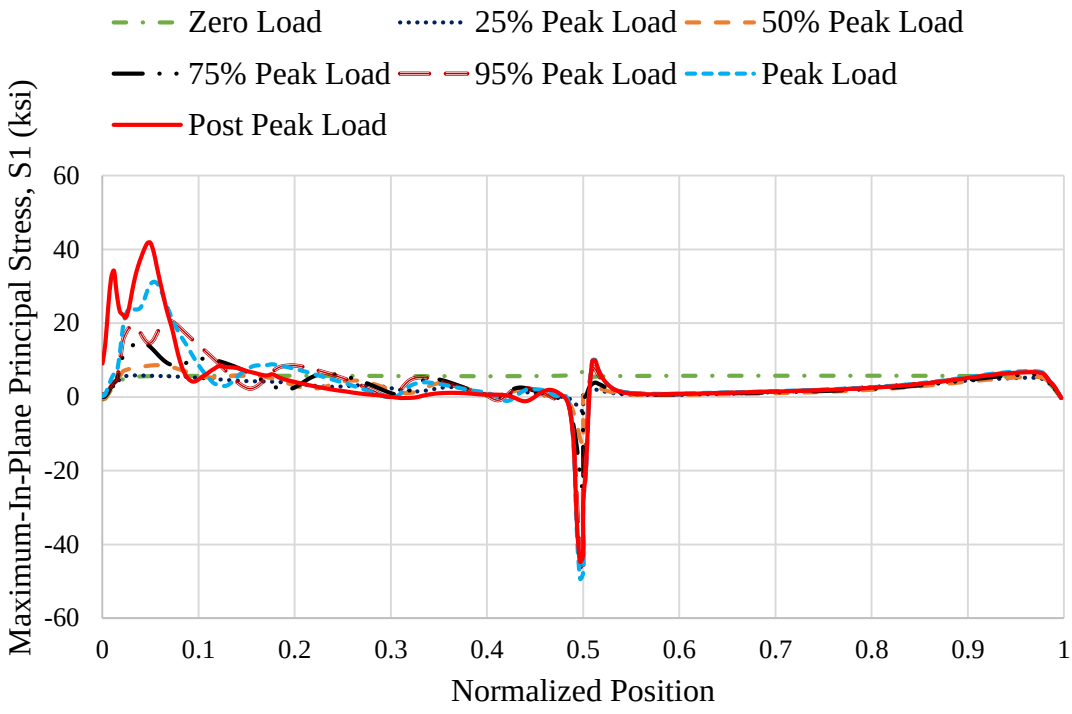

Fig. 6-31. Maximum In-Plane Principal Stress *S1* versus position along the web top.

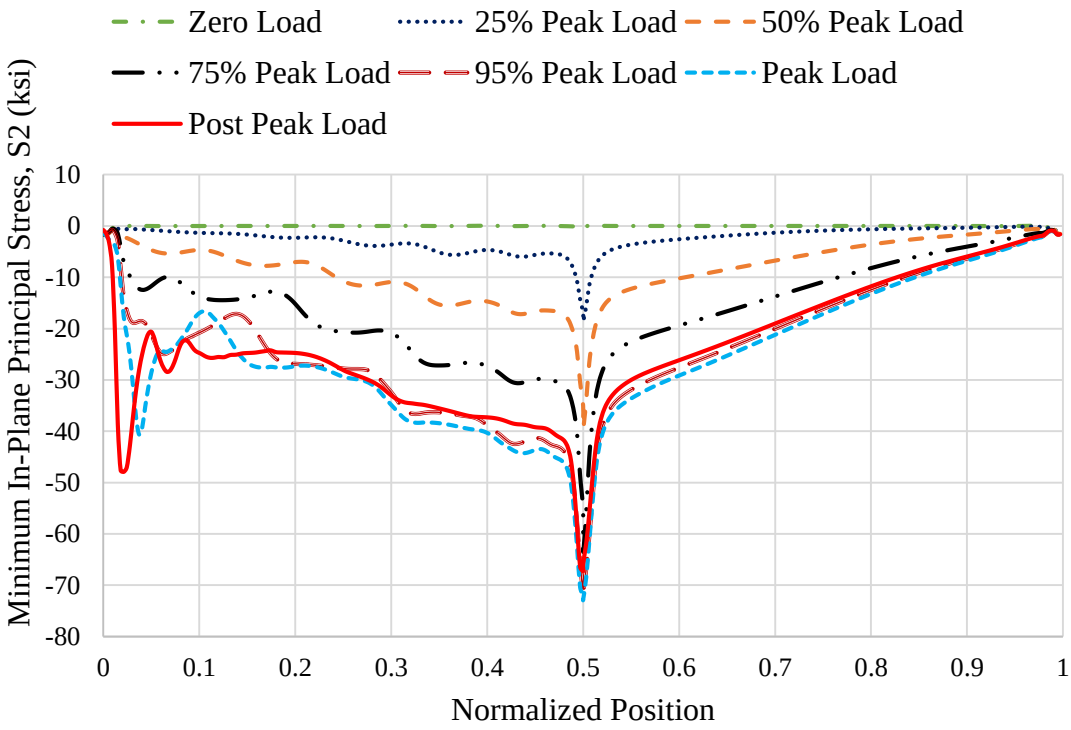

Fig. 6-32. Minimum In-Plane Principal Stress *S2* versus position along the web top.

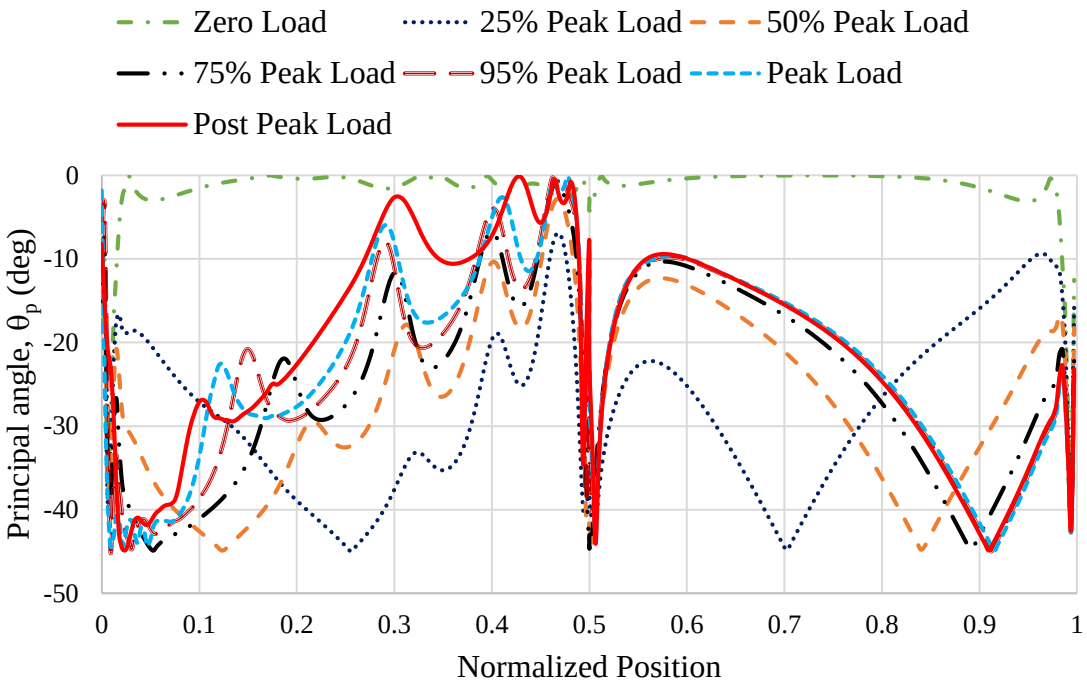

Fig. 6-33. Principal Angle θ_p versus position along the web top.

The normal stress *S22* (Fig. 6-28) is approximately zero for almost the entire length of the beam except at the mid-span where the concentrated load is applied. Even at 95% of the peak load, this stress is very small (except at the mid-span). This indicates that, there are no substantial transverse forces applied to the flange. At 95% of the peak load, the maximum value of stress other than near the mid-span, is 2.08 ksi. This value occurs near the left-hand support. However, at the peak load, the maximum compressive stress increases to 10.7 ksi. As the load increases from 95 % of the peak load to the peak load, this stress increases by approximately 415%. This indicates that the top flange is subjected to extremely low transverse forces except near the support and at near the peak load. The location of maximum *S22* coincides with the location of maximum *S11*. Even at post peak load, *S22* remains almost equal to zero except near the left end of the panel. This is where the web buckle meets the top flange as well as where forces transferred by diagonal tension

toward the top of the web need to be balanced by a vertical compression force transfer to the left-end support. This is similar to behavior of girder G7 (Fig. 5-28).

At 25% of the peak load, the maximum *S12* (Fig. 6-29) occurs near the mid-span. As the load is increased, this maximum shifts towards left end of the specimen and the profile becomes more and more oscillatory and at the peak load level, maximum *S12* occurs near the left end of the panel, like G7 (Fig. 5-29). However, the variation is much more cyclic in UK6. At 95% of the peak load, shear stress *S12* has the maximum value of 23 ksi. However, there is only one predominant peak at peak load. The maximum *S12* at the peak load is 32 ksi. As the load increases from 95 % of the peak load to the peak load, this stress increases by approximately 40% and its location coincides with the location of maximum *S11* and *S22*. This effect is much more pronounced at the post peak load. For the right side of the specimen, the shear stresses found from simulations and shear stress from beam theory, $S12 = VQ / I_x t_w$, are identical showing that there is no shear buckling of thicker part. The results from beam theory are not shown for clarity.

At 95% of the peak load, the von Mises stress *S* plot (Fig. 6-30) is around 40 ksi and it increases by almost 50% to 60 ksi for 5% increase in the load. At the peak load, there is yielding of web top over a small length. For specimen G7, there is yielding even for 95% of the peak load and this yielding at the post peak load is distributed over a larger length. This variation in the extent of yielding due to comparatively smaller *a/h* of G7.

The behavior of the principal stresses *S1* and *S2* (Fig. 6-31 and 6-32, respectively) is very similar to behavior of these stresses on G7 (Fig. 5-31 and 5-32, respectively). The principal stresses *S1* and *S2* are large at the left-hand end of the panel. The stress *S2* and *S1* increases at left end of the panel due to increase in *S12* near the left end. The Elements near the mid-span (right end of the panel) are subjected to compressive flexural stress and almost zero *S12* and *S22*. This results in *S1* being close to zero for almost the entire length

of the except near the left transverse stiffener. *S2* follows the curve of *S11* for almost the entire length of specimen except near the left end of the panel.

6.2.1 Boundary Condition between the Top Flange and the Web

The procedure of Section 5.2.1 is repeated for Specimen UK6 in this section. Four Elements along the left-half length of the specimen are selected at the web-top. Fig. 6-34 shows the location of selected Elements.

The first Element is selected at 12 inches from the left end, location where the maximum *S22* occurs at the peak load. The second, third and fourth Element are selected at a distance of 57, 107 and 157 inches respectively from the left end of the specimen. Figures 6-35 through 6-38 show the variation of *S22* at the different surfaces as a function of the applied load.

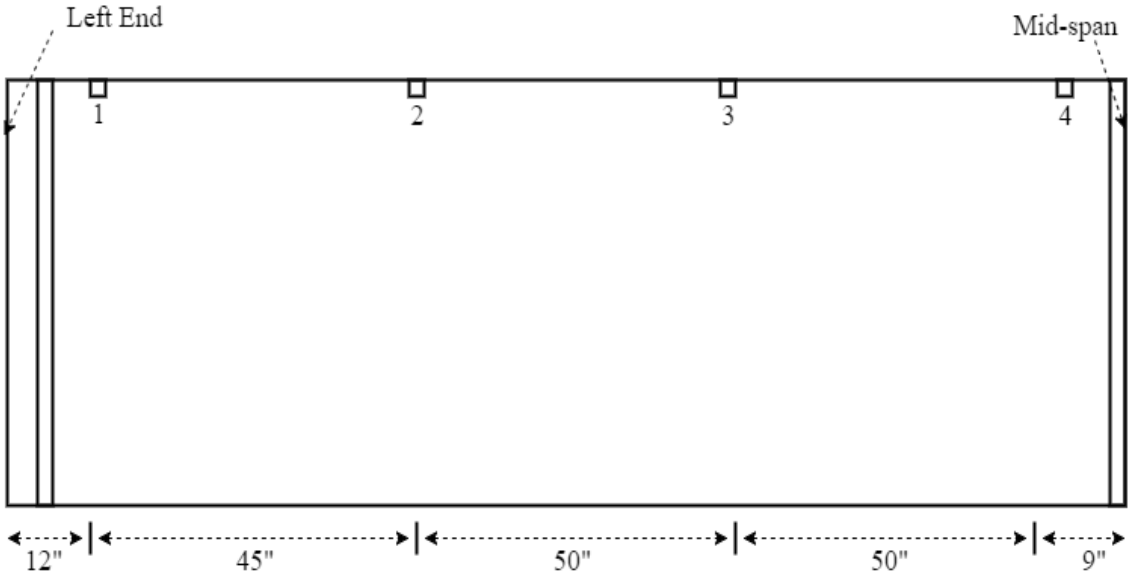

Fig. 6-34. Elements along the web-top.

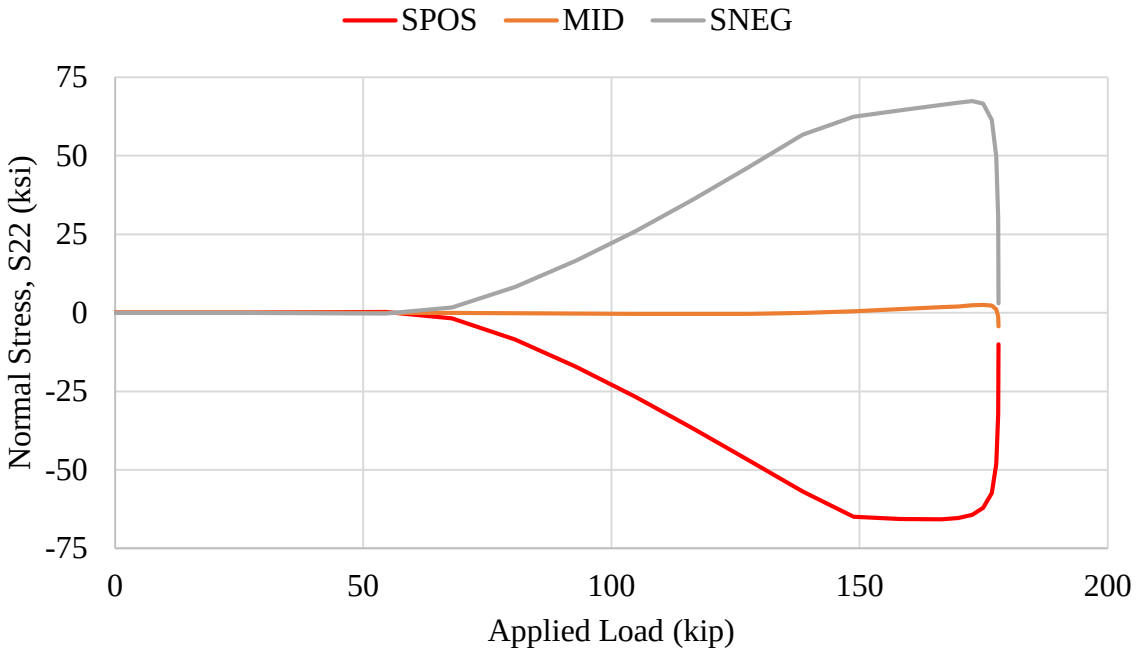

Fig. 6-35. Normal Stress *S22* at top, mid and bottom surface of the web versus applied load for Element 1 at the web-top.

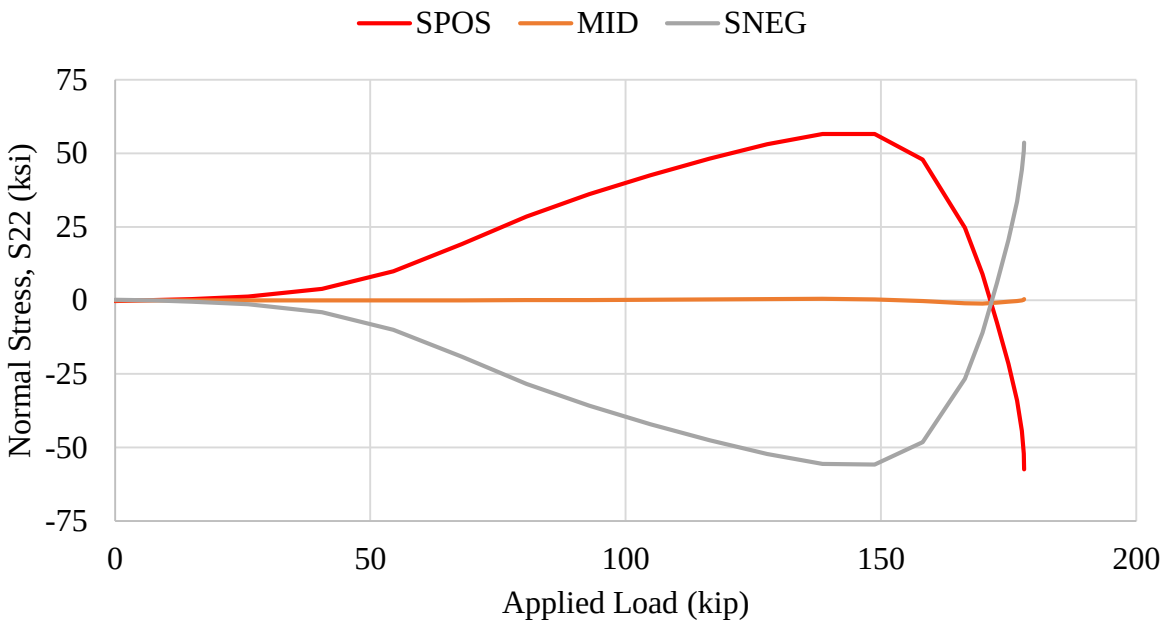

Fig. 6-36. Normal Stress *S22* at top, mid and bottom surface of the web versus applied load for Element 2 at the web-top.

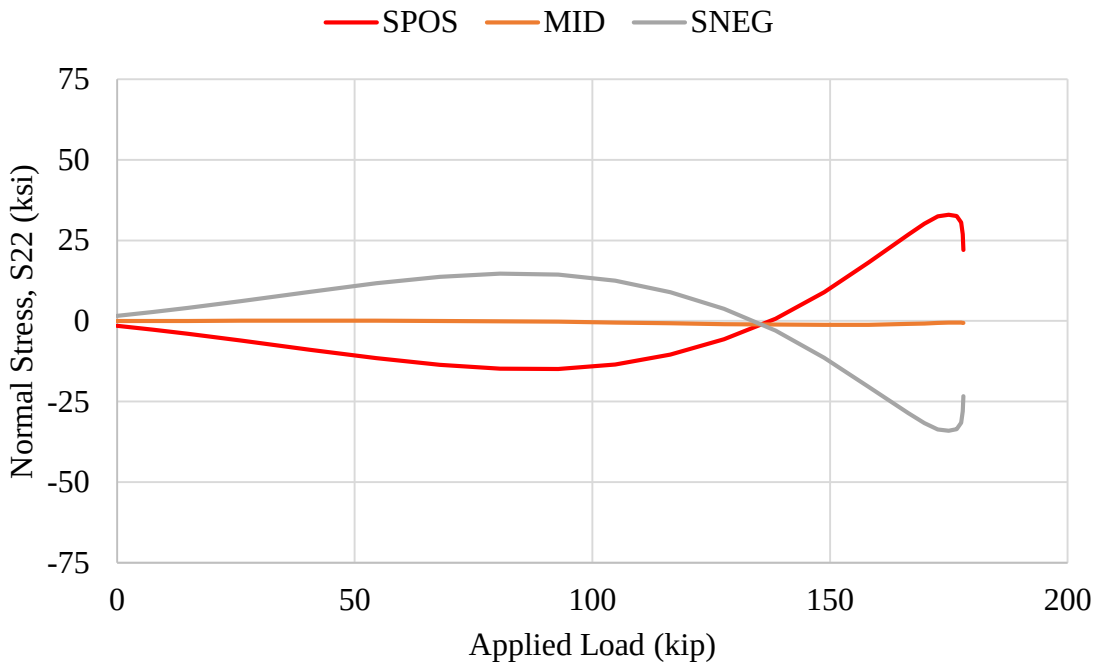

Fig. 6-37. Normal Stress *S22* at top, mid and bottom surface of the web versus applied load for Element 3 at the web-top.

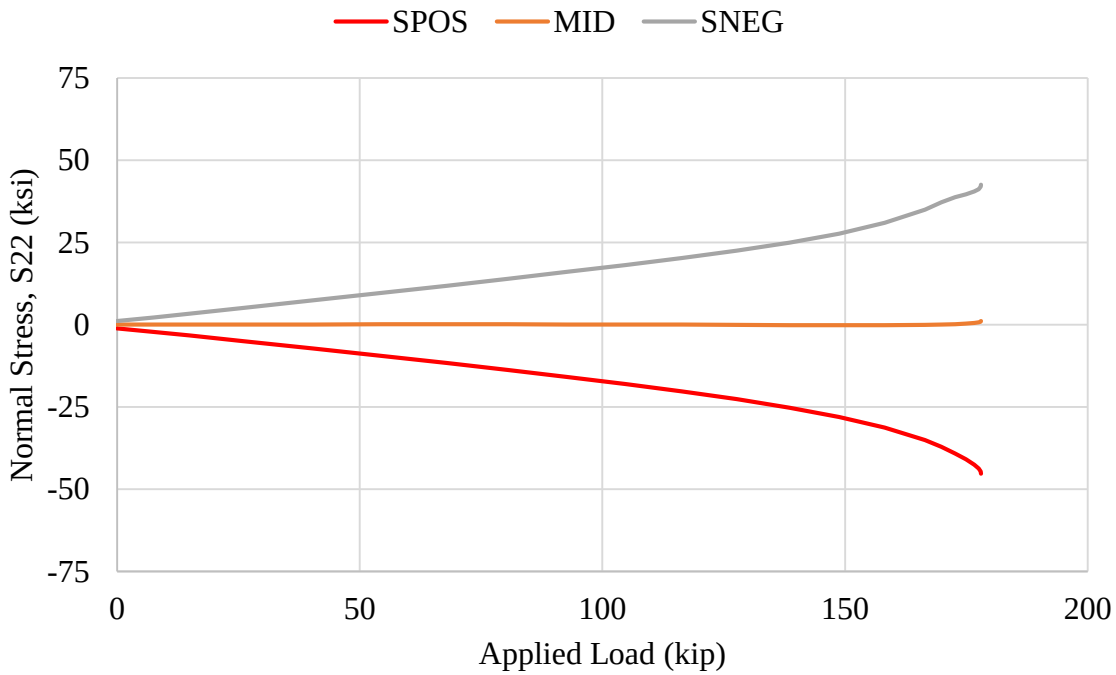

Fig. 6-38. Normal Stress *S22* at top, mid and bottom surface of the web versus applied load for Element 4 at the web-top.

The stress, *S22* at the mid-surface remains nearly equal to zero up until almost the peak load for Elements 2, 3 and 4. For Element 1, there is considerable increase in the *S22* at the peak load. *S22* increases significantly between 95% of the peak load and the peak load.

From these plots, it can be stated that the top-flange provides substantial torsional restraint to the top of the web throughout the loading and into post-peak. However, from Fig. 6-28, it is clear that the web membrane force remains very small until about 95% of the peak load. At peak load, however, there are considerable membrane stresses being developed between flange and web at Element 1 and this effect amplifies at the post peak load (Fig. 6-28). Similar behavior was observed for girder G7.

6.3 Responses at a Section Along the Length at the Bottom of the Web

A procedure similar to that discussed in Section 5.3 is repeated in this section for the web and bottom flange juncture of Specimen UK6. The quantities plotted are the web membrane stresses, *S11*, *S22* and *S12*, the von Mises stress, *S*, the maximum principal tensile membrane stress (*S1*), the maximum principal compressive membrane stress (*S2*) and the orientation of the principal stresses (θ_p). Figures 6-39 through 6-45 show variation of these quantities, in that order, at a section along the length at the web bottom for different levels of loading.

In all these figures, the behavior of right side of the specimen follows the results from beam theory and the variations are similar to the variations at the top flange.

At 25% of the peak load in Fig. 6-39, the *S11* values from simulation and beam theory match closely with one another when the initial residual stress is included with the beam theory stresses. The results obtained from beam theory are not shown in the graph for clarity. The behavior remains the same at 50% of the peak load. However, the stress from simulations is lesser than results obtained from simulations at 75% of the peak load. At

95% of the peak load, the the stress *S11* at 146 inches from the left free end is 36.41 ksi. However, at the peak load, there is sudden decrease in tensile stress near the mid-span at at normalized position of approximately 0.43 from left free end of the beam. As the load increases from 95 % of the peak load to the peak load, this stress decreases by approximately 40%. This is where the failure band in the web meets the bottom flange. At the post peak load level, this behavior is much more pronounced and is visible over a longer length. This behavior has some similarity to the response at the top of the web on the left-hand end of the panel. This behavior is also seen in girder G7 (Fig. 5-39). However, at the post peak load level, this behavior extends over a longer fraction of the panel length in the case of G7.

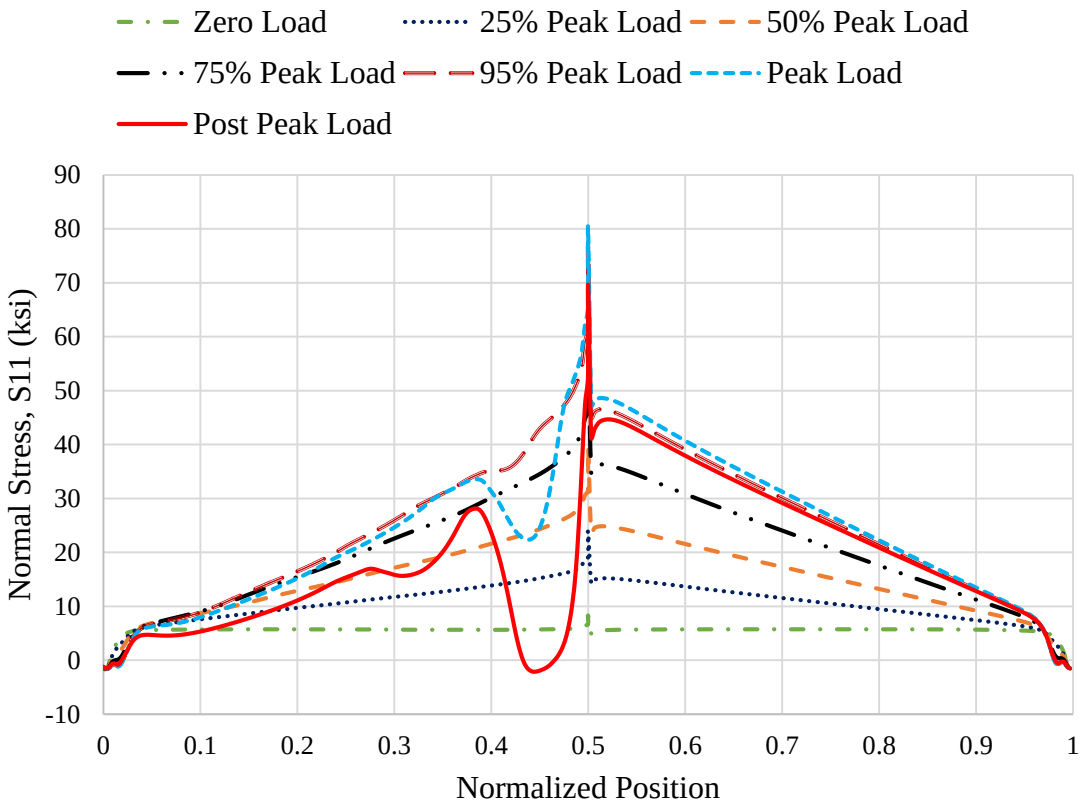

Fig. 6-39. Normal Stress *S11* versus normalized position along the web bottom

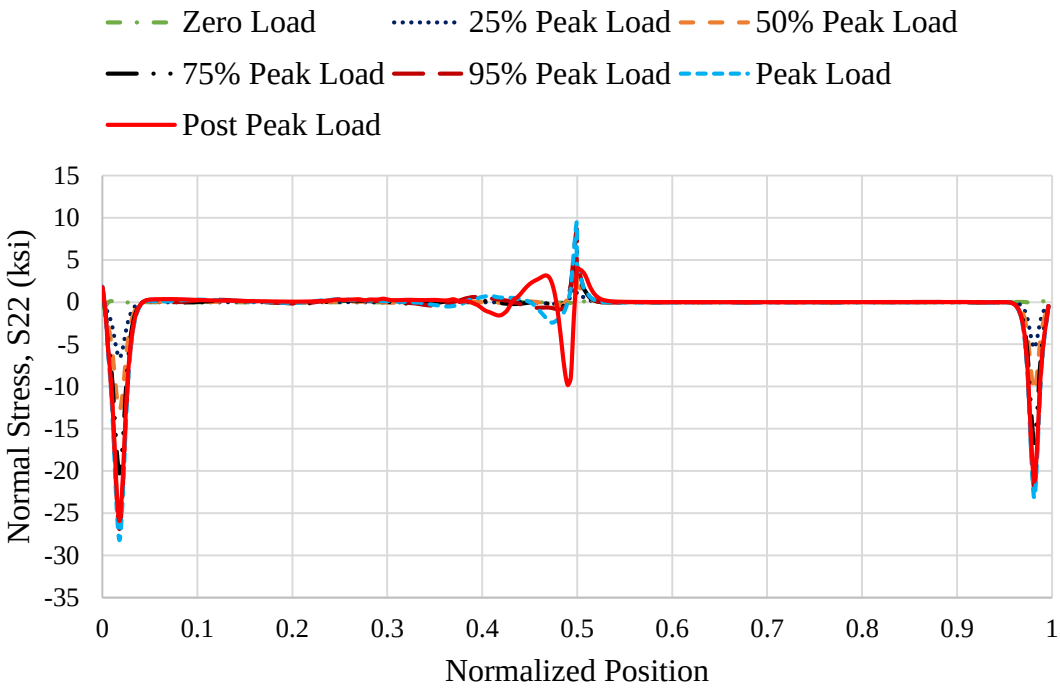

Fig. 6-40. Normal Stress *S22* versus normalized position along the web bottom.

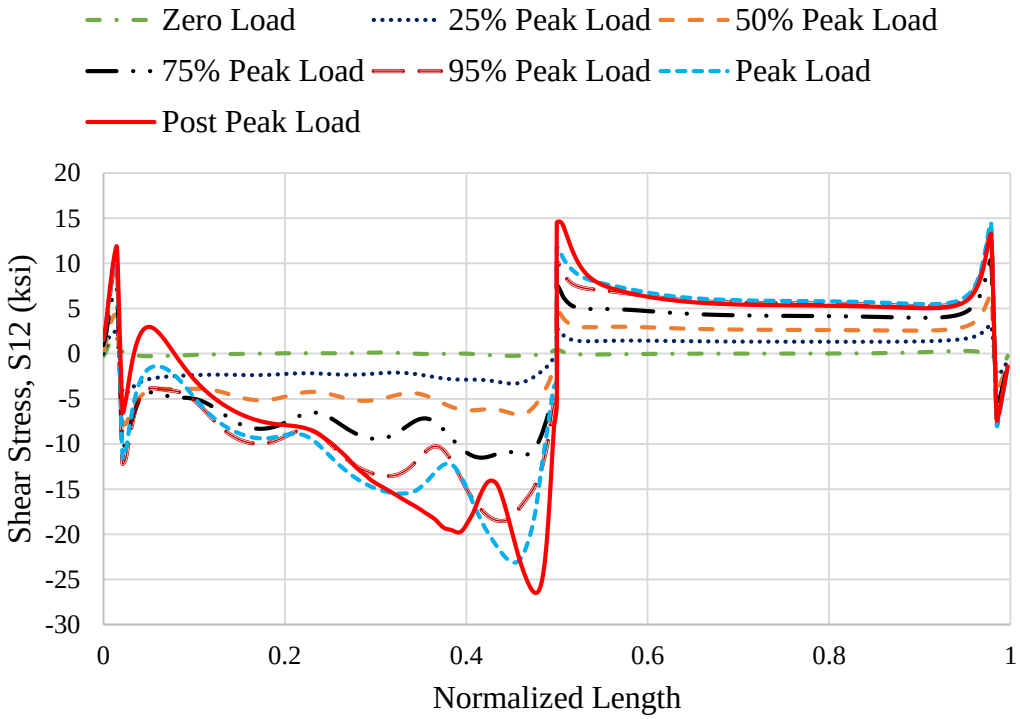

Fig. 6-41. Shear Stress *S12* versus normalized position along the web bottom.

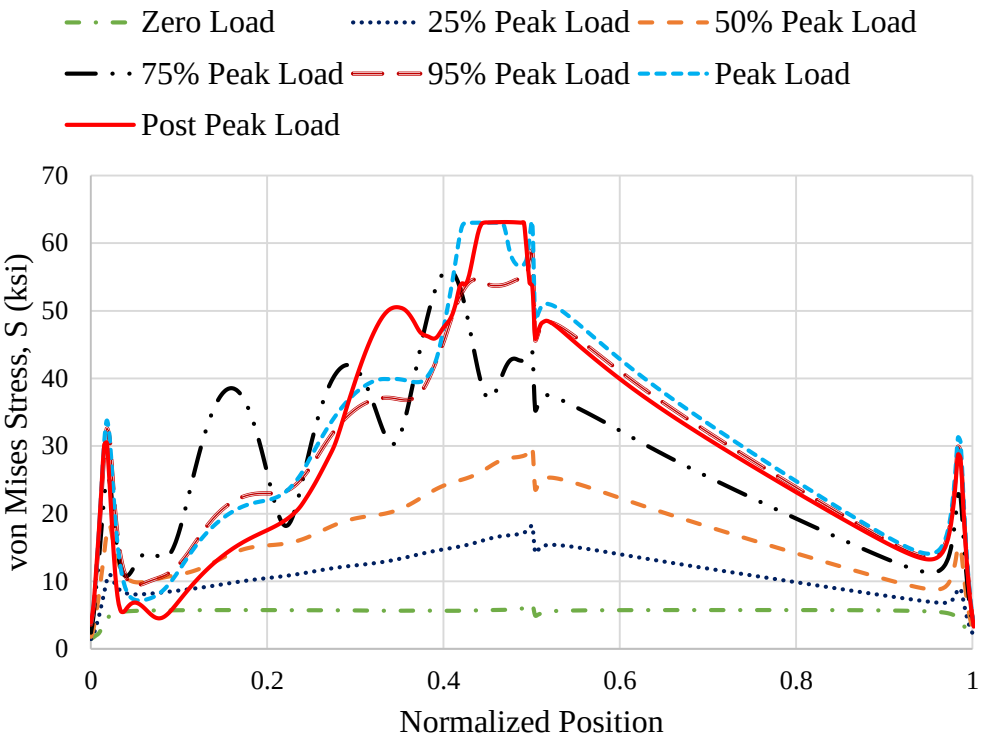

Fig. 6-42. von Mises stress *S* versus position along the web bottom.

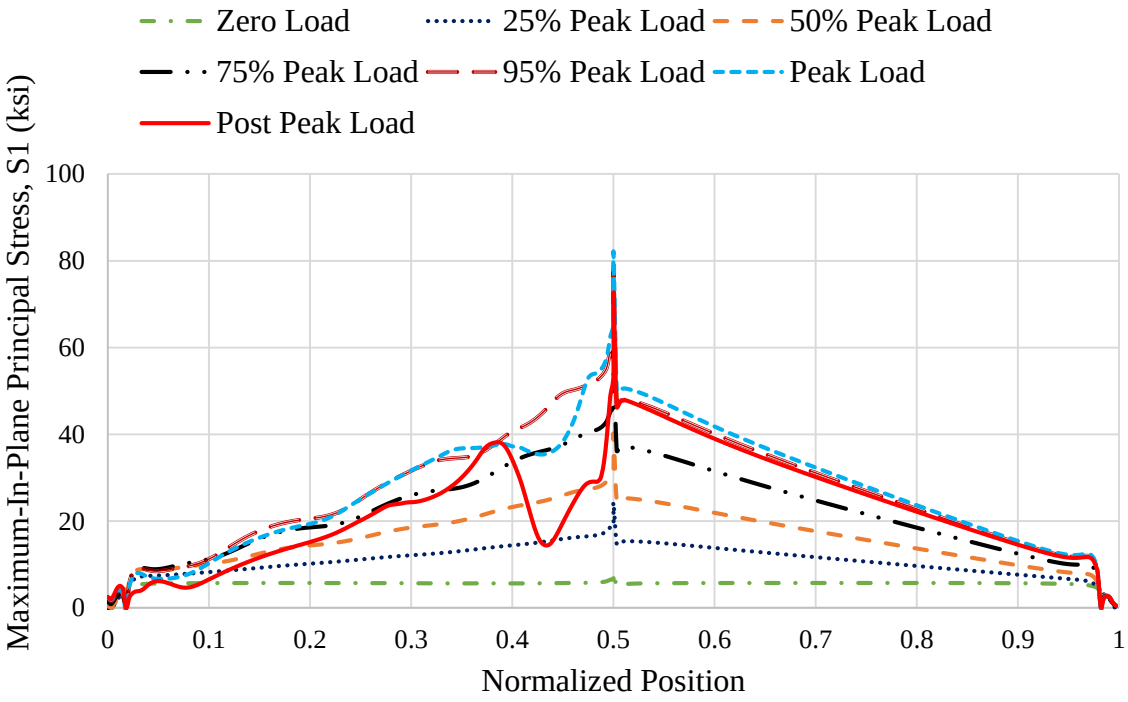

Fig. 6-43. Maximum In-Plane Principal stress *S1* versus position along web bottom.

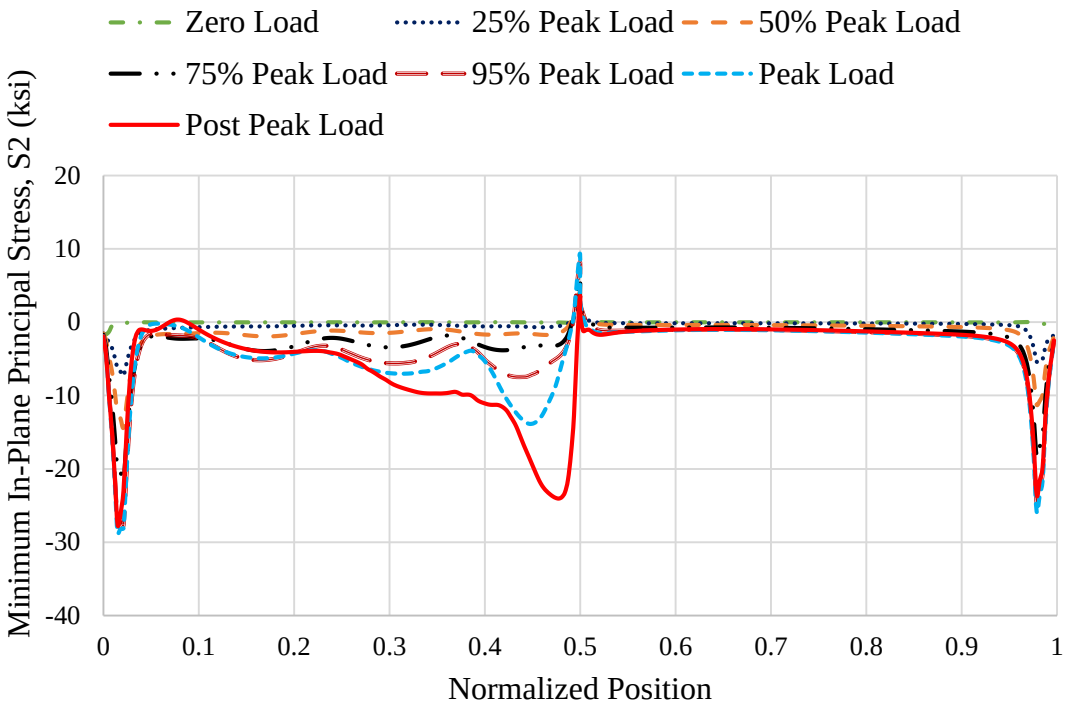

Fig. 6-44. Minimum In-Plane Principal stress *S2* versus position along web bottom.

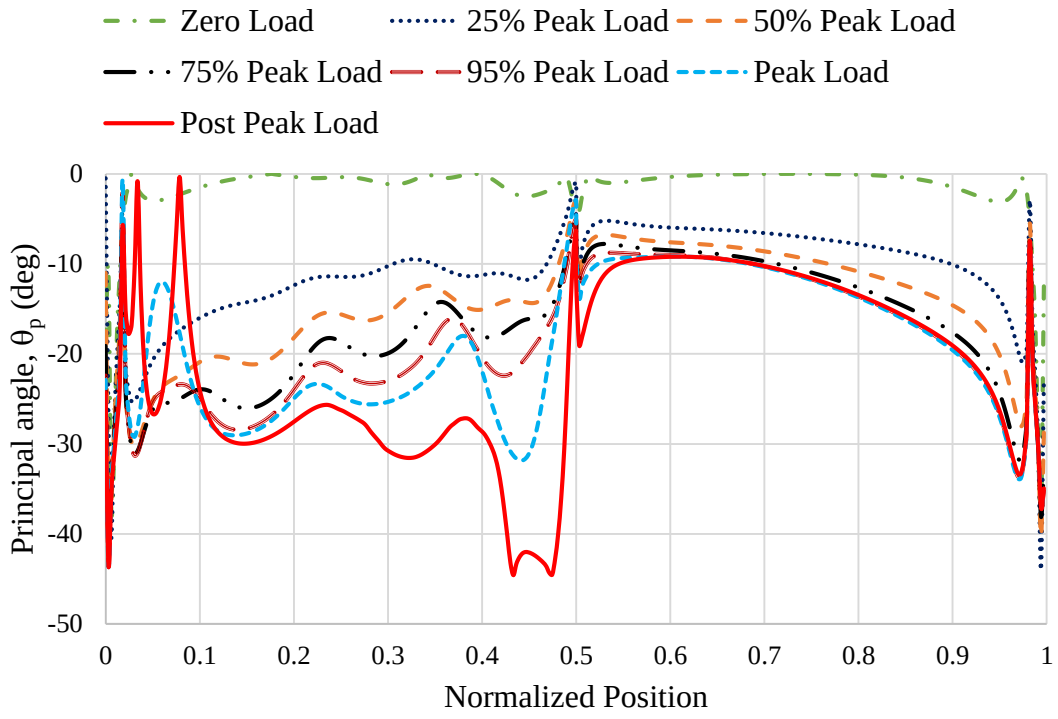

Fig. 6-45. Principal Angle θ_p versus position along the web bottom.

Similar to the top flange, *S22* at the bottom flange (Fig. 6-40) remains almost zero except at the mid-span and at the supports, for all the loading levels until 95% of the peak load. The maximum value of *S22* is 0.83 ksi at 95% of the peak load. However, at the peak load, the maximum compressive stress increases to 2.46 ksi. For an increase in 5% of the load from 95 % of the peak load to the peak load, the stress increases by approximately 200%. Even at the peak load, *S22* is relatively less compared to the stress developed at post peak. Even the post peak load, *S22* remains almost equal to zero except near mid-span. This is where the tension bands meet the bottom flange. This behavior is comparable to the stress development in girder G7 (Fig. 5-40). However, this behavior extends over a larger length in G7.

Figure 6-41 shows that, along the bottom flange, the Elements near mid-span are subjected to the largest shear stress and the Elements near the support are subjected to smaller shear stress. The opposite behavior happens at the top flange, where the Elements near the support are subjected to maximum shear near the support and minimum shear near the mid-span of the specimen. This is similar to the behavior of G7. At 95% of the peak load, shear stress *S12* has a maximum value of 18.5 ksi. The pattern of the stress variation is similar to 75% of the peak load. The value of maximum at the peak load increases to 23 ksi and there is only one predominant peak at peak load. As the load increases from 95 % of the peak load to the peak load, the maximum *S12* increases by approximately 25%. This increase is more pronounced at the post peak level. At the post peak load level, the maximum *S12* occurs exactly at the same position as the maximum *S22* (Fig. 6-40). This develops the diagonal tension in the panel.

The von Mises stress *S* (Fig. 6-42), similar the top flange of the Specimen UK6 indicates no yielding of the web top until 95% at the web bottom. In addition, at the peak and post peak load levels, the behavior is very similar to top flange except the fact that

there is yielding near the right end of the panel. In G7, this behavior extended over a larger length.

The behavior of the principal stresses *S1* and *S2* at the bottom flange (Fig. 6-43 and 6-44, respectively) can be related to the behavior at top flange. *S1* follows the curve of *S11* for almost the entire length of specimen and the increase in *S2* near the right end of the panel is due to the increase in *S12* at that location. This behavior is similar to the behavior for G7 at the bottom flange.

6.3.1 Boundary Condition between the Bottom Flange and the Web

A procedure similar to that in Section 6.2.1 is repeated at the bottom flange in this section. Four Elements are selected along the bottom flange to investigate the boundary condition between the bottom flange and the web.

The first, second and third Element are selected at a distance of 12, 157 and 107 inches respectively from the left end of the specimen. The fourth Element is selected at 9 inches from the mid-span, location where the maximum *S22* occurs at the peak load. The definitions SPOS, MID and SNEG are defined in Section 5.2.1. Figure 6-46 shows the location of these Elements. Figures 6-47 through 6-50 shows the variations of *S22* at these Elements as a function of the applied load.

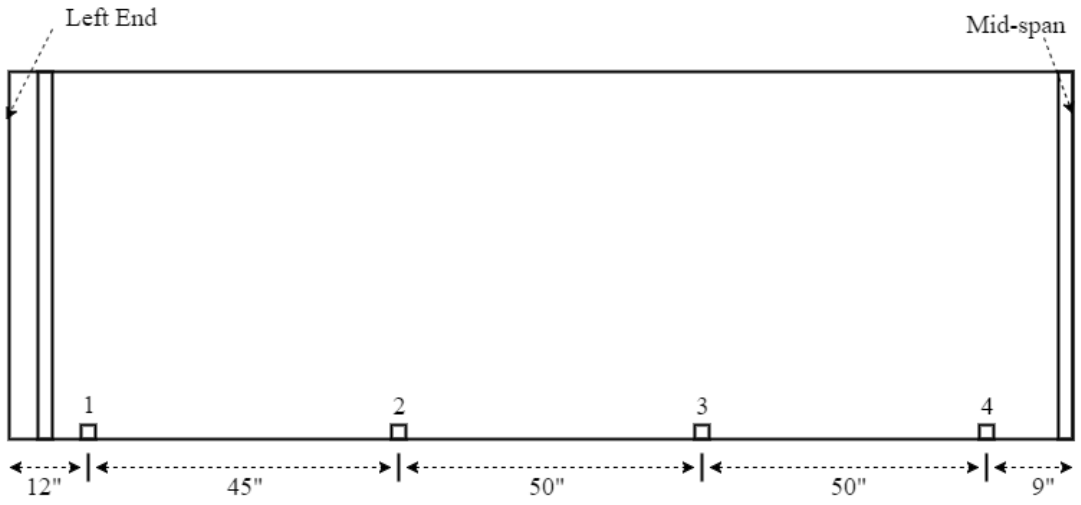

Fig. 6-46. Elements along the web-bottom.

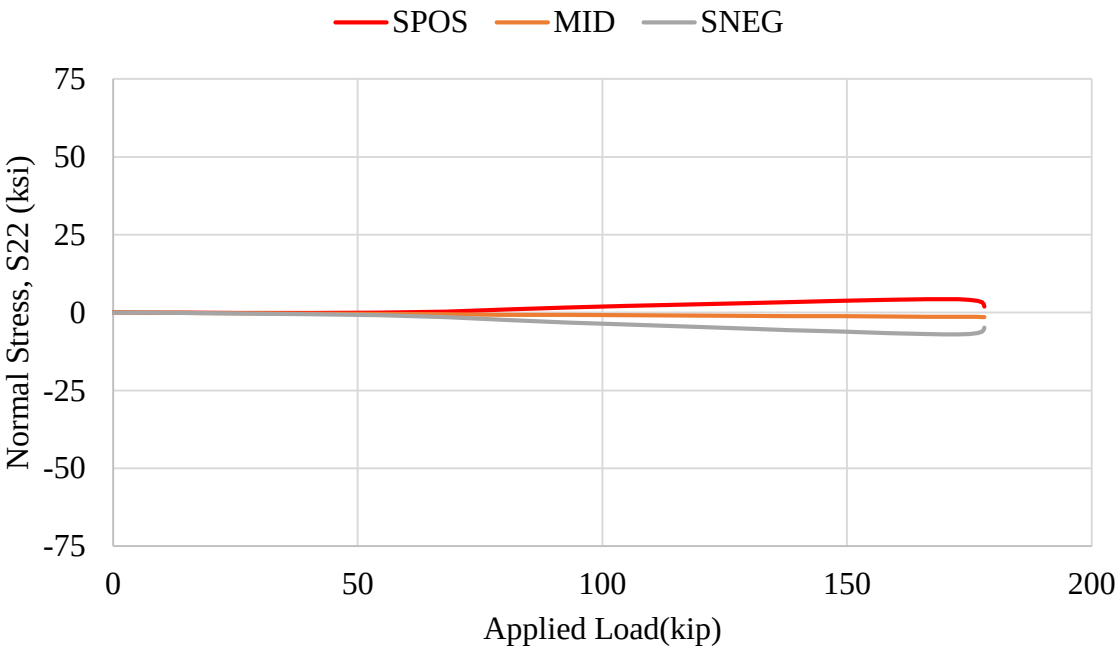

Fig. 6-47. Normal Stress *S22* at top, mid and bottom surface of web versus applied load for Element 1 at the web-bottom.

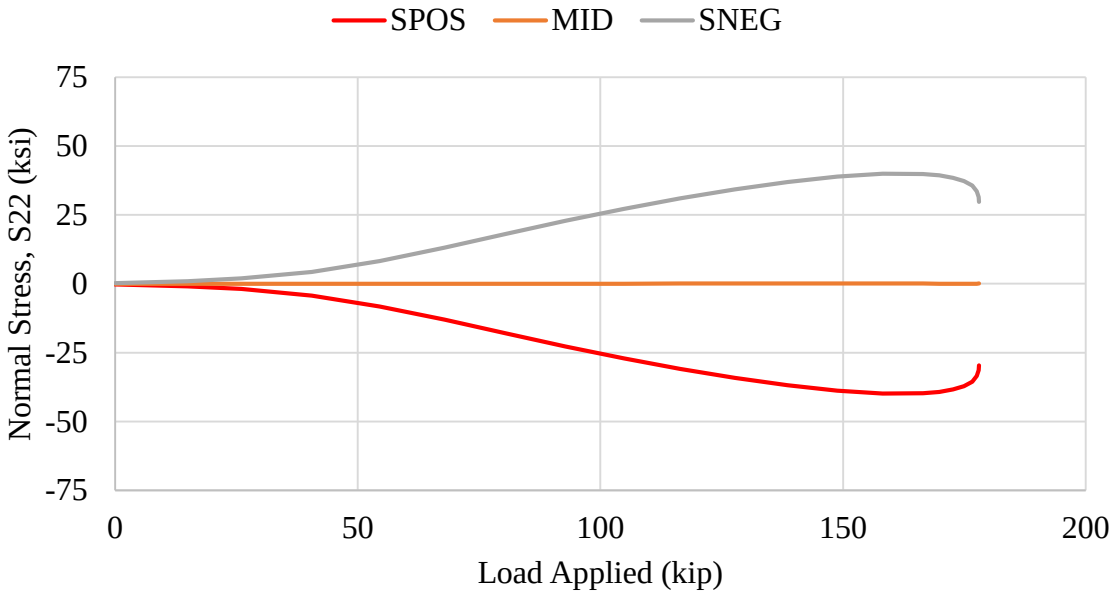

Fig. 6-48. Normal Stress *S22* at top, mid and bottom surface of web versus Load for Element 2 at the web-bottom

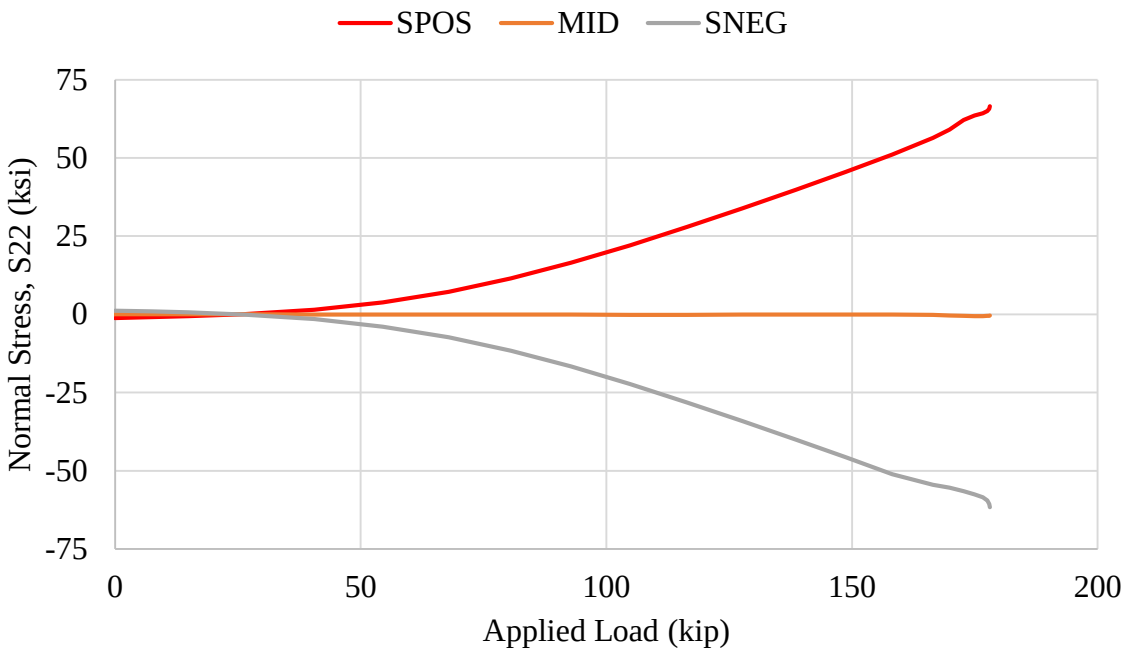

Fig. 6-49. Normal Stress *S22* at top, mid and bottom surface of web versus applied load for Element 3 at the web-bottom

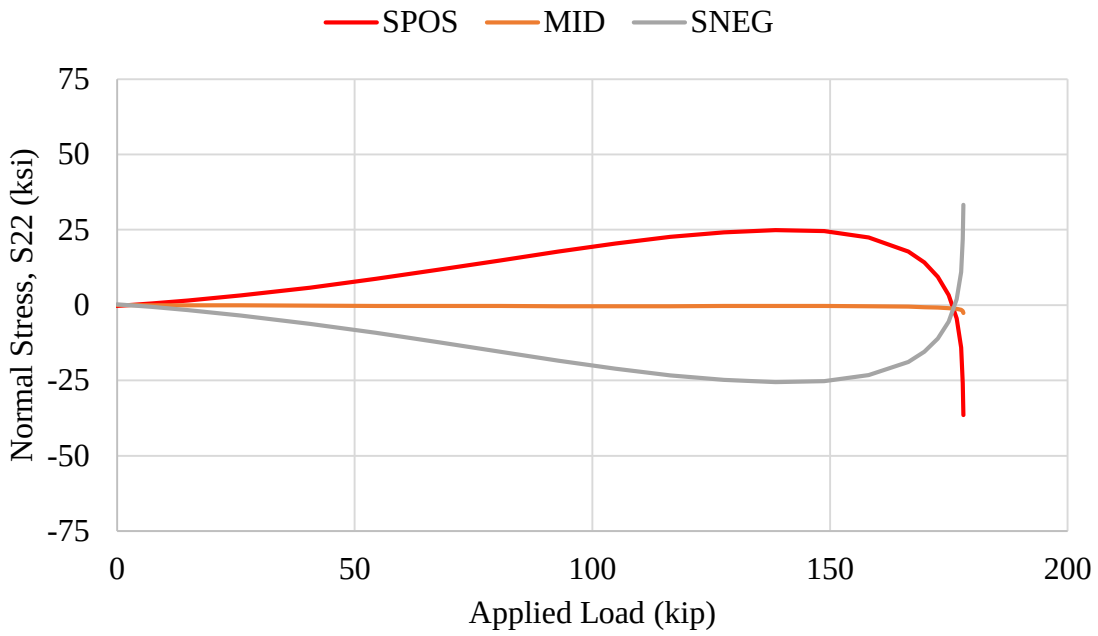

Fig. 6-50 Normal Stress *S22* at top, mid and bottom surface of web versus applied load for Element 4 at the web-bottom.

The *S22* values at the top and bottom surface of the web are smaller for Element 1 compared to Elements 2, 3 and 4, indicating that there is lesser tendency for rotation of the web about the web-flange juncture near the transverse stiffener on the left-hand end of the panel at the bottom-flange. From Fig. 6-40, it is clear that the web membrane force remains essentially at zero until 95% of the peak load but increases slightly at the peak load level. However, *S22* for Element 4 increases significantly at the post peak load level and there is significant pushing and pulling of the top flange in the vicinity of the right-hand end of the panel.

6.4 Stresses at Several Sections Through the Web-Depth

In this section the procedure followed in Section 5.4 is followed for Specimen UK6. The quantities plotted are the web membrane stresses, *S11*, *S22* and *S12*. Figures 6-52

through 6-63 show these quantities, at several sections taken through the web-depth for different levels of loading. The locations of these sections along the web-depth are shown in Fig. 6-51. The first Section is located at 7 inches from the left end of the panel. The second Section is selected at 50 inches from the left free end of the specimen, this is where maximum *S11* occurs at the peak load. The third Section is selected at the mid-length of the panel and the fourth Section is selected at 7 inches from the right end of the panel.

To simplify the plots, the normalized position along the web-depth is employed. The position 0.0 denotes the web bottom and 1.0 denotes the web top. Position 0.5 is located at the web mid-depth. The normalized position is plotted as the ordinate, emphasizing the fact that these section cuts are vertical rather than horizontal.

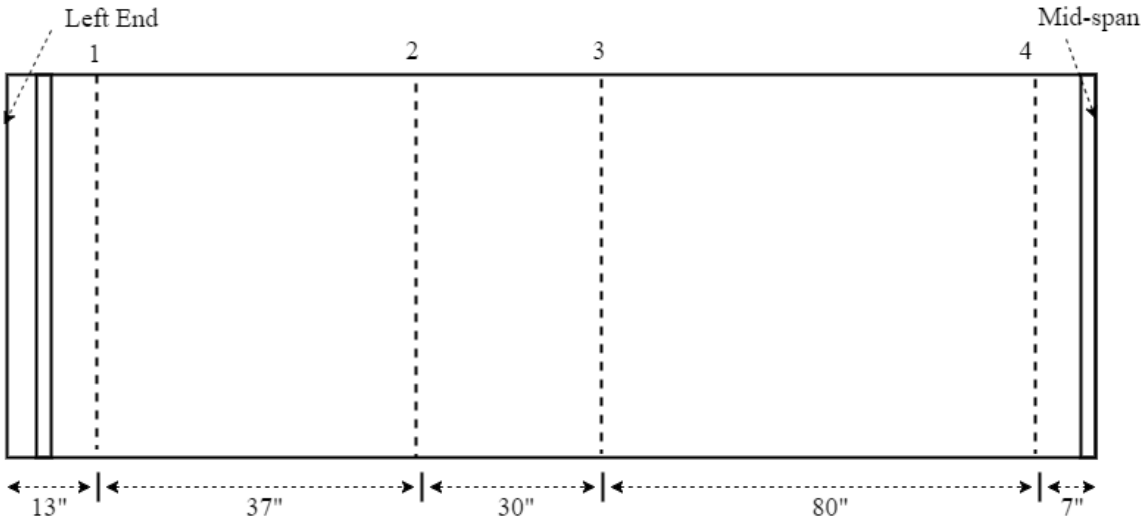

Fig. 6-51. Sections along the web-depth.

1. Stresses at Section 1

This Section is cut at 7 inches from the left end of the panel.

The normal stress *S11* (Fig. 6-52) relatively small up to 75% of the peak load. However, at loadings at and above that load level, significant diagonal tension is developing near the transverse stiffener. This increase in normal stress is located more in the top half of the

web. At post peak, a significant amount of diagonal tension is developed in the Section. The compressive values at the web bottom are due to the local effects of the reaction at supports.

The normal stress *S22* (Fig. 6-53) is relatively small at the top of the web until almost 75% of the peak load, and it increases considerably at the peak and the post peak load levels. The stress *S22* at bottom is close to zero.

The shear stress *S12* (Fig. 6-54) does not increase much at the web bottom after 50% of the peak load. However, *S12* increases at top of the web. This is because of the web buckling which causes increases in *S12* at top of the web in the vicinity of Section 1. *S12* decreases at the web bottom at the post peak load level.

The behavior at this Section is very similar to behavior at Section 1of girder G7.

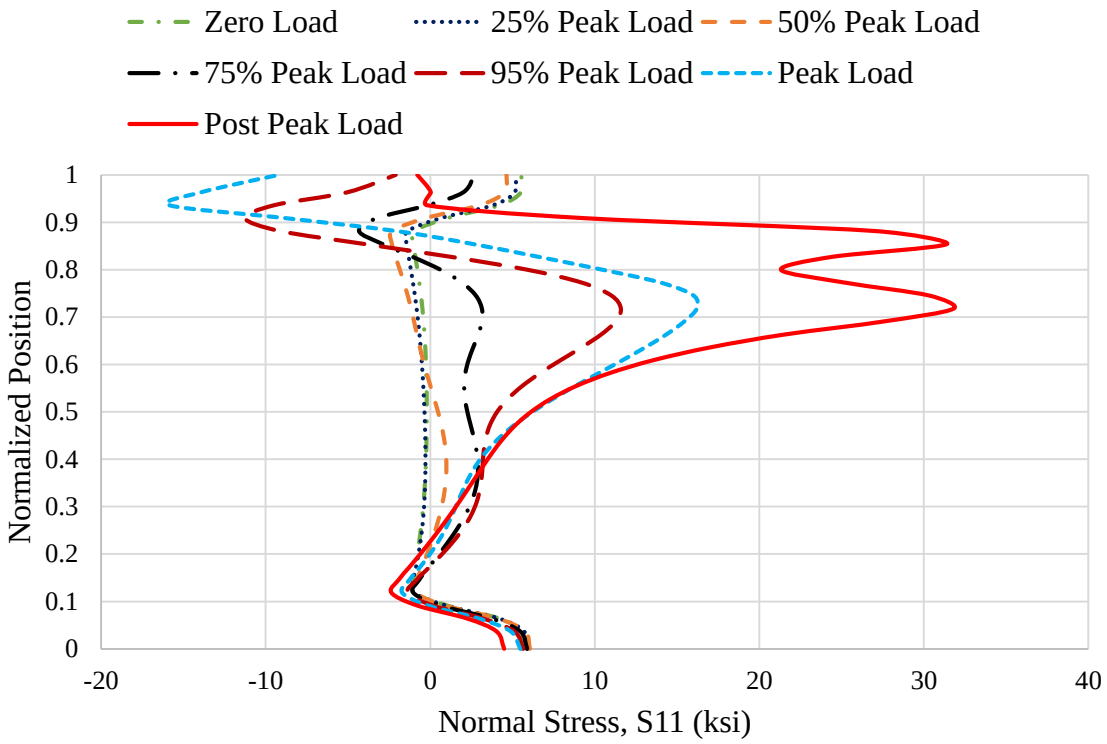

Fig. 6-52. Normalized position versus normal stress *S11* at Section 1.

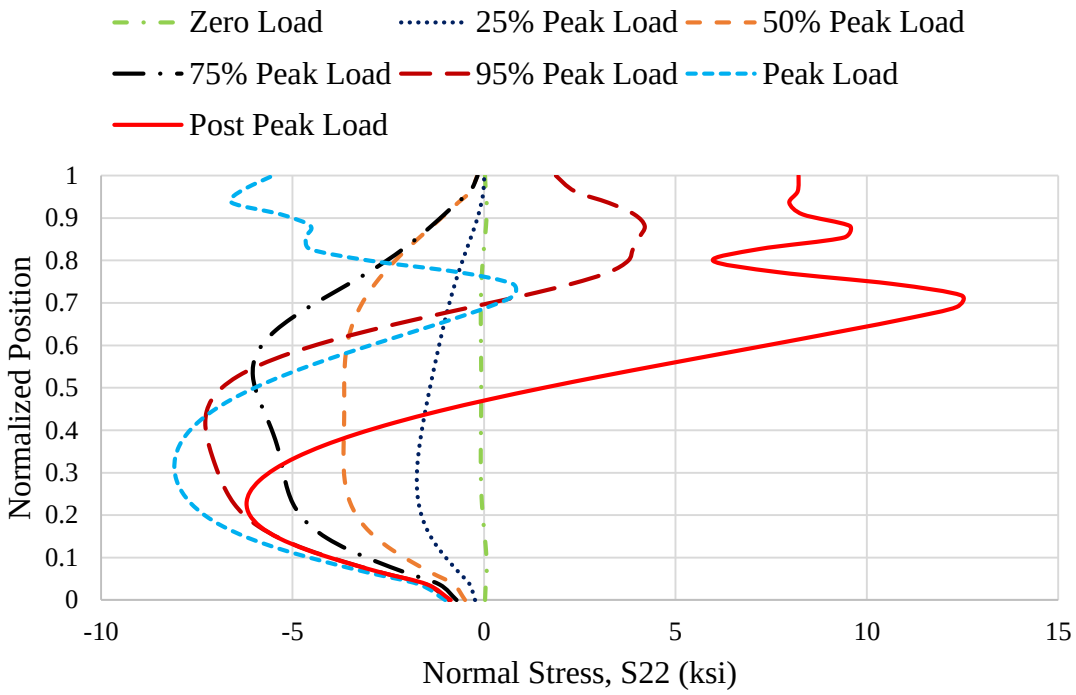

Fig. 6-53. Normalized position versus normal stress *S22* at Section 1.

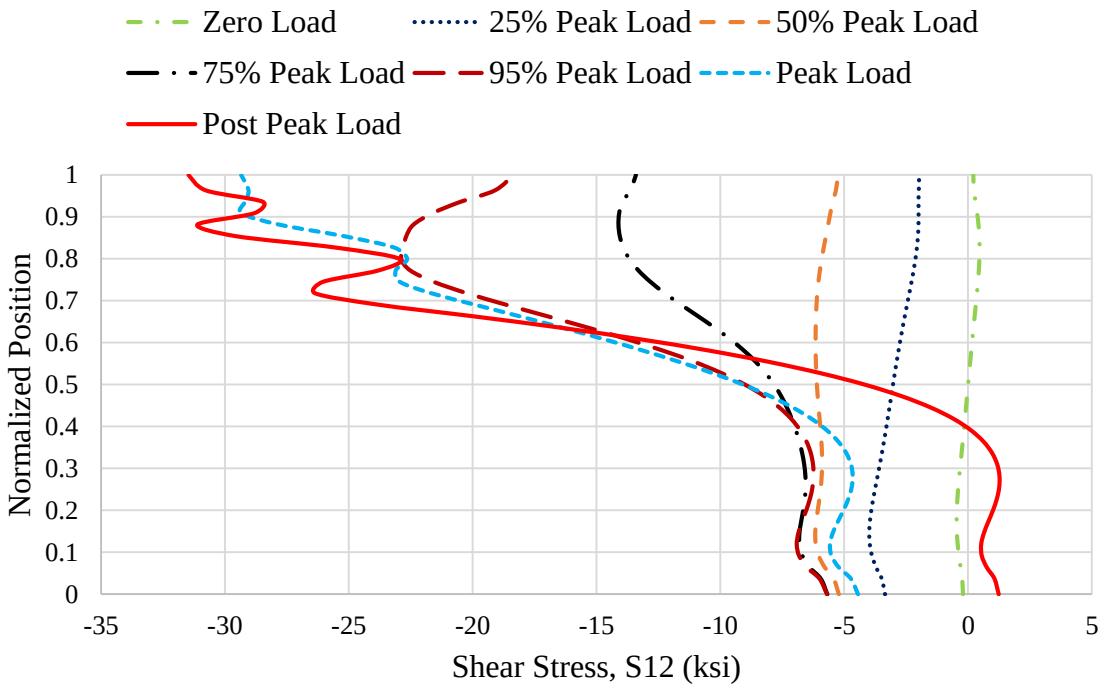

Fig. 6-54. Normalized position versus shear stress *S12* at Section 1.

2. Stresses at Section 2

This Section is located at 50 inches from the left-hand free end of the specimen.

The normal stress *S11* (Fig. 6-55) is caused by both the diagonal tension and the flexural stresses at Section 2. At the mid-depth *S11* due to flexure is zero and we can clearly see considerable diagonal tension forming even at 75% of the peak load. However, as the loading is increased further, *S11* increases at a higher rate.

S22 is almost zero at top and bottom of the web for all the levels of loadings.

The shear stress *S12* (Fig. 6-57) at the web top is more than the *S12* at the bottom. This is because this Section is closer to the left end of the panel. However, this behavior is much more pronounced in Section 1 (close to the left panel).

This behavior is similar to behavior of Section 2 in girder G7.

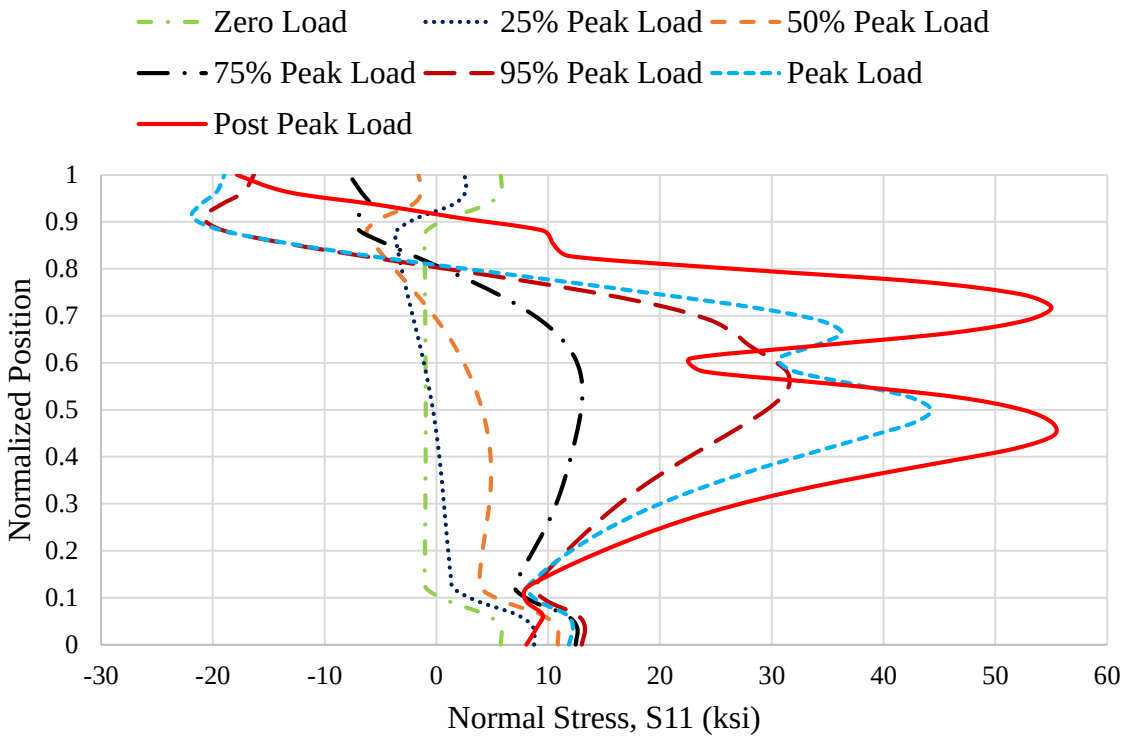

Fig. 6-55. Normalized position versus normal stress *S11* at Section 2.

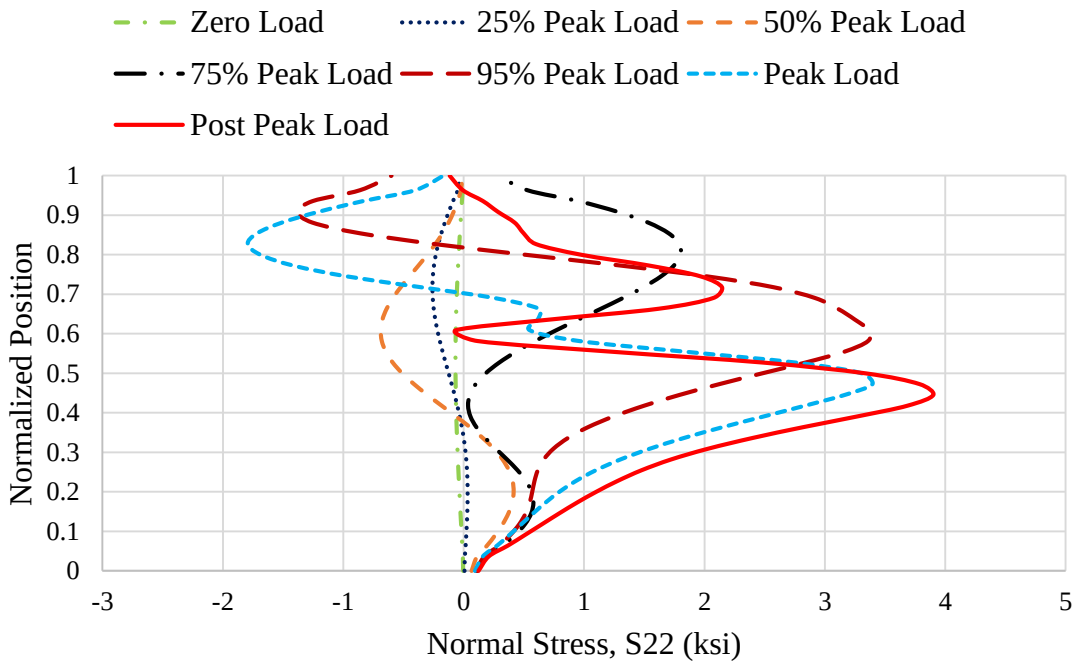

Fig. 6-56. Normalized position versus normal stress *S22* at Section 2.

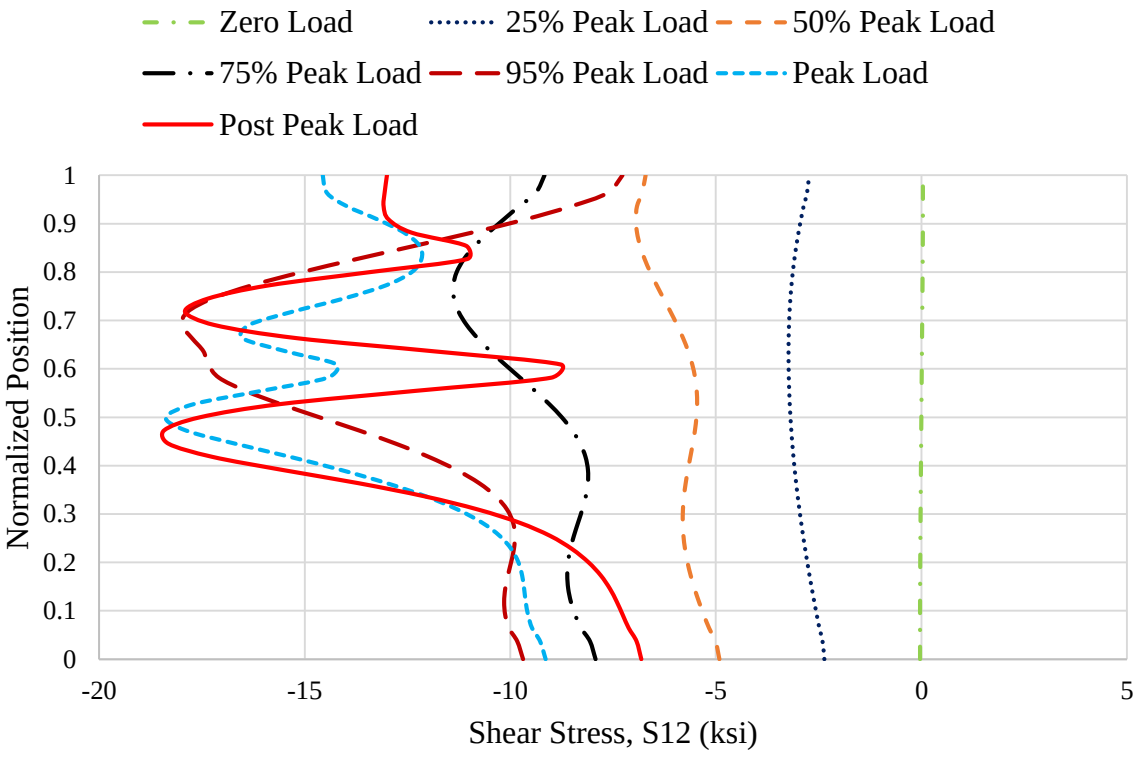

Fig. 6-57. Normalized position versus shear stress *S12* at Section 2.

3. Stresses at Section 3

This Section is located at the mid-length of the panel.

The behavior of *S11* in Section 3 is similar to the behavior in Section 2. However, diagonal tension at 75% of the peak load is higher for Section 3.

Similar to Section 2, the normal stress *S22* is almost zero at both the top and bottom of the web.

The shear stress *S12* follows the behavior of *S12* at Section 2 until about 95% of the peak load. At post peak load, *S12* is bottom at larger than at top.

This behavior is similar to the behavior of Section 2 of girder G7.

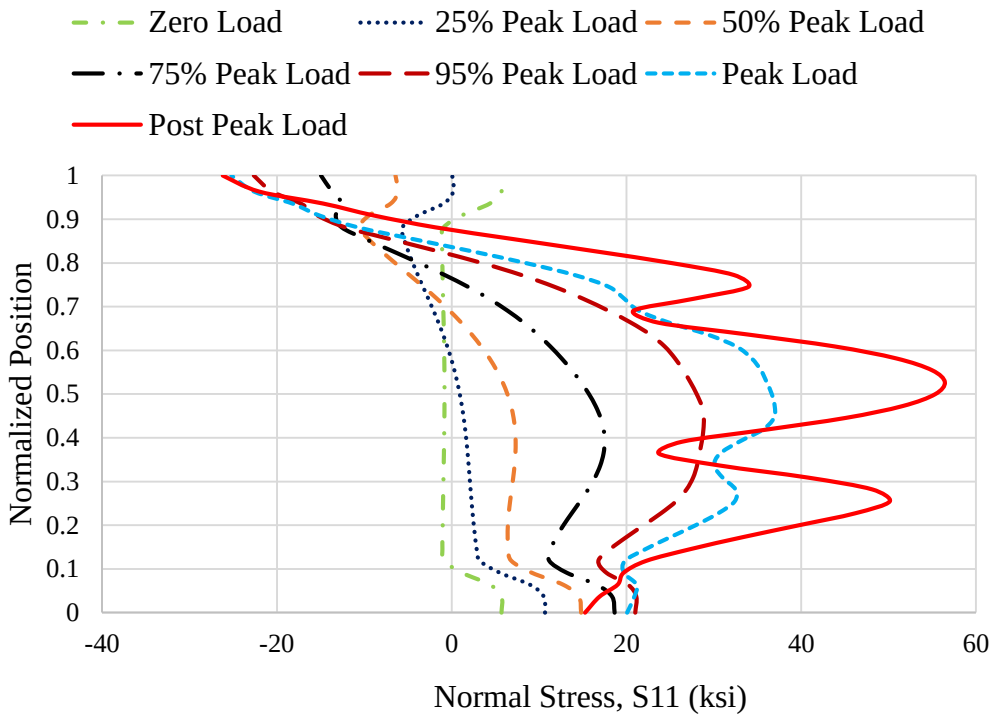

Fig. 6-58. Normalized position versus normal stress *S11* at Section 3.

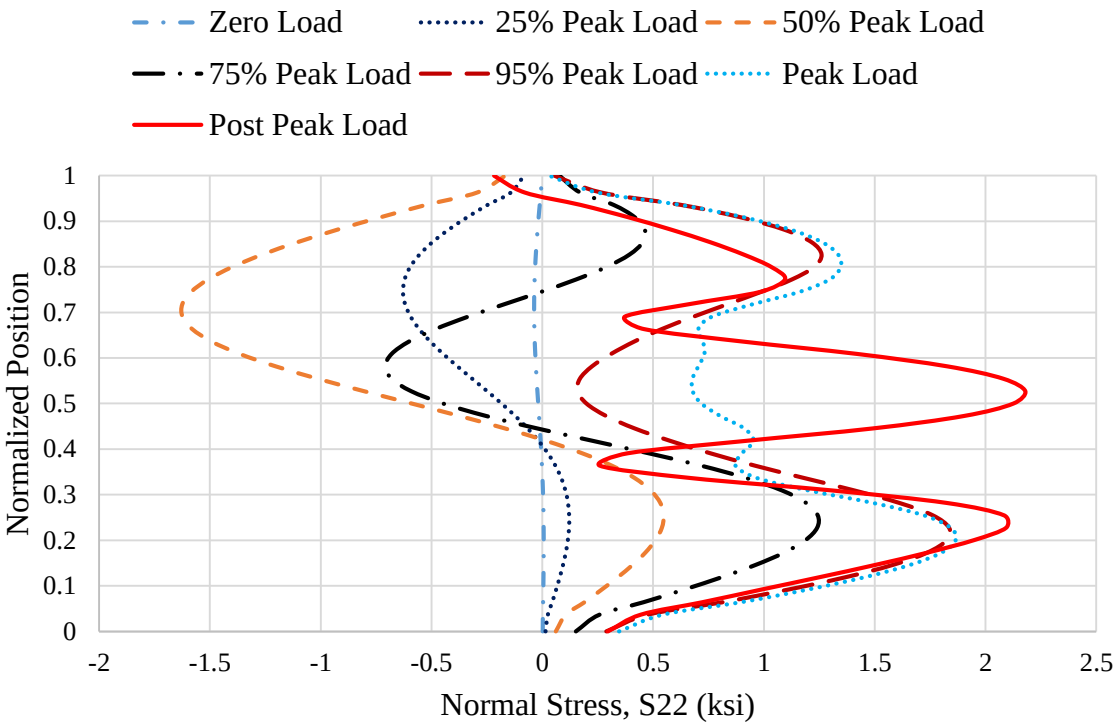

Fig. 6-59. Normalized position versus normal stress *S22* at Section 3.

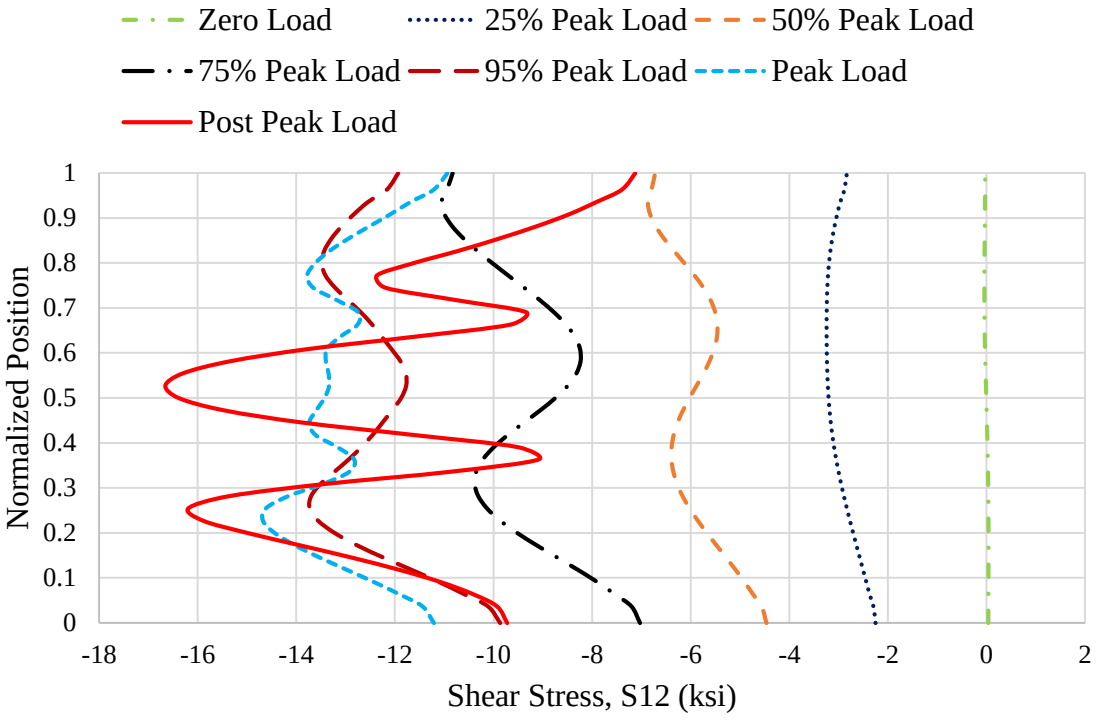

Fig. 6-60. Normalized position versus shear stress *S12* at Section 3.

4. Stresses at Section 4

This Section is located at 7 inches from the right end of the panel.

The normal stress *S22* (Fig. 6-62) increases at the mid-depth of the web at this Section. This is due to the presence of the applied compressive load at the mid-span. However, there is considerable increase after the peak load is reached.

The shear stress *S12* (Fig. 6-63) is largely unchanged at the web top after the 25% of the peak load. However, *S12* increases significantly at bottom of the web. This is because of the web buckling of the web which causes an increase in *S12* at bottom of the web in the vicinity of Section 4. This behavior is similar to the behavior of Specimen G7 at Section 3 (near the right end of the panel).

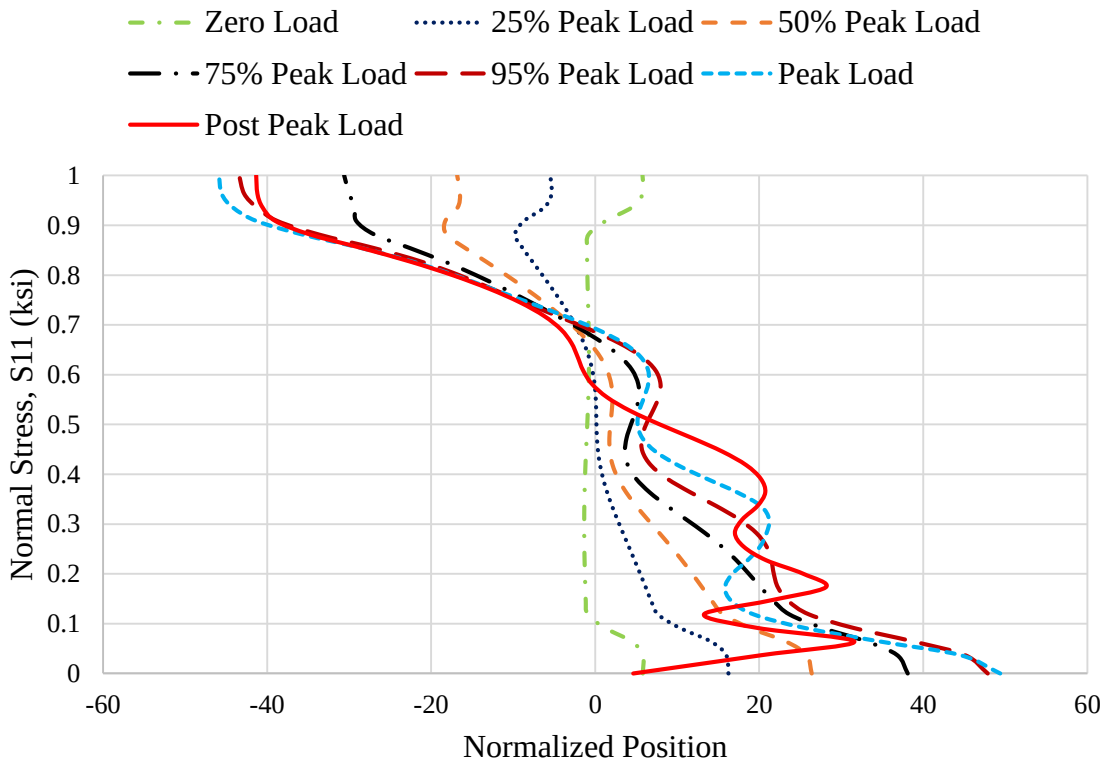

Fig. 6-61. Normalized position versus normal stress *S11* at Section 4.

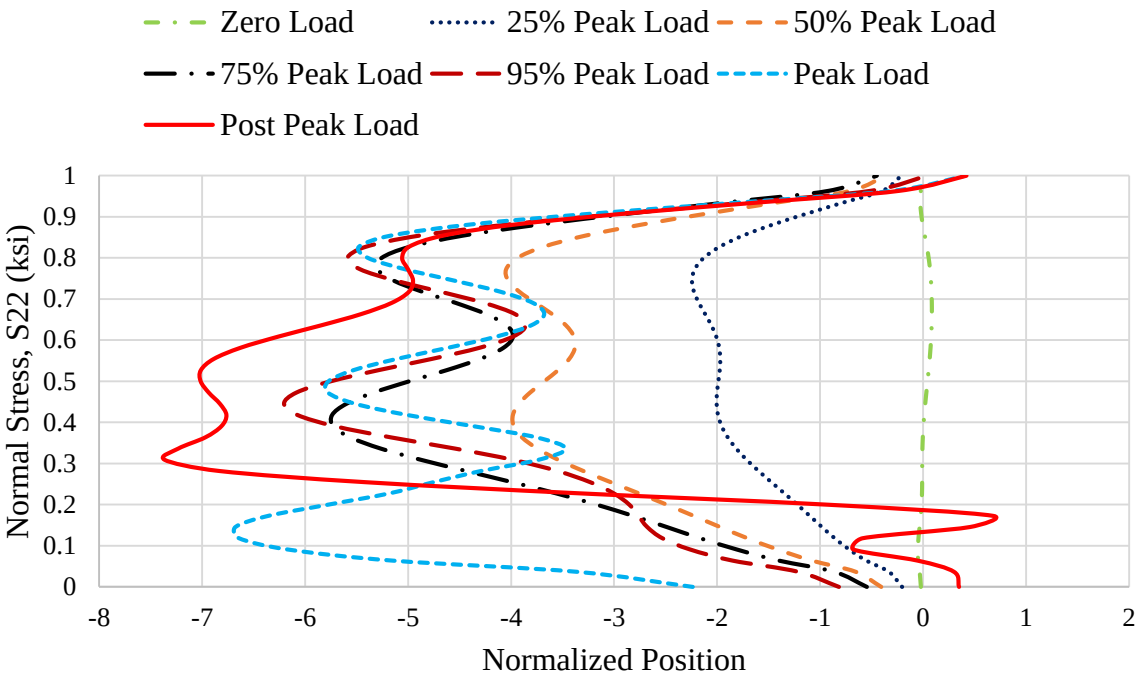

Fig. 6-62. Normalized position versus normal stress *S22* at Section 4.

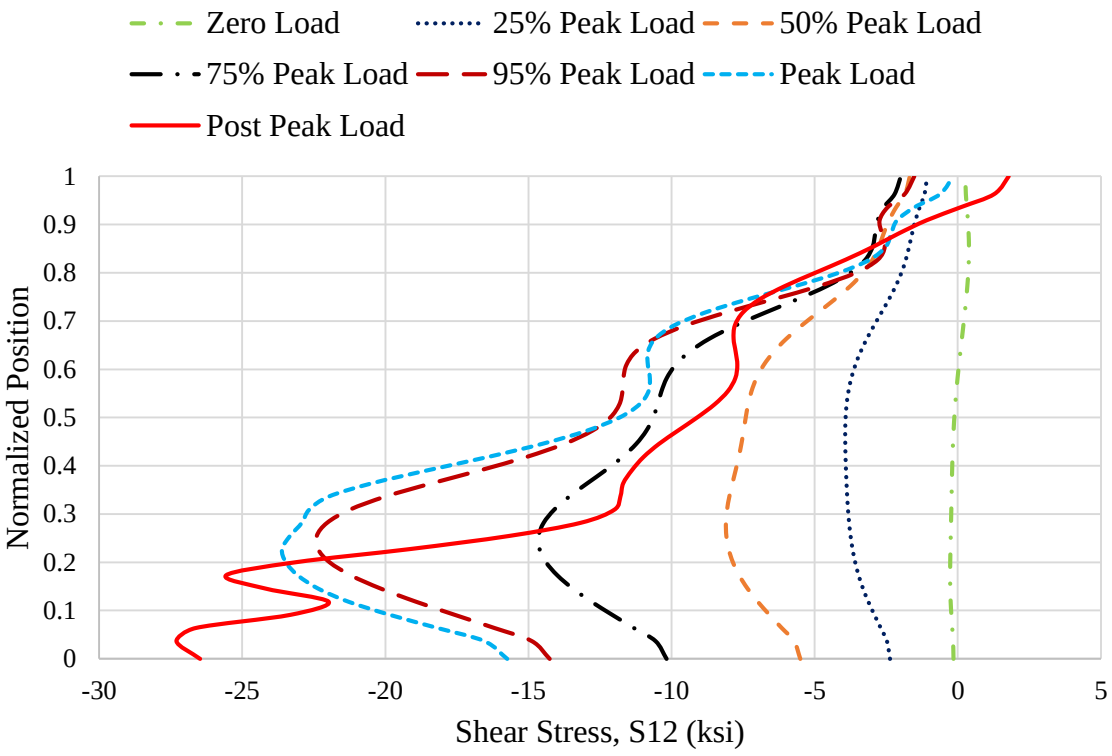

Fig. 6-63. Normalized position versus shear stress *S12* at Section 4.

6.5 Comparison of Results from Simulation and Theory

A procedure similar to Section 5.5.1 is repeated for Specimen UK6.

6.5.1 Stress Variations along the Length

The quantities plotted in this section are *S11* at the web top and bottom, flange stress *S11* at top and bottom flange and *S12* at the web top, mid-depth and web bottom. Figures 6-64 through 6-72 show the variation of these quantities, in that order at a section along the length.

S11 at the top of the web drops near the left end of the panel. This is where the buckled web meets the top flange. The web stress state at the peak load is used up by the shear actions near the left panel. The difference between results from theory and simulations for the rest of the left-side of the web is due to the web acting like a Pratt truss and thus inducing some compression in the top and bottom chords (flanges in this case).

Similar behavior occurs at the bottom flange. However, the drop in *S11* is near the right end of the panel and the drop is much more pronounced at the bottom flange. This is because there is extensive yielding of the web bottom at the peak load due to the interaction of shear, flexural tension and plate bending. Near the left end of the panel, the flexural stresses are small due to the small moment.

The normal stress *S11* on both top and bottom flange (Fig. 6-66 and 6-67, respectively) drops below the theoretical stress even at 50% of the peak load and there is some additional compressive stress acting in the flanges. Theoretically, there should be no difference between the results from simulations and beam theory. However, due to the anchorage of the longitudinal force, N_h, given by Eq. 1-15, there is additional compressive stresses in the flanges.

S11 along the top and bottom flange at the peak load also indicate that there is a large additional compressive stress (deviation from theoretical results) acting on the flanges.

S12 at the web top follows the expected trend, i.e., *S12* maximum near the left end of the panel and minimum near the right end of the panel. However, at the web bottom, *S12* is maximum near the right end of the panel and minimum near the right end of the panel.

S12 at the web mid-depth is a reasonable predictor of the results obtained from simulations. There is some oscillatory nature in the shear stresses and the there is one peak at the peak load near the left end of the panel.

The behavior of all these stresses are very similar to the behavior of girder G7 (Figs. 5-60 through 5-68). However, due to higher *a/h* than G7, the behavior is much more cyclic for UK6.

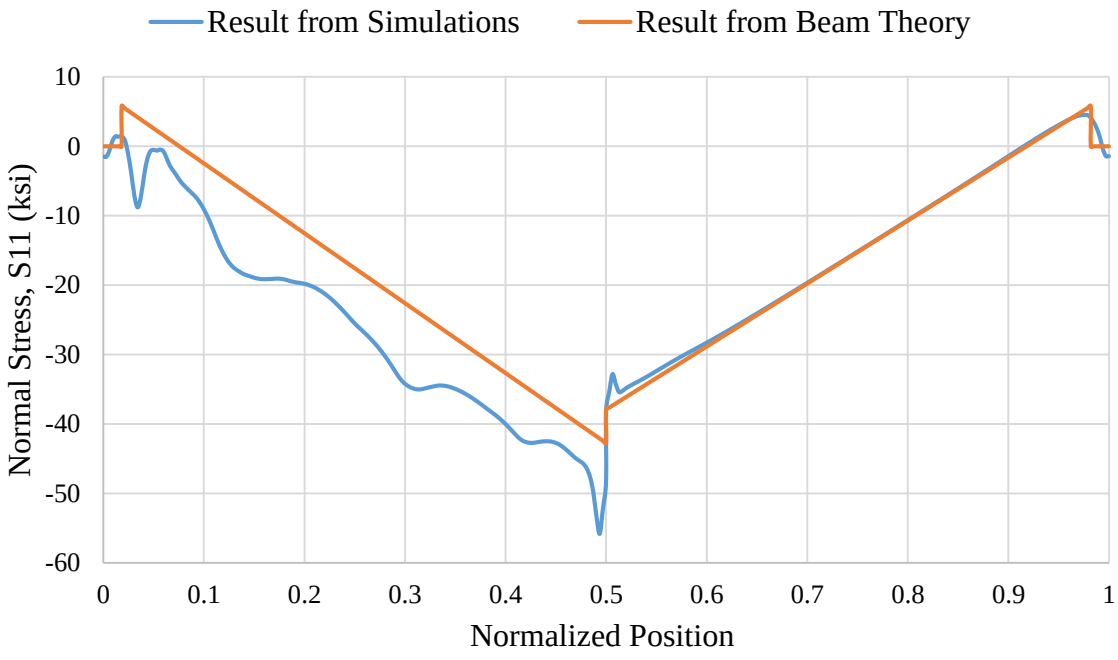

Fig. 6-64. Normal stress *S11* at the peak load versus normalized position at web top.

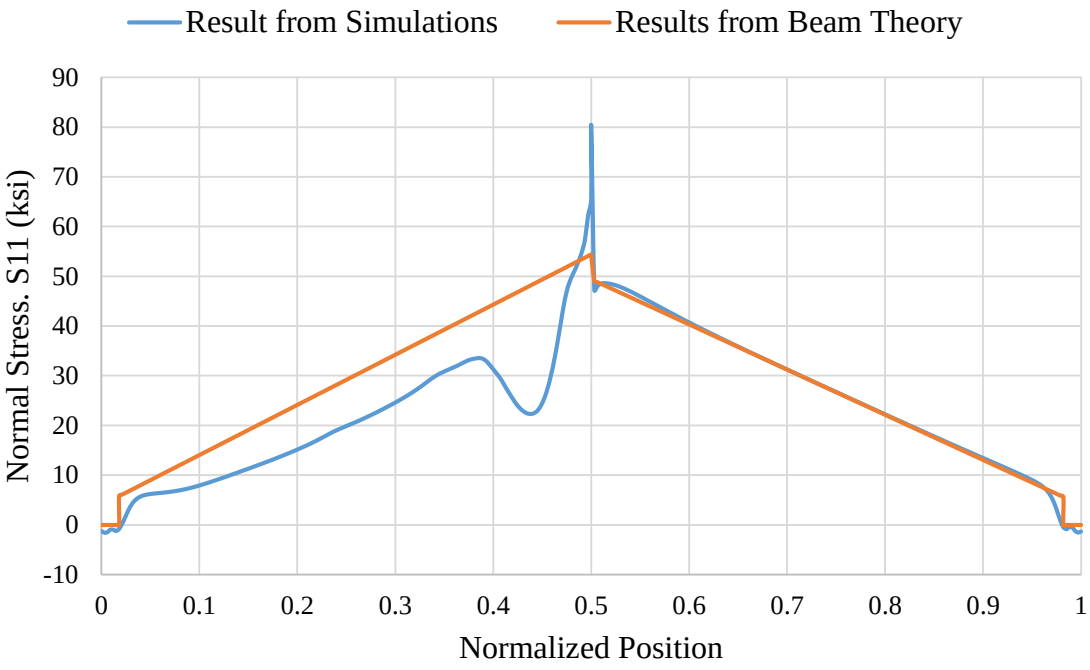

Fig. 6-65. Normal stress *S11* at the peak load versus normalized position at web bottom.

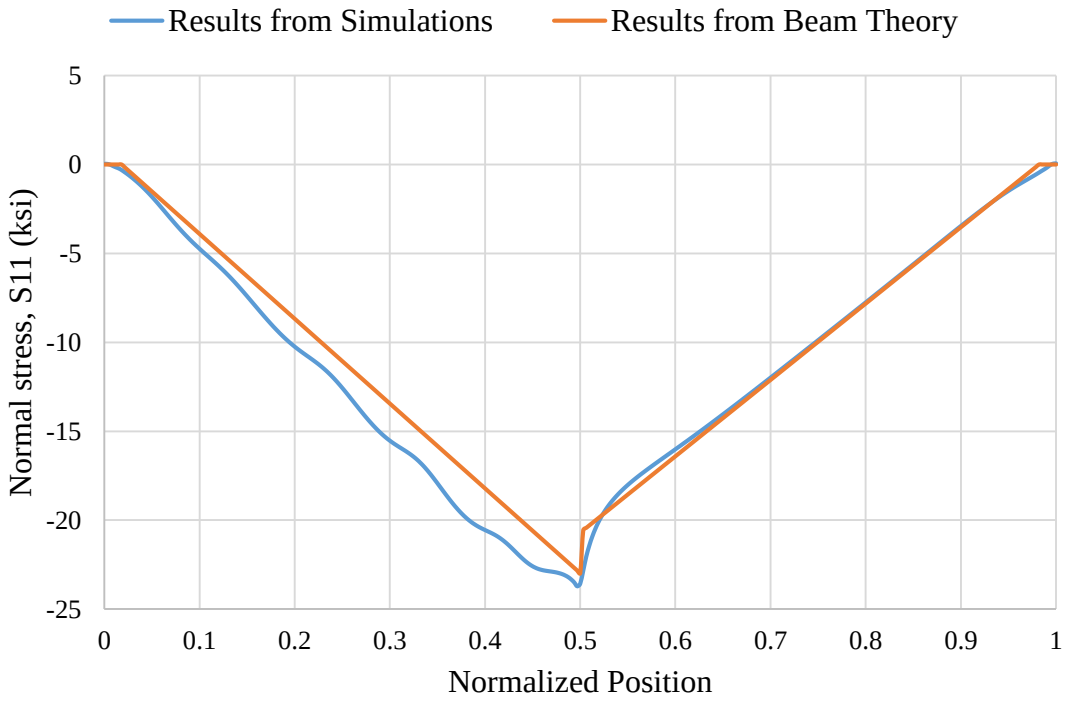

Fig. 6-66. Normal stress *S11* at 50% of the peak load versus normalized position at top flange.

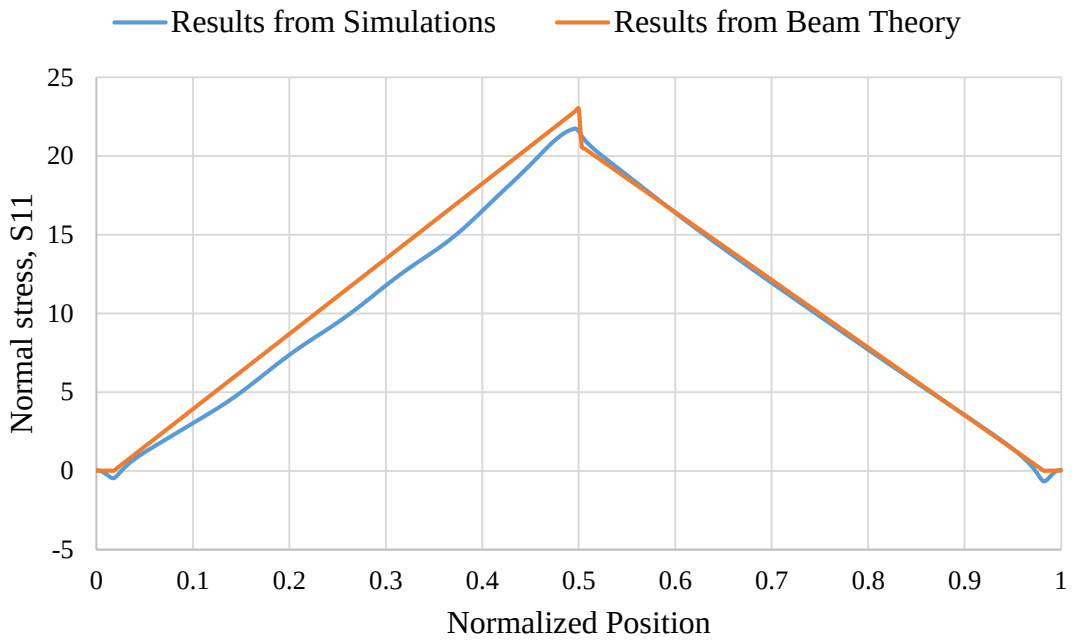

Fig. 6-67. Normal stress *S11* at 50% of the peak load versus normalized position at bottom flange.

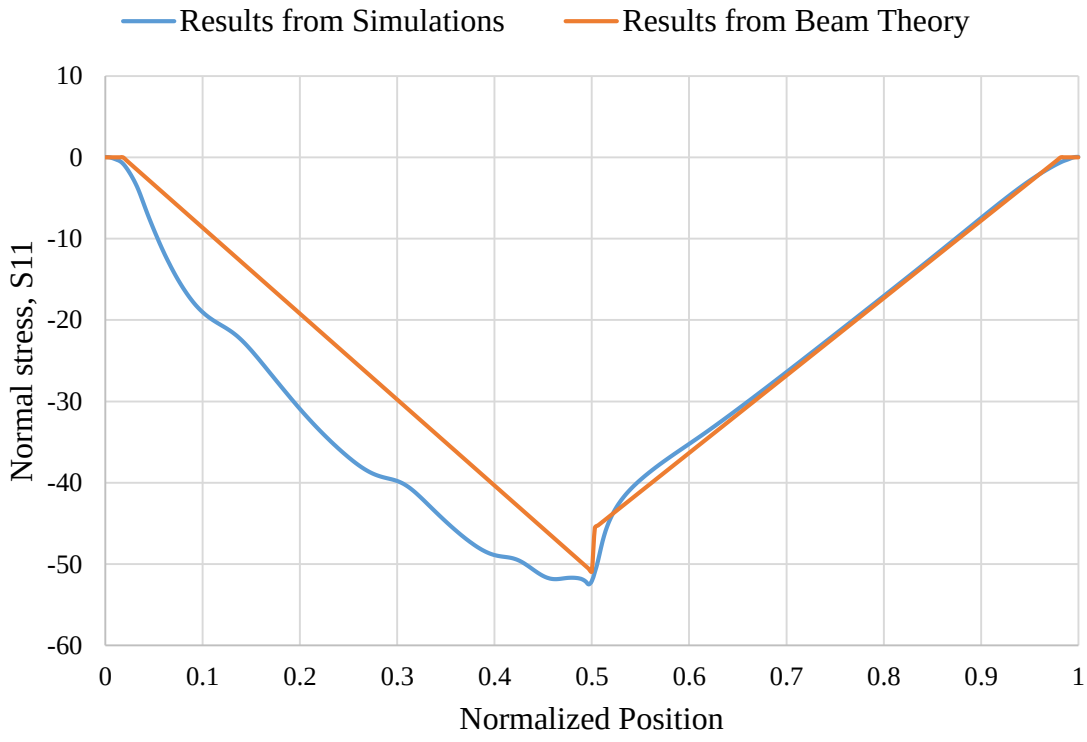

Fig. 6-68. Normal stress *S11* at the peak load versus normalized position along top flange.

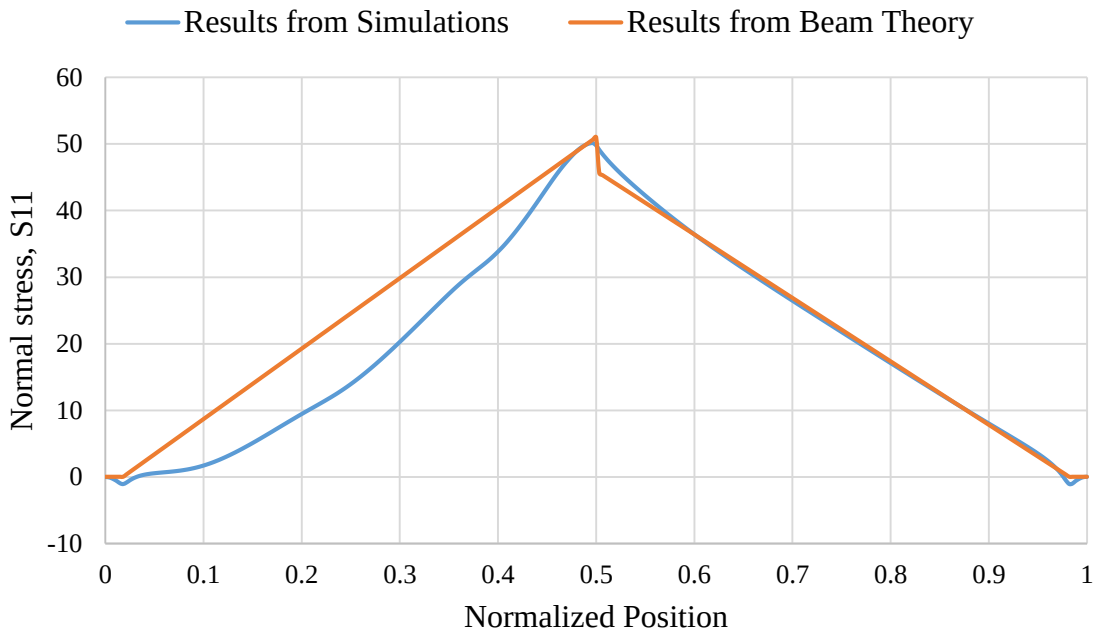

Fig. 6-69. Normal stress *S11* at the peak load versus normalized position along top flange.

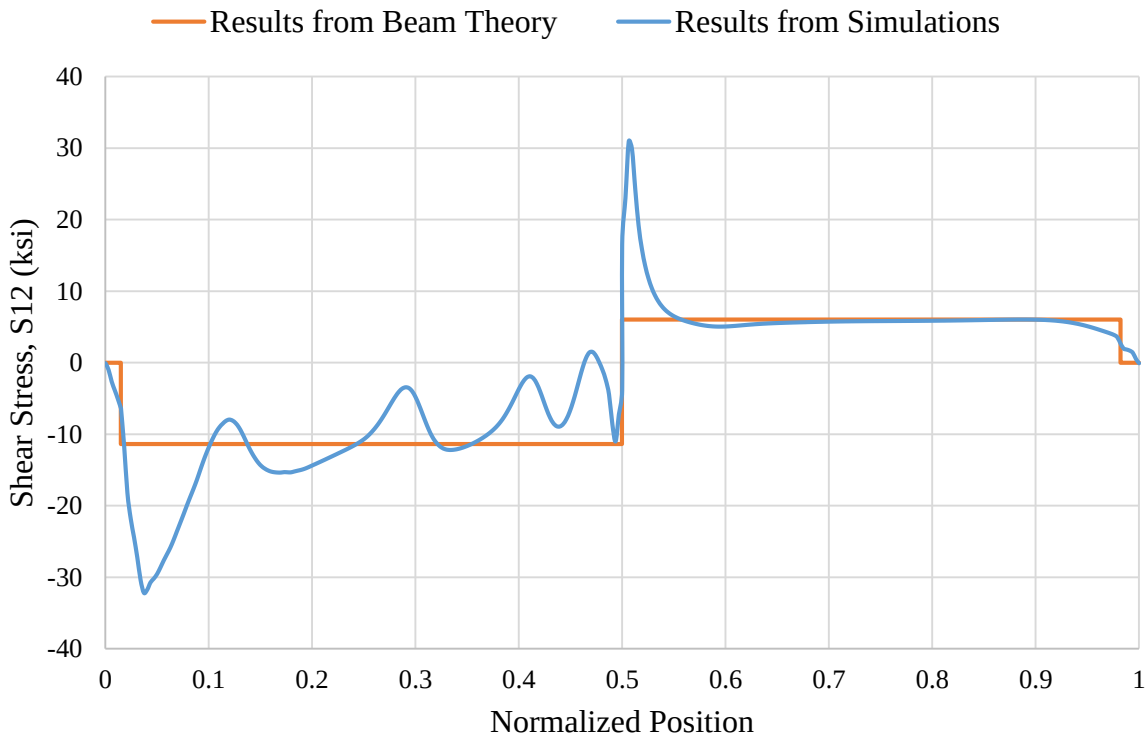

Fig. 6-70. Shear stress *S12* at the peak load versus normalized position at web top.

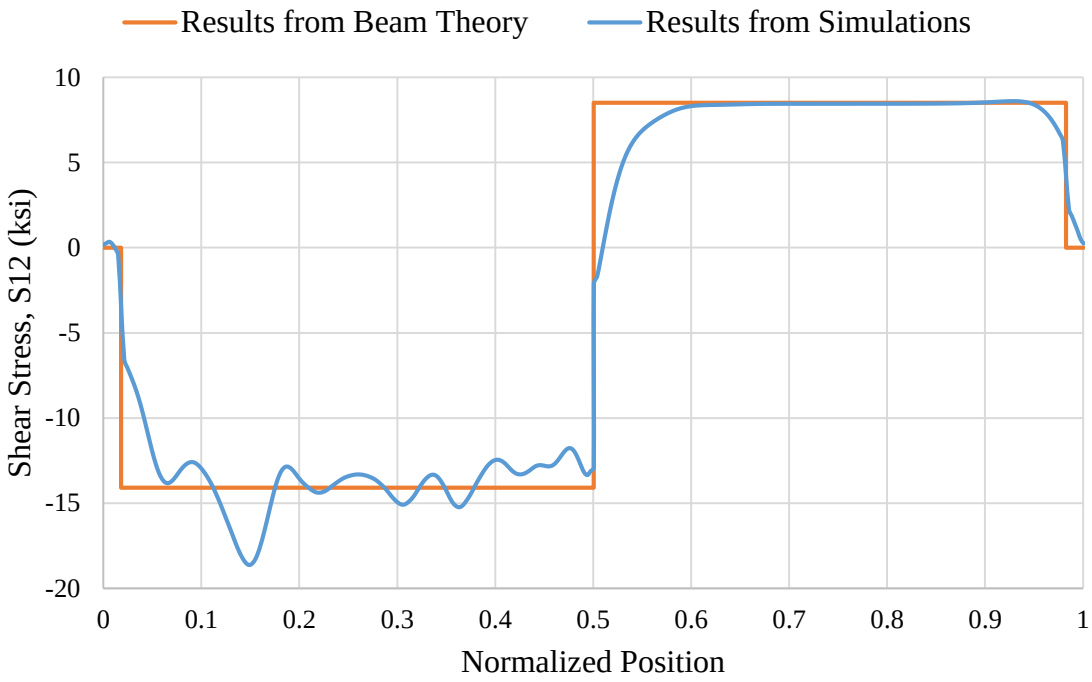

Fig. 6-71. Shear stress *S12* at the peak load versus normalized position at web mid-depth.

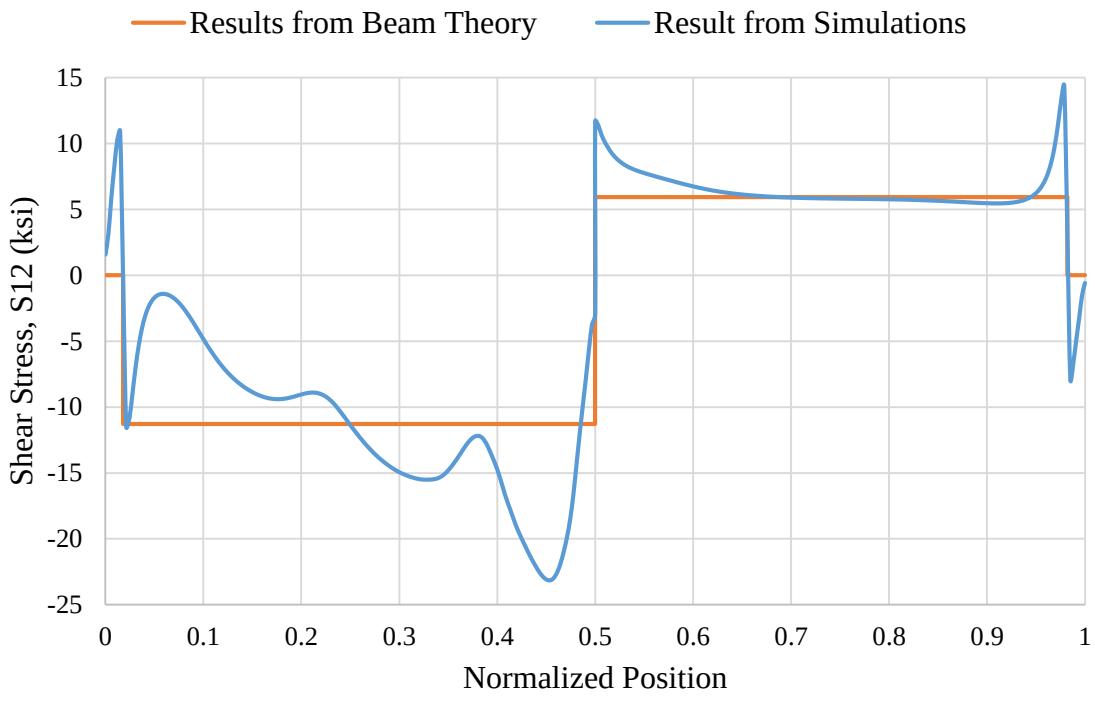

Fig. 6-72. Shear stress *S12* at the peak load versus normalized position at web bottom.

6.5.2 Stress Variations through the Web-Depth

The locations of Sections employed for this study are already explained in Section 6.4. The quantities plotted in this section are *S11* and *S12* at Sections 1, 2, 3 and 4. Figures 6-73 through 6-80 show the variation of these quantities, in that order, at a section along the web-depth. The ordinate is the same as employed in Section 6.4, i.e., normalized position. This procedure is similar to the procedure used in the Section 5.5.2. In the theoretical normal stresses, the specified residual stress is included.

S11 at Section 1 develops significant diagonal tension at the top half of the web. At Section 2 and 3, almost the entire section is under diagonal tension. However, this diagonal tension is maximum at the web mid-depth and minimum at web and flange juncture. Of all the four Sections selected for study, Section 4 develops the least diagonal tension and most closely follows the theoretical equations.

S12 is significantly different from the results obtained from theory. At Section 1, the top half of the web has higher stress and at Section 4, the bottom half of the web has higher stress. The deviation in *S12* at Section 2 and 3 from the beam theory is not much when compared with Section 1 and 4.

Section 1 is similar to Section 1 of Specimen G7, Section 4 is similar to Section 3 of Specimen G7 and Section 2 and 3 of Specimen UK6 behaves somewhat similar to Section 2 of Specimen G7.

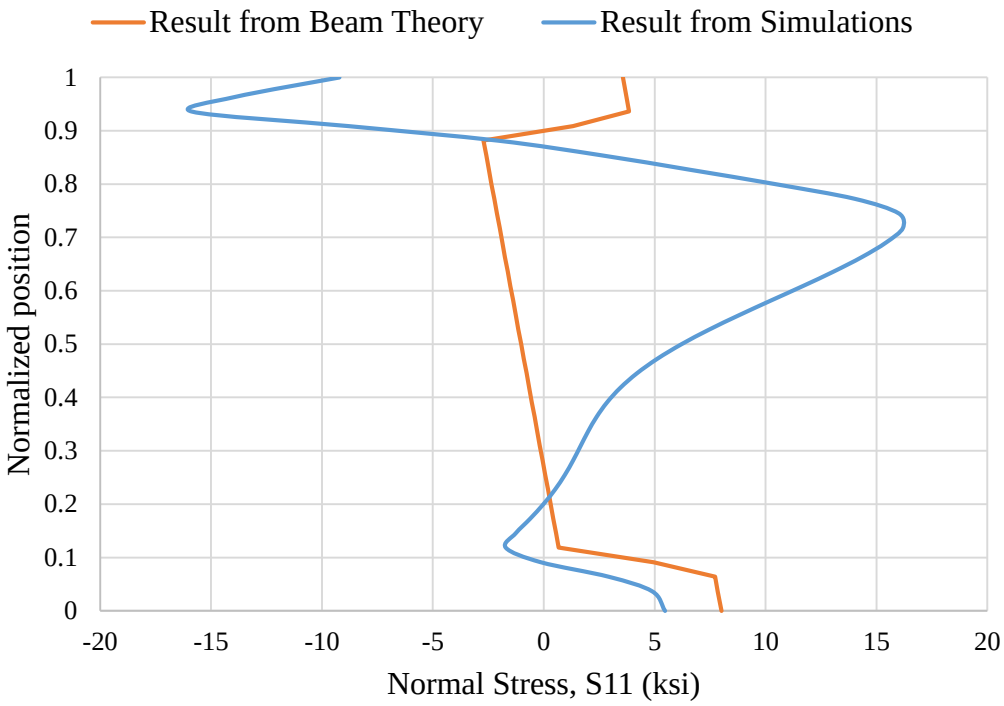

Fig. 6-73. Normalized position versus normal stress *S11* at the peak load at Section 1.

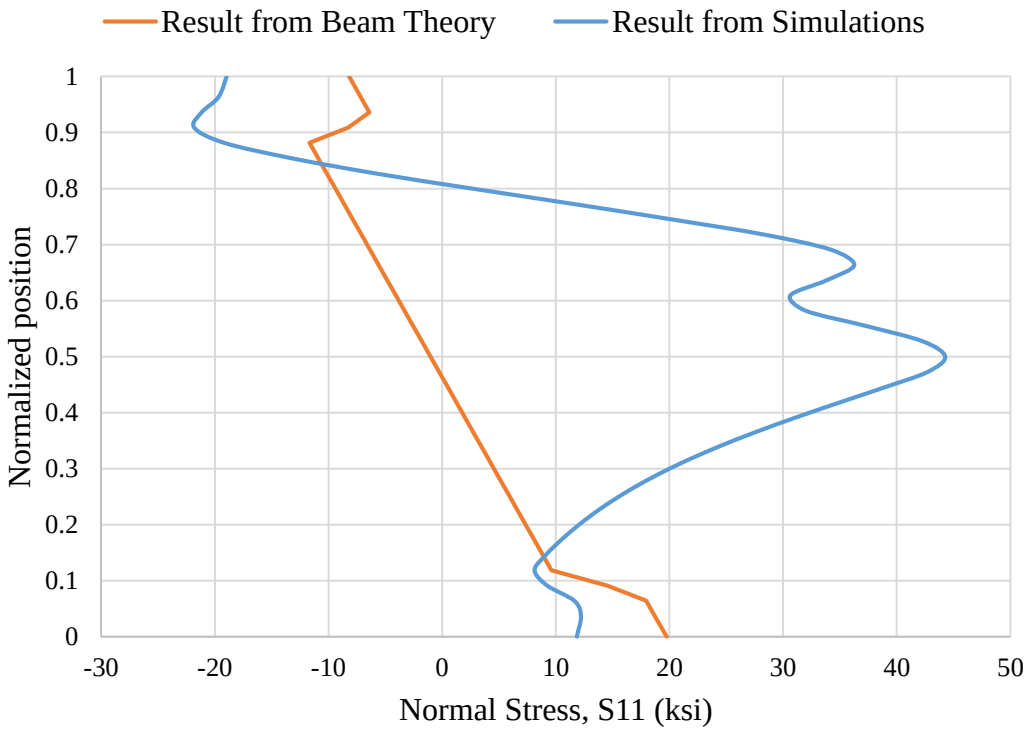

Fig. 6-74. Normalized position versus normal stress *S11* at the peak load at Section 2.

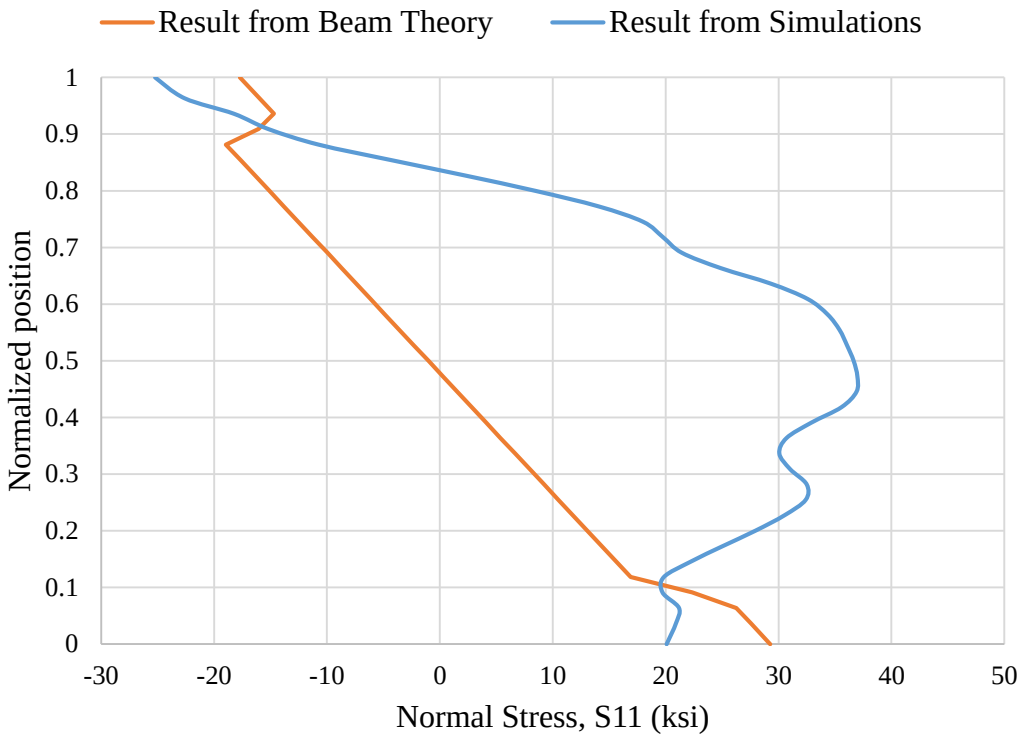

Fig. 6-75. Normalized position versus normal stress *S11* at the peak load at Section 3.

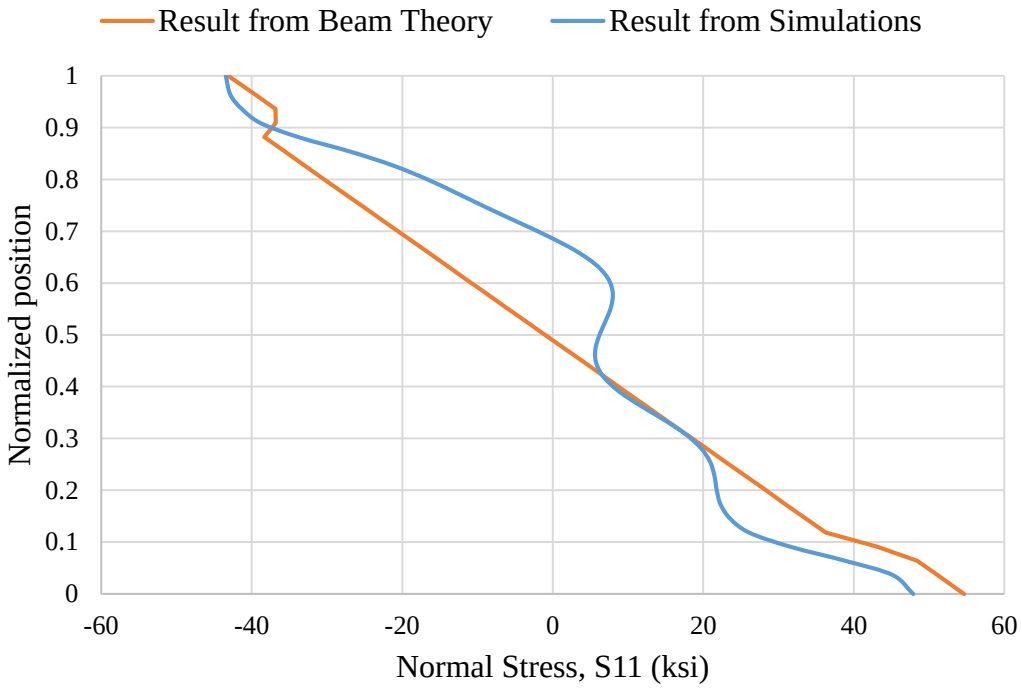

Fig. 6-76. Normalized position versus normal stress *S11* at the peak load at Section 4.

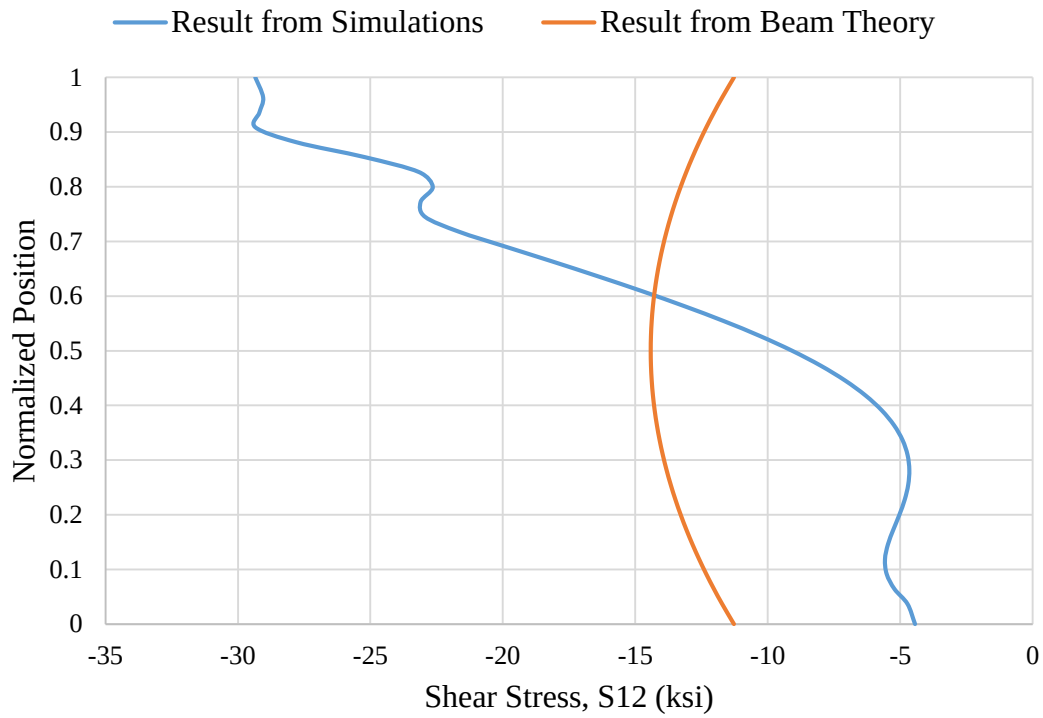

Fig. 6-77. Normalized position versus shear stress *S12* at the peak load at Section 1.

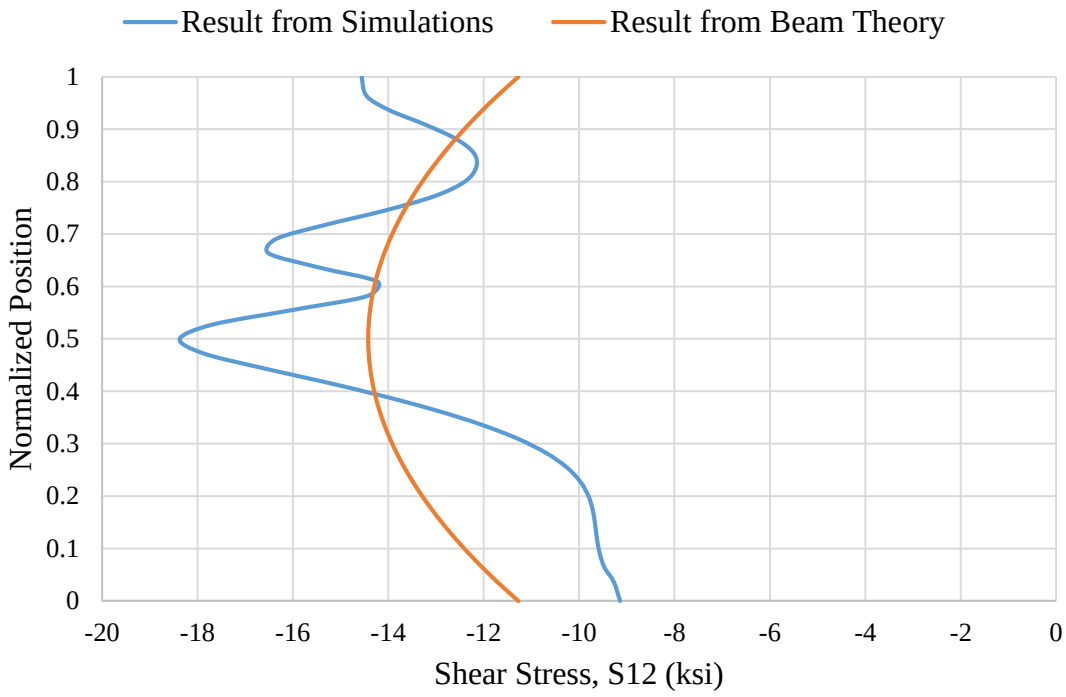

Fig. 6-78. Normalized position versus shear stress *S12* at the peak load at Section 2.

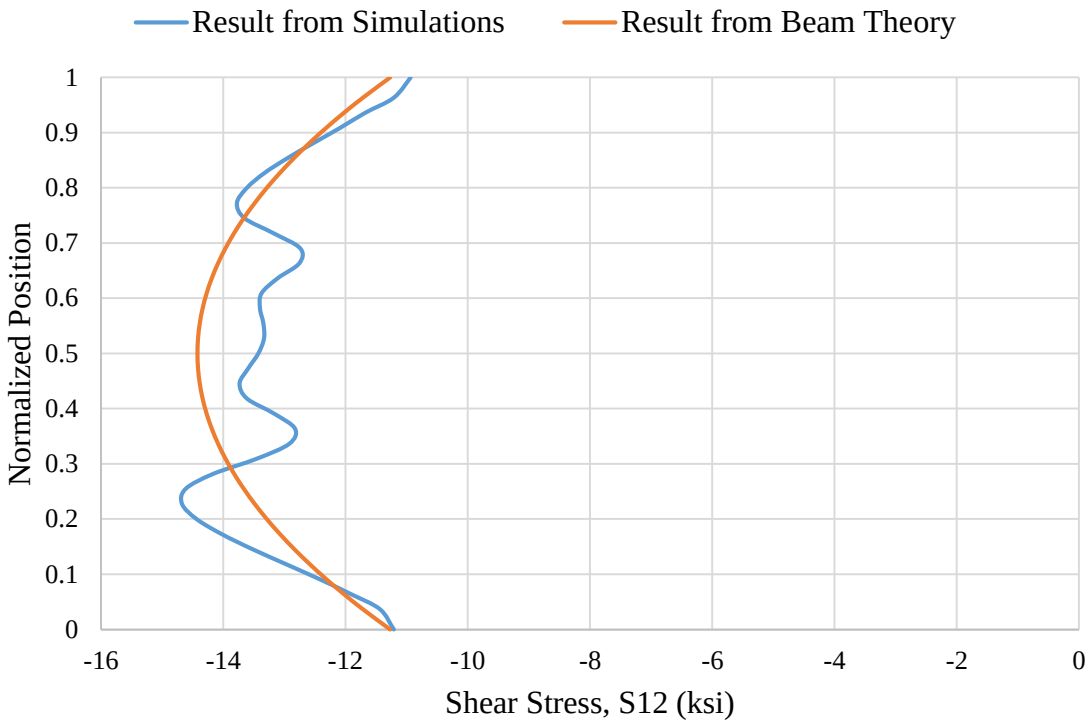

Fig. 6-79. Normalized position versus shear stress *S12* at the peak load at Section 3.

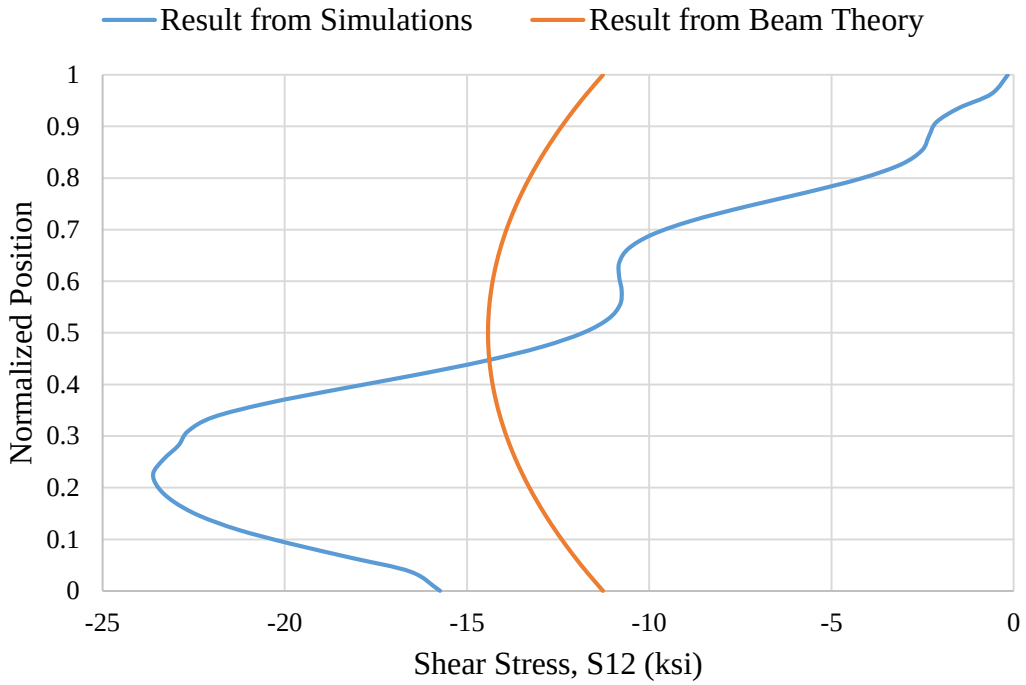

Fig. 6-80. Normalized position versus shear stress *S12* at the peak load at Section 4.

CHAPTER 7

MECHANISM OF SHEAR DEVELOPMENT IN A LONG UNSTIFFENED PANEL

The specimen selected for this study is UK7 (Daley and Davis 2015). It has an *a/h* of 8.04 and h/t_w of 164. Experimentally, this specimen failed by the formation of a shear buckle that extended over 6 ft. of its half-span length (see Figs. 4-13 and 4-14). To explain the mechanism of shear development, the procedure in Chapters 5 and 6 is repeated here. Figure 7-1 shows the overall geometry for the UK7 simulation model.

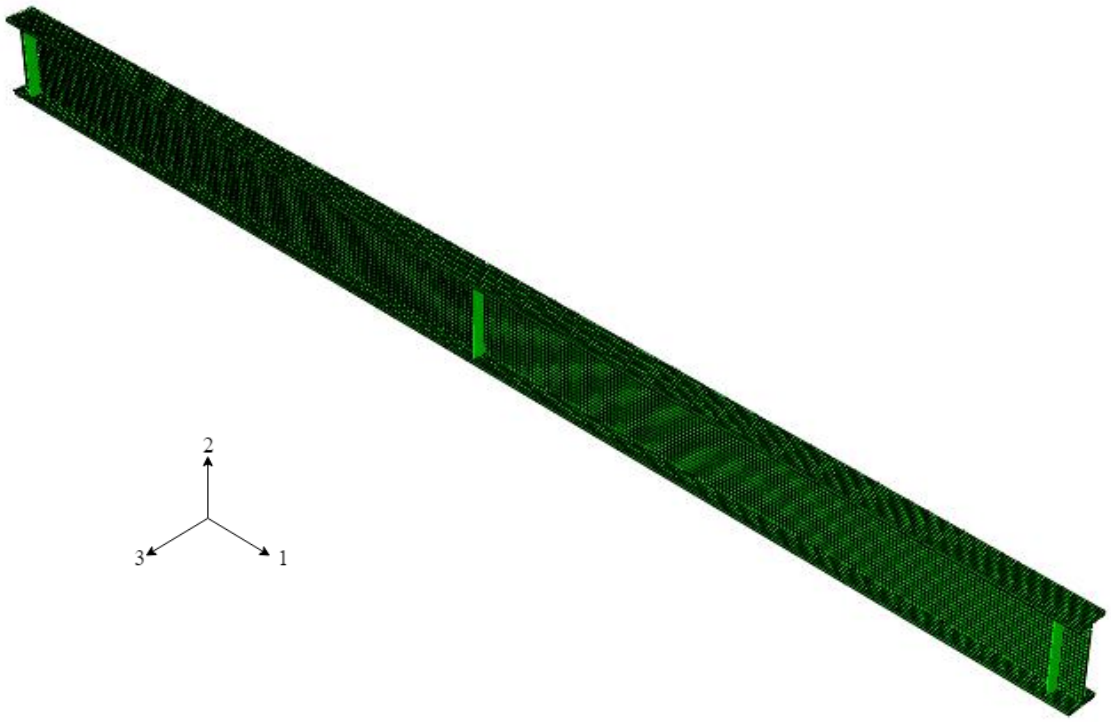

Fig. 7-1. Isometric view of the FE model for Specimen UK7.

The notation for the displacements and stresses is defined in Chapter 5.

Figure 7-2 shows a plot of the applied vertical load versus the vertical displacement (*U2*) at the mid-span of girder UK7. The markers in the Fig. 7-2 show various load stages considered in the following. The load magnitudes selected for the study are; zero load, 25% peak load (23.8 kips), 50% peak load (42.8 kips), 75% peak load (68 kips), 95% peak load (83.6 kips), peak load (87 kips) and post peak load (70.7 kips).

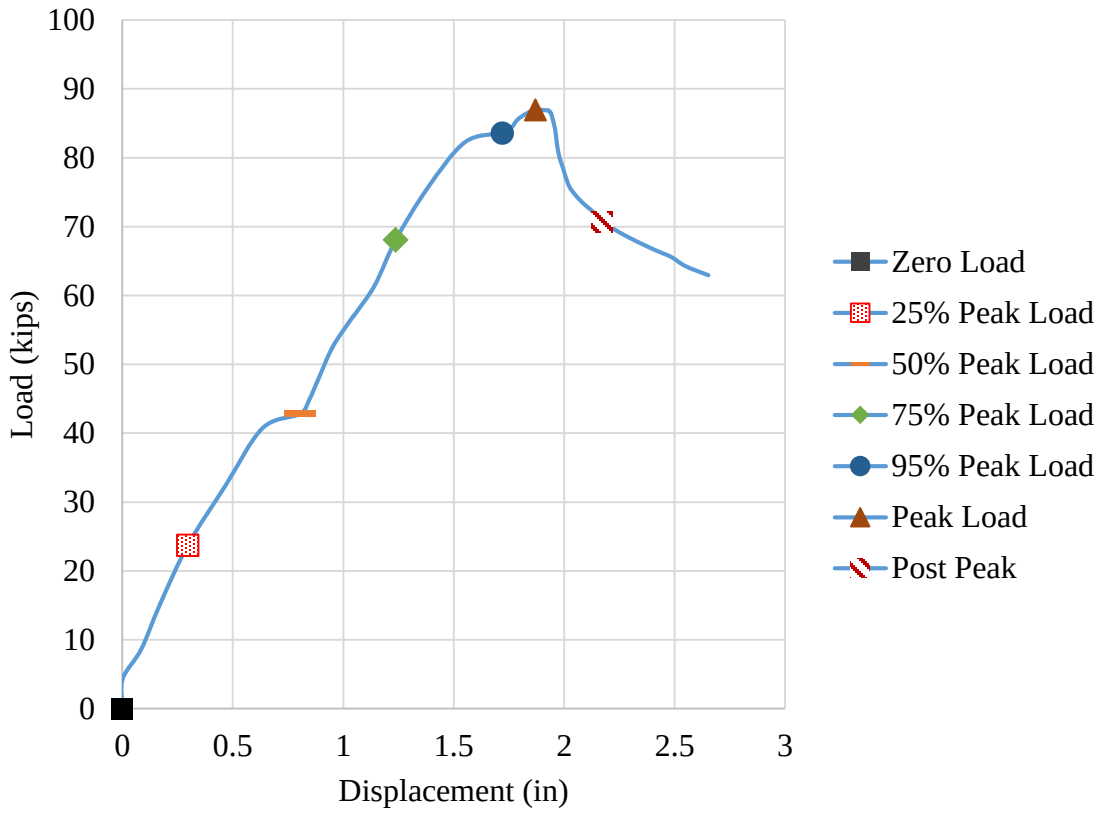

Fig. 7-2. Load versus vertical displacement at the mid-span of Specimen UK7.

In this section, the procedure in Section 5.1 through 5.5 is repeated for the Specimen UK7. In all the graphs, unless noted otherwise, the position along the length, measured from the left end of the specimen, is plotted as the abscissa. To simplify the plots, the normalized position along the length of the beam is employed. The normalized position 0.0 denotes the left-most free end of the specimen and 1.0 denotes the right-most free end of

the specimen. The left side of the specimen (normalized position less than 0.5) corresponds to the test segment having the thinner web.

7.1 Responses at a Section Along the Length at the Web Mid-Depth

In this section, the procedure of Section 5.1 is repeated for Specimen UK7. The quantities plotted are the lateral displacement *U3*, the web membrane stresses, *S11*, *S22* and *S12*, the von Mises stress *S*, the maximum principal tensile membrane stress *S1*, the maximum principal compressive membrane stress *S2* and the orientation of the principal stresses θ_p. Figures 7-3 through 7-10 show the variation of these quantities, in that order, at a section along the length at the web mid-depth for different levels of loading.

In all these graphs, the right side of the specimen follows the beam theory, like UK6, because there is no buckling of the web due to the thicker web on the right side of the beam.

At 25% of the peak load, the maximum lateral displacement *U3* (Fig. 7-3) is near the mid-span of the member and the displacement is almost zero near the supports. At 50% of the peak load, the displacements are cyclic in nature throughout the entire left span with all the peaks of almost the same amplitude. Also, as the limit load is approached, the locations of the peaks shift towards the left end of the specimen. This is due to the web buckles becoming more pronounced at higher load levels. At lower levels of loads, the out-of-plane deflections are following the path of the initial imperfections and as the loads are increased, the deflections are increasing due to the web buckling. At higher levels of load, *U3* is increasing at a much higher rate. For the 5% increase in load, from 95% of the peak load to the peak load there is an increase in lateral displacement of 55%. At the post-peak load level this effect is much more significant. This behavior is very similar to behavior of G7 (Fig. 5-4) and UK6 (Fig. 6-3). However, the pattern of *U3* for UK7 consists of more cyclic variations. *U3* at the peak load is smaller than *U3* for UK6 because of larger h/t_w of UK6

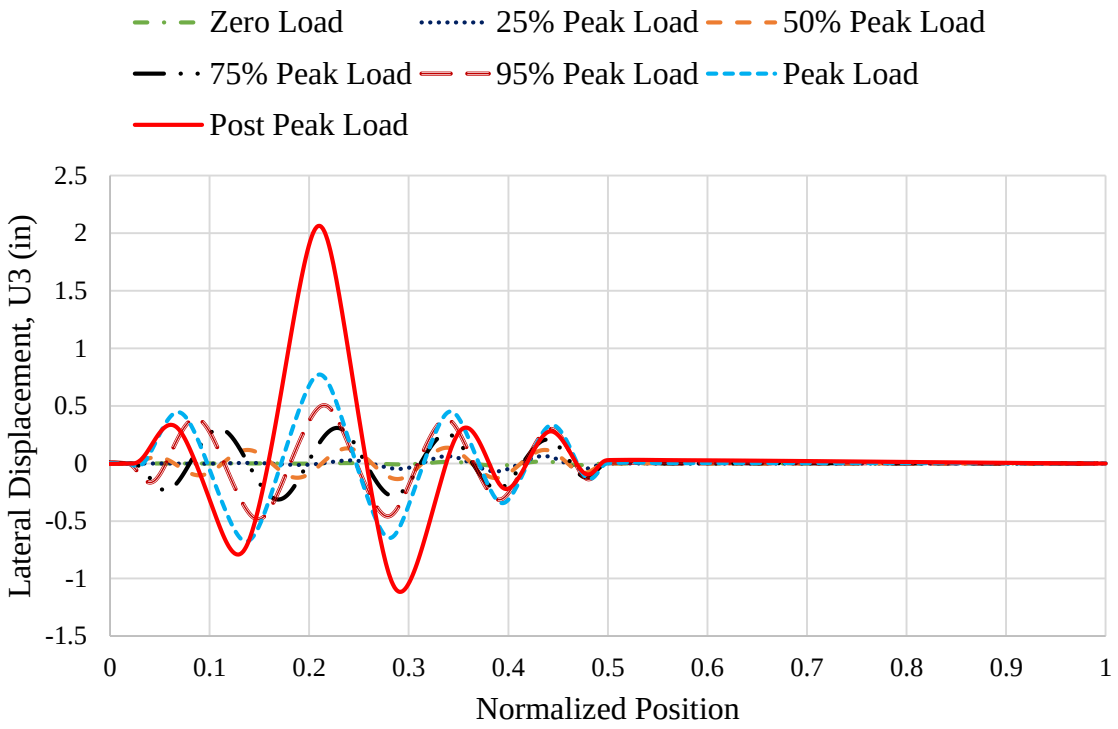

Fig. 7-3. Lateral Displacement *U3* versus normalized position along the web-mid depth.

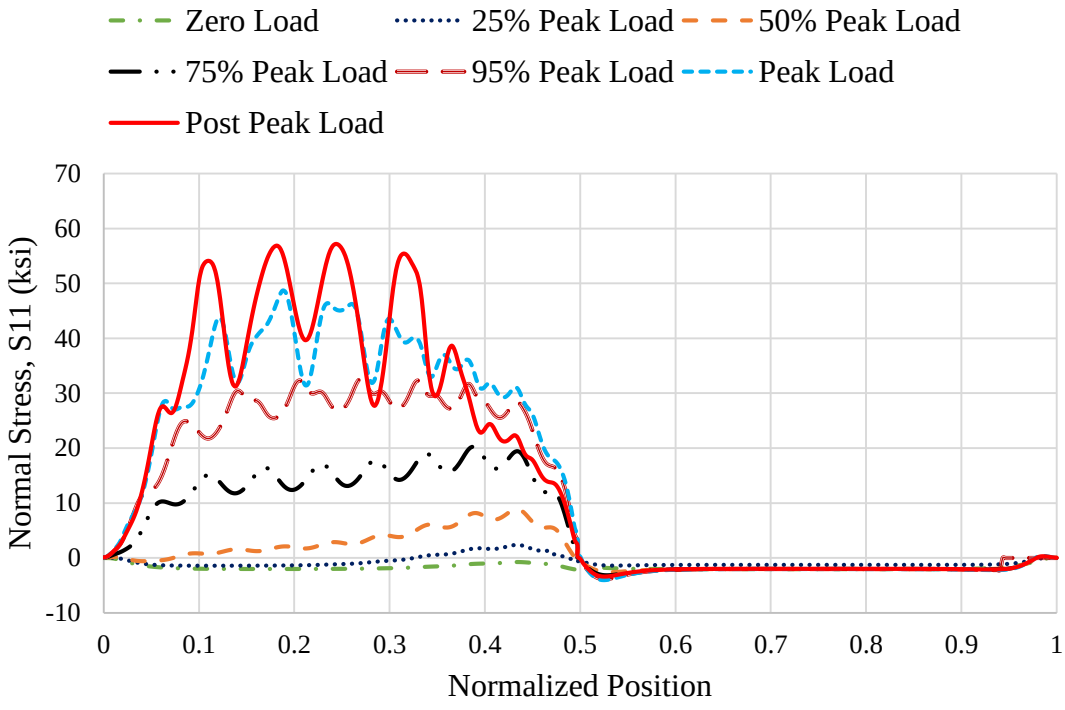

Fig. 7-4. Normal Stress *S11* versus normalized position along the web-mid depth.

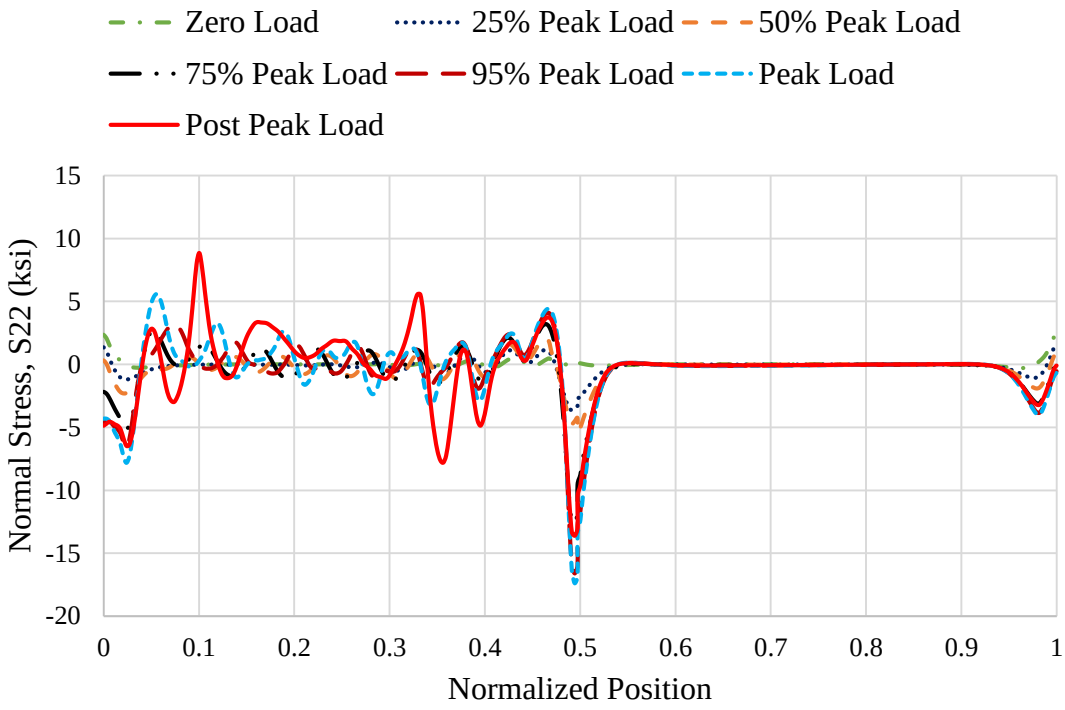

Fig. 7-5. Normal Stress *S22* vs normalized position along the web mid-depth.

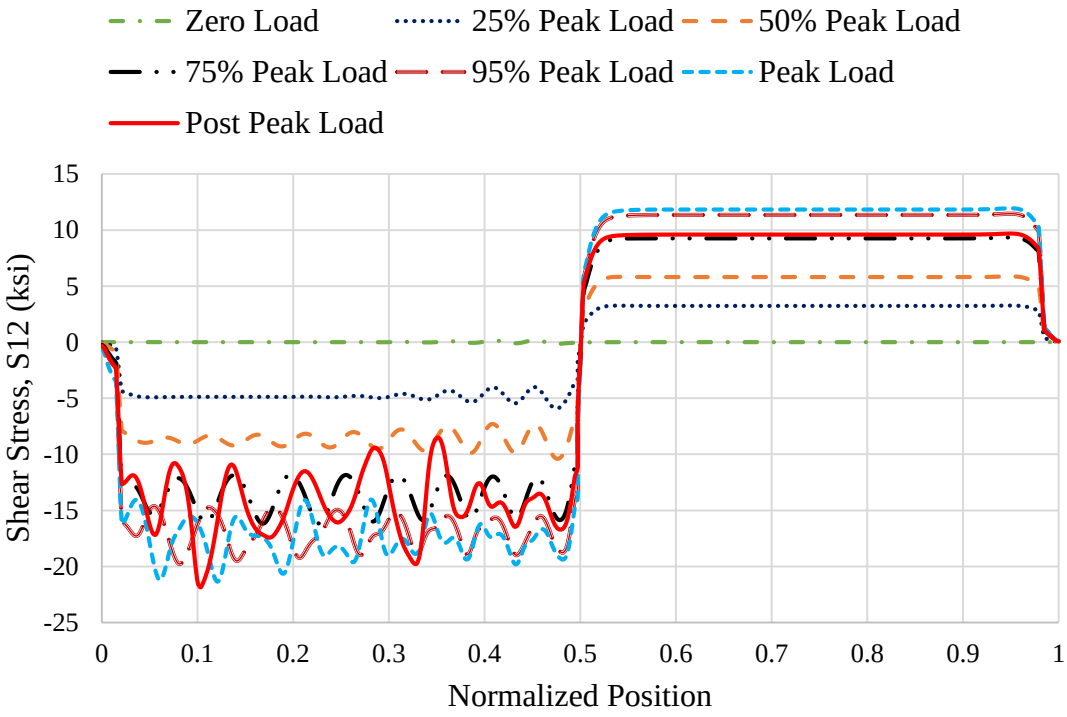

Fig. 7-6. Normal Stress *S12* vs normalized position along the web mid-depth.

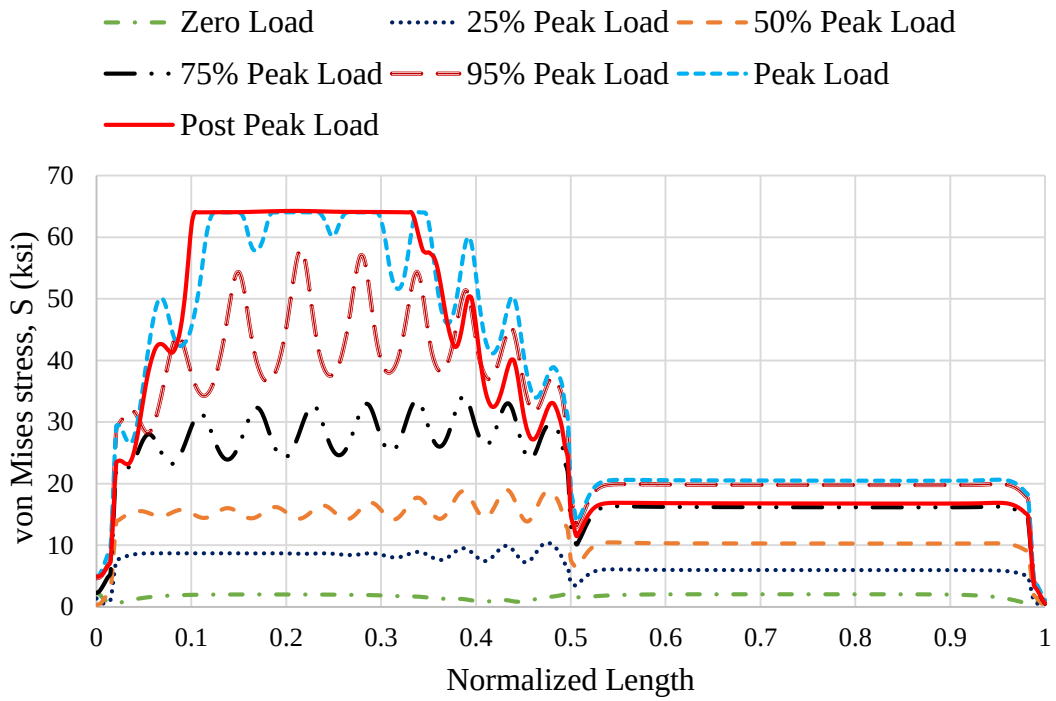

Fig. 7-7. von Mises stress *S* versus normalized position along the web mid-depth.

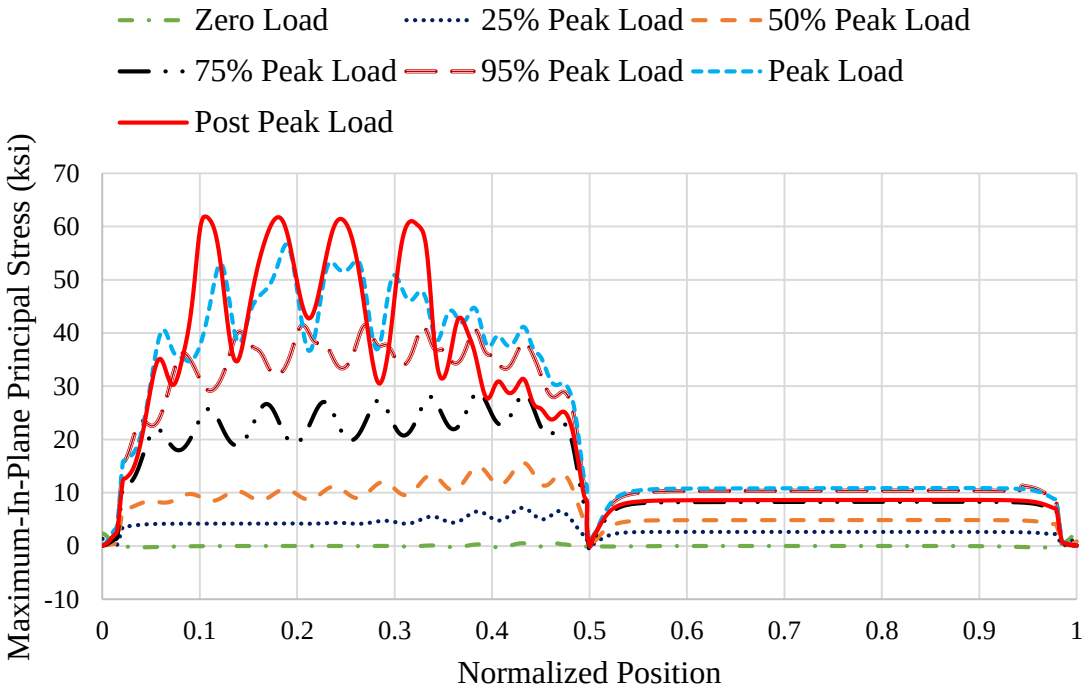

Fig. 7-8. Maximum-In-Plane Principal Stress *S1* versus normalized position along the web mid-depth.

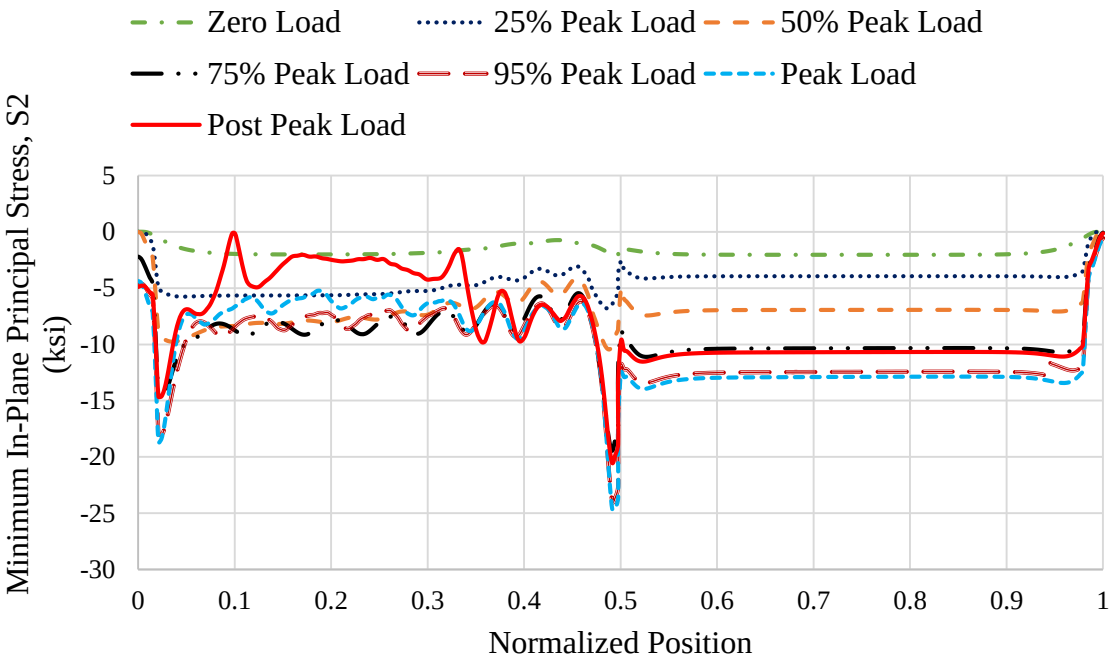

Fig. 7-9. Minimum-In-Plane Principal Stress *S2* versus normalized position along the web mid-depth.

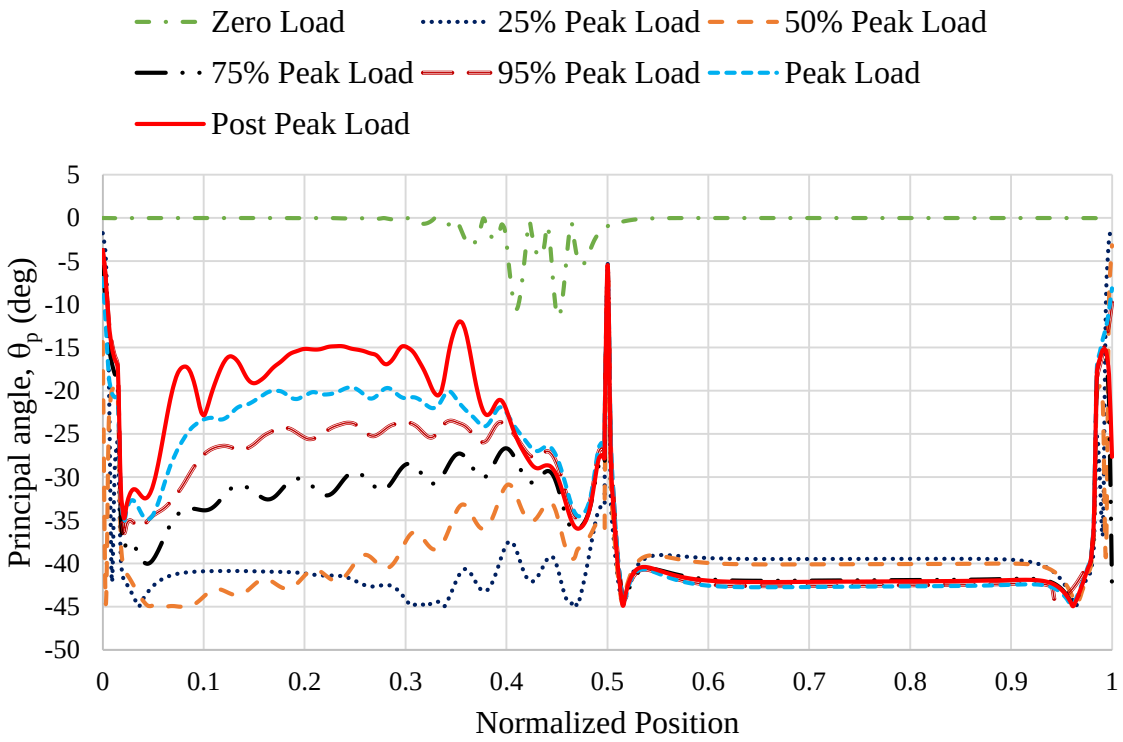

Fig. 7-10. Principal angle θ_p versus normalized position along the web mid-depth.

At 25% of the peak load, *S11* (Fig. 7-4) is tensile between approximately 0.3 and 0. 5 of the specimen length. At 50% of the peak load, *S11* is tensile throughout the half-length of the beam corresponding to the test specimen. As the loads are increased, the peak of *S11* is shifting toward the left end of the panel. This shows that there is significant tensile stress developing at this load level. There appears to be some correlation with the location of the peak *S11* values and the position of the peak lateral displacements, *U3*. Many peaks are formed at 95% of the peak load, almost all of the same amplitude. With the increasing load the tensile normal stress is also increasing. For a 5% increase in load, from 95% of peak load to peak load, *S11* increases by almost 50%. At the post peak load also, many peaks are formed. This is an indication that whole cross-section of the thinner web is forming tensile stress bands. In case of UK6 and G7, comparatively lesser peaks were formed. This is because of significantly longer panel length for UK7. Like UK6 and G7, *S11* is not constant along the length of the test specimen.

The normal stress *S22* (Fig. 7-5) has its peak at the mid-span and at the supports, the locations where the load is applied and where the beam end reaction is developed into the web. Due to large *a/h* for this specimen, *S22* variation is much more cyclic compared to UK6 (Fig. 6-5). Similar to G7 and UK6, *S22* is significantly lower.

For lower levels of loading (25% and 50% of the peak load), the maximum *S12* (Fig. 7-6) occurs near the mid-span. However, at the higher levels of loading *S12* is maximum near the left end of the specimen, like UK6 (Fig. 6-6). For all levels of loadings, the plot of *S12* can be related to the profile of *U3*. The *S12* behavior is much more oscillatory in nature compared to UK6 (Fig. 6-6) and G7 (Fig. 5-7). This is because of significantly longer length of the panel. At post peak load, two predominant peaks are formed, like UK6 and G7.

The variation of von Mises stress *S* for Specimen UK7 (Fig. 7-7) is similar to its variation in G7 (Fig. 5-8) and UK6 (Fig. 6-7). At the peak load, like G7, considerable

length of the panel has yielded. However, due to higher h/t_w of UK6, at the peak load, the extent of yielding is concentrated over a much shorter length. Like G7 and UK6, at the post peak, there is yielding of significant length of the thinner web.

The maximum principal stress *S1* (Fig. 7-8) is calculated using Eq. 5-1. *S1* most closely follows the curve of *S11* for higher levels of loading and curve of *S12* for lower levels of loading. For 25% of the peak load, the stress *S1* is almost identical to *S12* (Fig. 7-7) throughout the left end of the beam. At this state, the beam can be assumed in the state of pure shear. As the loading is increased, there is considerable increase in the diagonal tension causing the peaks as seen in the Fig. 7-7. For 5% increase in the load, from 95% of the peak load to the peak load, maximum *S1* increases by almost 40%. This behavior is similar to UK6 and G7 (Fig. 6-8 and 5-9, respectively) and shows that considerable diagonal tension is developed even for long panels with *a/h* approximately equal to 8. Just like UK6 and G7, *S1* varies significantly throughout the left side of the specimen. However, *S1* is much more cyclic in nature than UK6 and G7 and more peaks are formed at post peak load level.

The minimum in-plane principal stress *S2* (Fig. 7-9) is calculated using Eq. 5-2. Near the supports and the mid-span, the stress the curve of *S22*. This is due to the effect of large compressive load being applied at the mid-span and the reactions at the supports. There is considerable increase in the *S2* after 25% peak load. However, there was lesser increase in *S2* for UK6. This is because of higher slenderness ratio of UK6 and hence lesser critical elastic shear stress τ_e. The elastic shear buckling stress, $\tau_{e,}$ calculated by Equation 1-1 and the plate buckling coefficient taken from Equation 1-3 comes out to be 5.25 ksi for UK7. After 50% of peak load, for the majority of the half-length on the left-hand side of the specimen, the stress *S2* remains close to τ_e. This behavior was also observed in UK6 and G7 (Fig. 6-9 and 5-10). However, owing to its large *a/h*, the behavior of *S2* is much more cyclic.

The principal stress orientation θ_p (Fig. 7-10) is calculated using Eq. 5-3. At 25% of the peak load, θ_p is almost equal to 45°, and up to this point, the specimen can be approximated in a state of pure shear. For the left end of the specimen, as the load is increased the principal angle decreases. This is because of the increase of *S1* without any significant change in *S2* for higher levels of loading. At the post peak load, the principal angle at middle of the panel decreases to almost 16°. The principal angle according to Eq. 1-18 is 15°. At this location, *S11* is equal to 56 ksi and addition of *S1* and *S2* is equal to 59 ksi. This is due to non-zero value of *S22*. This behavior is also seen in the Specimens UK6 and G7. This shows that Höglund's theory is a good approximation of shear strength development mechanism for specimens of varying panel length. However, the behavior is much more complex. Basler's Tension Field Action Model is not applicable to unstiffened panels. However, if it were applied, the orientation of the diagonal tension comes out to be 4°.

7.1.1 Principal Stresses in Selected Elements at the Web Mid-Depth

The procedure of Section 5.1.1 is repeated in this section for UK7. Four Elements along the left-half length of the specimen are selected at web mid-depth and the principal stresses are drawn as arrows on these Elements to explain the mechanism of the shear strength development. Figure 7-11 shows the location of Elements along the web mid-depth.

The Element 1 is located at approximately 10 inches from the left end of the specimen. The second Element selected for study is at 50 inches from the first Element. The third Element is at 50 inches from the second Element and fourth Element is selected such that it is near mid-span. The arrows on the Elements indicate the orientation of the principal stresses and their numerical values are written in the brackets. Figures 7-12 through 7-25

shows the variation of principal stresses for different level of loading. The word "Element" is abbreviated as "Ele." to fit all the Elements in one row to understand the plots better.

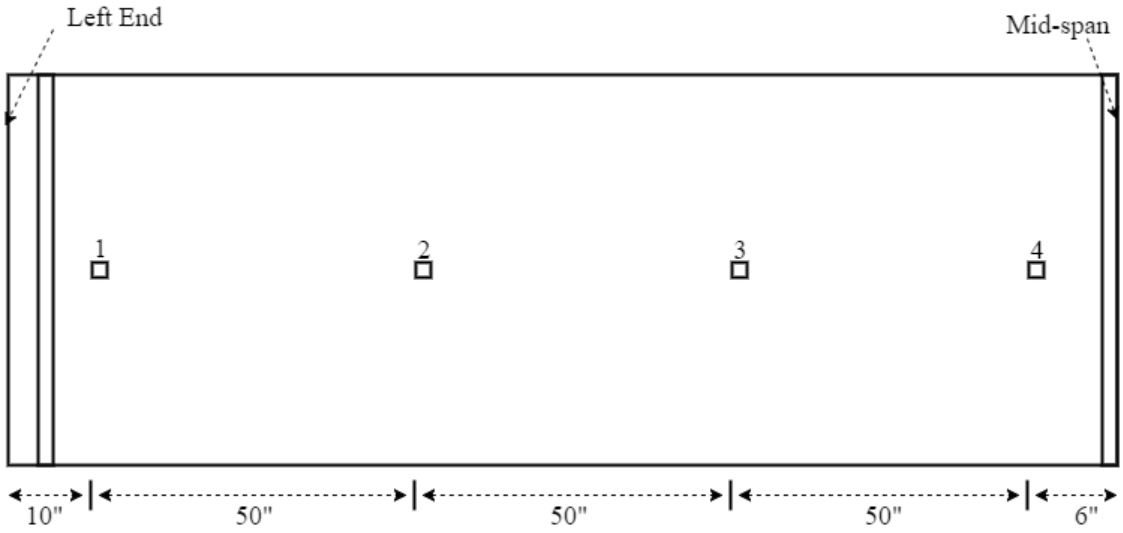

Fig. 7-11. Elements along the web mid-depth.

1. Principal stresses at zero Load

The values of principal stresses are approximately equal to zero and the principal angle for maximum in-plane principal is almost 90°. However, for Element 4 it is slightly different, this is due of the initial web imperfections.

Ele. 1 (-0.22 ksi) Ele. 2 (0.00 ksi) Ele. 3 (0.02 ksi) Ele. 4 (0.16 ksi)

Fig. 7-12. Maximum In-Plane Principal Stress *S1* and their orientation at zero load.

Ele. 1 (-0.95 ksi) Ele. 2 (-2.01 ksi) Ele. 3 (-1.69 ksi) Ele. 4 (-1.50 ksi)

Fig. 7-13. Minimum In-Plane Principal Stress *S2* and their orientation at zero load.

2. Principal stresses at 25% peak load

Elements 2 and 3 at 25% peak load can be approximated to be in the state of pure shear. *S2* at Elements 1 and 4 is comparatively higher due to the presence of compressive stress as a result of the reaction and concentrated load at the mid-span respectively.

Ele. 1 (3.79 ksi) Ele. 2 (4.22 ksi) Ele. 3 (5.16 ksi) Ele. 4 (5.36 ksi)

Fig. 7-14. Maximum In-Plane Principal Stress *S1* and their orientation at 25% peak load.

Ele. 1 (-5.51 ksi) Ele. 2 (-5.62 ksi) Ele. 3 (-4.69 ksi) Ele. 4 (-6.31 ksi)

Fig. 7-15. Minimum In-Plane Principal Stress *S2* and their orientation at 25% peak load.

3. Principal stresses at 50% peak load

The increase in *S2* values for Element 1 and 4 is due to the effect of transverse stiffeners and development of compressive stress due to the concentrated load. For Element 2 and 3, we can clearly see a large diagonal tension forming and there is not much increase in the *S2*.

Ele. 1 (7.29 ksi) Ele. 2 (10.43 ksi) Ele. 3 (12.46 ksi) Ele. 4 (12.10 ksi)

Fig. 7-16. Maximum In-Plane Principal Stress *S1* and their orientation at 50% peak load.

Ele. 1 (-9.66 ksi) Ele. 2 (-7.91 ksi) Ele. 3 (-6.32 ksi) Ele. 4 (-9.21 ksi)

Fig. 7-17. Minimum In-Plane Principal Stress *S2* and their orientation at 50% peak load.

4. Principal stresses at 75% peak load

At 75% of the peak load, the *S1* at Element 2 and 3 are larger than *S1* at Element 4, this similar behavior was also observed in UK6. *S2* for Elements 1 and 4 continues to increase. *S2* for Elements 2 and 3 do not increase much after 50% of the peak load.

Ele. 1 (12.10 ksi) Ele. 2 (22.86 ksi) Ele. 3 (26.63 ksi) Ele. 4 (21.27 ksi)

Fig. 7-18. Maximum In-Plane Principal Stress *S1* and their orientation at 75% peak load.

Ele. 1 (-13.95 ksi) Ele. 2 (-8.75 ksi) Ele. 3 (-7.82 ksi) Ele. 4 (-12.56 ksi)

Fig. 7-19. Minimum In-Plane Principal Stress *S2* and their orientation at 75% peak load.

5. Principal stresses at 95% peak load

There has been continual increase in *S1* values of Element 2 and 3 showing definite diagonal tension. There is not a lot of increase in *S1* for Element 4, this is because since this Element is close to the mid-span and there is not a pronounced effect of diagonal tension.

Ele. 1 (19.18 ksi) Ele. 2 (32.33 ksi) Ele. 3 (41.14 ksi) Ele. 4 (27.54 ksi)

Fig. 7-20. Maximum In-Plane Principal Stress *S1* and their orientation at 95% peak load.

Ele. 1 (-16.53 ksi) Ele. 2 (-7.37 ksi) Ele. 3 (-7.91 ksi) Ele. 4 (-12.84 ksi)

Fig. 7- 21. Minimum In-Plane Principal Stress *S2* and their orientation at 95% peak load.

6. Principal stresses at peak Load

There is evident rotation of principal angle for higher levels of loading and the principal angles are close to 20º. The trend for Element 1 remains same for all the levels of loading with continual increase in *S2*. For Elements 2 and 3, *S1* increased significantly from 95% of the peak load and *S2* has increased only slightly after 50% of the peak load. *S1* for Elements 2 and 3 increased at a much higher rate compared to Element 4 after 50% of the peak load, this is because diagonal tension is not predominant near the ends of the panel. This behavior was also observed for Element 4 of Specimen UK6 (Figs. 6-12 to 6-25).

Ele. 1 (16.97 ksi) Ele. 2 (53.96 ksi) Ele. 3 (47.50 ksi) Ele. 4 (29.12 ksi)

Fig. 7-22. Maximum In-Plane Principal Stress *S1* and their orientation at peak load.

Ele. 1 (-15.54 ksi) Ele. 2 (-5.44 ksi) Ele. 3 (-6.81 ksi) Ele. 4 (-12.64 ksi)

Fig. 7-23. Minimum In-Plane Principal Stress *S2* and their orientation at peak load.

7. Principal stresses at post peak

At post peak, the maximum value of *S1* occurs at Element 2. The principal angles for Element 2 and 3 are close to 15^o with the horizontal. The compressive stress *S2* varies relatively slightly (close to τ_e) for all the levels of loading after 50% of the peak load except for Element 1 and Element 4.

Ele. 1 (13.94 ksi) Ele. 2 (61.70 ksi) Ele. 3 (58.76 ksi) Ele. 4 (23.55 ksi)

Fig. 7-24. Maximum In-Plane Principal Stress *S1* and their orientation at post peak load.

Ele. 1 (-12.94 ksi) Ele. 2 (-2.18 ksi) Ele. 3 (-1.73 ksi) Ele. 4 (-12.05 ksi)

Fig. 7-25. Maximum In-Plane Principal Stress *S2* and their orientation at post peak load.

7.2 Responses at a Section Along the Length at the Top of the Web

In this section, the procedure of Section 5.2 is repeated for Specimen UK7. The quantities plotted are the lateral displacement *U3*, the web membrane stresses, *S11*, *S22*

and *S12*, the von Mises stress, *S*, the maximum principal tensile membrane stress (*S1*), the maximum principal compressive membrane stress (*S2*) and the orientation of the principal stresses (θ_p). Figures 7-26 through 7-33 show variation of these quantities, in that order, at a section along the length at web top for different levels of loading.

The lateral displacement *U3* (Fig. 7-26) plots follow the expected pattern for the load levels; zero, 25%, 50% and 75% of the peak load, i.e. the lateral displacement is zero at all the lateral bracing locations and follows the expected deflected shape. There is considerable increase in displacement at the peak load when compared to 95% of the peak load near the supports, at second unbraced length from the left end of the specimen. This effect is much more pronounced in the post peak load. At peak load, there is change in the direction of curvature in the unbraced length at the second unbraced length from the support. However, this change in curvature was more predominant in the unbraced length near the support for UK6, in the first unbraced length. This is due to higher *a/h* for UK7.

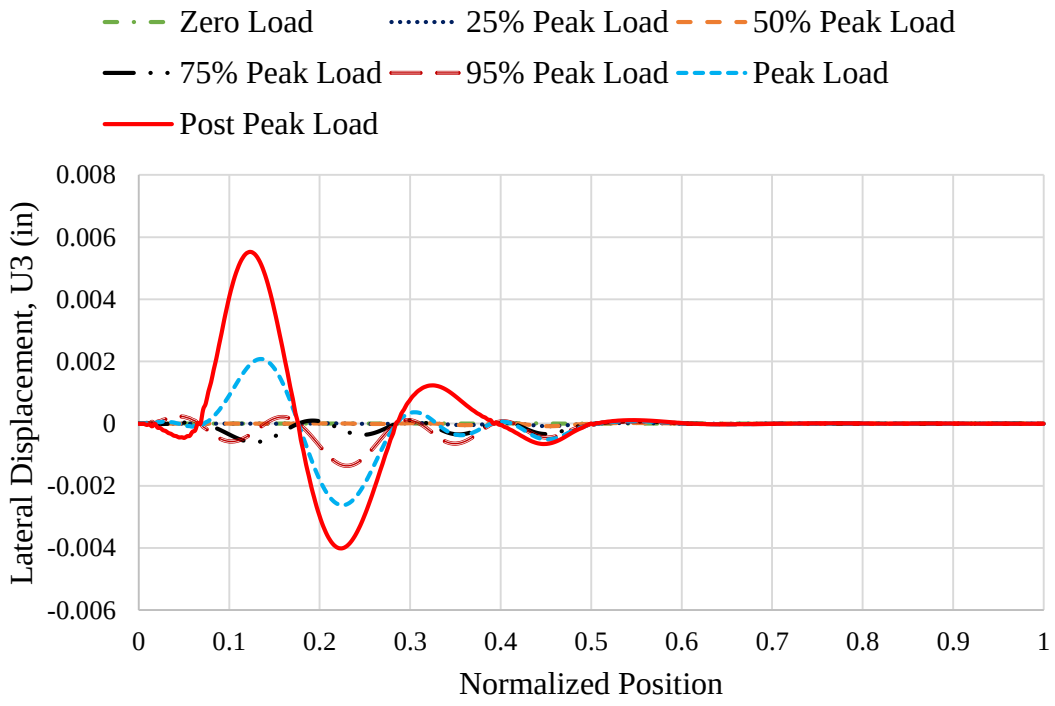

Fig. 7-26. Lateral Displacement, *U3* versus normalized position along the web top.

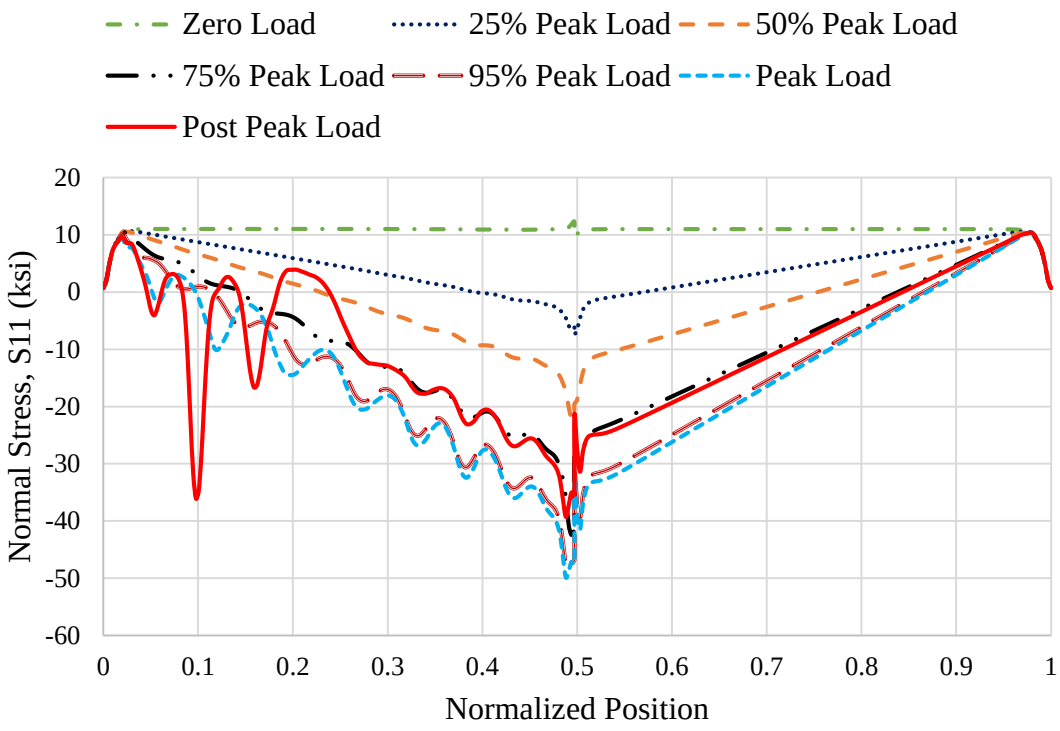

Fig. 7-27. Normal Stress *S11* vs normalized position along the web top.

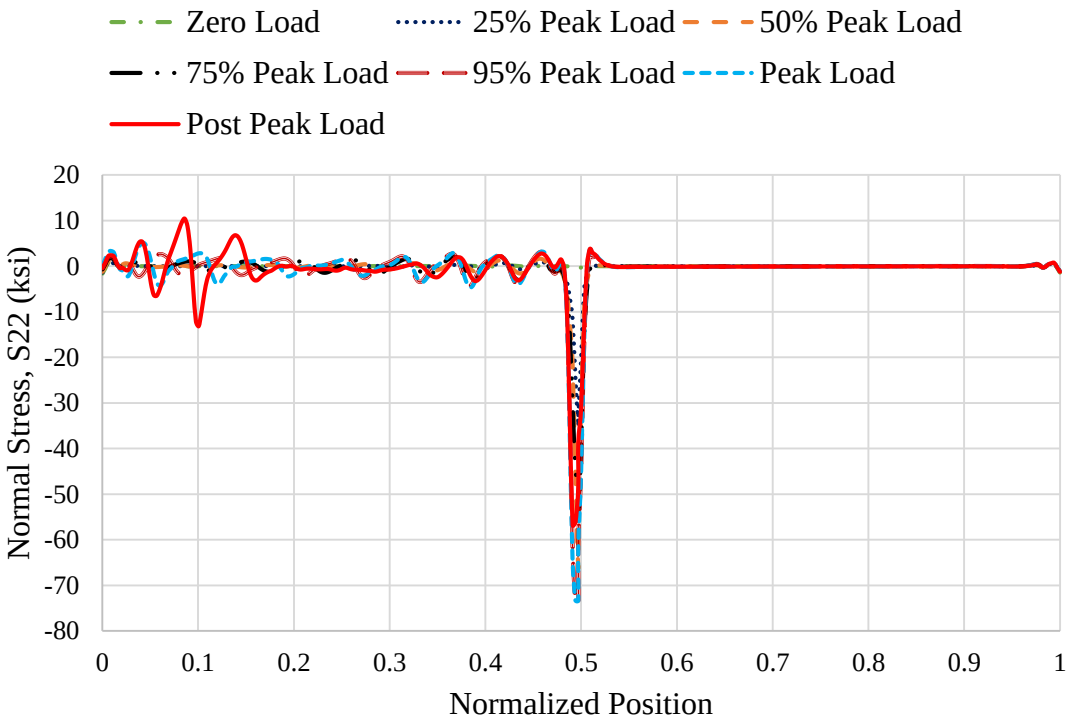

Fig. 7-28. Normal Stress *S22* versus normalized position along the web top.

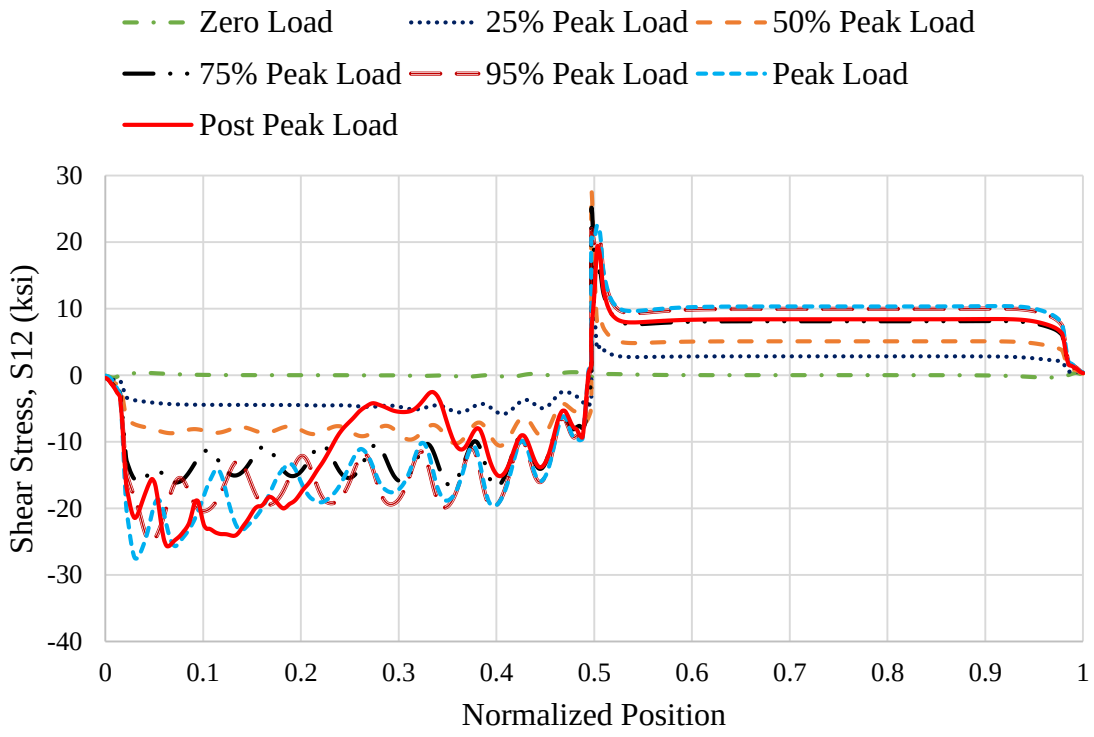

Fig. 7-29. Shear Stress *S12* versus normalized position along the web top.

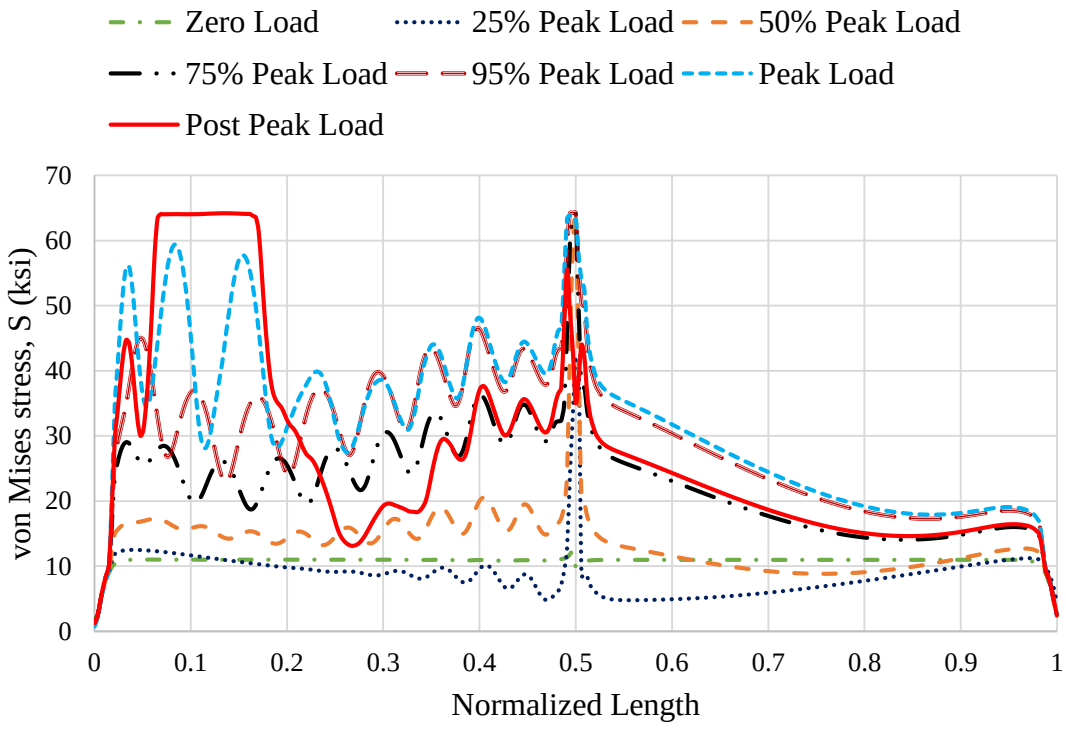

Fig. 7-30. von Mises stress *S* versus normalized position along the web top.

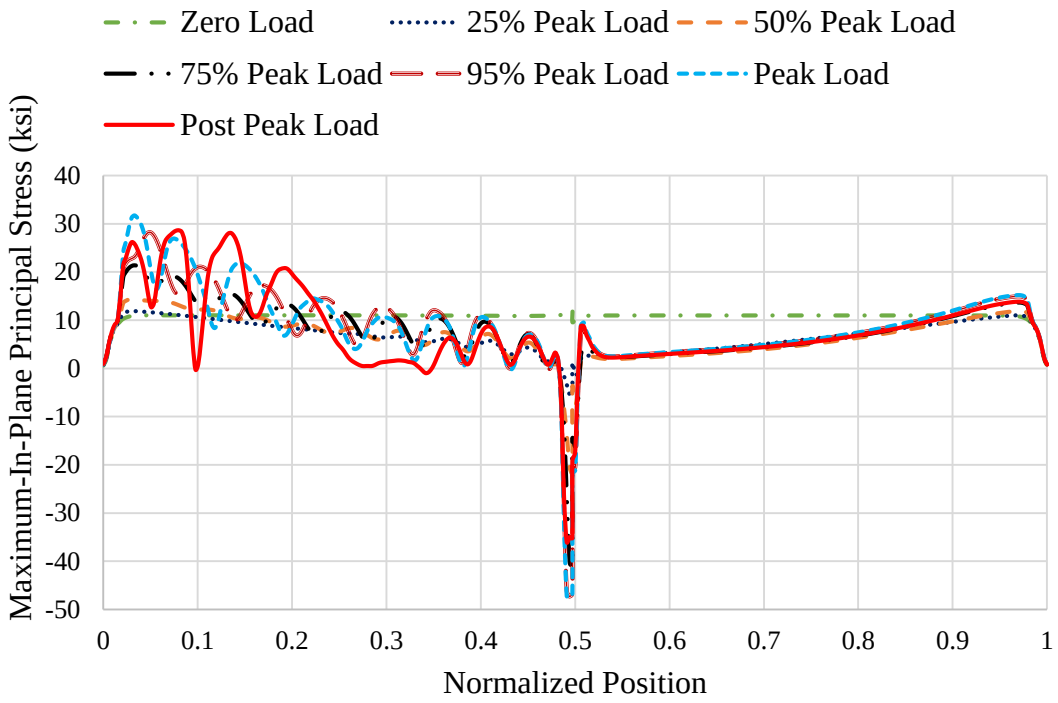

Fig. 7-31. Maximum In-Plane Principal Stress *S1* versus position along the web top.

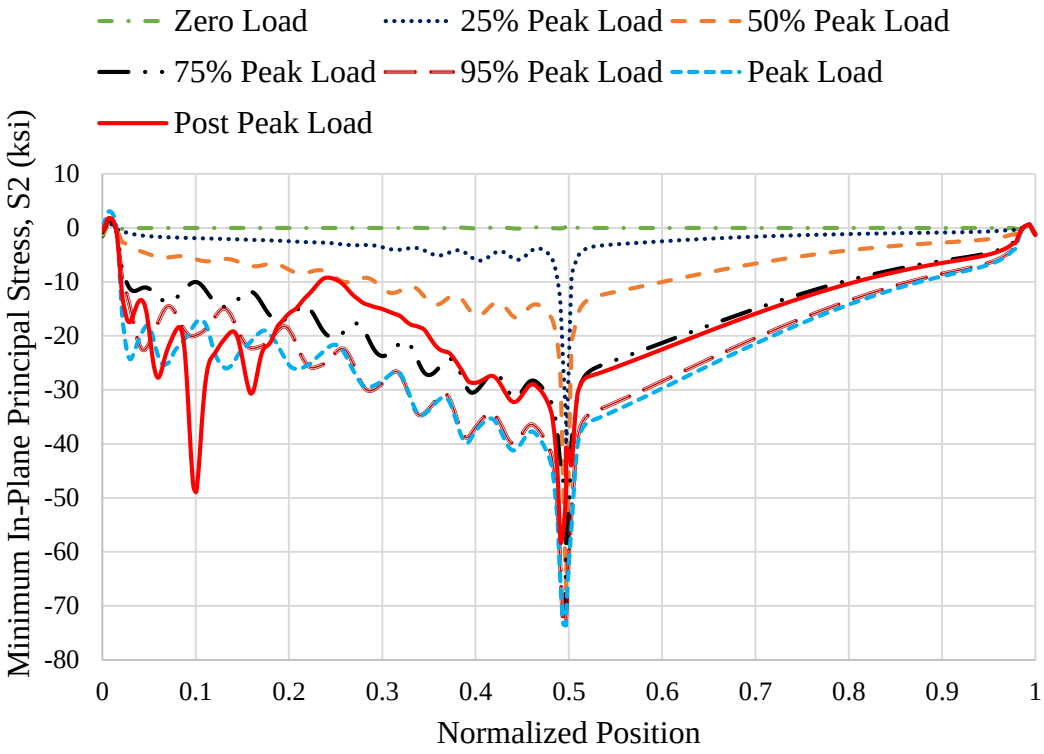

Fig. 7-32. Minimum In-Plane Principal Stress *S2* versus position along the web top.

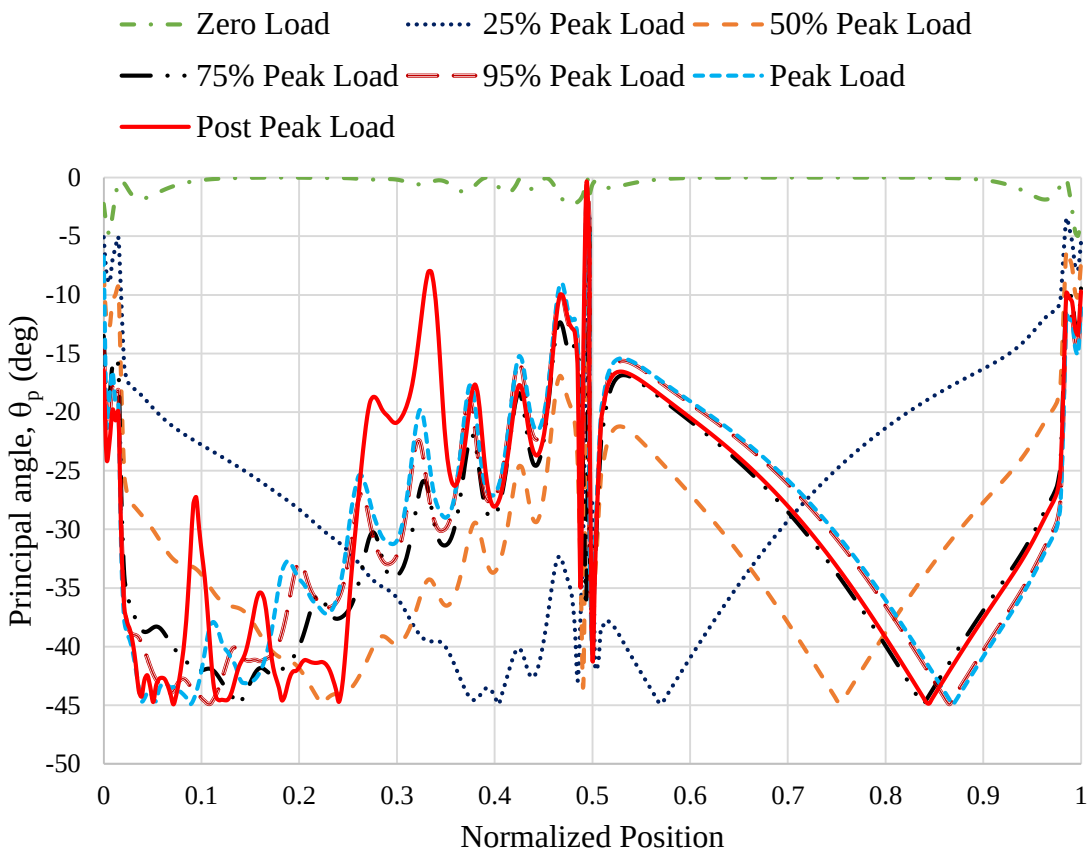

Fig. 7-33. Principal Angle θ_p versus position along the web top.

The behavior of *S11* (Fig. 7-27) for UK7 is similar to UK6. However, the variation of *S11* for UK7 is lot more cyclic owing to large *a/h* and smaller h/t_w; hence higher rigidity of the web. At 95% of the peak load, there are no peaks and the variation of *S11* on the left part of the specimen follows the sinusoidal nature of lateral displacement, *U3*. However, at the post peak load there is sudden increase in compressive stress near support at 37 inches from the left end of the beam. This is where the failure band formed in the web meets the flange. For the Specimens UK6 and G7 (Fig. 6-27 and 5-27 respectively), this change in the compressive stress was near the right transverse stiffener.

For almost all load cases, *S22* (Fig. 7-28) follows a cyclic behavior which was not seen in UK6 and G7 (Fig. 6-28 and 5-28, respectively), this is because of large *a/h* of the

specimen. Large *S22* values near the mid-span even for lower load levels is due to initial web imperfections and high rigidity of the web. However, these values do not increase much after the peak load indicating this has nothing to do with the forming of web buckle. *S22* near mid-span was almost zero for Specimen G7 and UK6 even at post peak load. For a 5% of increase in load from 95% of the peak load to peak load, *S22* increased by almost 100% (not taking into account values near the mid-span). However, this value is still relatively less compared to *S22* at peak load. The location of maximum *S22* coincides with the location of maximum *S11* which is at 41 inches from the left end. At post peak load, *S22* is maximum at 0.1 normalized position. *S11* was minimum at this location and this is where the web buckle meets the top flange. At post peak stage, the behavior is similar to UK6 and G7. However, for UK6 and G7 the failure bands meet the flange near the left end of the panel but for UK7, due to its higher *a/h*, the failure band meets at a certain distance (37 inches) from the left-end of the specimen.

The cyclic nature of *S12* (Fig. 7-29) can be related to the pattern of lateral displacement *U3* and is much more cyclic compared to UK6 and G7 (Fig. 6-29 and 5-29, respectively). For lower levels of loads, the maximum *S12* is near the mid-span of the specimen. As the load is increased, this maximum shifts towards left end of the specimen and the profile becomes more and more oscillatory and at the peak load level, maximum *S12* occurs near the left end of the panel, like G7 and UK6. At the post peak, this effect is much more pronounced and is visible over a much larger length.

Even at the peak load, there is no yielding of the web top (Fig. 7-30). This is due to higher *a/h* of 8.04 for UK7. At the peak load, in Specimen UK6 (with *a/h* of 4.12), there is yielding of web top over a small length (Fig. 6-30) and in Specimen G7 (with *a/h* of 2.0), yielding is distributed over a larger length (Fig. 5-30). Moreover, due to higher *a/h*, at the post peak load, the web yielding is at a distance away from the left end of the panel, this is

where the buckled web meets the top flange. In Specimens UK6 and G7, yielding was concentrated over a length near the left end of the panel.

The behavior of the principal stresses *S1* and *S2* (Fig. 7-31 and 7-32, respectively) is similar to behavior of these stresses on G7 (Fig. 5-31 and 5-32, respectively) and UK6 (Fig. 5-31 and 5-32, respectively), however the variation of these stresses in UK7 is much more cyclic. The principal stresses *S1* and *S2* are large at the left-hand end of the panel. The stress *S2* and *S1* increases at left end of the panel due to increase in *S12* near the left end. The Elements near the mid-span (right end of the panel) are subjected to compressive flexural stress and almost zero *S12* and *S22*. This results in *S1* being close to zero for almost the entire length of the except near the left transverse stiffener. *S2* follows the curve of *S11* for almost the entire length of specimen except near the left end of the panel. Maximum *S2* at the post peak load, is maximum at the location where buckled web meets the top flange. This is due to large *S22* at this location at post peak load.

7.2.1 Boundary Condition between the Top Flange and the Web

The procedure of Section 5.2.1 is repeated for Specimen UK6 in this section. Four Elements along the left-half length of the specimen are selected at the web-top. Fig. 7-34 shows the location of selected Elements.

The first Element is selected at 10 inches from the left end. The second Element is selected at 31 inches from the first Element, this is the location where the maximum *S22* occurs at the peak load. The third and fourth Element are selected at a distance of 101 inches and 161 inches respectively from the left end of the specimen. Fig. 7-35 through 7-38 shows the variation of *S22* on different surfaces as a function of the applied load.

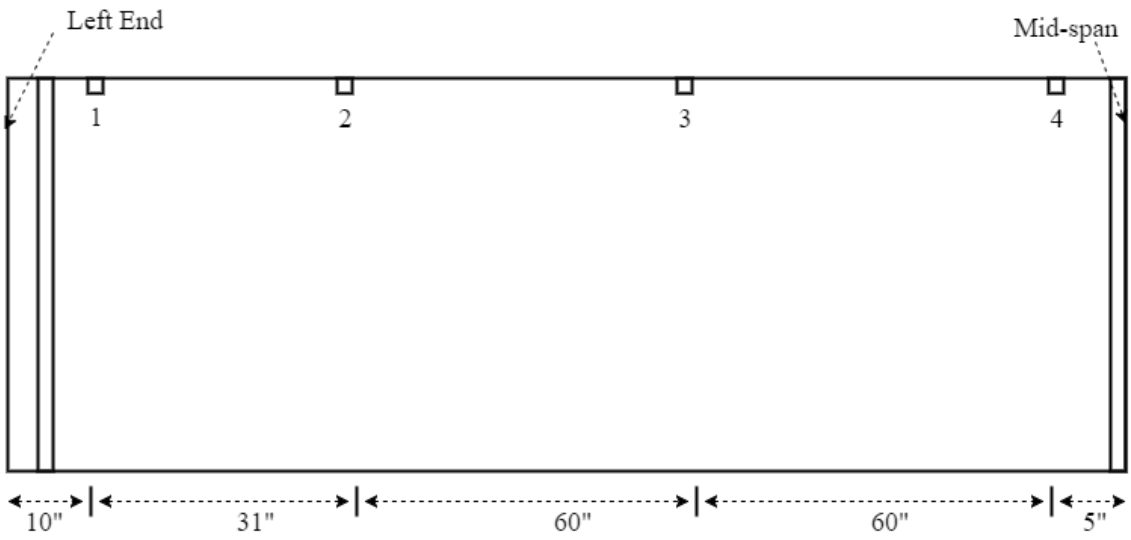

Fig. 7-34. Elements along the web-top.

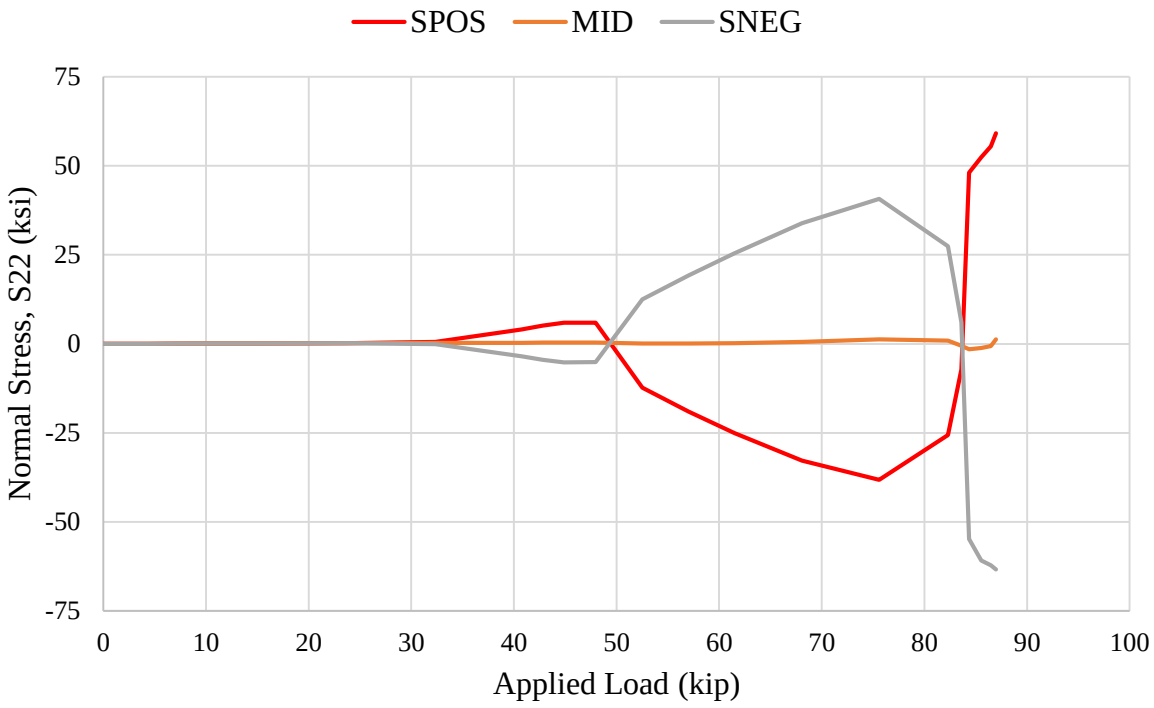

Fig. 7-35. Normal Stress *S22* at top, mid and bottom surface of the web versus applied load for Element 1 at web-top.

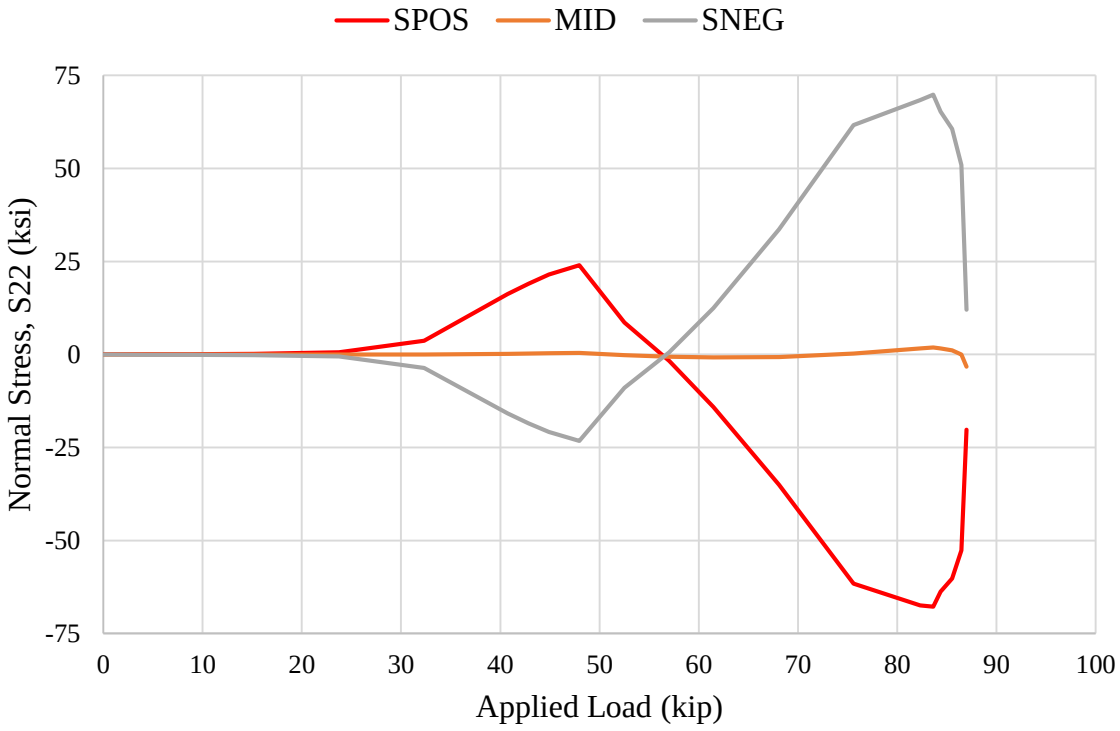

Fig. 7-36. Normal Stress *S22* at top, mid and bottom surface of the web versus applied load for Element 2 at web-top.

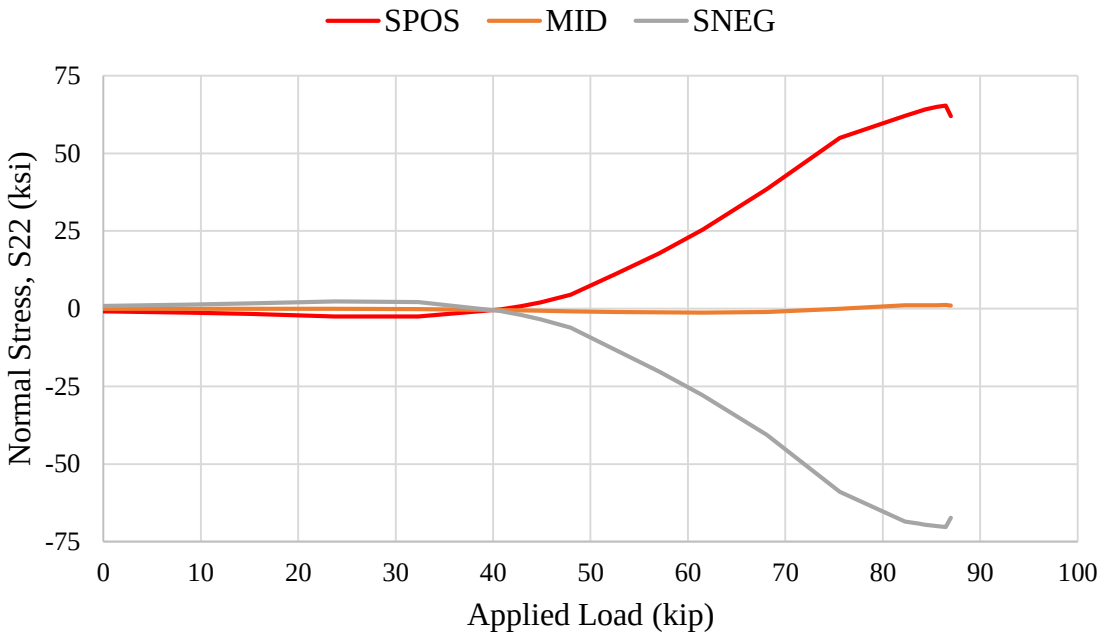

Fig. 7-37. Normal Stress *S22* at top, mid and bottom surface of the web versus applied load for Element 3 at web-top.

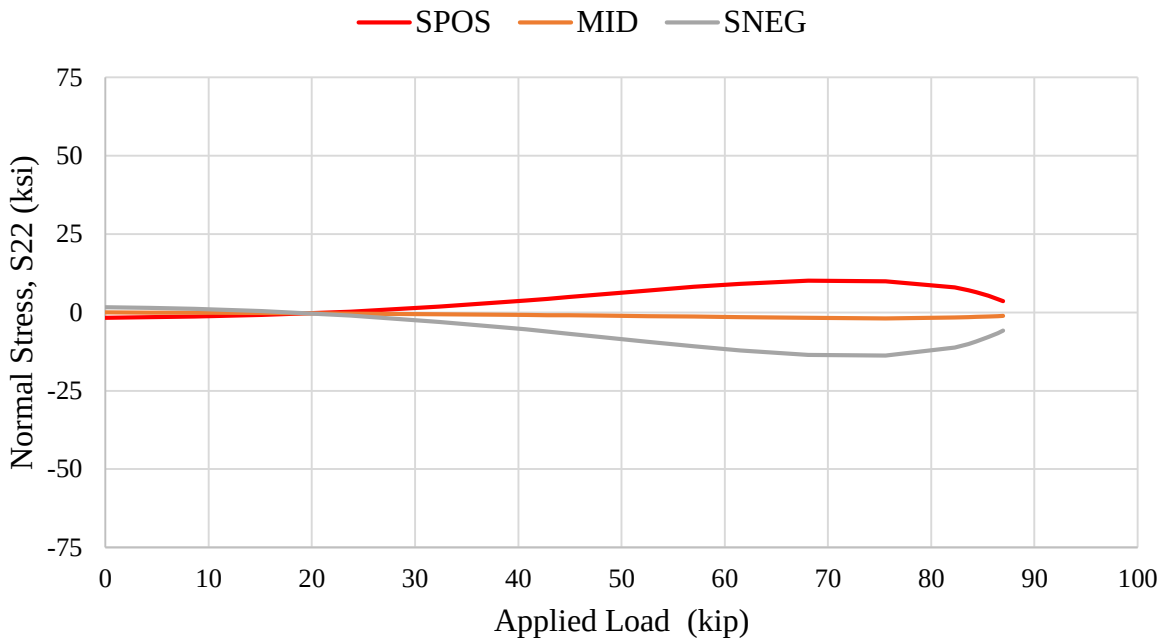

Fig. 7-38. Normal Stress *S22* at top, mid and bottom surface of the web versus applied load for Element 4 at web-top.

For Element 2, the stress, *S22* at the mid-surface remains nearly equal to zero up to almost 95% of the peak load. After this, there is a small increase in the stress at mid-surface. The maximum *S22* at the peak load for Specimens UK6 and G7 occurred near the transverse stiffener. However, due to high *a/h* of UK7, maximum *S22* happened at 31 inches from the transverse stiffness. The stresses *S22* at the mid-surface at Elements 1 and 3 remain approximately equal to zero for all levels of loading. The *S22* value at the mid-surface for Element 4 increases progressively from zero load until almost 80% of the peak load. After that it decreases slightly. At the post peak, *S22* increases further (Fig. 7-28) showing that this Element is unaffected by the web buckling. The *S22* values at the top and bottom surface of the web are smaller for Element 4 compared to Elements 1, 2 and 3, indicating that there is lesser tendency for rotation of the web about the web-flange juncture near the transverse stiffener on the right-hand end of the panel at the top-flange.

From these plots, it can be stated that the top-flange provides substantial torsional restraint to the top of the web throughout the loading and into post-peak. However, from Fig. 7-28, it is clear that the web membrane force remains almost zero until 95% of the peak load but increases significantly at the post peak load level and there is significant pushing and pulling of the top flange at a certain distance from the leftmost end of the specimen.

7.3 Responses at a Section Along the Length at the Bottom of the Web

A procedure similar to that discussed in Section 5.3 is repeated in this section for the web and bottom flange juncture of Specimen UK6. The quantities plotted are the web membrane stresses, *S11*, *S22* and *S12*, the von Mises stress, *S*, the maximum principal tensile membrane stress (*S1*), the maximum principal compressive membrane stress (*S2*) and the orientation of the principal stresses *(θ_p).* Figures 7-39 through 7-45 show variation of these quantities, in that order, at a section along the length at the web bottom for different levels of loading.

In all these figures, the behavior of right side of the specimen follows the results from beam theory and the variations are similar to the variations at the top flange.

Similar to UK6 and G7 (Fig. 6-39 and 5-39, respectively), for 95% of the peak load and the peak load, there is a sudden decrease in the compressive stress *S11* (Fig. 7-39) near the mid-span. Though, for post peak load, *S11* is minimum at a normalized position of 0.33 which is around 100 inches from the left end of the specimen, this is where the buckled web meets the bottom flange. This buckled web met UK6 and G7 near the mid-span and due to high *a/h* of UK7, this meets at a distance from the mid-span of the specimen.

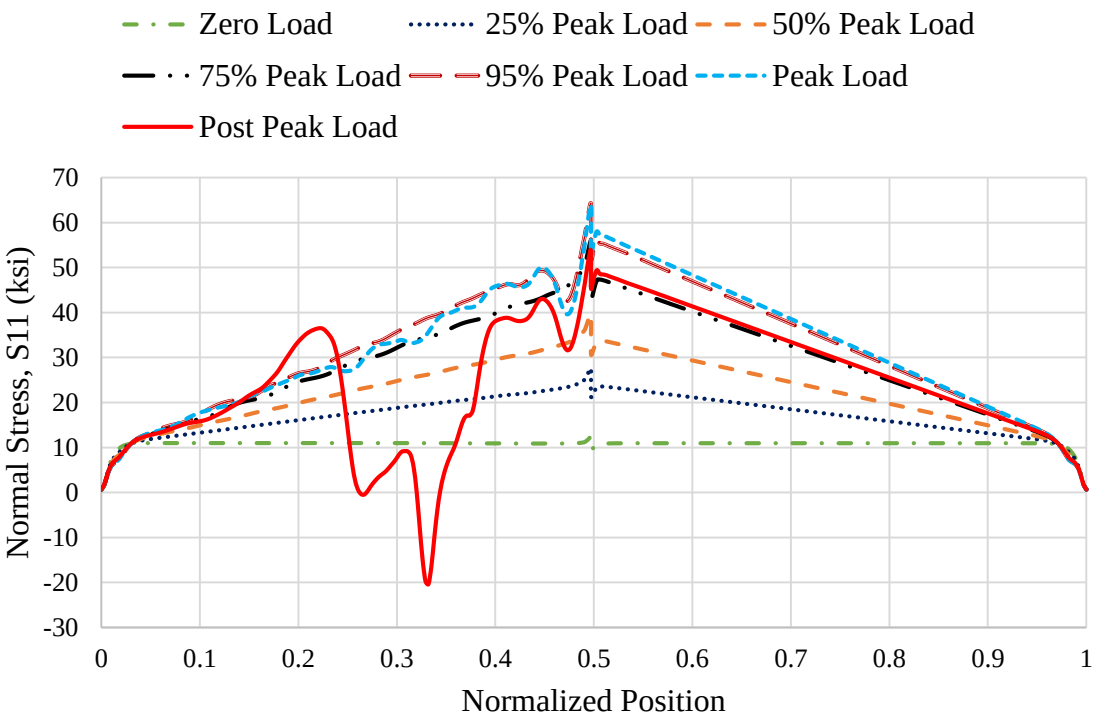

Fig. 7-39. Normal Stress *S11* vs normalized position at web bottom.

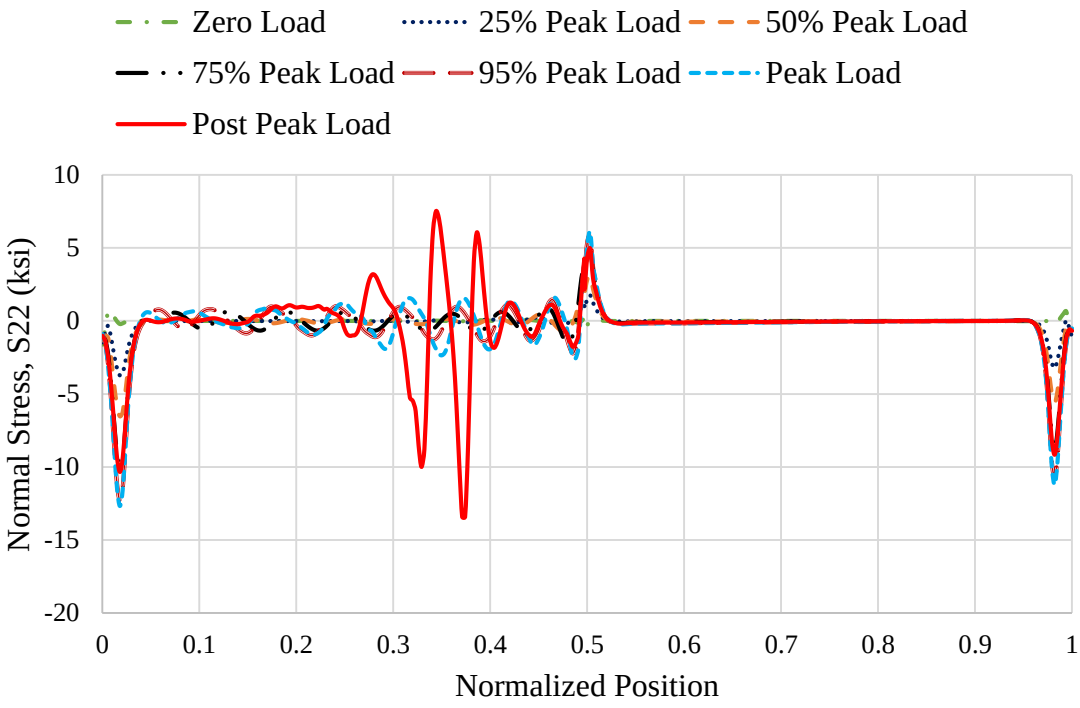

Fig. 7-40. Normal Stress *S22* versus normalized position along the web-bottom.

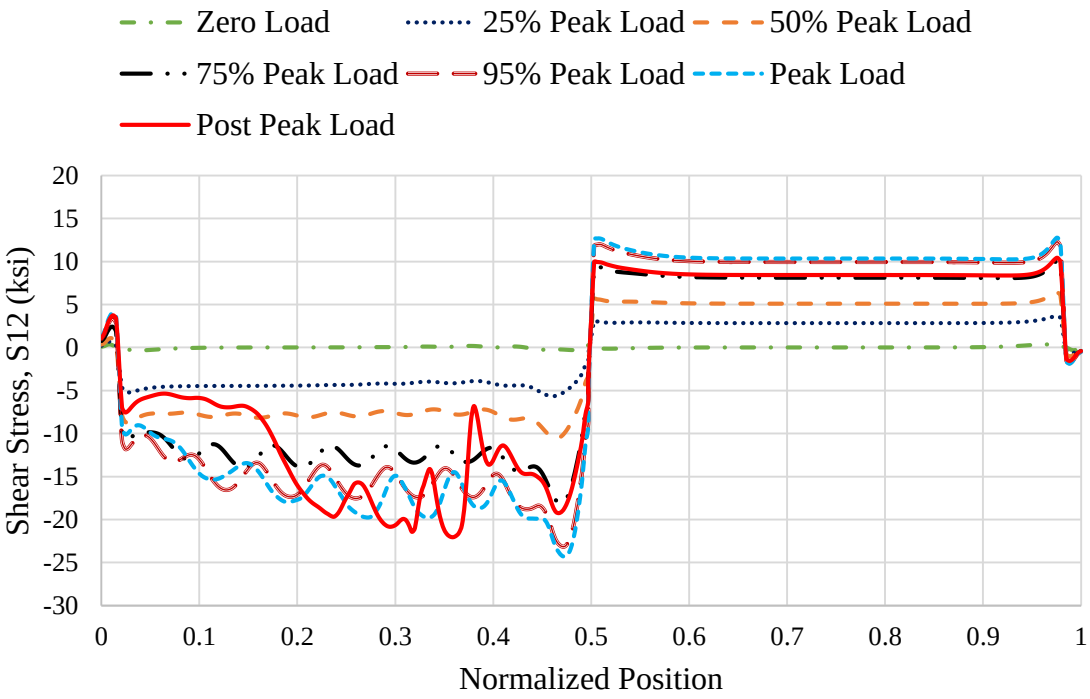

Fig. 7-41. Shear Stress *S12* vs normalized position along the web-bottom.

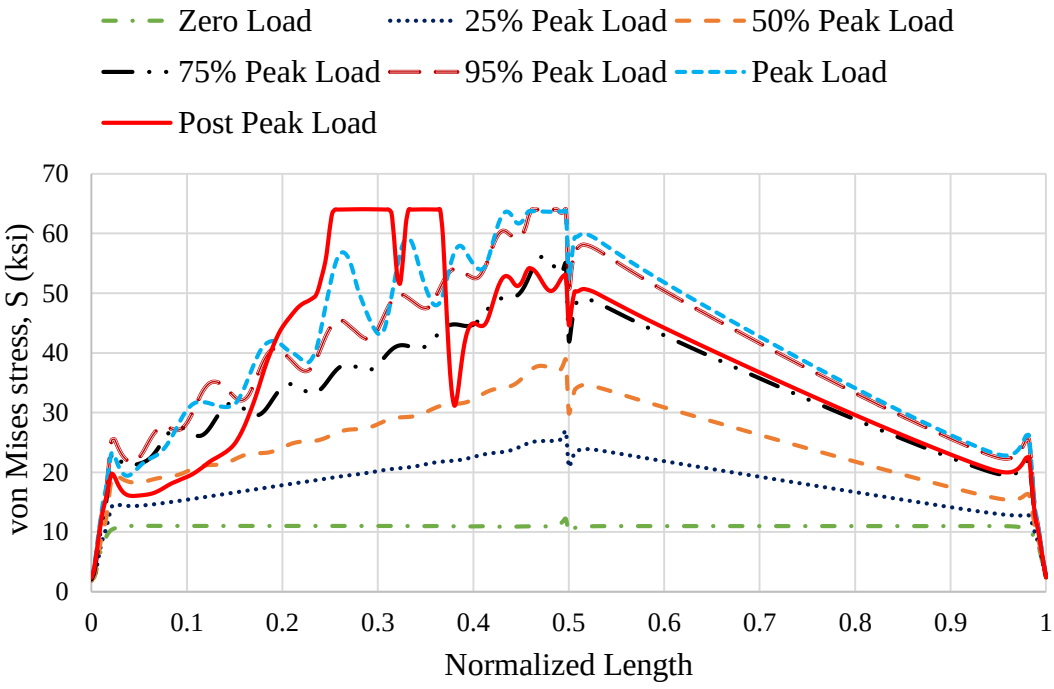

Fig. 7-42. von Mises stress *S* versus position along the web bottom.

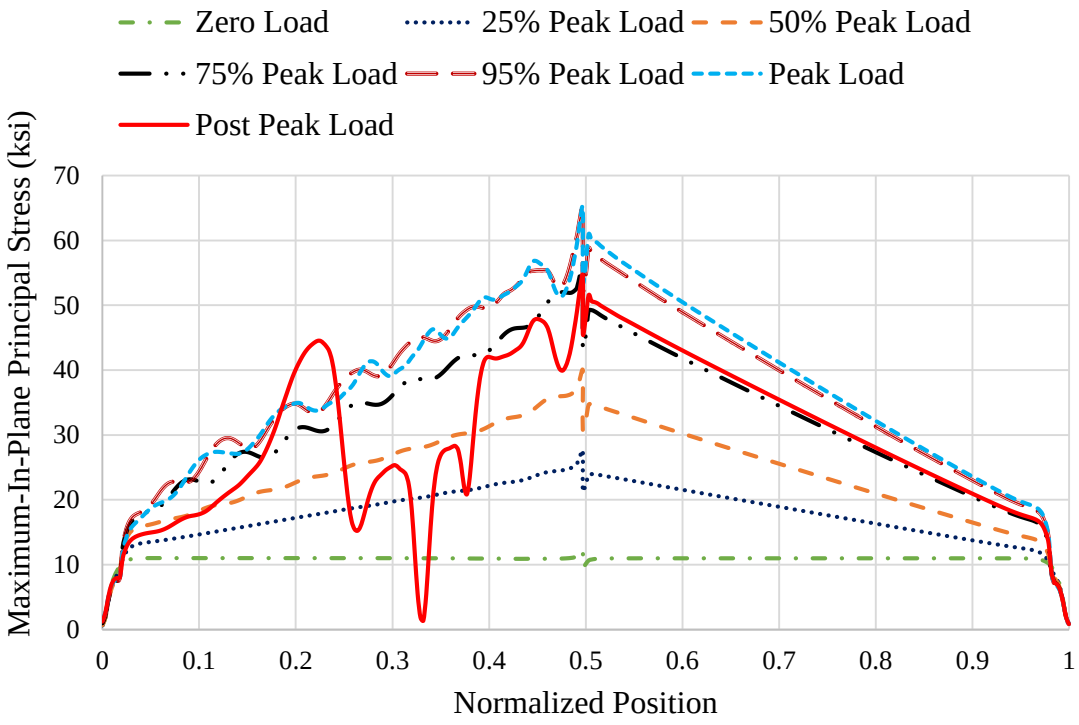

Fig. 7-43. Maximum In-Plane Principal stress *S1* versus position along web bottom.

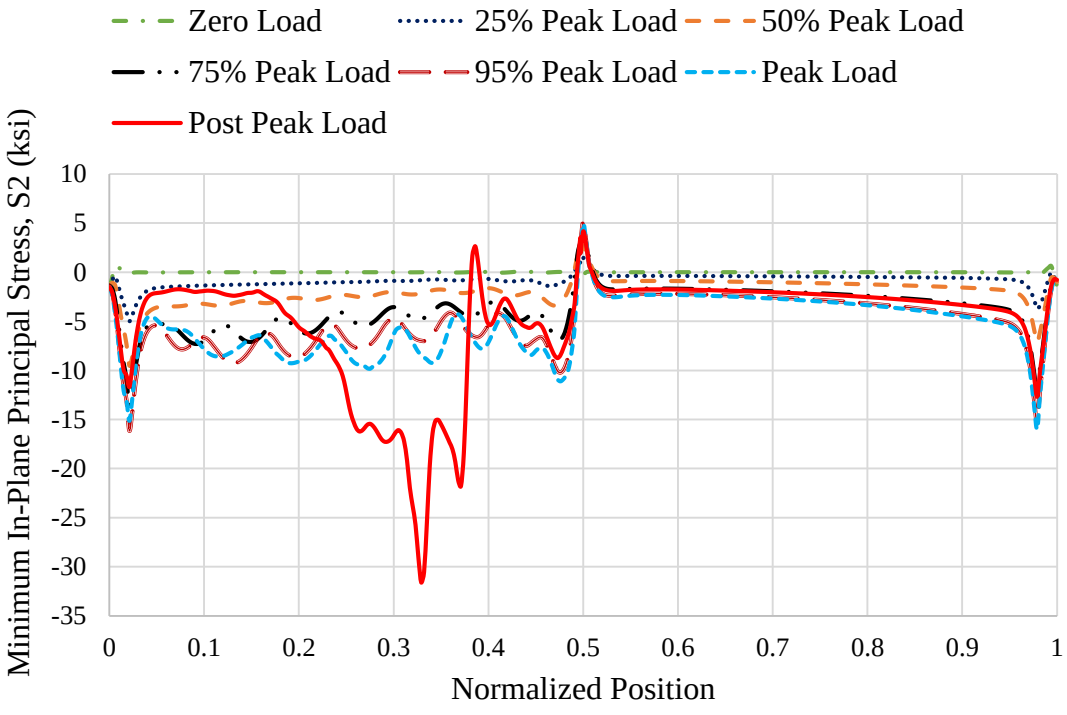

Fig. 7-44. Minimum In-Plane Principal stress *S2* versus position along web bottom.

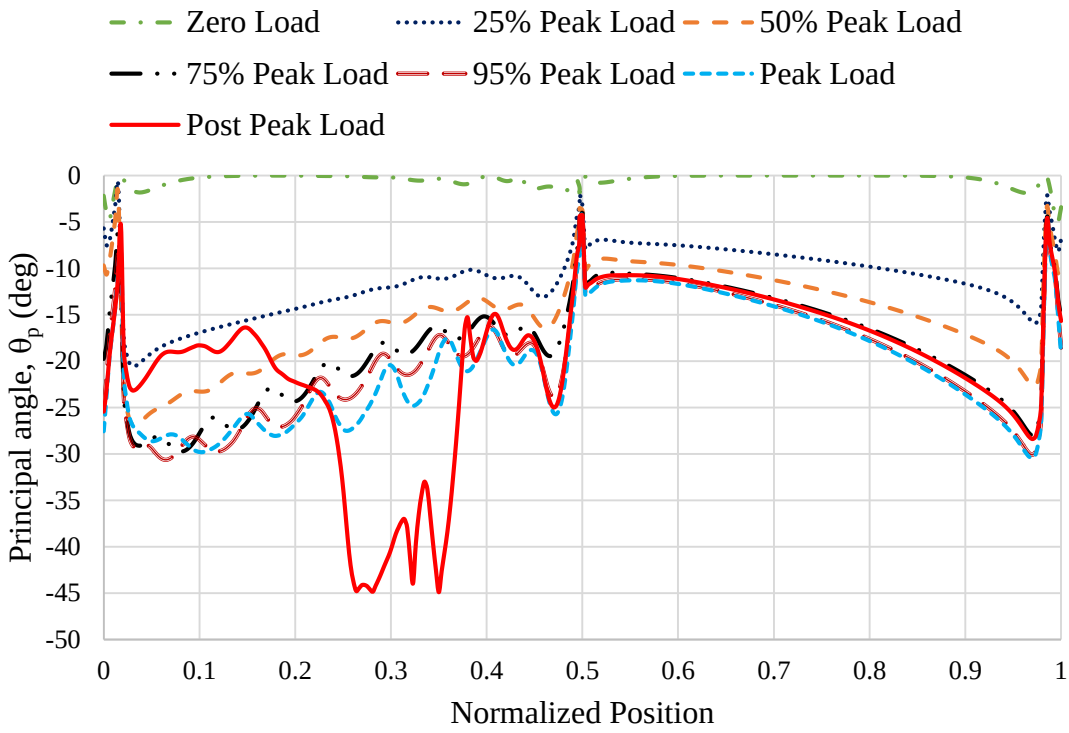

Fig. 7-45. Principal Angle θ_p versus position along the web bottom.

Similar to the top flange, *S22* (Fig. 7-40) follows the cyclic nature for almost all the load levels. The behavior was not at all cyclic for UK6 (Fig. 6-40). At post-peak load, *S22* increases extremely at the location of minimum *S11* at the post peak load. This where the web buckle meets the bottom flange as well as where forces transferred by diagonal tension need to be balanced by a vertical compression force transfer to the applied load location. The failure band meets the bottom flange at a normalized position of 0.33. This failure band met UK6 and G7 near the mid-span and due to high *a/h* of UK7, this meets at a distance from the transverse stiffener of the panel.

Along bottom flange (Fig. 7-41), the Elements near mid-span are subjected to the largest shear stress and the Elements near the support are subjected to smaller shear stress until the peak load. This was also observed for specimen G7 and UK6. (Fig. 5-41 and 6-

41, respectively). However, at the post peak load, the maximum *S12* occurs at the location where buckled web meets the bottom flange.

The von Mises stress *S* (Fig. 7-42), indicates that there is some yielding of the web bottom even at 95% of the peak load. This yielding is also due to high normal stress *S11* in near the mid-span. However, as we go in the post peak load, the yielding of the web is concentrated at the location where buckled web meets the bottom and there is no yielding of the web near the mid-span. At the post peak, this yielding in G7 and UK7 (Fig. 5-42 and 6-42, respectively) occurred near the right end of the panel.

The behavior of the principal stresses *S1* and *S2* at the bottom flange (Fig. 7-43 and 7-44, respectively) can be related to the behavior at top flange. *S1* follows the curve of *S11* for almost the entire length of specimen and the increase in *S2* near the right end of the panel is due to the increase in *S12* at that location until peak load. However, at the peak load, the stresses increase at normalized length 0.33. Due to high *a/h*, the buckled web meets the top and bottom meets at a distance from the ends of the panel. For Specimen G7 and UK6, due to comparatively lower *a/h*, the buckled web meets the ends of the panel and the stresses *S1* and *S2* at the post peak are higher near the ends of the panel.

7.3.1 Boundary Condition between Bottom Flange and Web

A procedure similar to that in Section 6.2.1 is repeated at the bottom flange in this section. Four Elements are selected along the bottom flange to investigate the boundary condition between the bottom flange and the web.

The first, second and third Element are selected at a distance of 12, 157 and 107 inches respectively from the left end of the specimen. The fourth Element is selected at 9 inches from the mid-span, location where the maximum *S22* occurs at the peak load. The definitions SPOS, MID and SNEG are defined in Section 5.2.1. Figure 7-46 shows the

location of these elements. Figures 7-47 through 7-50 shows the variations of *S22* at these Elements as a function of the applied load.

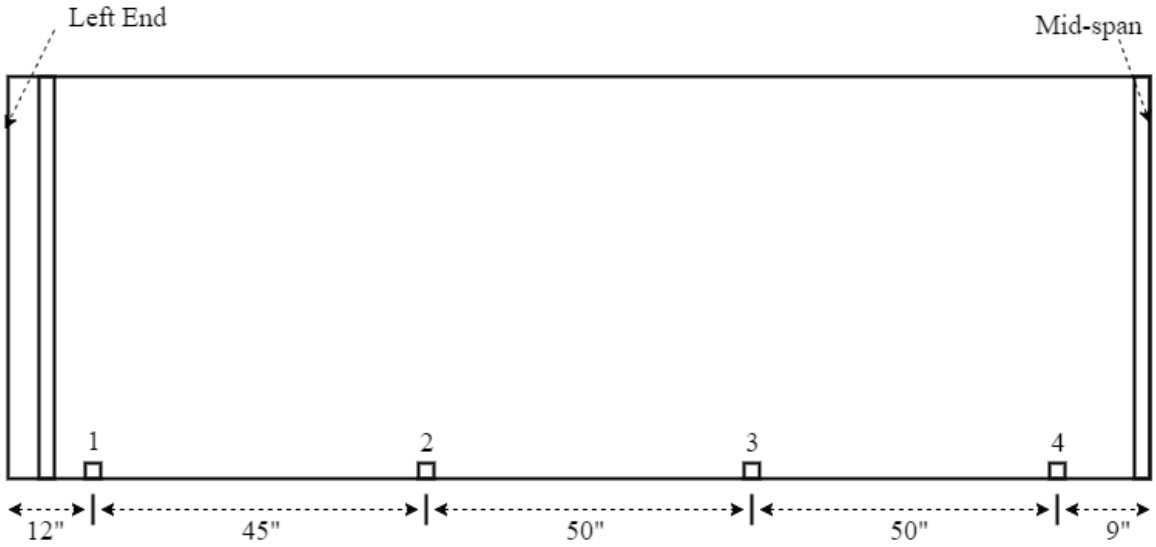

Fig. 7-46. Elements along the web bottom.

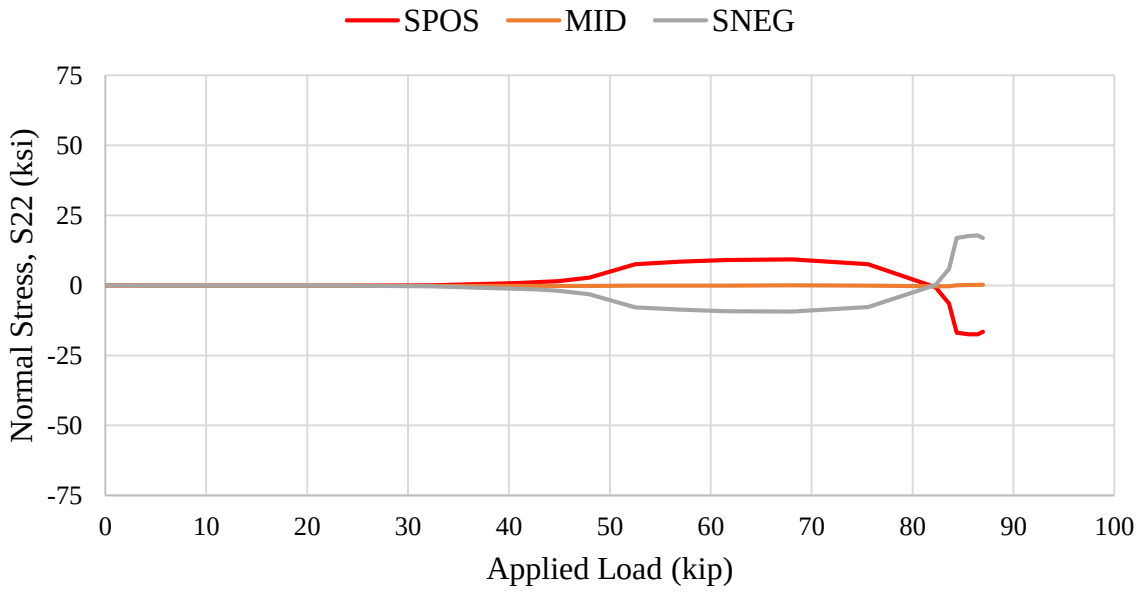

Fig. 7-47. Normal Stress *S22* at top, mid and bottom surface of web versus applied load for Element 1 at web-bottom

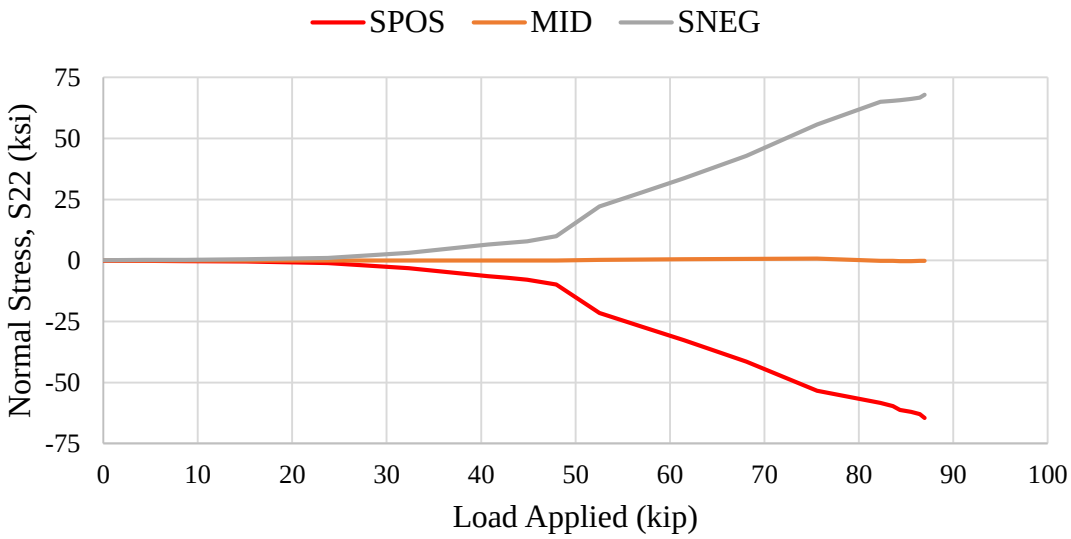

Fig. 7-48. Normal Stress *S22* at top, mid and bottom surface of web versus applied load for Element 2 at web-bottom.

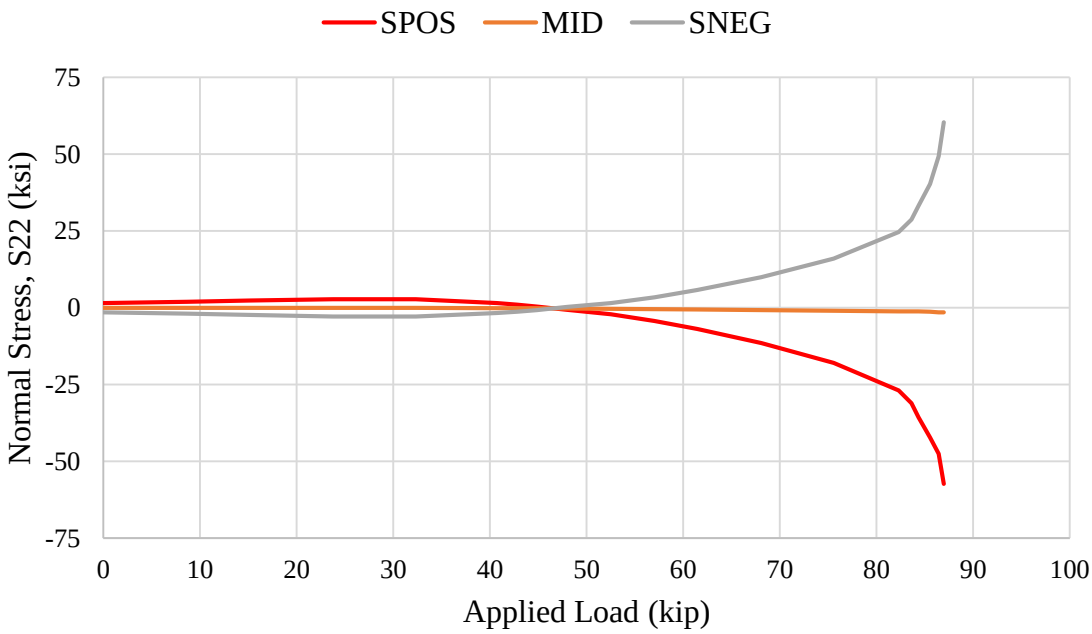

Fig. 7-49. Normal Stress *S22* at top, mid and bottom surface of shell versus applied load for Element 3 at web-bottom.

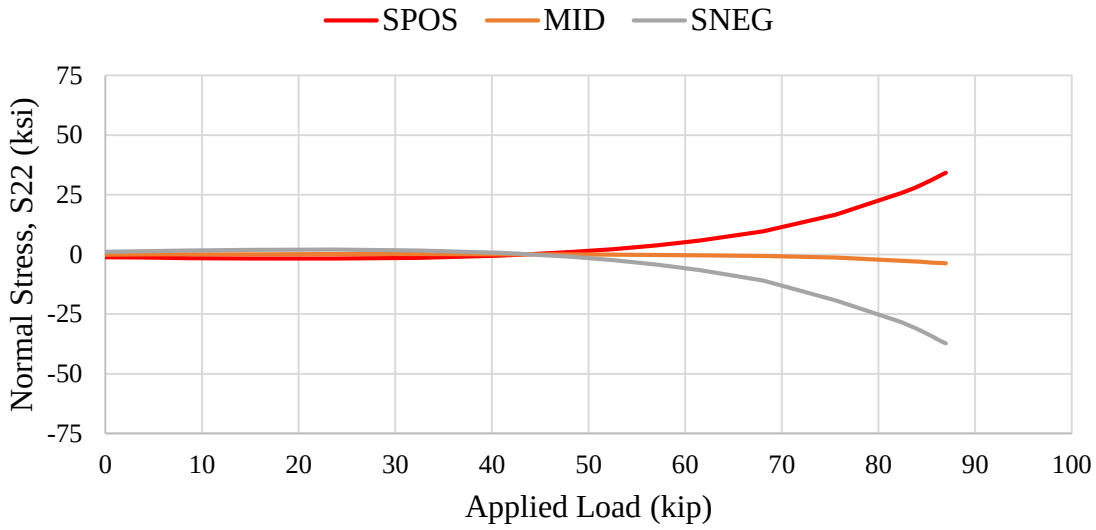

Fig. 7-50. Normal Stress *S22* at top, mid and bottom surface of shell versus applied load for Element 4 at web-bottom.

The behavior illustrated by these figures is very similar to the behavior at the web top flange juncture, except that the rightmost element has the maximum membrane stress at the peak load and the rotation of elements near the left end of the specimen is minimum. However, the web buckle meets at a distance from the right end of the panel, unlike UK6 and G7. From Fig. 7-40, it is clear that there is significant pushing and pulling of the bottom flange at a distance from mid-span at the post peak load level.

7.4 Stresses at Several Sections Through the Web-Depth

In this section the procedure followed in Section 5.4 is followed for Specimen UK7. The quantities plotted are the web membrane stresses, *S11*, *S22* and *S12*. Figures 7-52 through 7-63 show these quantities, at several sections taken through the web-depth for different levels of loading. The locations of these Sections along the web-depth are shown in Fig. 7-51. The first Section is located at 10 inches from the left end of the panel. The

second Section is selected at 33 inches from the left free end of the specimen, this is where maximum *S22* occurs at the post peak load and the buckled web meets the top flange. The third Section is selected at the mid-span of the panel. The fourth Section is selected at 110 inches from the left free end of the specimen, this is where maximum *S22* occurs at the post peak load and the buckled web meets the bottom flange. The fifth Section is selected at 10 inches from the right end of the panel.

To simplify the plots, the normalized position along the web-depth is employed. The position 0.0 denotes the web bottom and 1.0 denotes the web top. Position 0.5 is located at the web mid-depth. The normalized position is plotted as the ordinate, emphasizing the fact that these section cuts are vertical rather than horizontal.

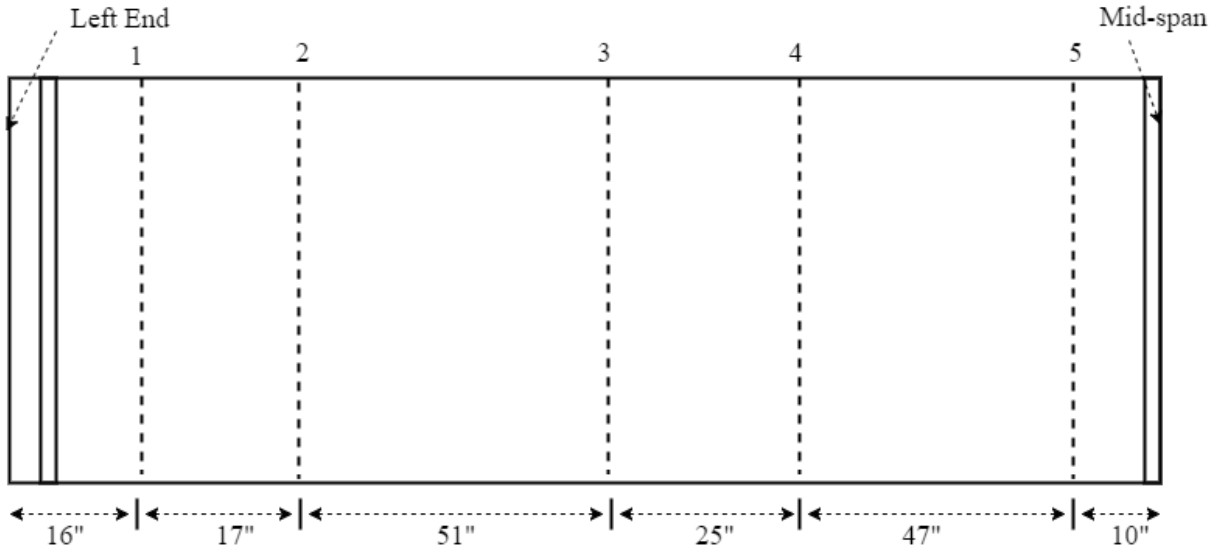

Fig. 7-51. Section along the web-depth.

1. Stresses at Section 1

This Section is cut at 10 inches from the left end of the panel.

The normal stress *S11* (Fig. 7-52) is relatively small at the web mid-depth up to 75% of the peak load. However, at loadings above that load level, significant diagonal tension is developing near the transverse stiffener. This increase in normal stress is located more in

the top half of the web. However, unlike G7 and UK6 (Fig. 5-51 and 6-52), *S11* after the peak load does not increase much. This is because the failure band is not predominant near the left end of the panel and meets at 27 inches from the left panel.

The normal stress *S22* (Fig. 7-53) is relatively small at the top of the web until almost 75% of the peak load, and it increases considerably at the peak load. The stress *S22* at bottom is close to zero. Similar to *S11* variation, *S22* does not increase after the peal load and there is a reduction in *S22* at the post peak load.

The shear stress *S12* (Fig. 7-54) does not increase much at the web bottom after 50% of the peak load. However, *S12* increases at top of the web. Similar to *S11* and *S12*, *S22* decreases at the post peak load. This is because the buckled web in UK7 does not meet the top flange at the left end of panel like UK6 and G7.

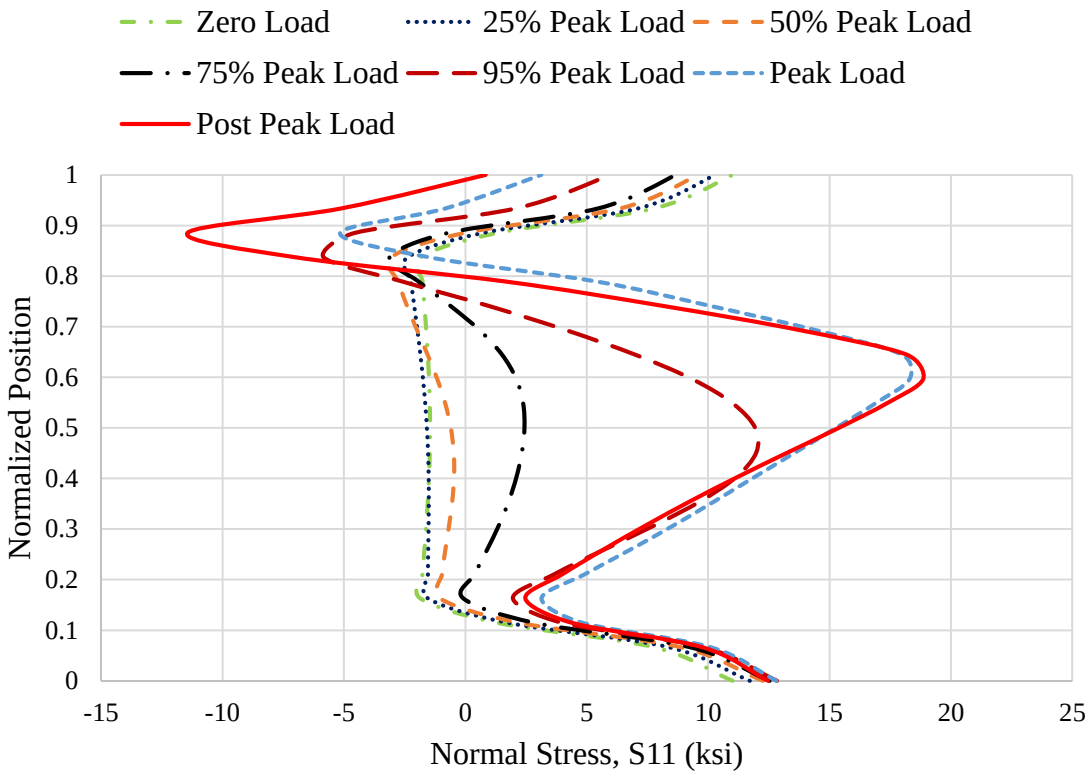

Fig. 7-52. Normalized position versus normal stress *S11* at Section 1.

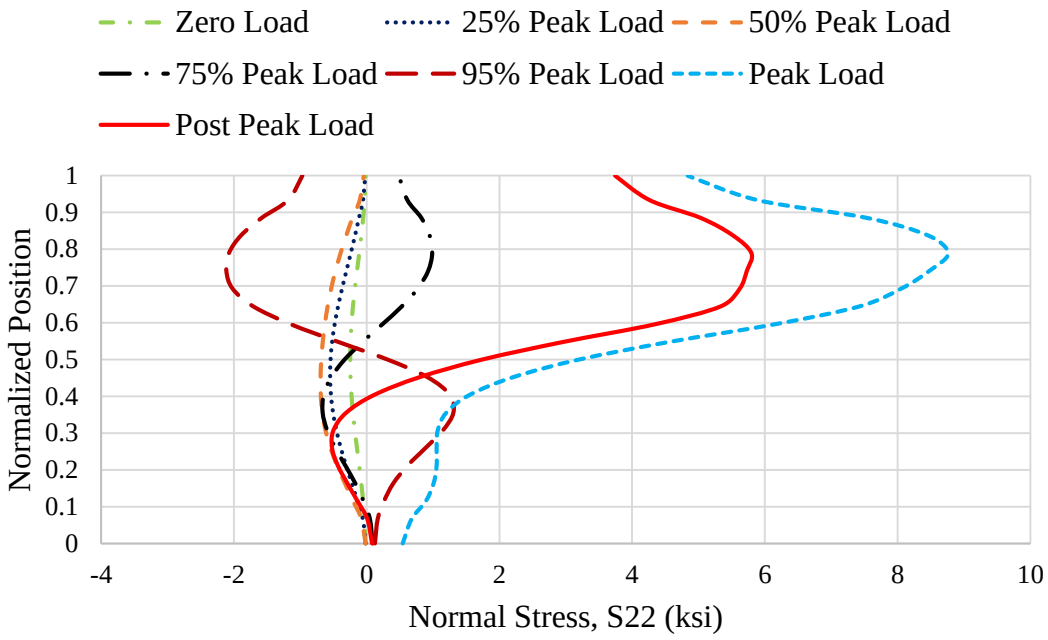

Fig. 7-53. Normalized position versus normal stress *S22* at Section 1.

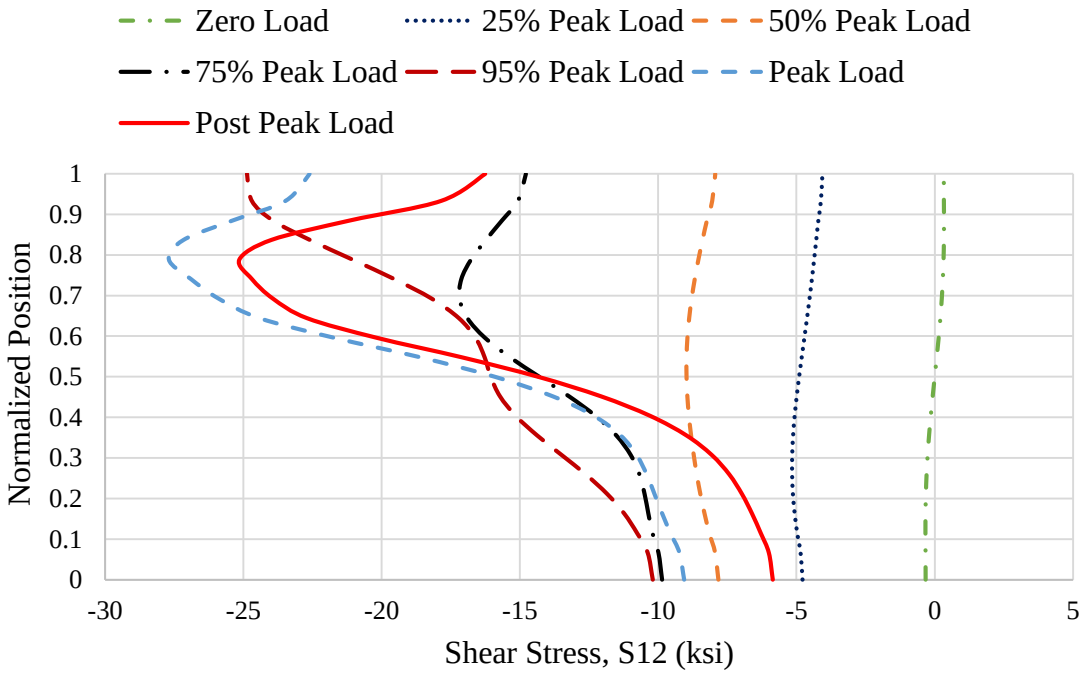

Fig. 7-54. Normalized position versus shear stress *S12* at Section 1.

2. Stresses at Section 2

This Section is located at 33 inches from the left-hand free end of the specimen. This is where the buckled web meets the top flange.

The normal stress *S11* (Fig. 7-55) is at the mid-depth is very small until about 50% of the peak load. However, we can clearly see considerable diagonal tension forming even at 75% of the peak load and it increases rapidly as the loadings is increased. At the post peak load, considerable amount of compression is formed at top of the web.

S22 is almost zero for all the levels of loadings at the bottom of the flange. However, at the top flange significant *S22* is formed at the post peak load.

The shear stress *S12* (Fig. 7-57) at the web top is more than the *S12* at the bottom. However, the difference increases considerably at the post peak load. At the peak load, there is not much effect of web buckling at this location, however at post peak load, this is the location where buckled web meets the top flange which causes such variations in *S12*, *S11* and *S22*.

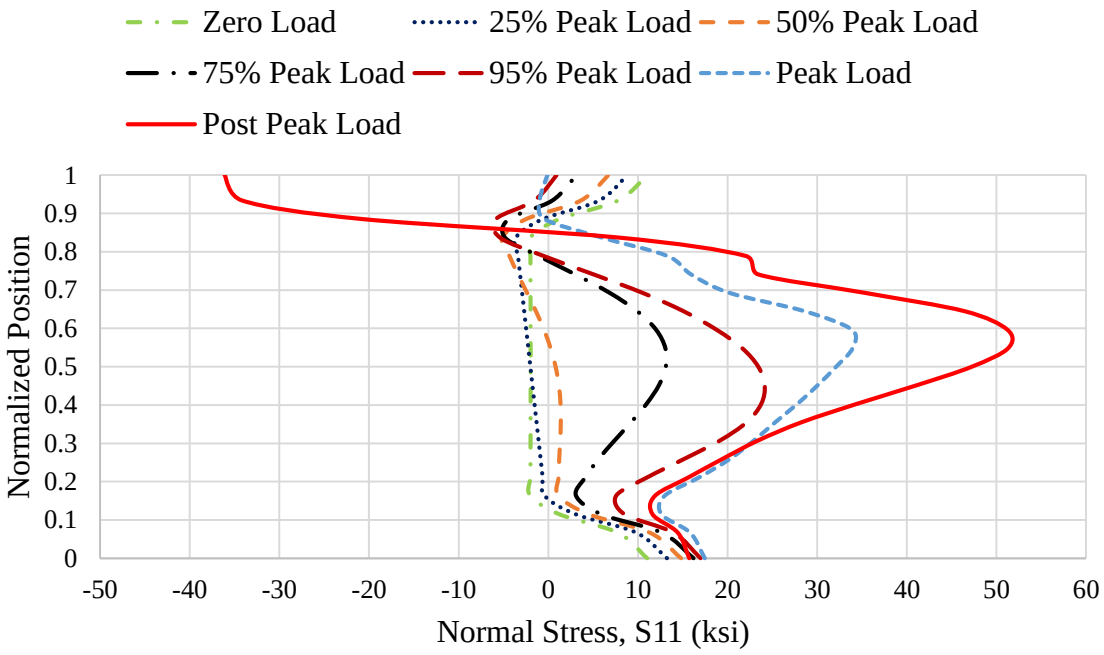

Fig. 7-55. Normalized position versus normal stress *S11* at Section 2.

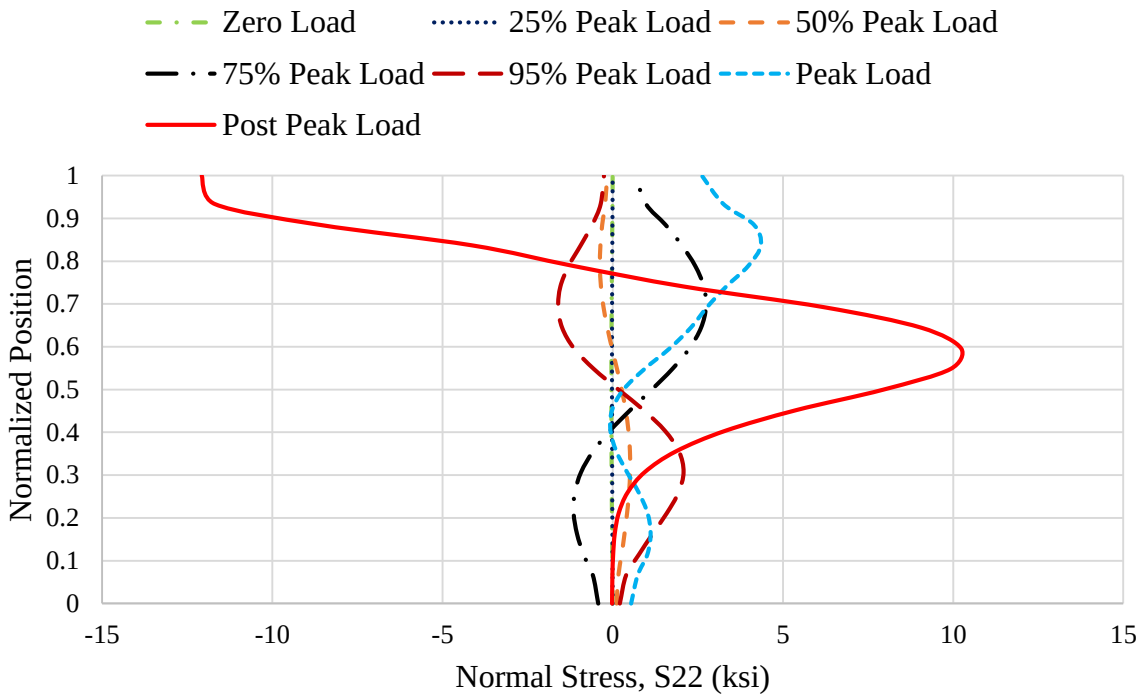

Fig. 7-56. Normalized position versus normal stress *S22* at Section 2.

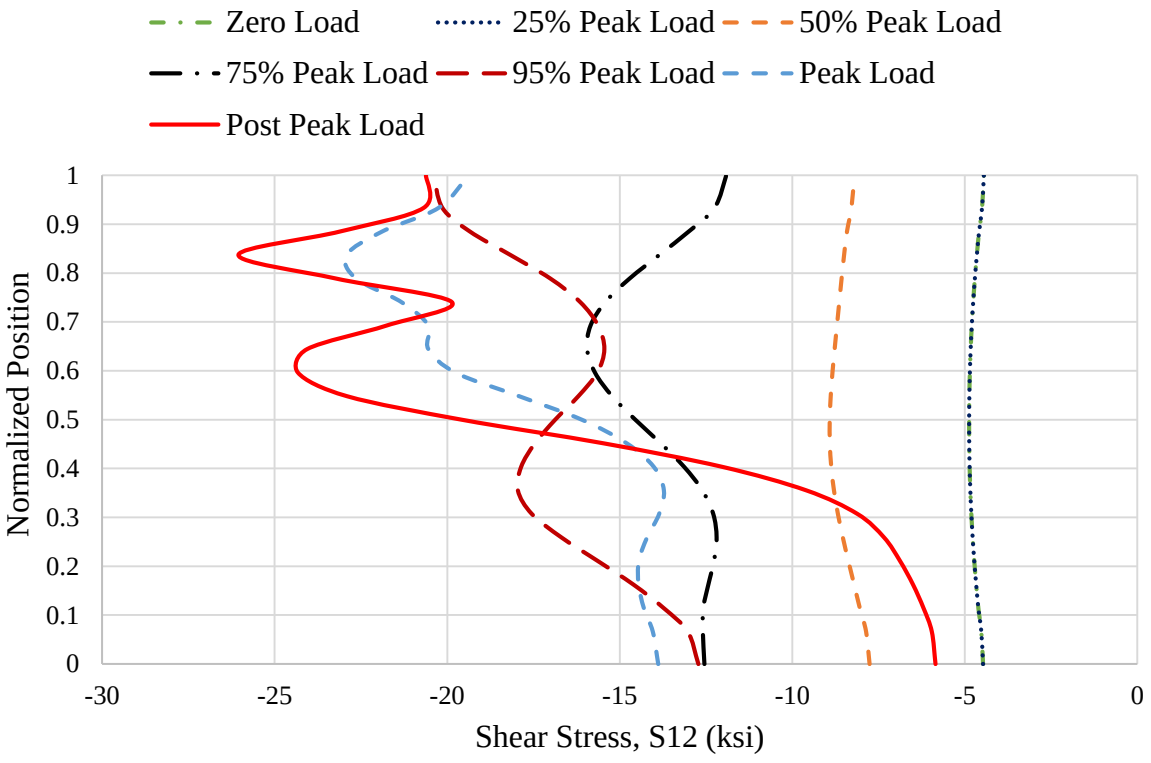

Fig. 7-57. Normalized position versus shear stress *S12* at Section 2.

3. Stresses at Section 3

This Section is located at the mid-length of the panel.

The behavior of *S11* in Section 3 is similar to the behavior in Section 1. However, diagonal tension at 75% of the peak load is higher for Section 3.

The normal stress *S22* at top and bottom of the web is higher than its values at the top and bottom at the mid-length of the panel for UK6 and G7. This is due to higher a/h of the panel for UK7. However, this value is relatively less compared to *S22* at top in Section 2 and *S22* at bottom in Section 4.

The shear stress *S12* at the top and bottom does not differ much until about 75% of the peak load. After that, *S12* at bottom increases and *S12* at top decreases.

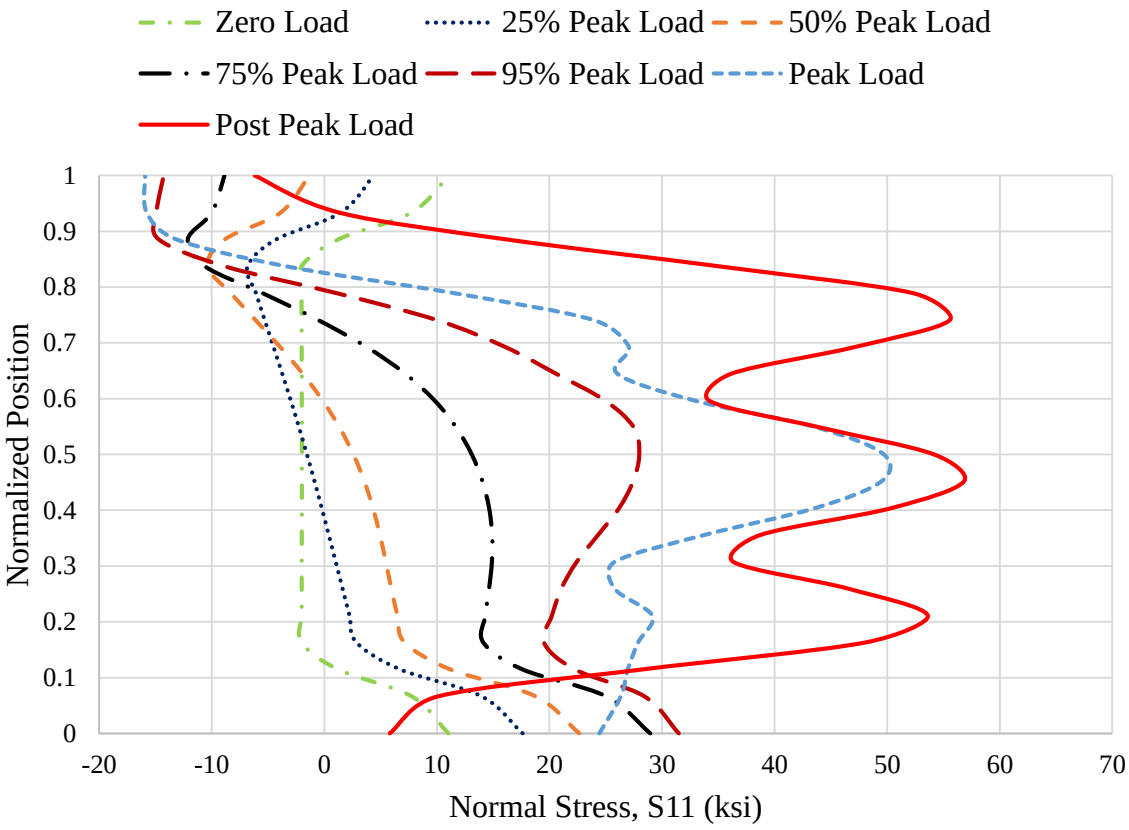

Fig. 7-58. Normalized position versus normal stress *S11* at Section 3.

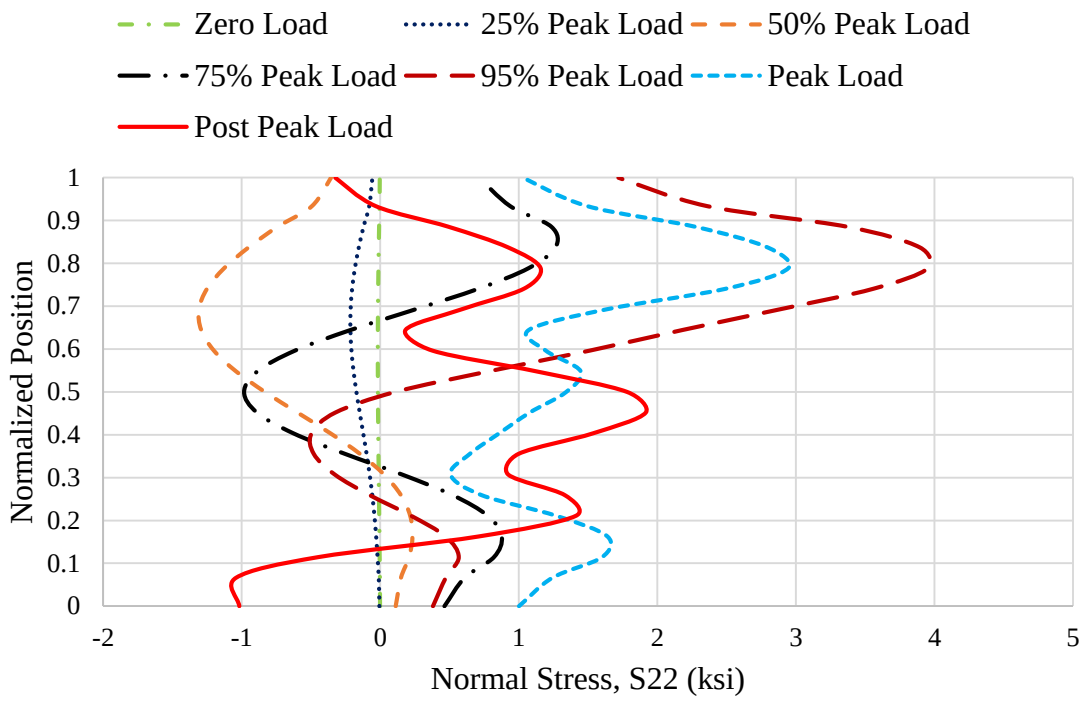

Fig. 7-59. Normalized position versus normal stress *S22* at Section 3.

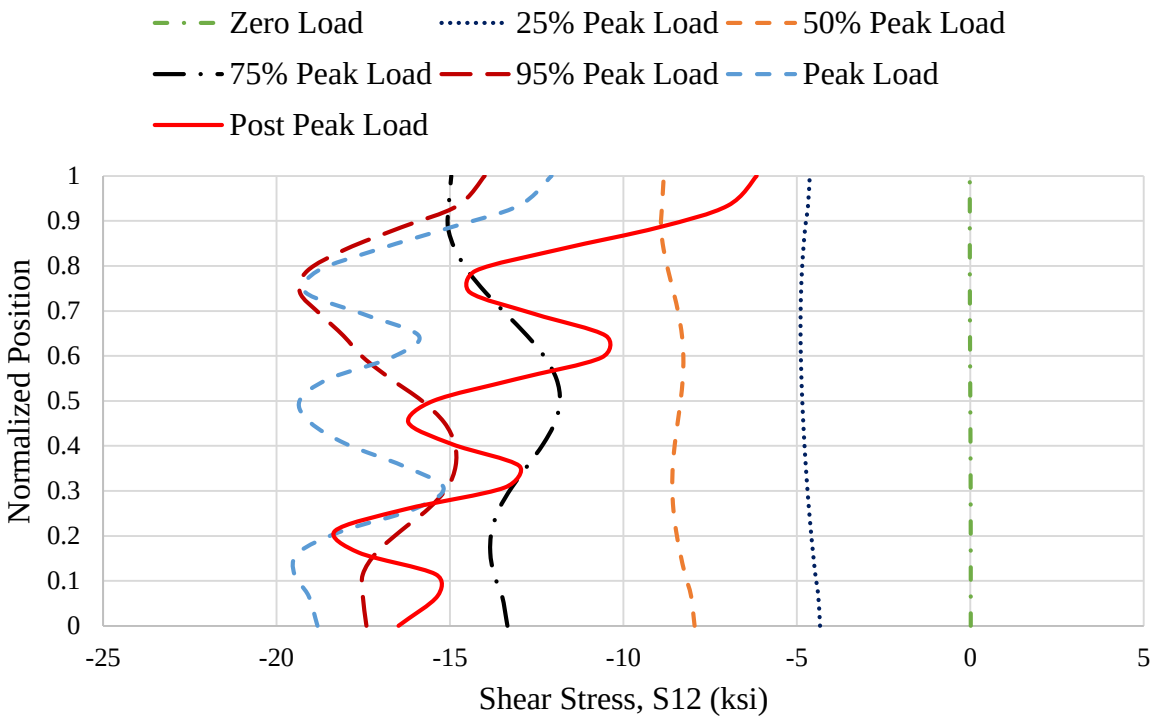

Fig. 7-60. Normalized position versus shear stress *S12* at Section 3.

4. Stresses at Section 4

This Section is located at 110 inches from the left-hand free end of the specimen. This is where the buckled web meets the bottom flange.

The normal stress *S11* is more concentrated towards the bottom half of the web at the post peak load, unlike Section 2, where it was more concentrated at the top half of the web. At the post peak load, considerable amount of compression is formed at bottom of the web.

S22 is almost zero for all the levels of loadings at the bottom of the flange except at the peak and the post peak load. Similar to Section 2, considerable *S22* is formed at the post peak load at the bottom of the web

The shear stress *S12* at the web top is less than the *S12* at the bottom. However, the difference increases considerably at the post peak load. At the peak load, there is not much effect of web buckling at this location, however at post peak load, this is the location where buckled web meets the bottom flange.

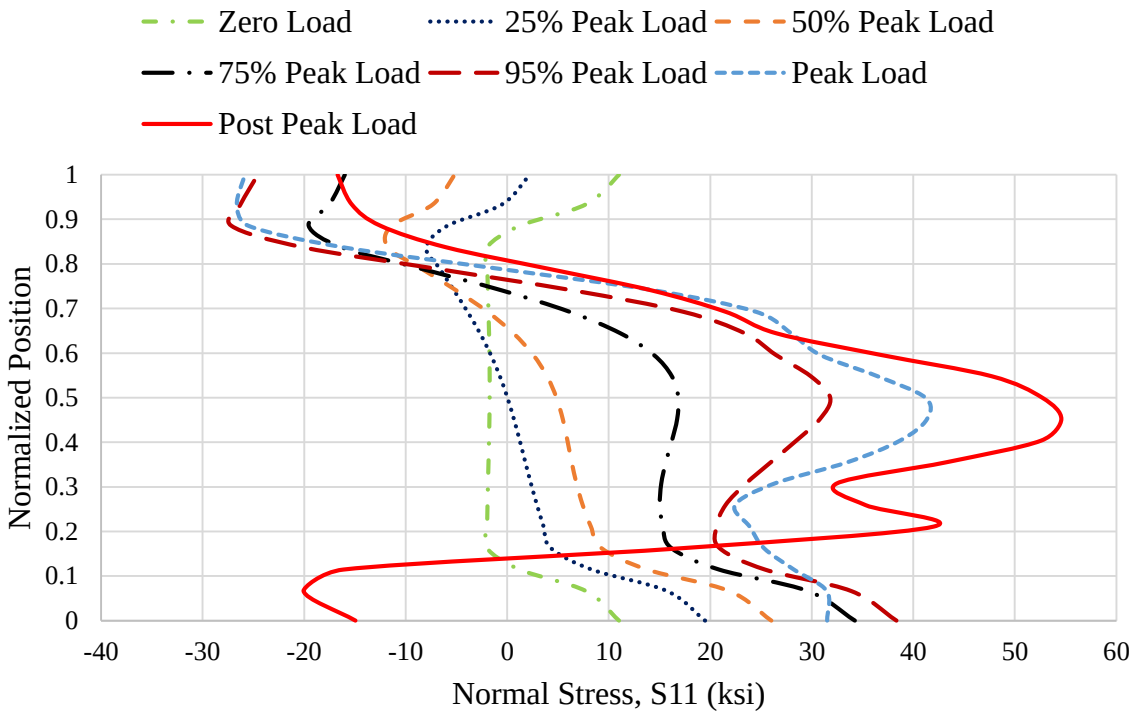

Fig. 7-61. Normalized position versus normal stress *S11* at Section 4.

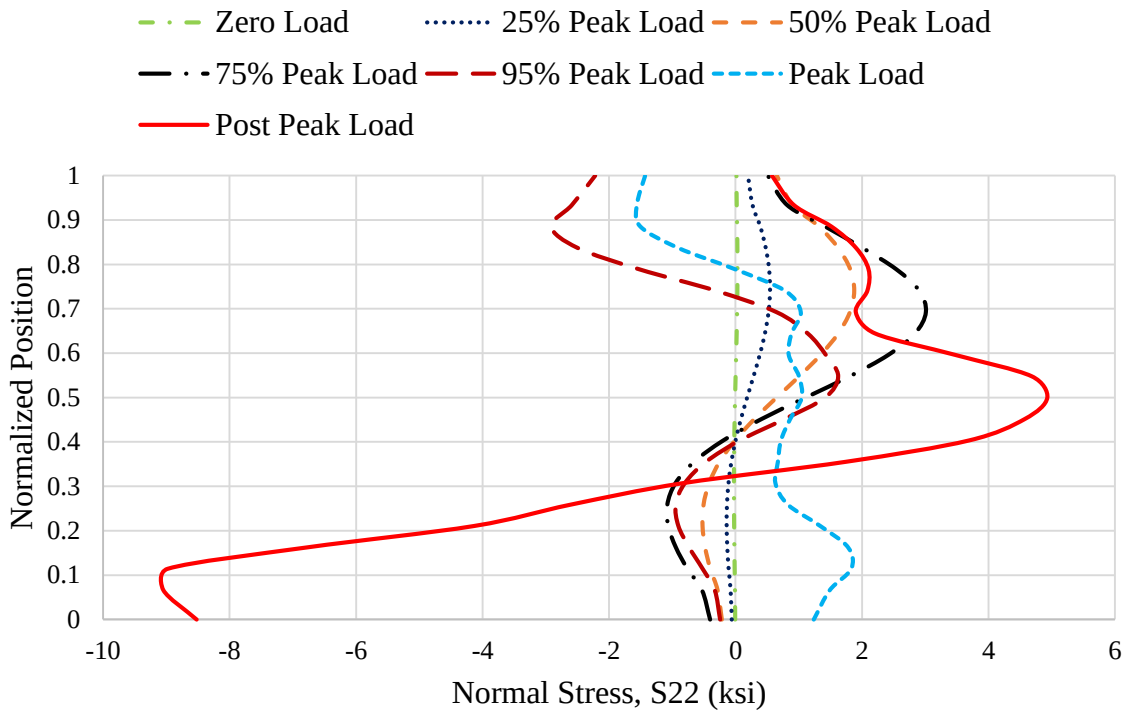

Fig. 7-62. Normalized position versus normal stress *S22* at Section 4.

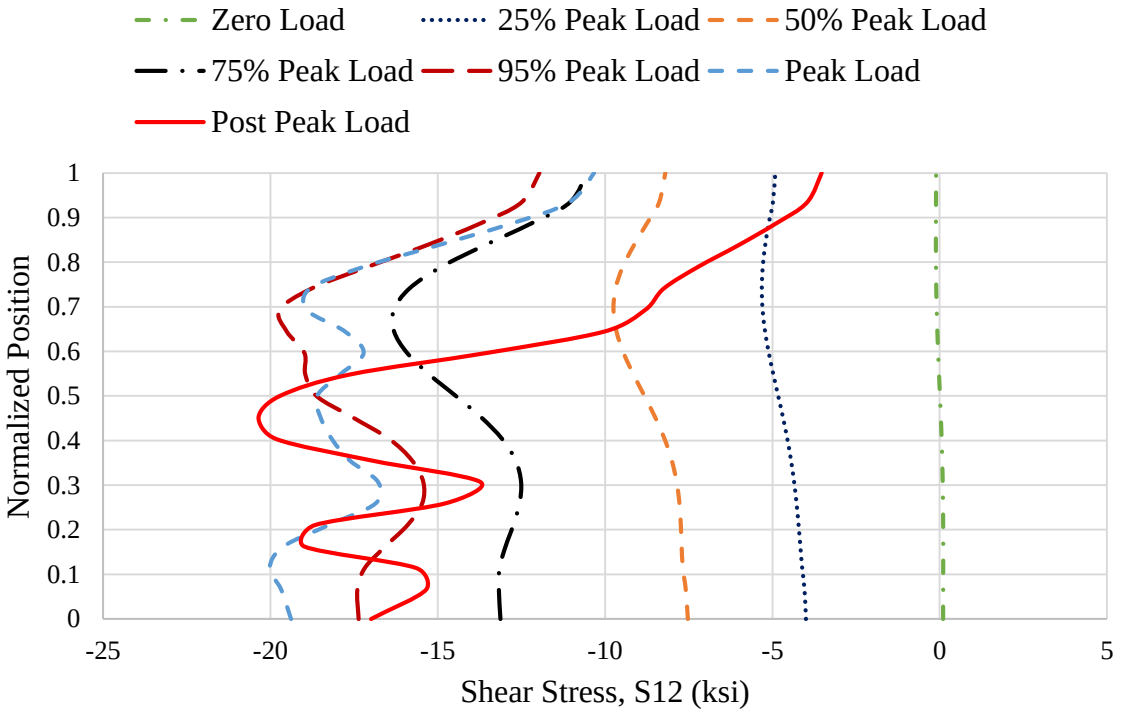

Fig. 7-63. Normalized position versus shear stress *S12* at Section 4.

5. Stresses at Section 5

This Section is located at 10 inches from the right end of the panel.

S11 is majorly affected by the flexural stresses. However, some diagonal tension is also developing causing in increase in *S11* at the mid-depth of the web.

S22 at top and bottom does not increase after the peak load and hence indicates that this is not the location where buckled meets the bottom flange. For girder G7 and Uk6, the buckled meets the flange near the right end of the panel.

The behavior of *S12* until the peak load is similar to behavior of *S12* at Section 3 for G7 and Section 4 for UK6, i.e., *S12* at bottom is more than *S12* at top. However, at post peak load *S12* decreases indicating this is not the location where buckled web meets the bottom flange.

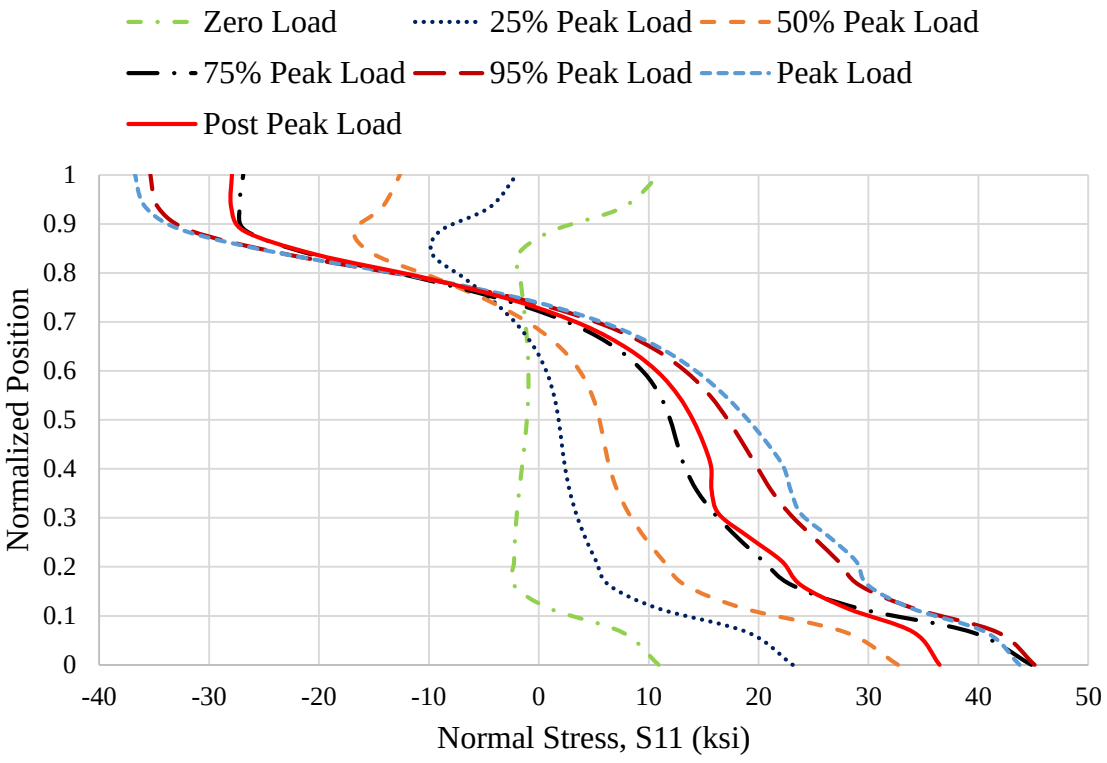

Fig. 7-64. Normalized position versus normal stress *S11* at Section 5.

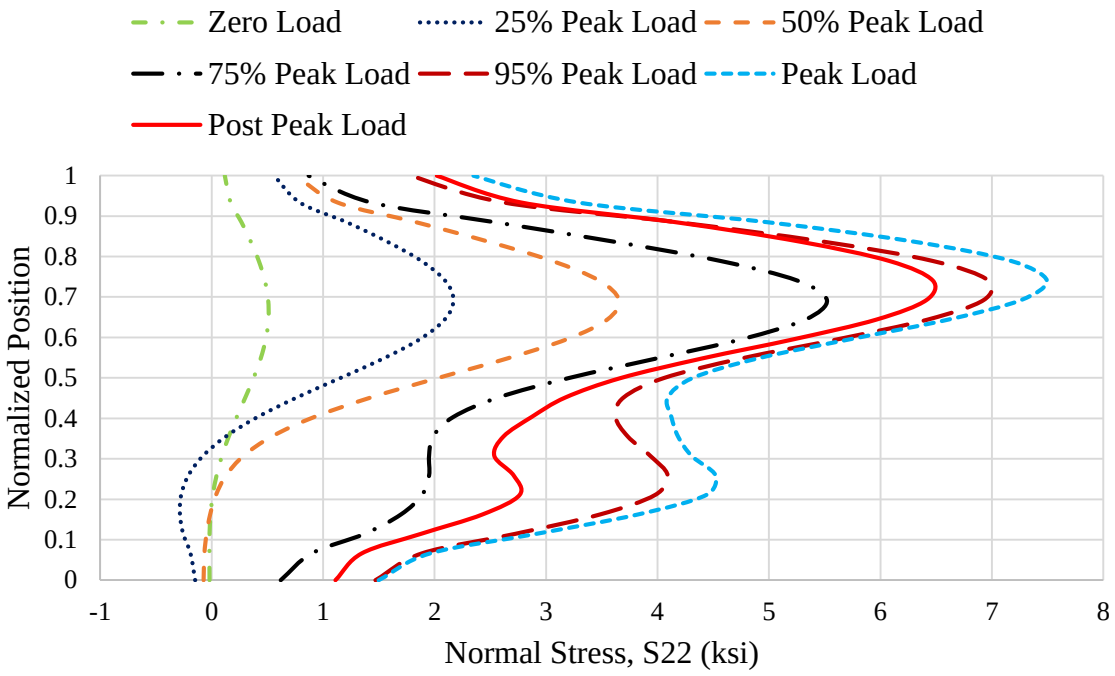

Fig. 7-65. Normalized position versus normal stress *S22* at Section 5.

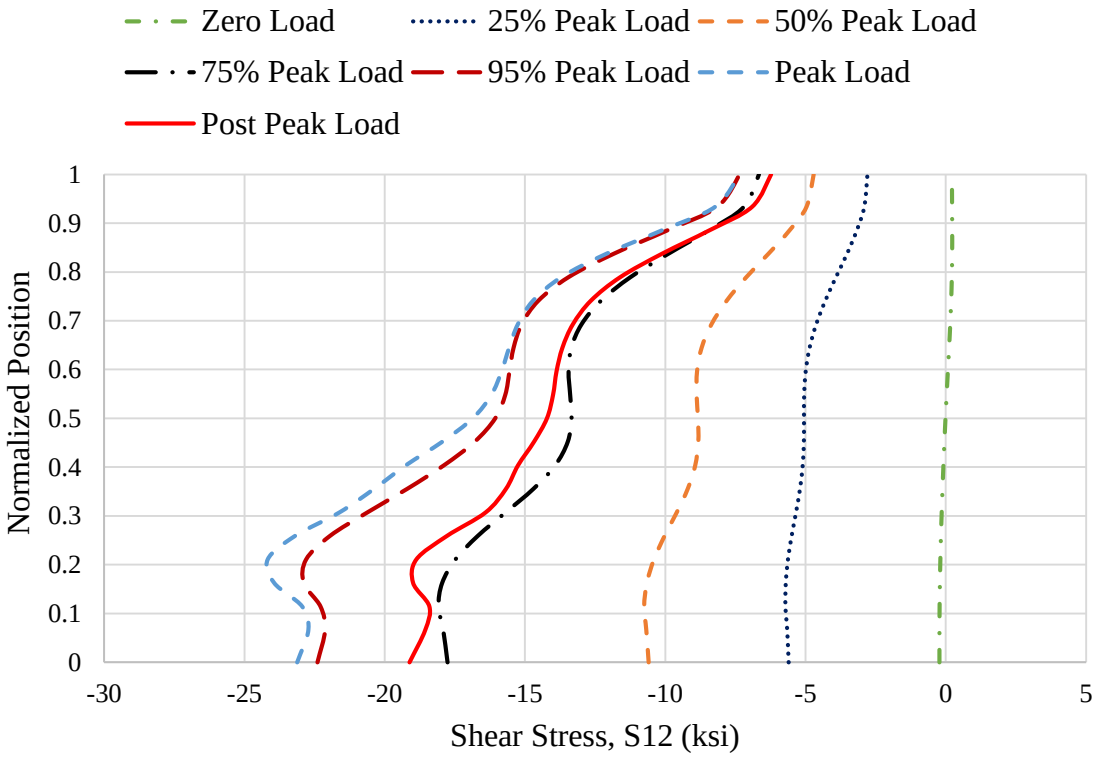

Fig. 7-66. Normalized position versus shear stress *S12* at Section 5.

7.5 Comparison of Results from Simulation and Theory

A procedure similar to Section 5.5.1 is repeated for Specimen UK7.

7.5.1 Stress Variations along the Length

The quantities plotted in this Section are *S11* at the web top and bottom, flange stress *S11* at top and bottom flange and *S12* at the web top, mid-depth and bottom. Figures 7-67 through 7-75 show the variation of these quantities, in that order at a section along the length.

Unlike girder G7 and UK6, *S11* at the top of the web follows a cyclic nature. This is due to the high *a/h* of the specimen.

There is predominant drop in the *S11* at the bottom flange. This was observed in girder G7 and UK6. This behavior was not seen in the top flange. This is because there is extensive yielding of the web bottom at the peak load due to the interaction of shear, flexural tension and plate bending. Near the left end of the panel, the flexural stresses are small due to the small moment.

The normal stress *S11* on both top and bottom flange (Fig. 7-78 and 7-79, respectively) drops below the theoretical stress even at 50% of the peak load and there is some additional compressive stress acting in the flanges. However, when compared to G7 and UK6, this difference is comparatively small, this is because of higher h/t_w and hence higher shear buckling stress, τ_e, of the UK7 (compared to UK6) and higher a/h (compared to both UK6 and G7).

S11 along the top and bottom flange at the peak load also indicate that there is a large compressive stress (deviation from theoretical results) acting on the flanges. However,

compared to UK6 and G7, lesser compressive stress is developed on Specimen UK7 at the peak load.

S12 at the web top follows the expected trend, i.e., *S12* maximum near the left end of the panel and minimum near the right end of the panel. At the web bottom, *S12* is maximum near the right end of the panel and minimum near the right end of the panel. This behavior is similar to Specimens UK6 and G7, however, the variations of stress *S12* is much cyclic in case of UK7.

S12 at the web mid-depth is a reasonable predictor of the results obtained from simulations. There is oscillatory nature in the shear stresses and the peaks at left end of the panel is higher than the peaks at right end of the panel.

The behavior of all these stresses are very similar to the behavior of girder G7 (Figs. 5-60 through 5-68) and girder UK6 (Figs. 6-64 through 6-72). However, due to higher *a/h* than G7 and UK6, the behavior is much more cyclic.

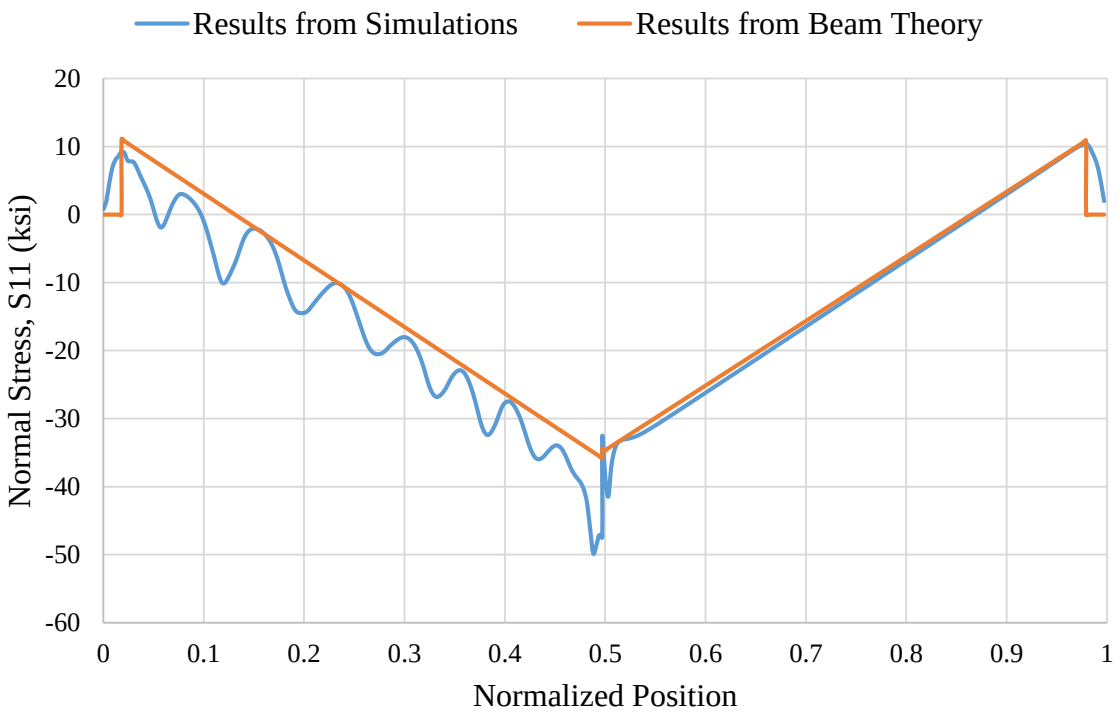

Fig. 7-67. Normal stress *S11* at the peak load versus normalized position at web top.

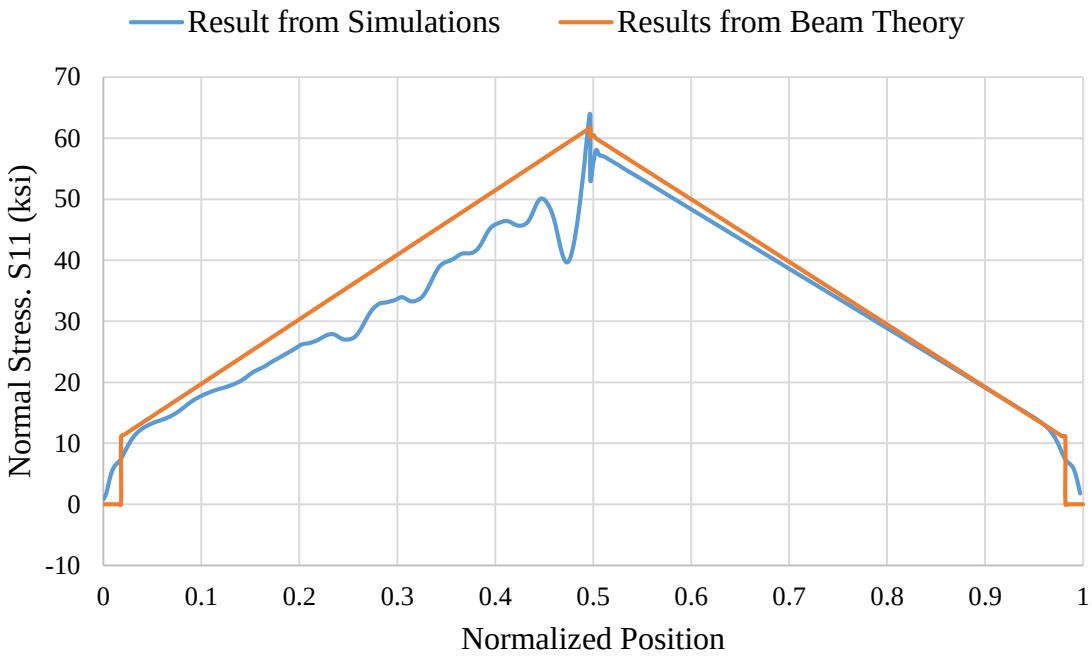

Fig. 7-68. Normal stress *S11* at the peak load versus normalized position at web bottom.

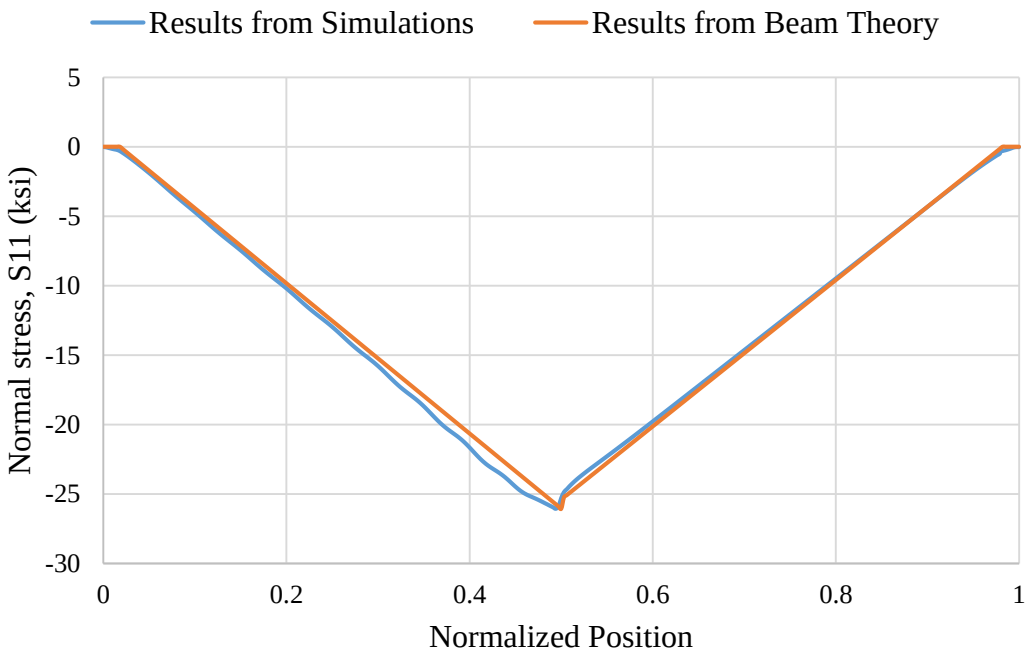

Fig. 7-69. Normal stress *S11* at 50% of the peak load versus normalized position at top flange.

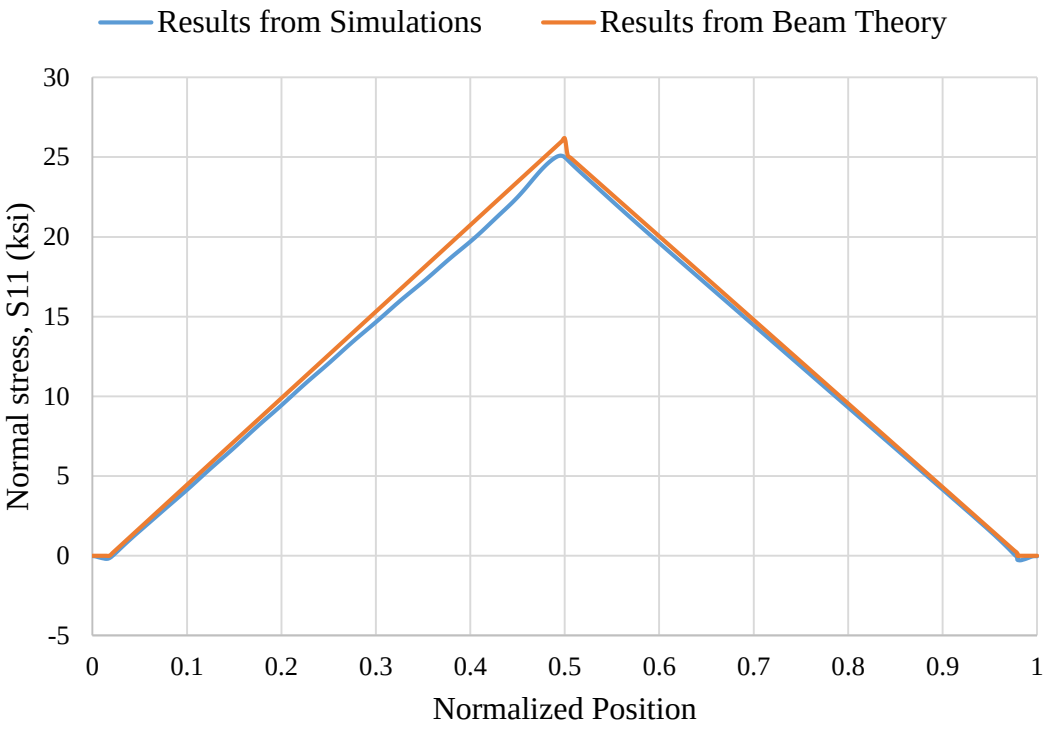

Fig. 7-70. Normal stress *S11* at 50% of the peak load versus normalized position at bottom flange

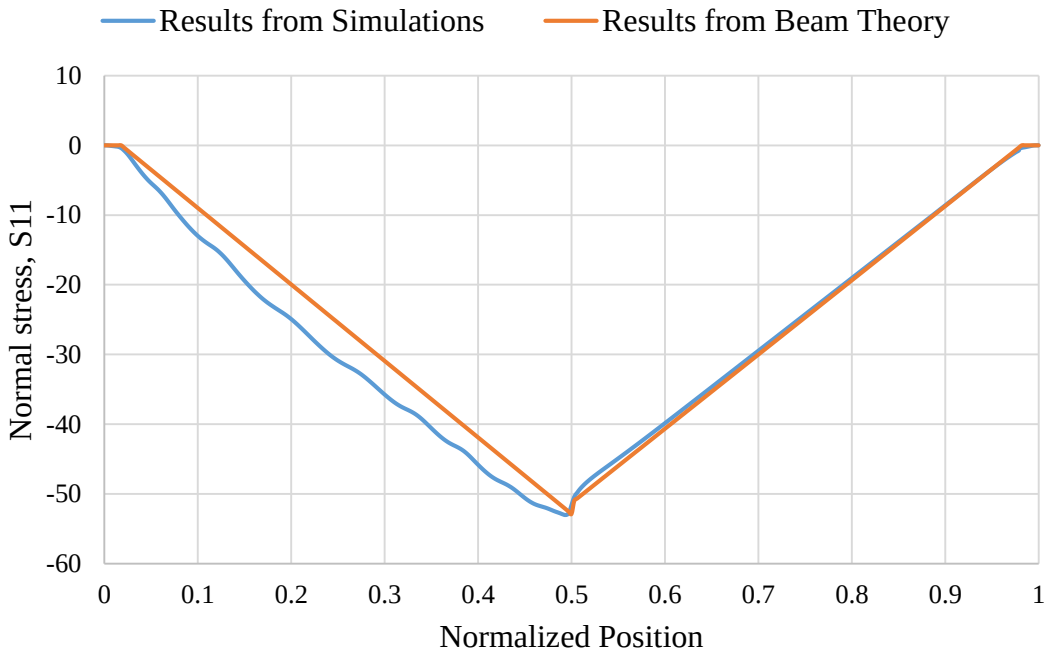

Fig. 7-71. Normal stress *S11* at the peak load versus normalized position along top flange.

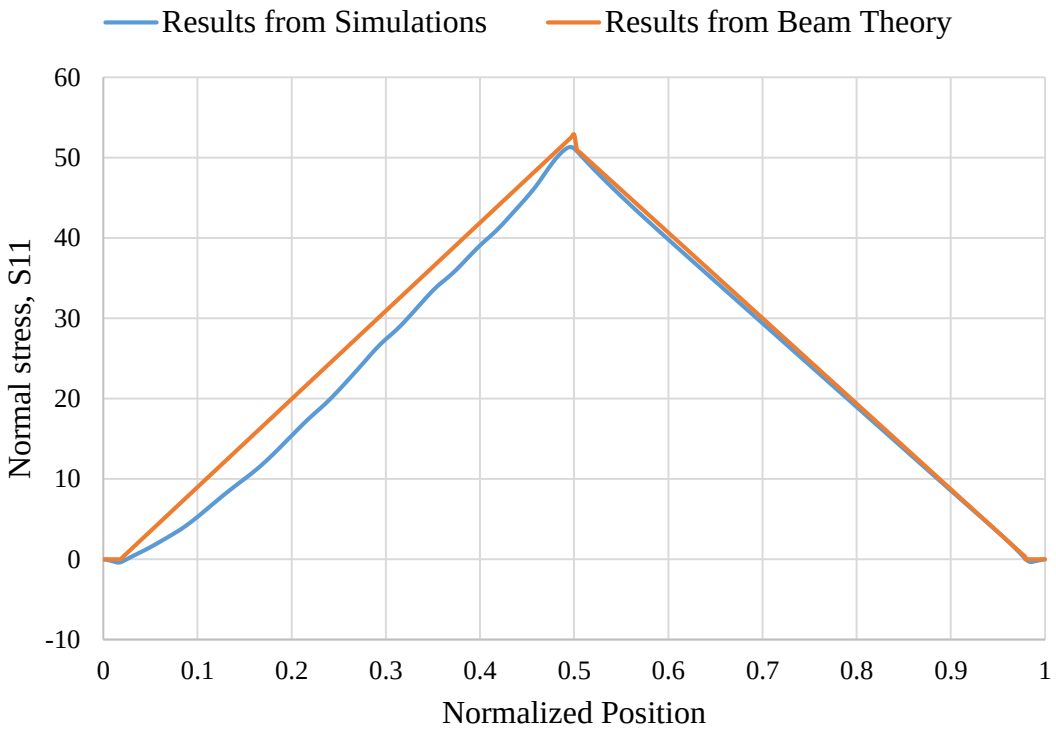

Fig. 7-72. Normal stress *S11* at the peak load versus normalized position along bottom flange.

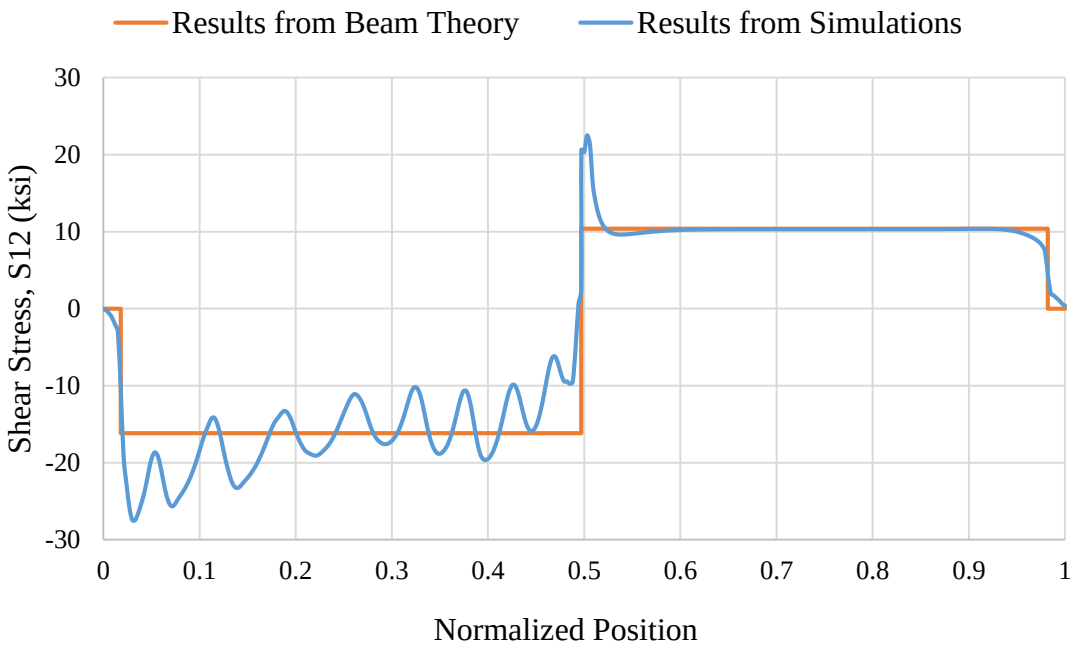

Fig. 7-73. Shear stress *S12* at the peak load versus normalized position at web top.

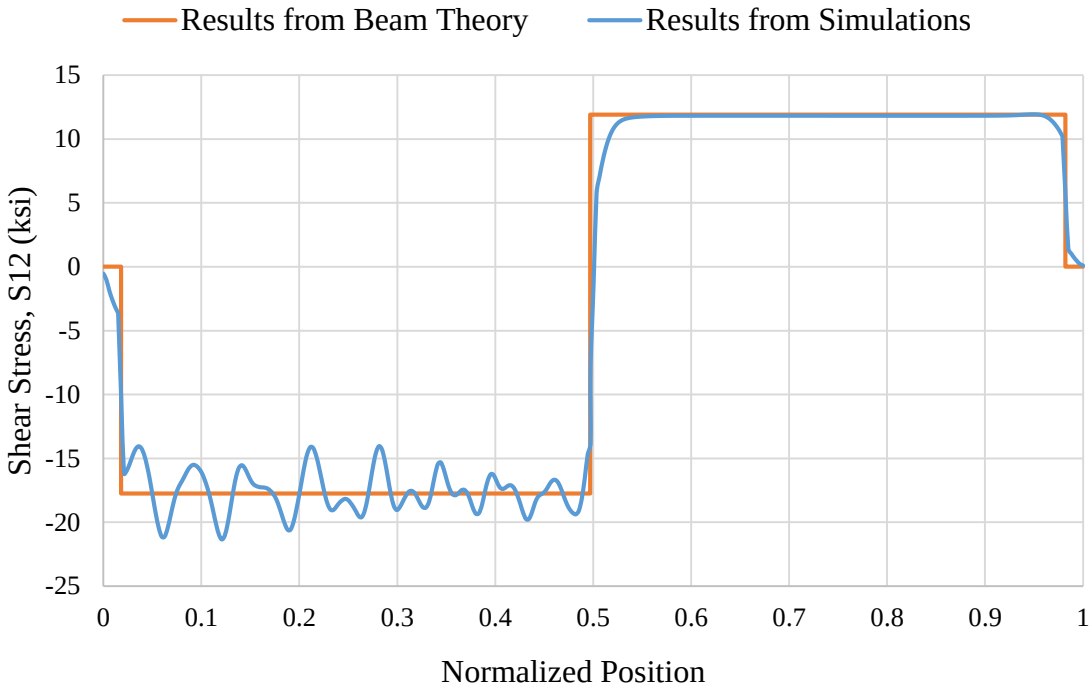

Fig. 7-74. Shear stress *S12* at the peak load versus normalized position at web mid-depth.

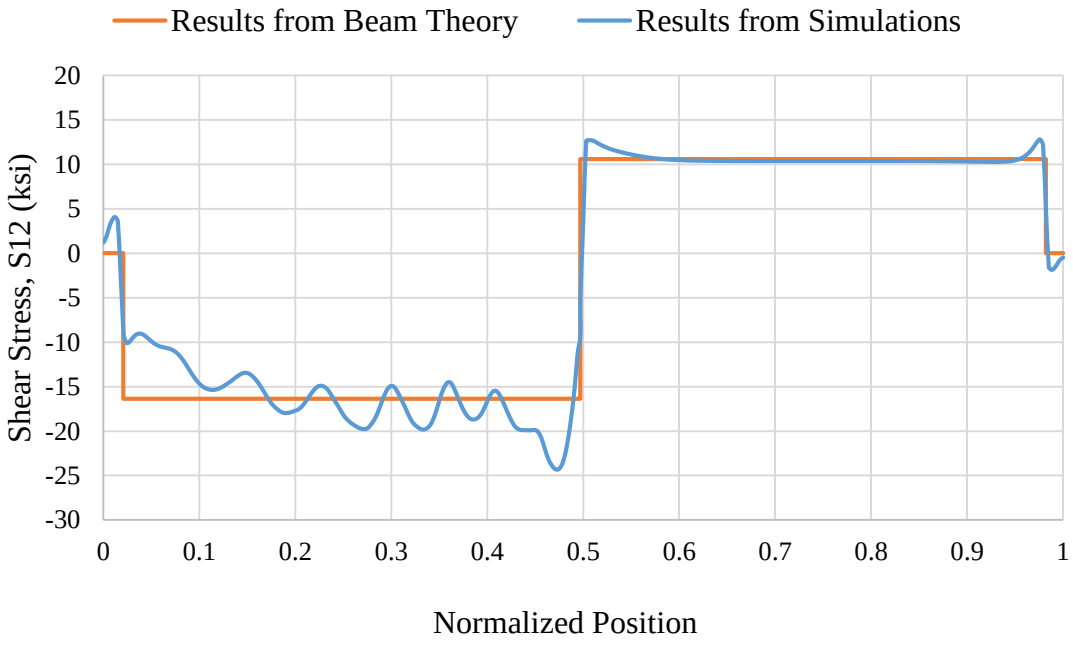

Fig. 7-75. Shear stress *S12* at the peak load versus normalized position at web bottom.

7.5.2 Stress Variations through the Web-Depth

The locations of Sections employed for this study is already explained in Section 7.4. The quantities plotted in this section are *S11* and *S12* at Sections 1, 2, 3, 4 and 5. Figures 7-76 through 7-85 show the variation of these quantities, in that order, at a section along the web-depth. The ordinate is the same as employed in Section 7.4, i.e., normalized position. This procedure is similar to the procedure used in the Section 5.5.2. In the theoretical normal stresses, the specified residual stress is included.

S11 at Section 1 develops significant diagonal tension at the top half of the web. At Section 2,3 and 4 almost the entire section is under diagonal tension. However, this diagonal tension is maximum at the web mid-depth and minimum at web and flange juncture. Of all the four Sections selected for study, Section 5 develops the least diagonal tension and most closely follows the theoretical equations. This is because it is very close to the mid-span.

S12 is significantly different from the results obtained from theory. At Section 1, the top half of the web has higher stress. At Section 2 also, the behavior is similar to Section 1, this is where the buckled meets the top flange. At Section 5, the bottom half of the web has higher stress. At Section 4 also, the behavior is similar to Section 5, this is where the buckled meets the bottom flange. The deviation in *S12* at Section 3 from the beam theory is the least when compared with Section 1 and 4.

Shear stress on Section 1 and Section 2 is similar to Section 1 of Specimens G7 and UK6 and shear stress on Section 4 and Section 5 is similar to Section 3 of Specimen G7 and Section 4 of Specimen UK6. The variation of stresses on Section 3 is similar to Section 2 of Specimen G7 and Section 3 of Specimen UK6.

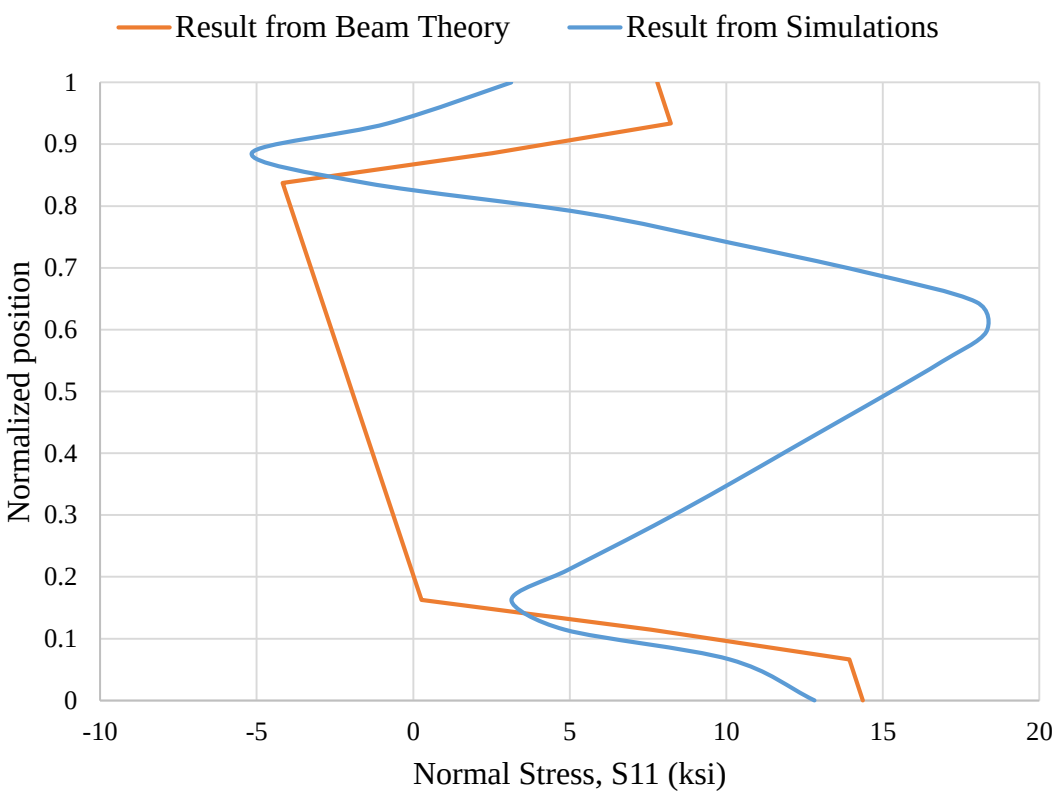

Fig. 7-76. Normalized position versus normal stress *S11* at the peak load at Section 1.

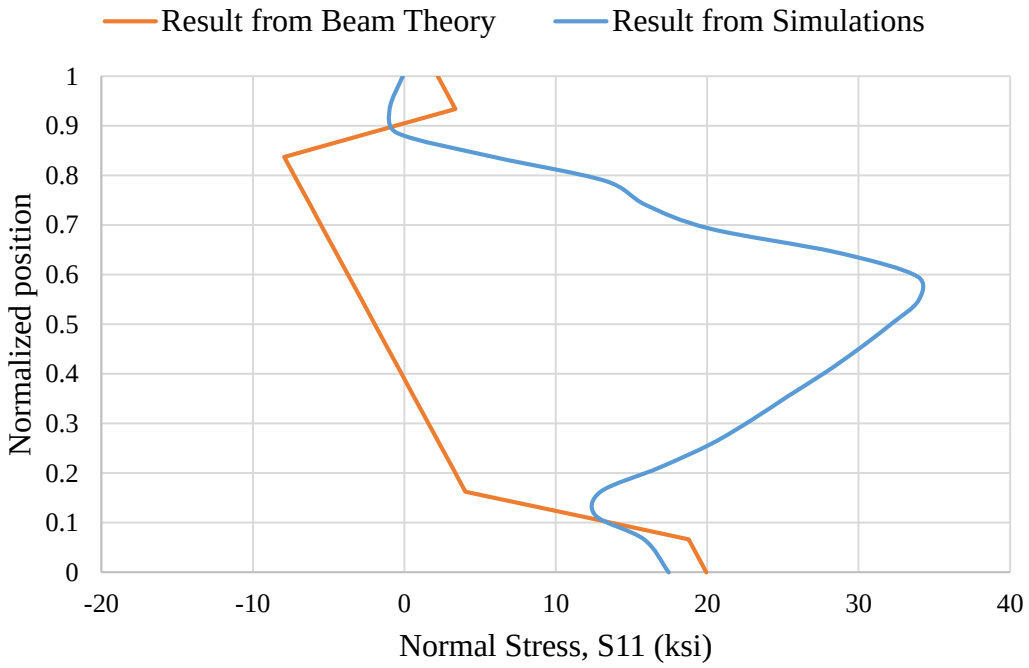

Fig. 7-77. Normalized position versus normal stress *S11* at the peak load at Section 2.

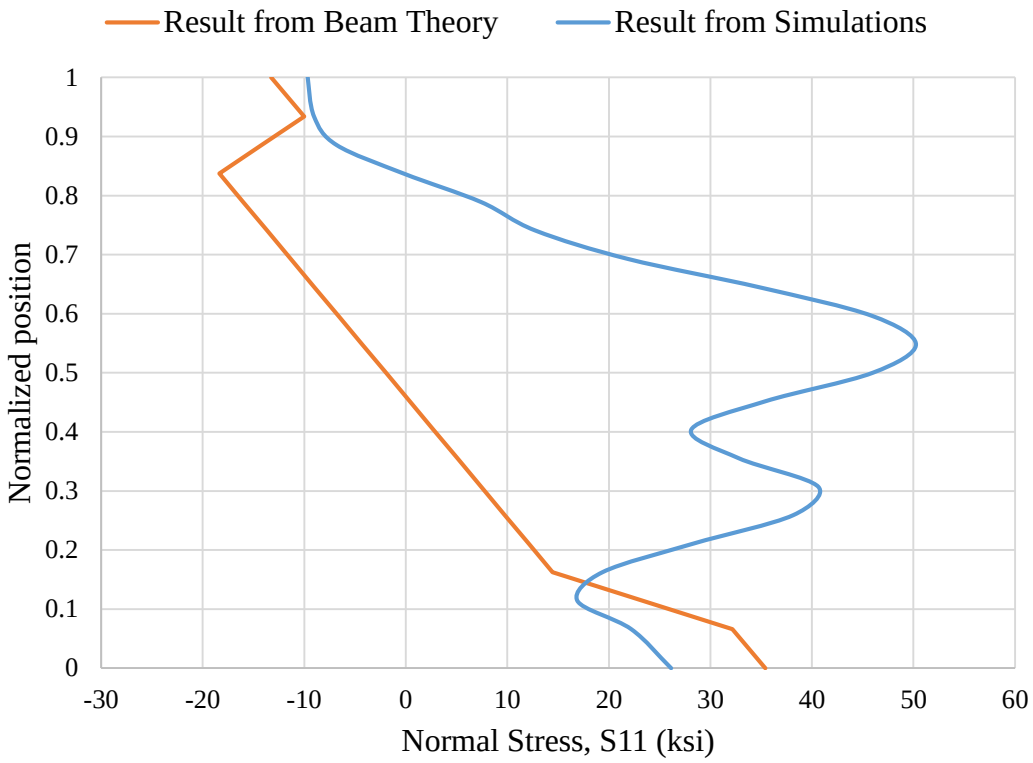

Fig. 7-78. Normalized position versus normal stress *S11* at the peak load at Section 3.

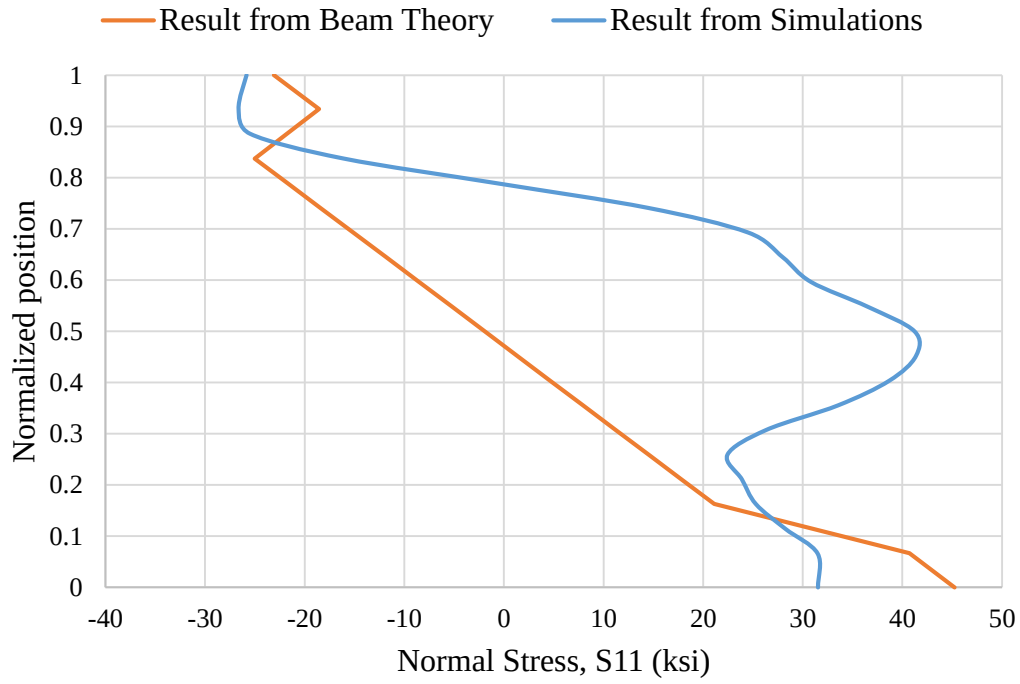

Fig. 7-79. Normalized position versus normal stress *S11* at the peak load at Section 4.

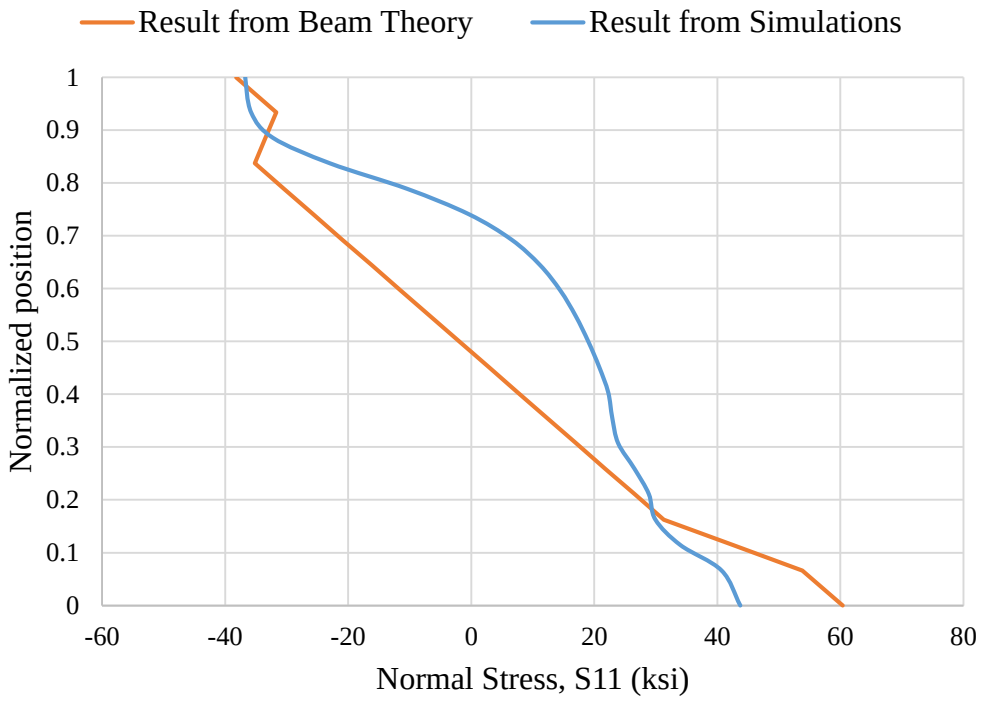

Fig. 7-80 Normalized position versus normal stress *S11* at the peak load at Section 5.

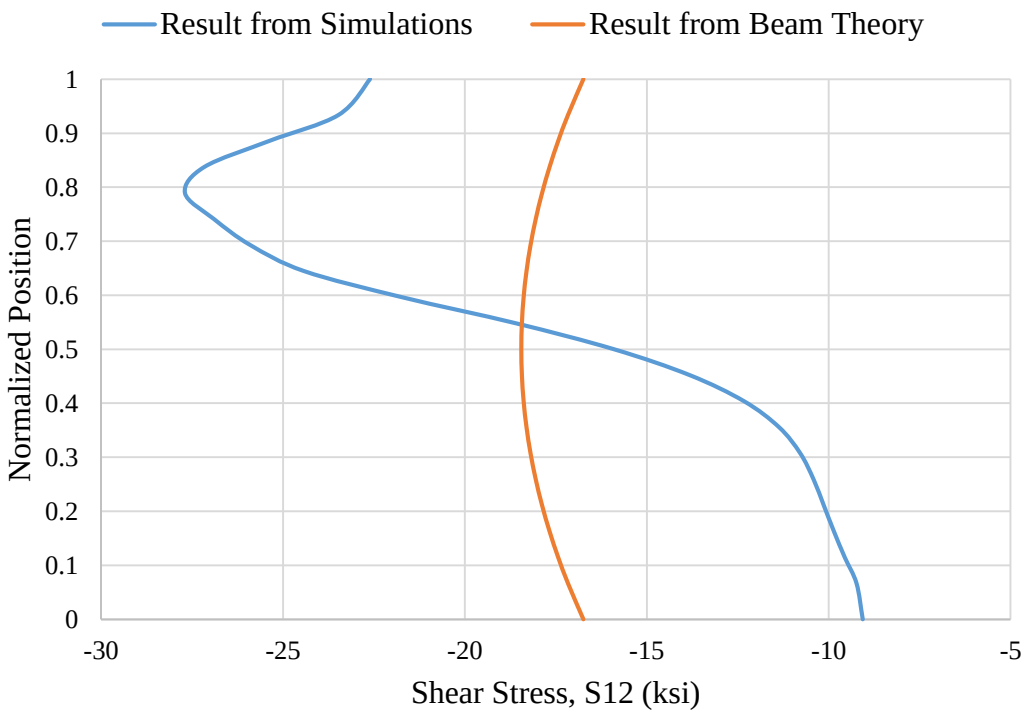

Fig. 7-81. Normalized position versus shear stress *S12* at the peak load at Section 1.

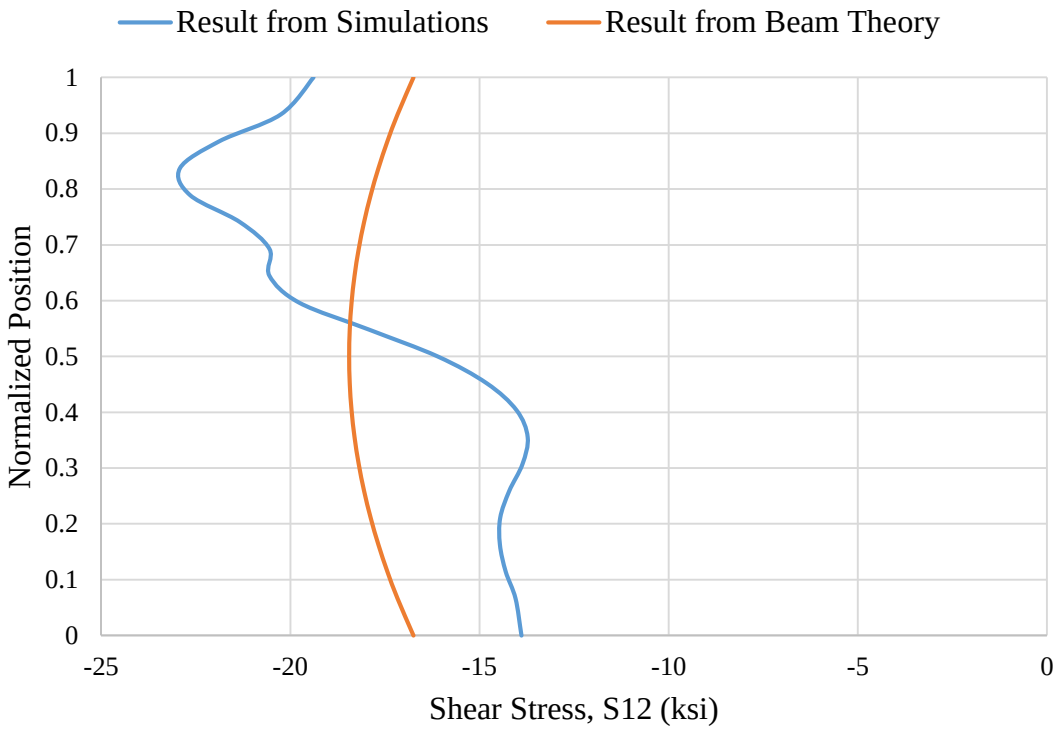

Fig. 7-82. Normalized position versus shear stress *S12* at the peak load at Section 2.

Fig. 7-83. Normalized position versus shear stress *S12* at the peak load at Section 3.

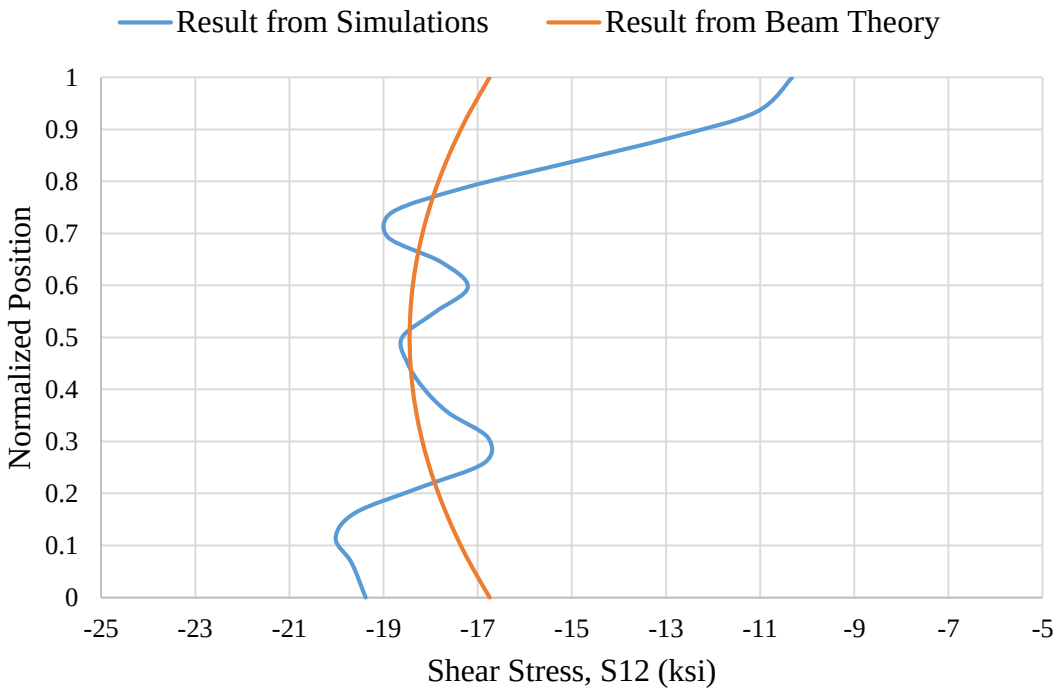

Fig. 7-84. Normalized position versus shear stress *S12* at the peak load at Section 4.

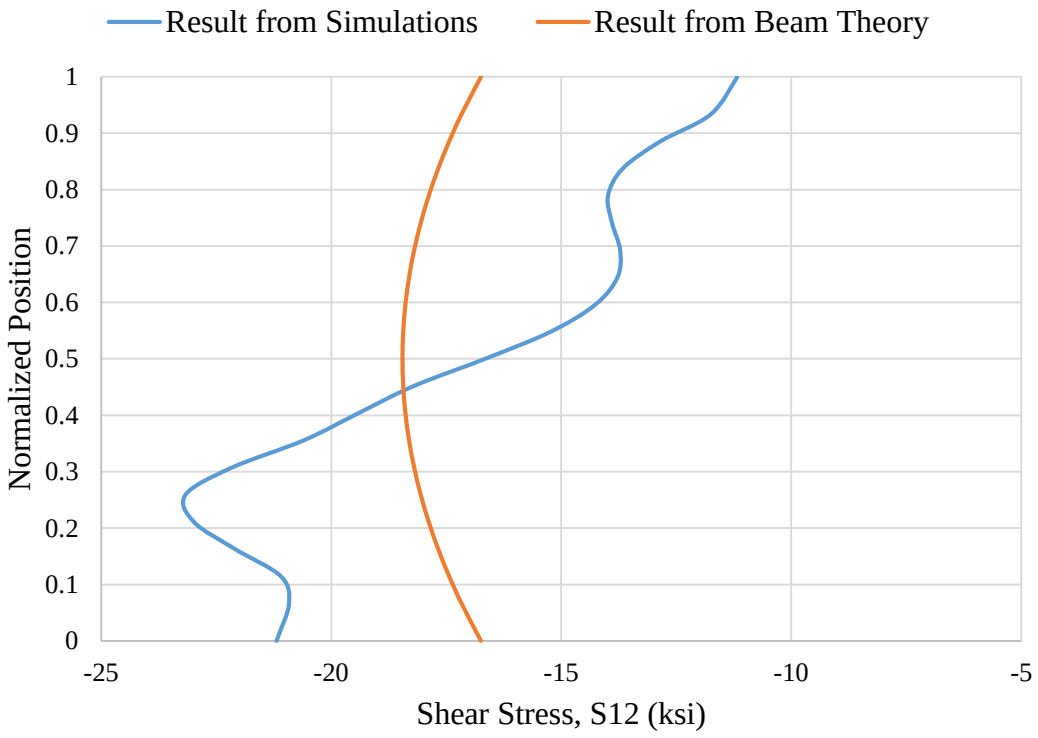

Fig. 7-85. Normalized position versus shear stress *S12* at the peak load at Section 5.

CHAPTER 8

EVALUATION OF SENSITIVITIES

In this chapter, the sensitivity of the shear strength to various factors is evaluated. The attributes studied are flange thickness, imperfection magnitude and details providing potential end anchorage.

8.1 Flange Thickness

In this section, the flange thickness of the specimens is changed and its effect on their shear strength is examined. The specimens selected for this study are G7, UK6 and UK7. According to the AISC (2010), Specification, the shear strength of stiffened or unstiffened webs is given by Eq. 1-6, where A_w is the area of web and is defined as the overall depth times the web thickness. With the change in flange thickness, there is a change in the overall depth of the specimen and hence, there is a small increase in the shear strength if the flange thickness is increased.

Table. 8-1 gives the effect of changing flange thickness on the shear strength. The fourth column of the table gives the percentage difference of the shear strength from the shear strength obtained from simulation for the original flange thickness employed in the experimental testing. The fifth column of the table gives the percentage difference of the shear strength from the that obtained using Eq. 1-6 (changing the overall depth due to change in flange thickness) and for the original flange thickness. The flange thickness is not reduced to an extent that the flexural resistance governs.

Table. 8-1. Comparison of shear-strength with changing flange thickness.

Specimen	t_f (in)	V_{sim} (kip)	% change in strength	% change in V_n (*change in* A_w)
G7	0.39*	56.0		
	0.50	56.9	+1.6	+0.9
	0.59	57.6	+2.6	+1.6
	0.69	58.2	+3.9	+2.4
UK6	0.750*	89.0		
	0.625	87.0	-2.2	-0.6
	0.875	91.0	+2.2	+0.6
	1.00	92.2	+3.5	+1.2
UK7	0.750*	43.5		
	1.000	44.0	+1.1	+2.3
	1.125	44.3	+1.8	+3.4

Note: * denotes specimen flange thickness used in the actual experiment.

There is noticeable change in the shear strength of Specimens UK6 and G7 due to changing of the flange thickness. For Specimen, UK7 the change in thickness of flange influences the shear strength to a lesser extent. This is believed to be due to the relatively large *a/h* of Specimen UK7.

The influence of flange rigidity on the shear-strength has been discussed by various investigators (White and Baker 2008). It is well established that the Vierendeel frame action of the flanges contribute to the shear strength of the web panels. Many of the theories take the contribution from the frame action of the flanges in the equations for the calculation of shear strength for stiffened panels. Basler (1961) and Lee and Yoo (1998)

do not recognize the contribution of flange rigidity on the postbuckling strength of web panels. To better understand the influence of flange rigidity on the shear strength, the procedure of Chapter 5 is repeated for several flange thicknesses in the following. All the results are plotted at the respective peak load of the specimens. To make the plots easier to understand, the responses for only one-half of the length of the specimen is considered. Specimen G7 is symmetrical about its mid-span. For Specimens UK6 and UK7, the graphs are plotted only for the left-side of the specimen. The right side of the specimen is thicker and does not buckle, even at the peak load. In all the graphs, unless noted otherwise, the position along the length, measured from the left end of the specimen, is plotted as the abscissa.

1. Specimen G7

The variation of normal stress *S11*, with the position along the length for a section along the web mid-depth at the peak load is shown in Fig. 8-1. There is essentially no change in the pattern and in the values due to change in the rigidity of the flanges. Therefore, it can be said that there is no variation in the tension field due to the change in the flange rigidity for this test.

The variation of normal stress *S22* with the position along the length for a section along the web-top at the peak load is shown in Fig. 8-2. There is slight change in the maximum *S22* (except at mid-span) near the left end of the panel due to changing the flange rigidity. The failure mode is essentially same for all the different flange thicknesses.

The variation of normal stress *S22* with the position along the length for a section along the web-bottom at the peak load is shown in Fig. 8-3. The variation of stress, *S22* is same

for all flange thicknesses. There is slight change in the maximum compressive *S22* near the right end of the panel due to changing the flange rigidity. This shows that for the stiffened web panel in test G7, changing the rigidity of the flange does not influence the forces acting on the flanges at the peak load.

To understand the influence of frame action on the shear strength, the ratio of local bending moment in the top flange plate about the horizontal axis of the cross-section, *M1*, and Local Flange Plastic Moment, M_{pf}, are plotted. The variation in $M1/M_{pf}$, with the position along the length for a section along the top-flange at the peak load is shown in Fig. 8-4. The maximum occurs exactly at the location of left stiffener of the panel. Excluding the high value at the left-stiffener, the maximum $M1/M_{pf}$ occurs exactly at the location of peak in *S22* (Fig. 8-2). Even though there is change in local flange bending moment, the $M1/M_{pf}$ does not change with the varying thickness of the flange. The maximum $M1/M_{pf}$ is around 0.22 at the right end of the panel, hence it is clear that no plastic hinges are formed.

The variation in $M1/M_{pf}$, with the position along the length for a section along the top-flange at the peak load is shown in Fig. 8-5. The maximum occurs exactly at the location of left bearing stiffener due to the end reaction of the beam. Excluding the high value at the support, the maximum $M1/M_{pf}$ occurs exactly at the location of peak in *S22* (Fig. 8-3) at the bottom flange. Even though there is change in local flange bending moment, the $M1/M_{pf}$ does not change with the varying thickness of the flange. The maximum $M1/M_{pf}$ is around 0.1 at the left end of the panel, hence it is clear that no plastic hinges are formed.

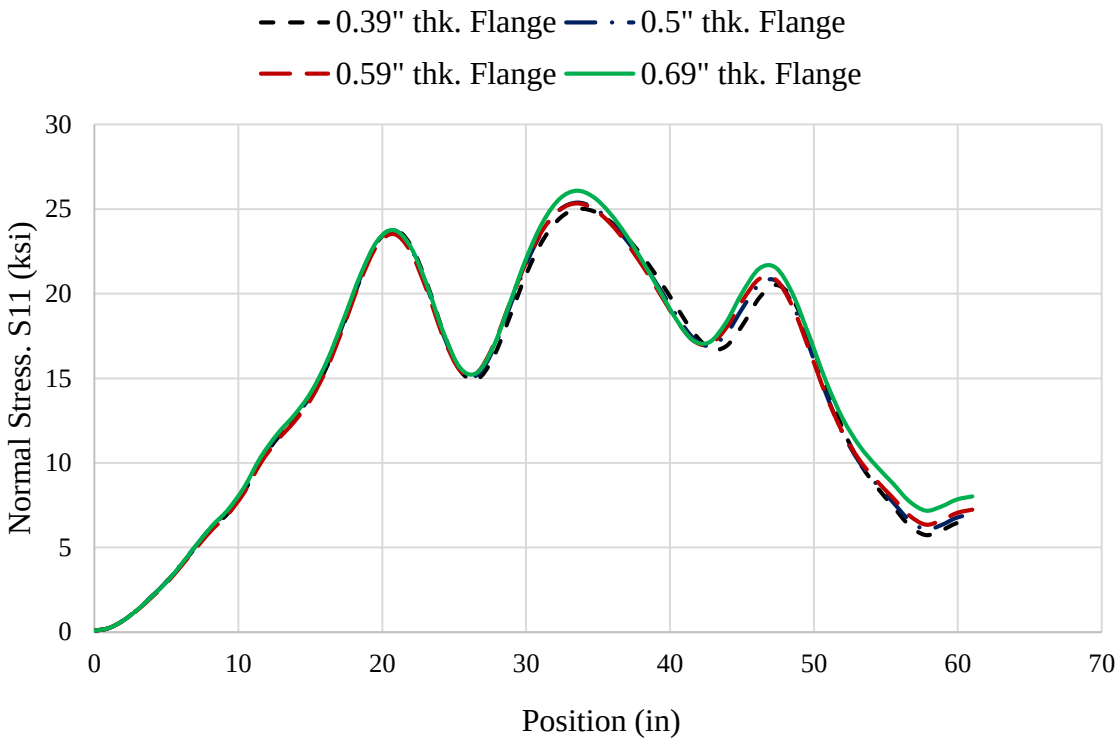

Fig. 8-1. Normal stress *S11* versus position along the web mid-depth.

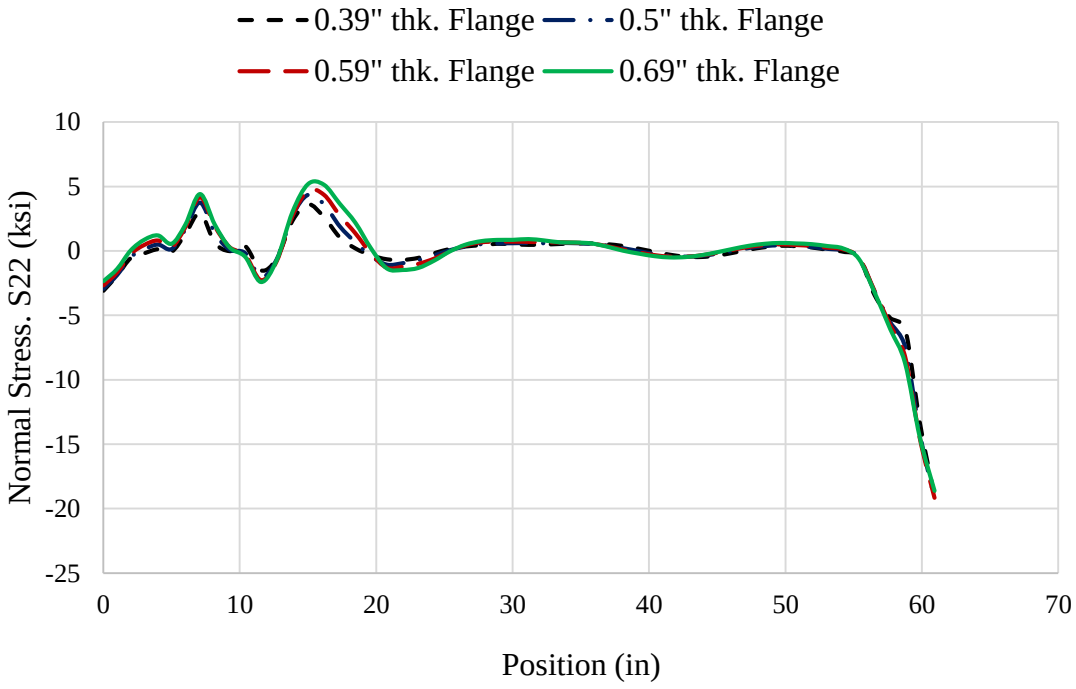

Fig. 8-2. Normal stress *S22* versus position along the web top.

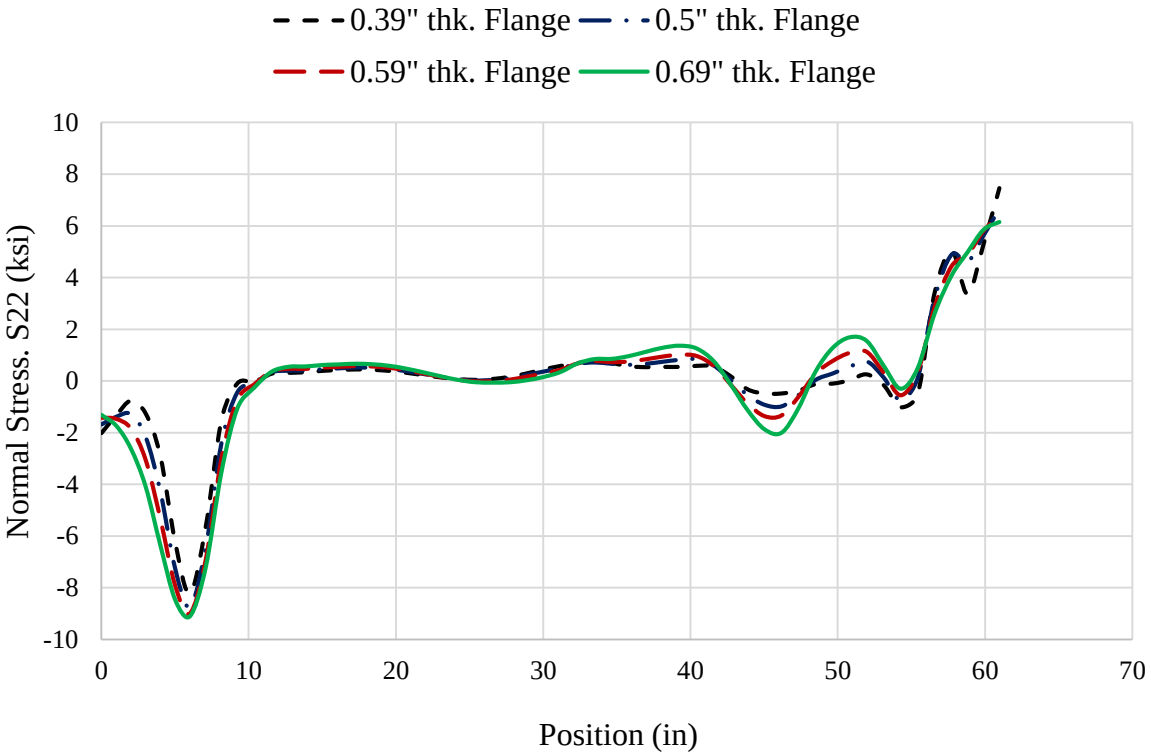

Fig. 8-3. Normal stress *S22* versus position along the web bottom.

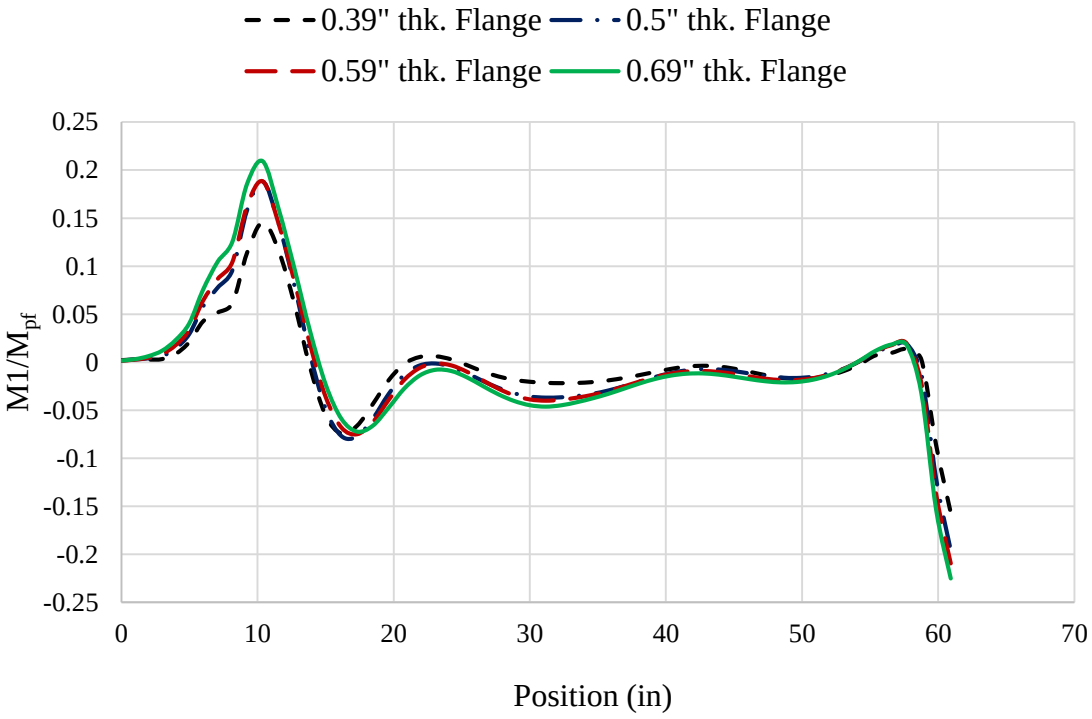

Fig. 8-4. *M1/M$_{pf}$* versus position along the top-flange.

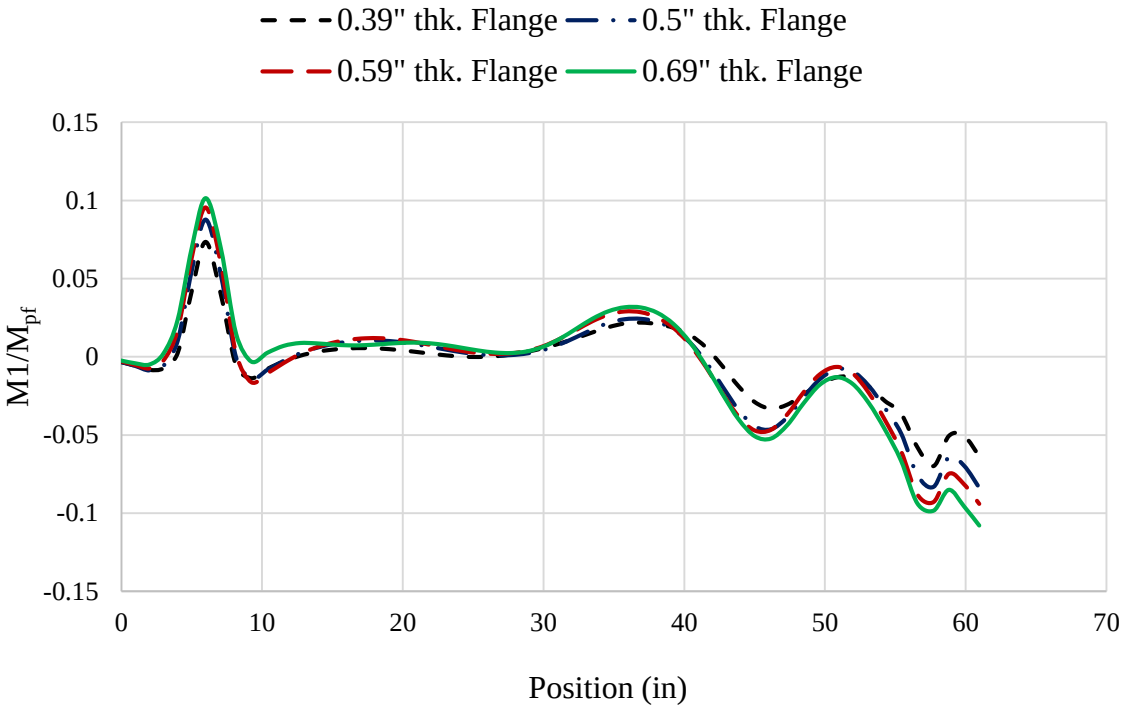

Fig. 8-5. *M1/M*$_{pf}$ versus position along the bottom-flange.

2. Specimen UK6

Figures 8-6 through 8-10 show a similar variation to that shown in Fig. 8-1 through 8-5 for Specimen UK6.

The pattern changes little as a function of the flange thickness (Fig. 8-6); however, there is considerable difference in the maximum *S11* at peak load for 1.0-in.-thick flange when compared to 0.625-in.-thick flange.

Maximum *S22* at top flange (Fig. 8-7) for 0.625-in.-thick flange (except at mid-span) is almost half of the maximum *S22* at peak load for 1.0-in.-thick flange. This is because of higher h/t_w (227). Even though there is considerable difference between maximum *S11* at web mid-depth and maximum *S22* at top-flange for 0.625-in. and 1-in.-thick flange, the

difference between peak loads in small. This is because the flanges are not subjected to any significant membrane forces until almost 95% of the peak load.

The maximum *S22* at bottom flange (Fig. 8-8) varies similar to the top flange, maximum for 1.0-in. flange and minimum for 0.625-in. thick flange.

The maximum $M1/M_{pf}$ at the top flange (Fig. 8-9) occurs exactly at the location of peak in *S22* (Fig. 8-7). Maximum $M1/M_{pf}$ for 0.625-in.-thick flange (near the left end of the panel) is almost half of the maximum $M1/M_{pf}$ at peak load for 1.0-in.-thkick flange. However, even for1.0-in.-thkick flange maximum $M1/M_{pf}$ is about 0.3 and hence no plastic hinge is formed even for a thick flange. Even though there is considerable difference between maximum $M1/M_{pf}$, there is not considerable difference between peak loads.

The maximum $M1/M_{pf}$ at the bottom flange (Fig. 8-10) occurs exactly at the location of left bearing stiffener due to the end reaction of the beam. Excluding the high value at the support, the maximum $M1/M_{pf}$ occurs exactly at the location of peak in *S22* (Fig. 8-10) at the bottom flange. Like $M1/M_{pf,}$ at the top flange there is considerable difference between maximum $M1/M_{pf}$ at the bottom flange.

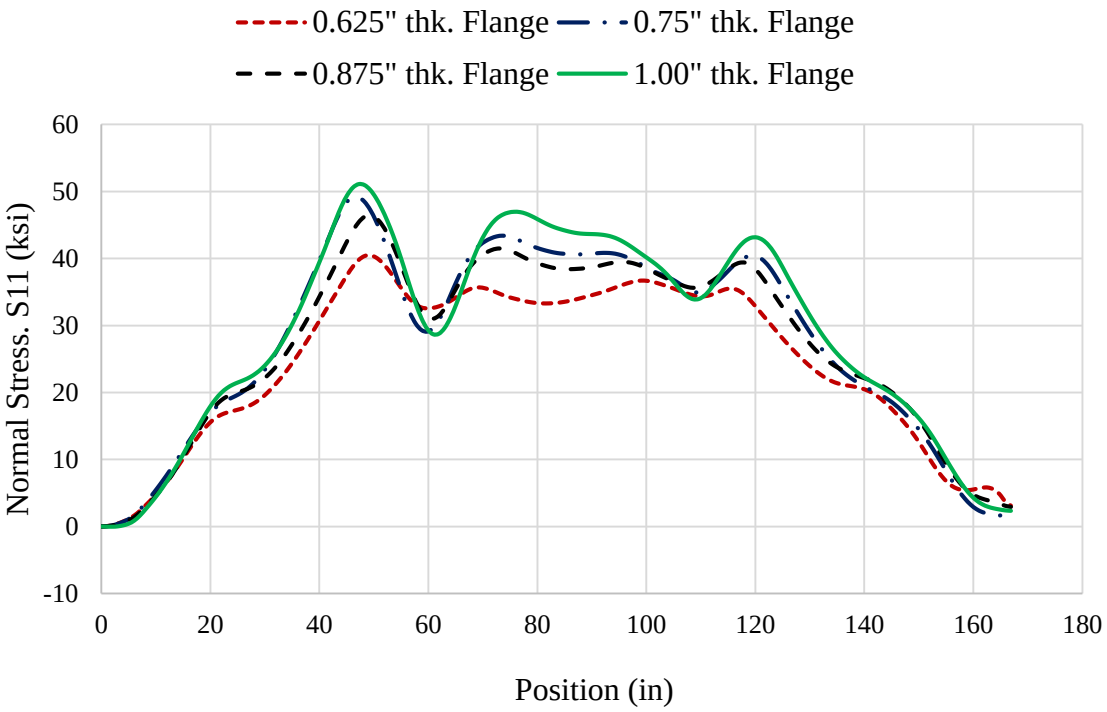

Fig. 8-6. Normal stress *S11* versus position along the web mid-depth.

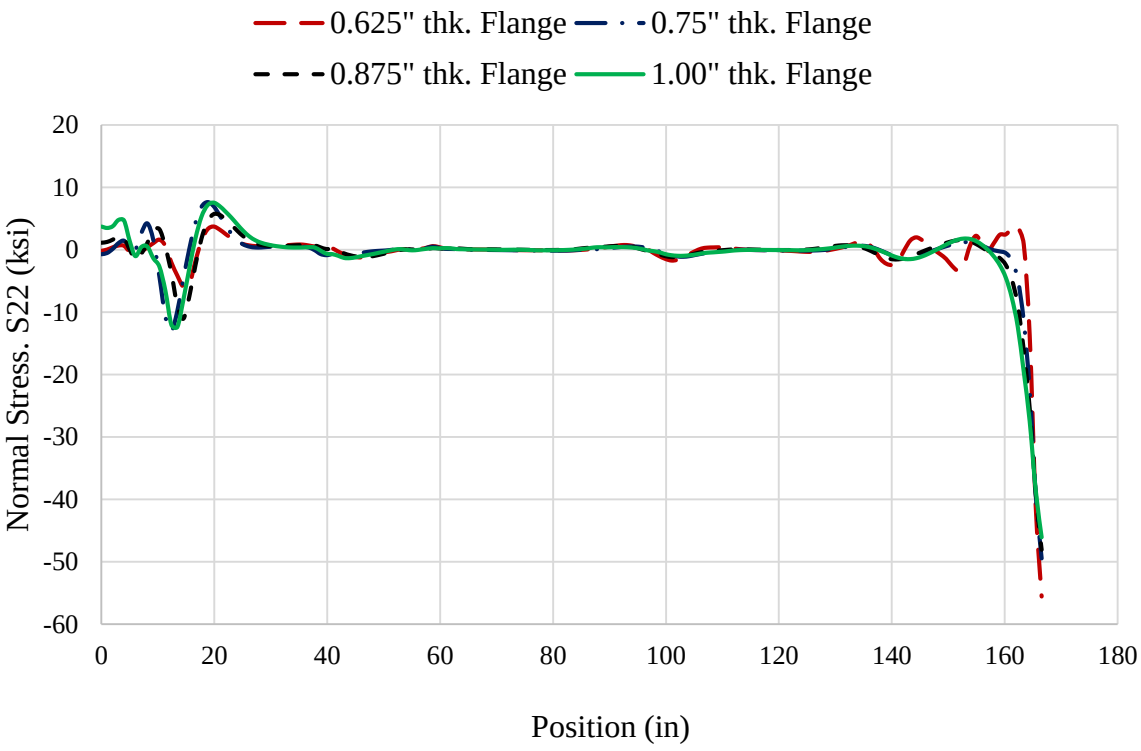

Fig. 8-7. Normal stress *S22* versus position along the web top.

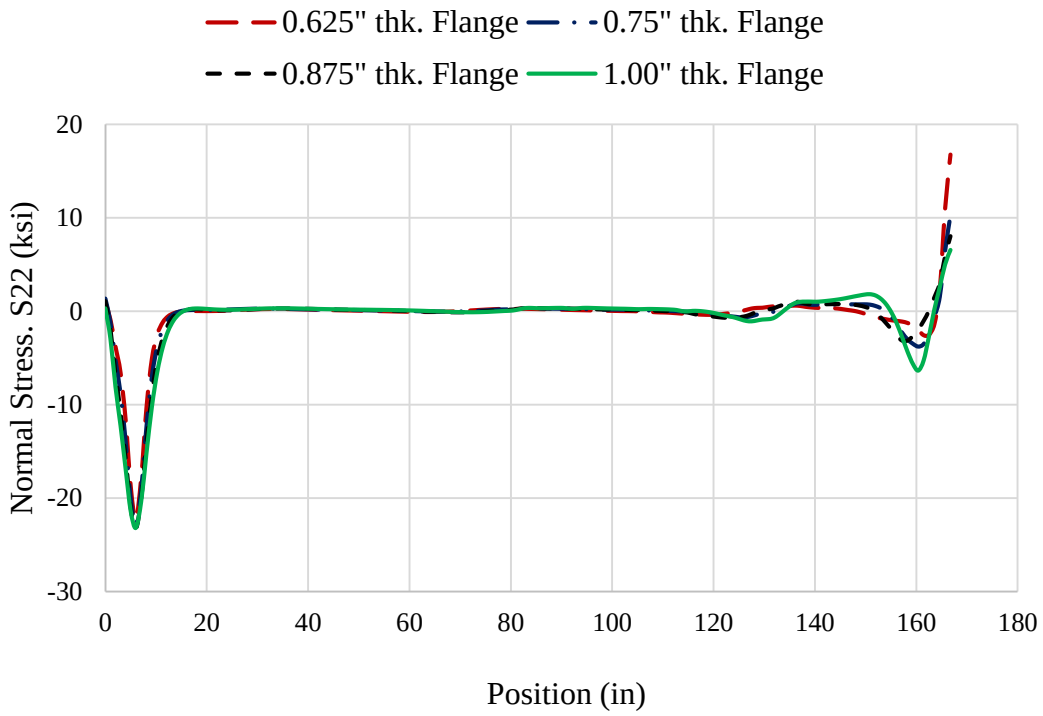

Fig. 8-8. Normal stress *S22* versus position along the web bottom.

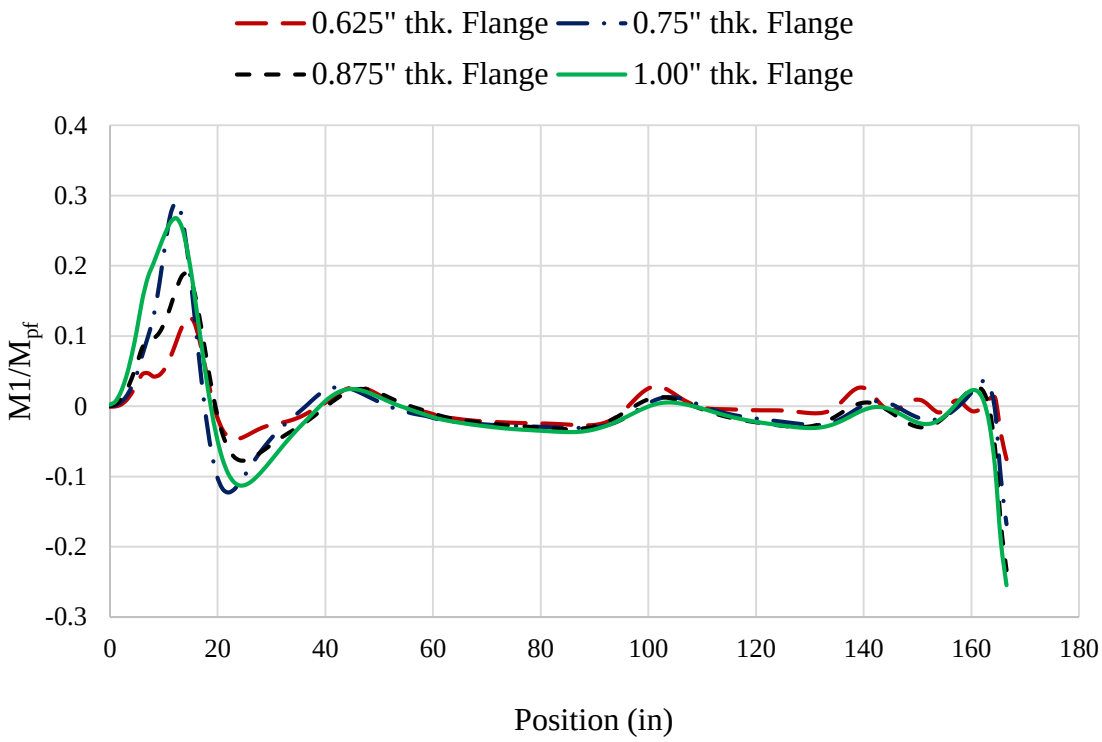

Fig. 8-9. *M1/M*$_{pf}$ versus position along the bottom-flange.

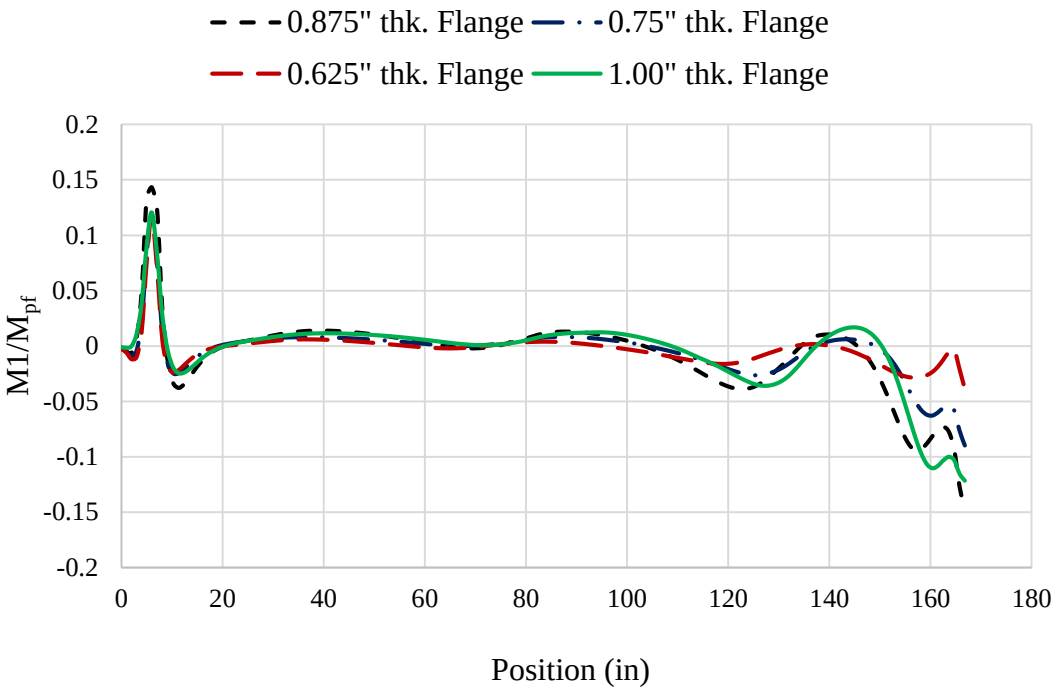

Fig. 8-10. *M1/M*$_{pf}$ versus position along the bottom-flange.

3. Specimen UK7

Figures 8-11 through 8-15 parallel Fig. 8-1 through 8-5 for Specimen UK7.

There was considerable difference between maximum *S11* values (Fig. 8-11) at peak load for 0.625-in.-thick flange and 1-in.-thick flange for Specimen UK6 (Fig. 8-6). However, there is not much difference in *S11* for UK7. This is because of larger influence of flange thickness for UK6 due to lower h/t_w for UK7.

There is absolutely no change in the *S22* at the top flange (Fig. 8-12) for changing flange thicknesses.

Even for bottom flange (Fig. 8-13), there is absolutely no change in the *S22* for changing flange thicknesses. However, the variation is much more cyclic compared to UK7 and G7 due to the large *a/h*.

Similar to *S22* (Fig. 8-13), the variation of $M1/M_{pf}$ (Fig. 8-14) is much more cyclic compared to UK6 and G7. For different thicknesses of flange, there is very small in the $M1/M_{pf}$. This proves that for a long unstiffened panel there is almost no influence of the changing flange thickness on the shear strength. However, clearly no plastic hinges are formed.

$M1/M_{pf}$ for the bottom-flange (Fig. 8-15) also changes little with varying flange thickness.

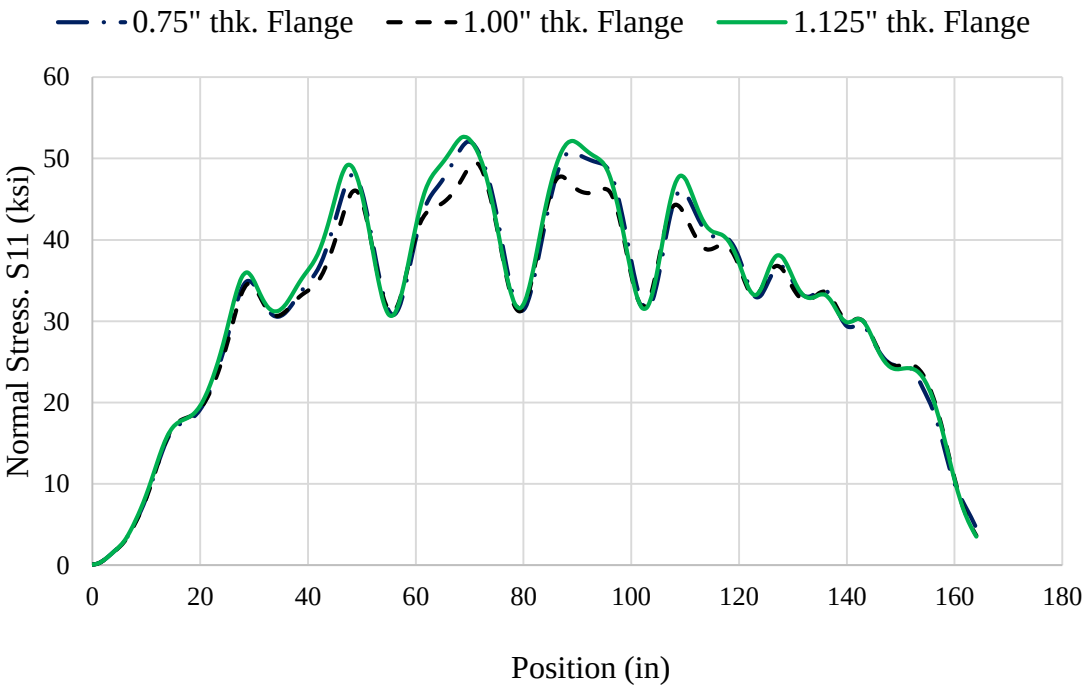

Fig. 8-11. Normal stress *S11* versus position along the web mid-depth.

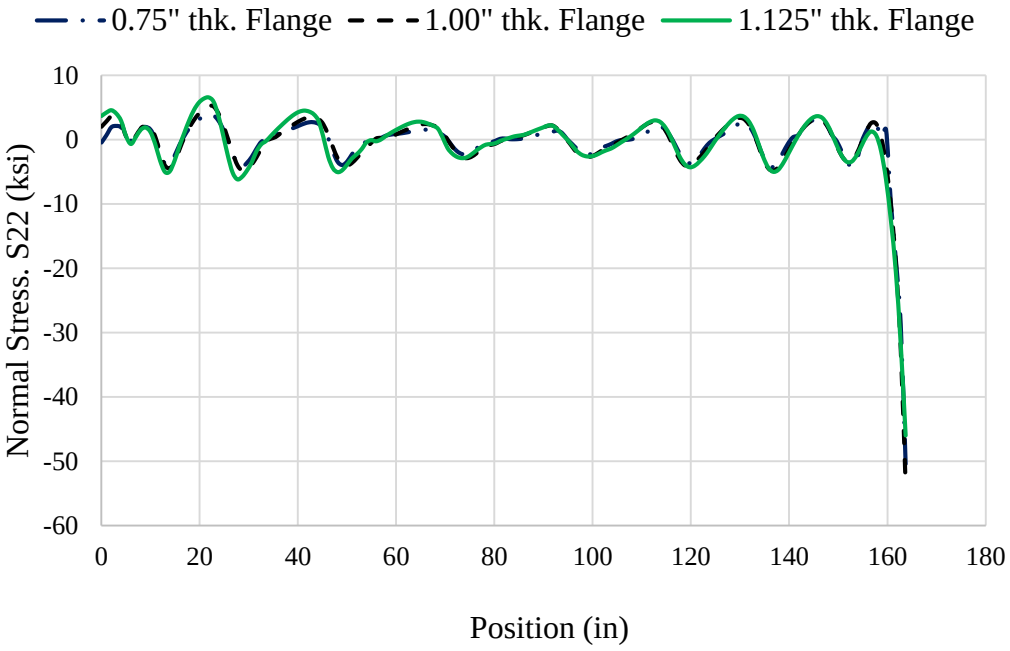

Fig. 8-12. Normal stress *S22* versus position along the web top.

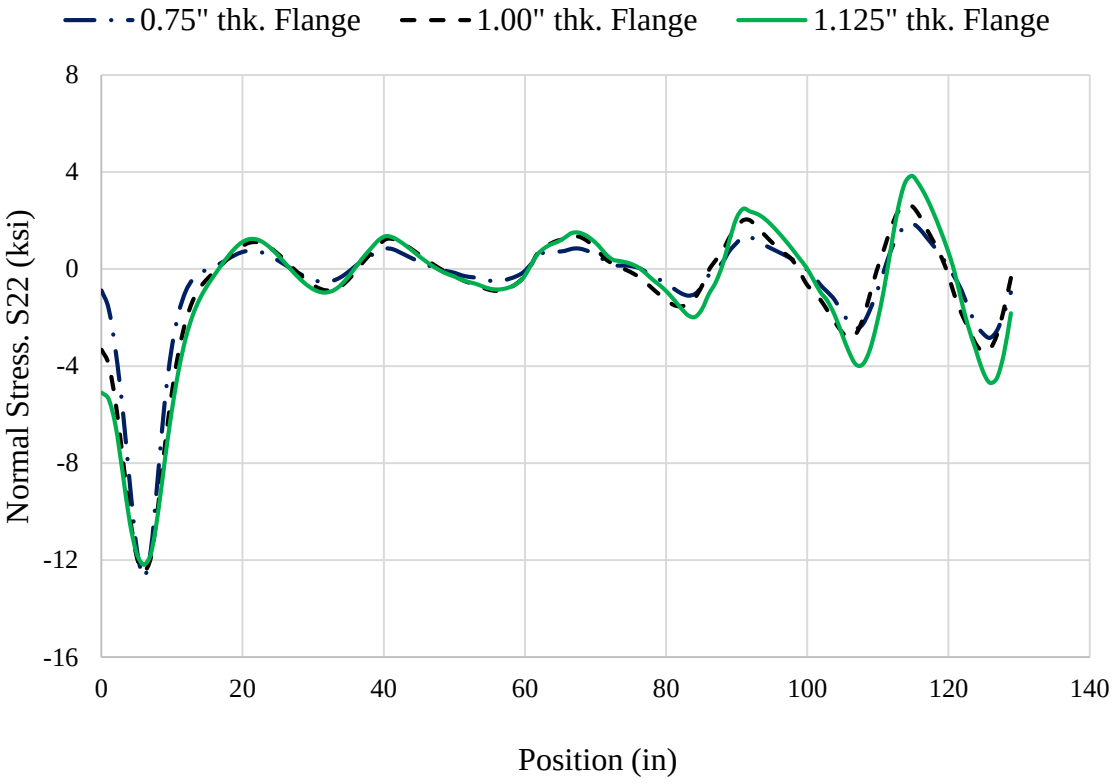

Fig. 8-13. Normal stress *S22* versus position along the web-bottom.

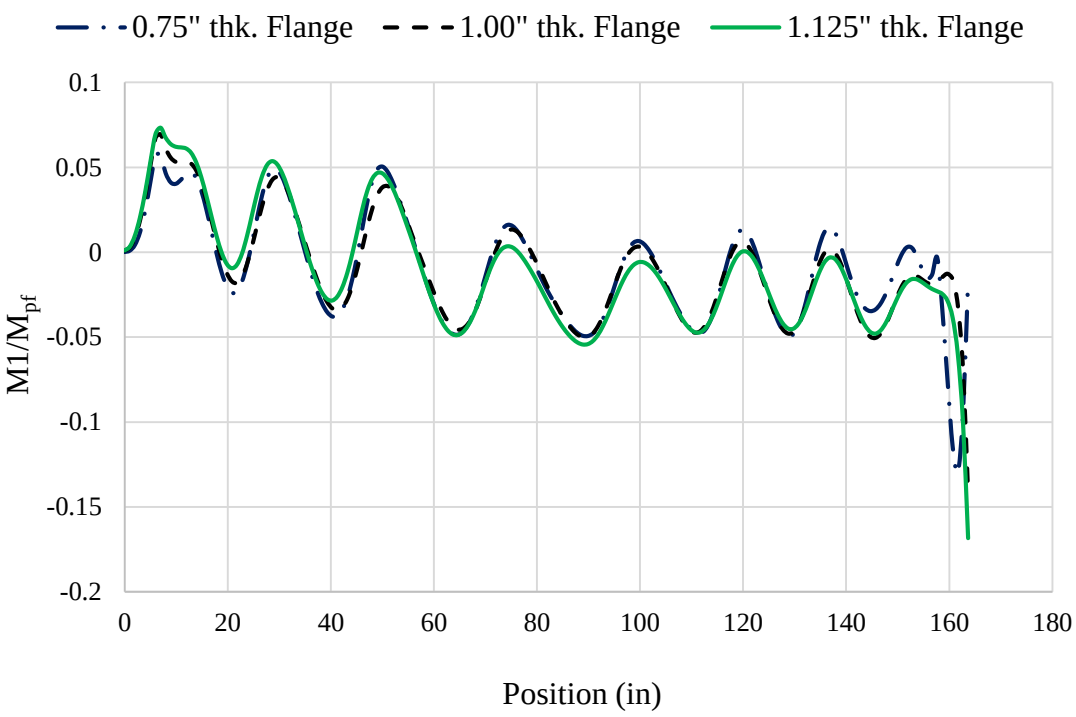

Fig. 8-14. *M1/M*$_{pf}$ versus position along the top-flange.

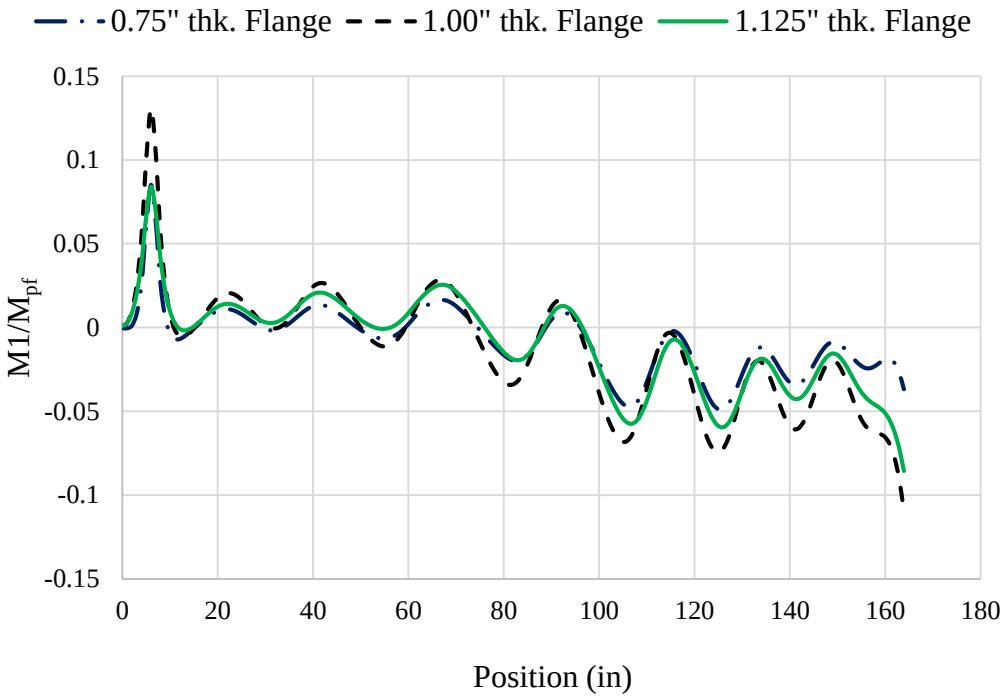

Fig. 8-15. *M1/M*$_{pf}$ versus position along the bottom-flange.

8.2 Imperfection Magnitude

In this section, the imperfection magnitude is changed and the simulation result is recorded. Table 8-2 gives the change in shear strength with different imperfection magnitudes. The imperfection magnitude used for the simulations is *D*/150 for all the simulations based on the Bridge Welding Code (AWS 2002). The specimens selected for this study are G7, UK6 and UK7.

Table. 8-2 . Change in shear strength with different imperfection magnitudes.

Specimen	Imp	V_{sim} (kip)	$\%_{change}$
G7	*D*/150	56.0	
	D/200	56.3	+0.5
	D/100	55.2	-1.4
	D/50	53.3	-4.8
UK6	*D*/150	89.0	
	D/200	88.5	-0.5
	D/100	89.0	0.0
	D/50	90.0	+1.1
UK7	*D*/150	43.5	
	D/200	43.2	-0.6
	D/100	43.5	0.0
	D/50	43.6	+0.2

There is slight change in the shear strength for the changes in imperfection magnitudes for UK6 and UK7. However, the variation is the largest for G7. This shows that, for typical specimens with long panel, there is essentially no effect increasing the imperfection magnitude by as much as a factor of three.

8.3 Potential End Anchorage

Höglund (1997), describes that in order to fully develop the rotated stress field, the ends of the beam need to be anchored by a transverse short beam called a *rigid end post.* However, he recognizes that there is substantial post buckling strength even for non-rigid end posts. The reduction factor to be applied for non-rigid end post is slenderness parameter λ_w, which is given by Eq. 1-22. Table 1 Höglund (1997), gives the reduction factor to be applied for the girders with different end conditions (rigid and non-rigid end post). However, this table shows that there is no difference in the strengths for members with non-rigid end posts versus rigid end posts until the slenderness parameter is greater than 1.08.

To check the effect of the end anchorage on the shear strength, the specimen is checked with end details that may be considered as rigid end posts. The specimen selected for this study is UK6, because of it has the highest h/t_w (227).

Table 8-4 gives the change in shear strength with changes in end conditions. The original configuration of UK6, had a bearing stiffener over the support with 6 inches of overhang. To check the effect of potential end anchorage, the end conditions are varied as shown in the table. The end condition variations consisted of changing the overhang length

and also adding a stiffener at the free end of the specimen. As it can be seen from the Table. 8-4, there is no change in the shear strength with the change in the end conditions.

Höglund (1973), Eq. (x) specifies the conditions for end stiffeners to be classified as rigid end posts. The most important condition is that the distance between two stiffeners should be more than 0.18*h*. For the end condition involving a 12-in. overhang with a second stiffener at its end, this condition is satisfied. However, even for that condition there is no change in the shear strength of the specimen.

Table. 8-3. Change in shear strength with change in end conditions.

End condition	V_{sim} (kip)
6” overhang	89.0
3” overhang and stiffener at end	89.0
6” overhang and stiffener at end	89.0
12” overhang	89.0
12” overhang and stiffener at end	89.0

CHAPTER 9

SUMMARY AND CONCLUSIONS

The main objective of this research is to study the mechanism of shear strength development in built-up I-section members. FEA simulations are used to explain the development of web shear force for stiffened and unstiffened webs in their postbuckled condition. In Chapter 4, the experimental results and results from test simulations are compared and it is established that the simulation results match well with the experimental results at an overall level.

To explain the mechanisms of the shear force development, three specimens with varying aspect panel ratio are selected: Specimen G7 (a/h = 2) from Lee and Yoo (1999), and UK6 (a/h = 4.12) and UK7 (a/h = 8.04) from Daley and Davis (2015). The first of these girders has a stiffened web per traditional AISC design rules whereas the second two girders have unstiffened webs per AISC. To explain the mechanism of shear development, various cuts are made along the length of the specimens and the displacements and stresses developed are plotted on these cut sections. The failure pattern is almost same for UK6 and G7, with the predominant web buckles intersecting the flanges at the ends of the critical panel. However, for UK7 the predominant web buckle forms only over approximately one-half the length of the panel. In all the cases, it is found that substantial amount of diagonal tension is developed at the peak load. Basler's equations do not account for postbuckling strength for panels with $a/h > 3.0$ because the assumptions employed in their development predict that the angle of the principal diagonal tension with respect to the longitudinal axis of the member is relatively small. However, in this study it is confirmed that a considerable

amount of postbuckling strength is available even for unstiffened panels. For the unstiffened panels and near the mid-length of the stiffened panel, there is a decrease in the angle of the principal stresses at the web mid-depth from 45^o as the load is increased. This decrease is represented approximately by predictions from Höglund's (1997) rotated stress field theory. The diagonal tension developed in the web is maximum at the web mid-depth at the mid-length of the panel and decreases at the top and bottom of the web. Near the end of the panel corresponding to the upward reaction at the bottom of the girder, the tension field is predominant on the top half of the web. Also, through plots it is shown that, at the web mid-depth there is slight or no increase in the principal compressive stress after reaching the shear elastic buckling load of the web except for elements near the ends of the panel. It is also established that the shear stress *S12* is maximum at the location where the predominant shear buckles meet the flanges and is minimum in magnitude at the opposite end of the flange. The stress *S22* at top and bottom of the web remains low until near the peak load and the principal stresses until these load levels are predominantly due to the combined shear and flexural stresses. Through plots of *S11* it has been shown that there is an additional compressive stress in the flanges due to the anchorage of the longitudinal force defined by Höglund (1997). The stresses and displacements at the peak load are significantly larger than at load levels only slightly smaller than peak load. For the thicker half-span of Specimens UK6 and UK7, all the equations from beam theory are valid at all the load levels.

The behavior has some similarity to that of a Pratt truss; however, the diagonal tension behavior is more complex than that of a simple diagonal tension strut. Considerable diagonal tension is present throughout the web mid-depth at the higher levels of loads. As

the panel length is increased, many such diagonal struts are formed. Furthermore, the vertical compression at the transverse stiffener locations is more complex than that of a simple vertical compression strut. The web and the transverse stiffeners participate in developing the loads into the web at the supports and the applied load locations.

In addition, the boundary condition between the flange and web is studied in detail. For all the three specimens tested, it is found that the top-flange provides substantial torsional restraint to the top of the web throughout the loading and into post-peak. The web membrane force remains low until about 95% of the peak load is reached. However, considerable *S22* is developed at the post-peak stage proving that flanges are pushed and pulled at the post peak stage. This significant *S22* at the post peak stage governs the behavior of principal stresses, *S1* and *S2* at the flange and web juncture. This increase in *S22* at the post peak load occurred near the ends of the panel for UK6 and G7. However, due to high *a*/*h* for UK7, this pushing and pulling of flanges happens at a distance from the ends of the panel. The increase in *S22* near the mid-span and near the transverse stiffeners is associated with the development of the reaction at the left-hand end and the applied load at the mid-span into the member. The normal stress *S22* is maximum at peak load for Specimen UK6. This is because of higher h/t_w (227).

Lastly, the sensitivity of the shear strengths to flange thickness, web imperfection magnitude and potential end anchorage details is studied. The change in shear strength with changes in the flange thickness is relatively small for the girders studied. For UK7, this change was minimum. Frame action of the flanges, and the development of the normal stresses *S22* at web top and bottom and *S11* at web mid-depth with changes in the flange thickness are studied in detail. It is established that there is a slight contribution of the flanges from frame action. The influence of changing the flange thickness was largest for test UK6. This is due to a combination of its intermediate a/h and high h/t_w ratio. This

effect was almost negligible for UK7, because of its large *a/h*. The effect of changing the imperfection magnitudes is essentially zero for unstiffened webs with large *a/h*. For G7, which had *a/h* = 2,0, there is a small reduction in shear resistance as the web out-of-flatness becomes large. Different end conditions were considered for UK6 to study the effect of details providing potential end anchorage. It was found that there is no change in the shear strength for the cases with potentially larger end anchorage, even for the conditions that may be classified as a rigid-end posts.

APPENDIX A

PREDICTION EQUATIONS FOR STIFFENED PANELS

This appendix summarizes several prominent prediction models for stiffened webs. White and Barker (2008) and Ziemian (2010) provide an overview of the corresponding theories.

1. Basler's Model

Basler (1961) takes tension field action into account for stiffened panels. His idealization to the postbuckling contribution to the strength is:

$$V_{PB} = \frac{0.87(1-C_v)}{\sqrt{1+(a/h)^2}} V_p \tag{A-1}$$

The total shear strength is hence specified as the sum of buckling and postbuckling resistances:

$$V_n = \left(C_v + \frac{0.87(1-C_v)}{\sqrt{1+(a/h)^2}} \right) V_p \tag{A-2}$$

where,

V_p is the plastic shear strength, $V_p = 0.6F_yA_w$

C_v is calculated using Eq. 1-8 and Eq. 1-9.

2. Lee and Yoo's Model

Lee and Yoo (1998) recommended quantifying postbuckling strength by Eq. 1-18 (Section 1.2.4). They expressed the ultimate shear strength using Eq. 1-19 with C values

from Eqs. 1-20 through 1-22. However, they concluded that the shear strength is influenced by geometric imperfection effects. To account for these effects, Lee et al. (2008) introduced the term R_d in Eq. 1-19:

$$R_d = 0.8 \text{ if } h/t_w < 1.12\sqrt{k_v E/F_y} \tag{A-3}$$

$$R_d = 0.8 + 0.2\frac{h/t_w\sqrt{F_y/(k_v E)} - 1.12}{1.12} \text{ for } 1.12\sqrt{k_v E/F_y} \le h/t_w \le 2.24\sqrt{k_v E/F_y} \tag{A-4}$$

$$R_d = 1 \text{ for } h/t_w > 2.24\sqrt{k_v E/F_y} \tag{A-5}$$

The total strength is then expressed as

$$V_n = R_d V_p (0.6C_v + 0.4) \tag{A-6}$$

In this study, the strength using Lee et al. is determined, with using R_d and without using R_d. This is because, Lee and Yoo (1999) do not consider the imperfection factor. Furthermore, recommendations by Yoo (2015) to the AISC (2016) Specification committee do not include the imperfection factor. However, Lee and Yoo (1998) propose the above equations for R_d.

3. Daley et al. (2016) Model

The model proposed by Daley et al. (2016) is presented in Section 1.2.5. AISC (2016) allows this model to be used for stiffened web panels as well, with k_v calculated using Eq. (1-10). AISC (2016) allows these equations to be used for stiffened panels. The Specification permits the nominal shear resistance to be taken as the larger of the strengths predicted from these equations or Eq. A-2.

4. Daley et al. (2016) Model with Contribution from Frame Action

The contribution from frame action of the flanges given by Höglund (1995, 1996 and 1997) may be written generally as

$$V_f = \frac{2m_{pft}}{c_t} + \frac{2m_{pfb}}{c_b} \tag{A-7}$$

where m_{pft} and m_{pfb} are the plastic bending resistances of the top and bottom flange. Höglund (1997) recommends that, for stiffened I-section members, the shear resistance may be calculated simply by adding this frame action contribution to the contribution from the web, which is expressed using the same equation as for unstiffened webs. The AISC (2016) Specification does not include this contribution, in the spirit of simplifying the calculations. However, it is correct conceptually for this contribution to be included with the web contribution quantified by Daley et al. (2016).

Various approximations for the frame action contribution of the flanges have been proposed in the literature. One simple estimate is (White and Barker 2008)

$$m_{pf} = \frac{F_y b_f t_f^{\,2}}{4}\left[1-\left(M / M_n\right)^2\right] \geq 0 \tag{A-8}$$

The term M in this expression is the maximum girder bending moment within the web panel, and M_n is taken as the overall nominal flexural resistance of the girder.

Höglund (1971, 1995,1996 and 1997) suggests the following equation for c_t and c_b:

$$c = a\left(0.25 + 6.4\frac{m_{pf0}}{t_w h^2 F_{yw}}\right) \leq a \tag{A-9}$$

where, m_{pf0} = plastic bending resistance of the flange element corresponding to M = 0. White and Barker (2008) adopt this equation for the c values in Eq. (A-7). The subscripts t and b are appended to the "c" variables in Eq. (A-7) to denote the top and bottom flange.

REFERENCES

AISC. (2015) *Specification for Structural Steel Buildings.* ANSI/AISC 360-15, Chicago, IL.

AISC. (2010) *Specification for Structural Steel Buildings.* ANSI/AISC 360-10, Chicago, IL.

AISC. (1986) *Specification for Structural Steel Buildings – Load and Resistance Factor Design,* 1st Ed., Chicago, IL.

AISC. (1963) *Specification for the design, fabrication and erection of Structural Steel for Buildings*, 6th Ed., New York.

AASHTO (2015). *LRFD Bridge Design Specifications,* American Association of Highway and Transportation Officials., Washington, D.C.

Basler, K. (1960). "Web Buckling Tests on Welded Plate Girders." Welded Plate Girders Report No. 251-11, Lehigh University Libraries, Bethlehem, PA.

Basler, K. (1961). "Strength of Plate Girders in Shear*." Journal of the Structural Division*, 87(ST7), 151-180.

Bleich, F. (1952). *Buckling Strength of Metal Structures.*, McGraw-Hill, New York.

*"*Bridge Welding Code., A Joint Publication of AASHTO and American Welding Society." (2002). *AASHTO/AWS D1.5M/D1.5:2002,* AASHTO, Washington D.C. and AWS Miami, FL.

Bulson, P.S. (1970). *The Stability of Flat Plates.*, Richard Clay Ltd., Bungay, Suffolk.

CEN (2006). *Eurocode 3: Design of Steel Structures – Part 1-5: Plated Structural Elements. EN 1993-1-5*, European Committee for Standardization, Brussels, Belgium.

Daley, A. and Davis, B. (2015). "Shear Strength of Prismatic Steel I-Shaped Members," Research Report, Metal Building Manufacturers Association, Cleveland, Ohio.

Daley, A., Davis, B. and White, D.W. (2016). "Shear Strength of Unstiffened Steel-I Section Members," *Journal of Structural Engineering*, ASCE, (to appear).

Höglund, T. (1971). "Behaviour and Strength of the Web of Thin Plate I-Girders", *Bulletin No. 93, Building Statics and Structural Engineering", The Royal Institute of Technology*, Stockholm, Sweden.

Höglund, T. (1973). “Design of Thin Plate I-Girders in Shear and Bending, with Special Reference to Web Buckling”, *Bulletin No. 94, Division of Building Statics and Structural Engineering, Royal Institute of Technology*, Stockholm, Sweden.

Höglund, T. (1995). “Strength of Steel and Aluminum Plate Girders- Shear buckling and overall buckling of trapezoidal webs – Comparisons with test.” *Technical Rep No. 1995:4-Steel Structures*, Dept. of Structural Engineering, Royal Institute of Technology, Stockholm, Sweden.

Höglund, T. (1996). “Shear Buckling Resistance of Steel and Aluminum Plate Girders.” *Proc., Bicentenary Conf. on Thin Walled Structures,* Univ. of Strathclyde, Glasgow, Scotland, U.K.

Höglund, T. (1997). “Shear Buckling Resistance of Steel and Aluminum Plate Girders.” *Thin-Walled Structures*, 29(1-4), 13-30.

Kim, Y.D. (2010). "Behavior and Design of Metal Building Frames Using General Prismatic and WebTapered Steel I-Section Members." Doctoral Dissertation, Georgia Institute of Technology, Atlanta, GA.

Lee, S.C., Davidson, J.S., and Yoo, C.H. (1996). “Shear Buckling Coefficients of Plate Girder Web Panels.” *Journal of Computers and Structures*, 59(5), 789-795.

Lee, S.C., and Yoo, C.H. (1998). “Strength of Plate Girder Web Panels under Pure Shear.” *Journal of Structural Engineering*, 124(2), 184-194.

Lee, S.C., and Yoo, C.H. (1999). “Experimental Study on Ultimate Shear Strength of Web Panels.” *Journal of Structural Engineering*, 125(8), 838-846.

Lee, S.C., Lee, D.S., and Yoo, C.H. (2008). “Ultimate Shear Strength of Long Web Panels.” *Journal of Constructional Steel Research*, 64(12), 1357-1365.

Prawel, S.P., Morrell, M.L., and Lee, G.C. (1974). "Bending and Buckling Strength of Tapered Structural Members*." Welding Research Supplement*, 53, 75-84.

Simulia (2013). ABAQUS/Standard Version 6.13-1, Simulia, Inc, Providence, RI.

Subramanian, L.P.P. (2015). "Flexural Resistance of Longitudinally Stiffened Plate Girders." Doctoral Dissertation, Georgia Institute of Technology, Atlanta, GA.

Studer, P.S. and Davis B. (2012). *"*Shear Strength of Web-Tapered I-Shaped Members.*"* Master’s Thesis, University of Kentucky, Lexington, KY.

Vincent, G.S. (1969). “Tentative Criteria for Load Factor Design of Steel Highway Bridges.” *AISI Bulletin No. 15*, American Iron and Steel Institute, Washington, D.C.

Wagner, H. (1931), *"Flat sheet metal girder with very thin metal web." Tech Memo. 604-606. National Advisory Committee for Aeronautics*, Washington, D.C.

White, D.W. and Barker, M.G. (2008). "Shear Resistance of Transversely Stiffened Steel I-Girders." *Journal of Structural Engineering*, 134(9), 1425-1426.

Yoo, C.H., and Lee, S.C. (2006). "Mechanics of Web Panel Post-buckling Behavior in Shear." *Journal of Structural Engineering*, 132(10), 1580-1589.

Yoo, C.H. (2015). Recommendation for changes to AISC (2016) Specifications, Chapter G.

Ziemian, R.D. (2010). *Guide to Stability Design Criteria for Metal Structures*, 6th ed., Structural Stability Research Council, John Wiley & Sons, Hoboken, N.J.